

DOCTORAL THESIS



Solar Wind Ions Inside the Induced Magnetosphere of Mars

Catherine Dieval



PhD thesis

Solar wind ions inside the induced magnetosphere of Mars

Catherine Diéval

14 December 2012

Department of Computer Science, Electrical and Space Engineering
Division of Space Technology
Graduate School of Space Technology
Luleå University of Technology
Rymdcampus 1
98 128 Kiruna, Sweden

Swedish Institute of Space Physics
Box 812
98 128 Kiruna, Sweden

Printed by Universitetstryckeriet, Luleå 2012

ISSN: 1402-1544
ISBN 978-91-7439-525-9

Luleå 2012

www.ltu.se

ABSTRACT

The subject of the thesis is analysis and modeling of the entry, transport, and atmospheric precipitation of solar wind ions, H^+ and He^{2+} , into the induced magnetosphere of Mars. The solar wind is a flow of charged particles emitted by the Sun. The solar wind carries with it a magnetic field, the interplanetary magnetic field (IMF). The IMF piles up on the dayside of the non-magnetized Mars and is then convected towards the nightside. The solar wind ions can normally not cross the magnetic barrier, formed by the pile up IMF. However, in situ observations by the Mars Express spacecraft reveal that downward moving solar wind H^+ and He^{2+} are sometimes present in the Martian ionosphere, below the magnetic barrier. The gyroradii of shocked solar wind ions may be comparable to the size of the dayside Martian magnetic barrier and for certain circumstances, these ions can gyrate through. Observations by Mars Express are used to analyze H^+ and He^{2+} penetrating through the magnetic barrier and precipitating into the Martian ionosphere, identified by the presence of ionospheric photo-electrons. A case study shows evidence of narrower energy distributions for H^+ (with energy \geq solar wind energy), as the spacecraft moves down in altitude. From this, the study concludes that the magnetic barrier prevents the lower energy H^+ , from reaching low altitudes. The thesis also describes a statistical study of precipitating H^+ fluxes, which indicate that H^+ precipitation is rare (detected during 3% of the dayside observation time only) and carries on average 0.2% of the upstream solar wind particle flux. In another statistical study, the thesis shows that the precipitation of H^+ and He^{2+} decreases even further when Mars encounters solar wind pressure pulses. A possible explanation is that the enhanced mass loading of the magnetic field flux tubes by planetary heavy ions, while the tubes drag through the ionosphere at lower altitudes, slows down their velocity and allows more magnetic flux to pile up. The magnetic barrier becomes a more effective obstacle to the solar wind ion precipitation. Furthermore, the thesis describes a model of H^+ precipitation onto the Martian upper atmosphere using a hybrid code of the Mars solar wind interaction. The spatial patterns of the precipitation depend on the H^+ energy, on the H^+ origin (solar wind or generated from the hydrogen corona) and on the altitude. Some features of the observed H^+ distributions are reproduced by simulations, while others are not, indicating a more complex physics than in the model. The thesis also describes a model study of transport of H^+ , fast H atoms and He^{2+} through the atmosphere using a Direct Simulation Monte Carlo model. This study demonstrates the crucial role of the magnetic field in determining the energy deposition of the solar wind ions in the topside atmosphere. For instance, a horizontal magnetic field with strength of 50 nT backscattered almost all H^+ , thus preventing these particles to deposit their energy at lower altitudes. The conclusion of the thesis work is that although some solar wind ions do precipitate, the magnetic barrier effectively protects the ionosphere from precipitating solar wind ions.

Large sections of this thesis are reproduced from a licentiate thesis (*Diéval, 2011*). Papers 1, 2, 4, 5 and 6, and figures 1.6, 3.3, 3.5, 4.1, 4.2 and 4.3 are reproduced with permission of American Geophysical Union. Paper 3 is reproduced with permission of Terrapub. Figure 1.1 is reproduced with permission of InterScience publishers New York. Figure 1.2 is reproduced with permission of Springer Verlag Berlin Heidelberg New York. Figure 1.3 is reproduced with permission of Cambridge University Press. Figures 1.5, 1.7 and 2.1 are reproduced with permission of Springer Science and Business Media.

SAMMANFATTNING

Ämnet för avhandlingen är analys och modellering av inflödet av solvindsjoner, H^+ och He^{2+} , genom Mars inducerade magnetosfär. Solvinden är ett flöde av laddade partiklar från Solen. Solvinden bär med sig ett magnetfält, det så kallade interplanetära magnetfältet (IMF). IMF packas ihop framför dagsidan av planeten innan det tar sig vidare mot nattsidan. Solvindsjoner kan vanligtvis inte passera denna magnetiska barriär som skapas då IMF packas ihop. Dock avslöjar in situ-observationer av rymdsonden Mars Express att nedåtflydande H^+ och He^{2+} från solvinden ibland påträffas inuti Mars jonosfär, nedanför den magnetiska barriären. Gyroradierna hos solvindsjoner i shockregionen kan vara jämförbara med storleken av den magnetiska barriären över Mars dagsida och i vissa fall kan jonerna gyrera igenom barriären. Observationer från Mars Express används för att analysera H^+ och He^{2+} som tar sig igenom den magnetiska barriären och ner i Mars jonosfär, vilken identifieras genom närvaron av jonosfäriska fotoelektroner. En fallstudie visar tecken på smalare energifördelningar av H^+ (med energi \geq solvindens energi), ju lägre rymdsonden tog sig. Från detta slutleder studien att den magnetiska barriären reflekterar H^+ med lägre energi och förhindrar dem från att nå lägre altituder. Avhandlingen beskriver även en statistisk studie av inflödande H^+ , vilken indikerar att inflödet av H^+ är sällsynt (observeras enbart under 3% av observationstiden över dagsidan) och bär i genomsnitt med sig 0.2% av partikelflödet som finns uppströms i solvinden. I en annan statistisk studie visar avhandlingen att inflödet av solvindsjonerna H^+ och He^{2+} minskar ytterligare när Mars möter tryckpulser i solvinden. En möjlig förklaring är att den ökade masslastningen av magnetfältets av tunga planetära joner, då magnetfältet släpas genom jonosfären på lägre höjd, bromsar upp magnetfältet och orsakar ytterligare hoppackning av magnetfältet. Det gör den magnetiska barriären till ett mer effektivt hinder för inflödet av solvindsjoner. Vidare beskriver avhandlingen en modell för inflöde av H^+ till Mars övre atmosfär genom att använda en hybridkod för Mars växelverkan med solvinden. Mönster i utbredningen av inflödet beror på energin hos H^+ , på källan till H^+ (solvinden eller skapad från vätekoronan), och på altituden. Vissa egenskaper hos H^+ -fördelningarna återskapas av simuleringar, medan andra inte gör det, vilket tyder på en mer komplicerad fysik än i modellen. Avhandlingen beskriver också en modellstudie av transport av H^+ , snabba H atomer, och He^{2+} genom atmosfären med en Direct Simulation Monte Carlo modell. Denna studie demonstrerar den avgörande roll som magnetfältet har i att bestämma energin som solvindsjoner avlämnar i den övre atmosfären. Till exempel reflekterade ett horisontellt magnetfält på 50 nT nästan allt H^+ , och förhindrade dessa partiklar från att avlämna sin energi på lägre altituder. Slutsatsen av avhandlingen är att även om vissa solvindsjoner tar sig igenom, så är den magnetiska barriären ett effektivt skydd av jonosfären mot infallande solvindsjoner.

APPENDED PAPERS

- **Paper 1:** C. Diéval, E. Kallio, S. Barabash, G. Stenberg, H. Nilsson, Y. Futaana, M. Holmström, A. Fedorov, R. A. Frahm, R. Järvinen and D. A. Brain, A case study of proton precipitation at Mars: Mars Express observations and hybrid simulations, *J. of Geophys. Res.*, 117, A06222, doi: 10.1029/2012JA017537, 2012.
- **Paper 2:** V. I. Shematovich, D. V. Bisikalo, C. Diéval, S. Barabash, G. Stenberg, H. Nilsson, Y. Futaana, M. Holmström and J.-C. Gérard, Protons and hydrogen atoms transport in the Martian upper atmosphere with an induced magnetic field, *J. of Geophys. Res.*, 116, A11320, doi: 10.1029/2011JA017007, 2011.
- **Paper 3:** C. Diéval, E. Kallio, G. Stenberg, S. Barabash and R. Järvinen, Hybrid simulations of proton precipitation patterns onto the upper atmosphere of Mars, *Earth Plan. Space*, 64, 121-134, doi: 10.5047/eps.08.015, 2012.
- **Paper 4:** C. Diéval, G. Stenberg, H. Nilsson and S. Barabash, A statistical study of proton precipitation onto the Martian upper atmosphere: Mars Express observations, *under revision for J. of Geophys. Res.*, 2012.
- **Paper 5:** C. Diéval, G. Stenberg, H. Nilsson, N. J. T. Edberg and S. Barabash, Reduced proton and alpha particle precipitations at Mars during solar wind pressure pulses: Mars Express results, *submitted to J. of Geophys. Res.*, 2012.
- **Paper 6:** V. I. Shematovich, D. V. Bisikalo, G. Stenberg, S. Barabash, C. Diéval and J.-C. Gérard, He²⁺ transport in the Martian upper atmosphere with an induced magnetic field, *submitted to J. of Geophys. Res.*, 2012.

CONTENTS

ABSTRACT	iii
SAMMANFATTNING	v
APPENDED PAPERS	vii
TABLE OF CONTENTS	ix
ACKNOWLEDGEMENTS	xi
CHAPTER 1 – THE MARS-SOLAR WIND INTERACTION	1
1.1 Mars	1
1.2 The solar wind	1
1.2.1 The solar wind and the interplanetary medium	1
1.2.2 Solar wind disturbances	3
1.2.3 Solar wind interaction with a non-magnetized obstacle	4
1.3 The structure of the Martian induced magnetosphere	6
1.3.1 The bow shock and the magnetosheath	7
1.3.2 The induced magnetosphere boundary (IMB) and the magnetic barrier	7
1.3.3 The ionosphere and the photoelectron boundary (PEB)	9
1.3.4 The magnetotail	10
1.3.5 Crustal magnetic fields	11
CHAPTER 2 – INSTRUMENTATION AND MODELING TOOLS	15
2.1 Spacecraft and instruments	15
2.1.1 Mars Express	15
2.1.2 ACE	18
2.1.3 MGS	18
2.2 Modeling techniques	18
2.2.1 Hybrid modeling	18
2.2.2 Direct Simulation Monte Carlo (DSMC) modeling	20

CHAPTER 3 – SOLAR WIND PARTICLE PRECIPITATION INTO THE MARTIAN IONOSPHERE	21
3.1 A mechanism for the solar wind ion precipitation	21
3.2 Proton precipitation	22
3.2.1 Observations	22
3.2.2 Modeling	24
3.3 Alpha particle precipitation	26
3.3.1 Observations	26
3.3.2 Modeling	27
3.4 Electron precipitation	27
3.5 ENA precipitation	28
CHAPTER 4 – ATMOSPHERIC EFFECTS OF SOLAR WIND ION PRECIPITATION ON MARS	31
4.1 Energy deposition of H/H ⁺ in the atmosphere	31
4.2 Backscattering of H from the atmosphere	35
4.3 Helium balance	36
CHAPTER 5 – SUMMARY OF PAPERS	37
5.1 Paper 1	37
5.2 Paper 2	38
5.3 Paper 3	38
5.4 Paper 4	39
5.5 Paper 5	39
5.6 Paper 6	40
REFERENCES	41
PAPER I	49
PAPER II	63
PAPER III	75
PAPER IV	91
PAPER V	115
PAPER VI	131

ACKNOWLEDGEMENTS

I acknowledge funding from the Swedish National Graduate School of Space Technology, the organizers of the 5th Alfven Conference in Sapporo (4–8 October 2011) and Kungliga Vetenskapsakademien.

I thank the other young IRF scientists: Charles Lue, Maria Smirnova, Shahab Fatemi, Maria Mihalikova, Rikard Slapak, Katarina Axelsson, Joan Stude, Joel Arnault, Jesper Lindkvist, Robin Ramstad, and Xiao Dong Wang.

I thank Stas Barabash, Hans Nilsson and Gabriella Stenberg for their supervision. Special thanks are due to Gabriella and Hans for taking the time to read my papers and thesis. I also thank the coauthors of my work. Special thanks are due to Esa Kallio for our fruitful collaboration.

I thank the rest of the IRF staff for their help on diverse occasions.

Finally, I thank Gerrit Holl for enriching my life, and I thank my parents.

The Mars-solar wind interaction

1.1 Mars

Mars is a terrestrial planet with a thin atmosphere that is dominated by carbon dioxide. Its geological features on the surface include canyons, deserts and volcanoes. Its geomorphology and mineralogy suggest that liquid water was once present on the surface (see e.g. the review by *McKay and Stoker*, 1989). However, other studies suggest instead that flow features on the surface were caused by CO₂ in liquid and gaseous phases (see e.g. *Hoffman*, 2000).

Currently, water exists as ice at and beneath the surface (e.g. *Schultz*, 2011). The atmospheric temperature and pressure today are too low for liquid water to exist on the surface. It would freeze and sublimate.

For many years, it was debated whether or not Mars possesses an internal magnetic field. Some authors claimed that Mars does not have an internal magnetic field (e.g. *Riedler et al.*, 1989), while others suggested that there may be a weak magnetic moment (e.g. *Dolginov*, 1978). It was finally established that the upper limit of the dipole moment is $2 \times 10^{21} \text{ G cm}^3$ (*Acuna et al.*, 1998), which is very weak compared with Earth, which has a dipole moment of $1 \times 10^{26} \text{ G cm}^3$. There also exists localized crustal magnetic fields whose strength can reach up to 220 nT at 400 km altitude in the southern hemisphere (see Section 1.3.5).

Table 1.1 provides further information about Mars and compares its physical properties with Earth.

1.2 The solar wind

1.2.1 The solar wind and the interplanetary medium

The solar wind is a plasma (a gas of charged particles) that is emitted outward from the Sun at supersonic speeds. It is set up by the pressure gradient between the solar

Parameter	Mars	Earth
Radius [km]	3397	6371
Mass [kg]	6.4×10^{23}	6.0×10^{24}
Average distance to the Sun [astronomical unit AU]	1.52	1.00
Orbital period [Earth days]	687	365
Average equatorial gravity [m s^{-2}]	3.7	9.8
Magnetic dipole moment [G cm^3]	$<2 \times 10^{21}$	1×10^{26}
Average surface pressure [bar]	0.01	1.01
Average surface temperature [K]	210	287
Average scale height at the surface [km]	11	8
Atmospheric composition	CO ₂ dominated (96%), traces of N ₂ , Ar	78% N ₂ , 21% O ₂ , traces of Ar, CO ₂ , H ₂ O

Table 1.1: Basic facts concerning Mars and Earth.

upper atmosphere and the interstellar medium in the presence of gravity. The major ions in the solar wind are protons H^+ . The solar wind also contains alpha particles He^{2+} (5%) and traces of oxygen, carbon, iron and other minor ions. The solar wind speed in the inner solar system typically varies from 300 km s^{-1} to 800 km s^{-1} . The solar wind number density decreases quadratically with distance from the Sun and is typically 2.5 cm^{-3} at Mars' orbit.

The Sun's magnetic field is frozen into the plasma flow and is carried with the solar wind, away from the Sun, while the footpoints of the magnetic field remain fixed in the solar atmosphere. This field is called the interplanetary magnetic field (IMF). The Sun's rotation causes magnetic field lines to form a spiral called the Parker spiral (*Parker*, 1963), similar to water emanating from a rotating garden hose (see Figure 1.1). Magnetic field lines have a more radial orientation close to the Sun, for a given solar wind speed (see Figure 1.1). At Mars' orbit, the Parker angle, the angle between the IMF and the Mars-Sun line, is typically 57° . The IMF strength decreases with distance from the Sun, and is typically 3 nT at Mars' orbit.

Solar activity follows an 11-year cycle. During the solar minimum, slow and dense solar wind streams are emitted from solar equatorial regions, while fast and tenuous solar wind streams are emitted from polar regions. During the solar maximum, the Sun is more active, and fast and slow streams are emitted from all latitudes.

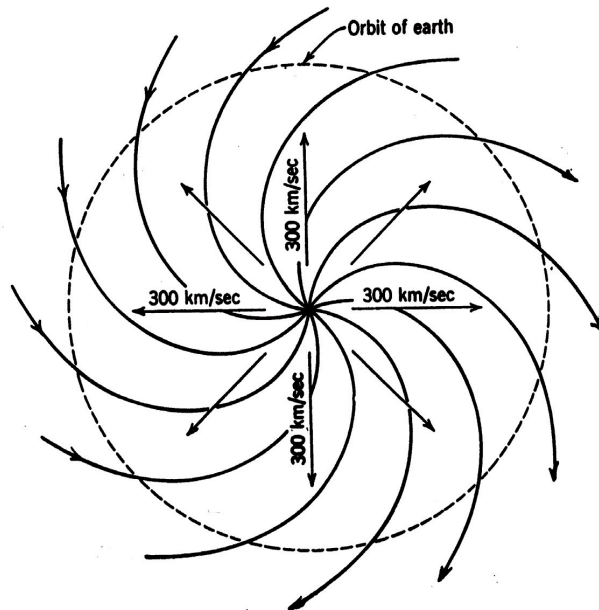


Figure 1.1: The solar magnetic field and solar wind in an inertial frame. The solar wind expands radially at 300 km s^{-1} . The Sun rotates anticlockwise and the view is from above the ecliptic plane. The figure is adapted from *Parker (1963)*.

1.2.2 Solar wind disturbances

Two important solar wind disturbances are corotating interaction regions (CIRs) and interplanetary coronal mass ejections (ICMEs).

1.2.2.1 CIRs

CIRs are recurrent disturbances of the interplanetary medium (e.g. *Hundhausen, 1972*), which follow the Parker spiral and corotate with the Sun. CIRs are formed when a fast solar wind stream overtakes a slow solar wind stream ahead and runs away from it (see Figure 1.2). A compression region with high density forms in the rear of the slow solar wind. A rarefaction region with low density forms in the rear of the fast stream. The compression region can have densities of several tens of cm^{-3} . The interplanetary magnetic flux tubes, carried by the solar wind flow, are also compressed across the CIR, and large magnetic field strengths are observed there (several tens of nT). An observer encountering such a structure would see a rapid rise in the solar wind speed, followed by a slow decrease. The typical duration of a CIR passage is 1 to 2 days to pass across an observer in the solar wind. CIRs can also develop shocks, which is more likely to happen beyond 1 AU.

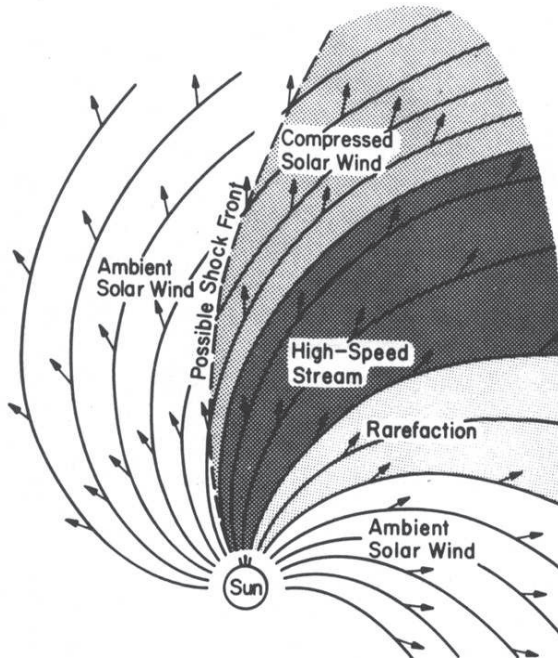


Figure 1.2: Schema of the interaction between a fast solar wind and slow solar wind. The view is from above the ecliptic plane. The figure is taken from *Hundhausen* (1972).

1.2.2.2 ICMEs

Coronal mass ejections (CMEs) are transient ejections of large amounts of plasma and twisted magnetic field lines from the Sun (see Figure 1.3). A CME moving faster than the ambient solar wind creates a shock front and a compression region characterized by a hot and dense shocked solar wind. CMEs are often characterized by a slow rotation of the magnetic field vector. Common characteristics of CMEs include large magnetic field strength, low plasma temperature, high charge state of ions and energetic particle signatures (*Jian et al.*, 2006). An ICME corresponds to the propagation of a CME in the interplanetary medium. It typically takes 1 to 2 days for an ICME to pass across an observer in the solar wind. ICMEs are more frequent during periods of high solar activity.

1.2.3 Solar wind interaction with a non-magnetized obstacle

The ionized upper part of the Martian atmosphere, the so-called ionosphere, is conductive, primarily due to the photoionization of atmospheric neutrals by solar

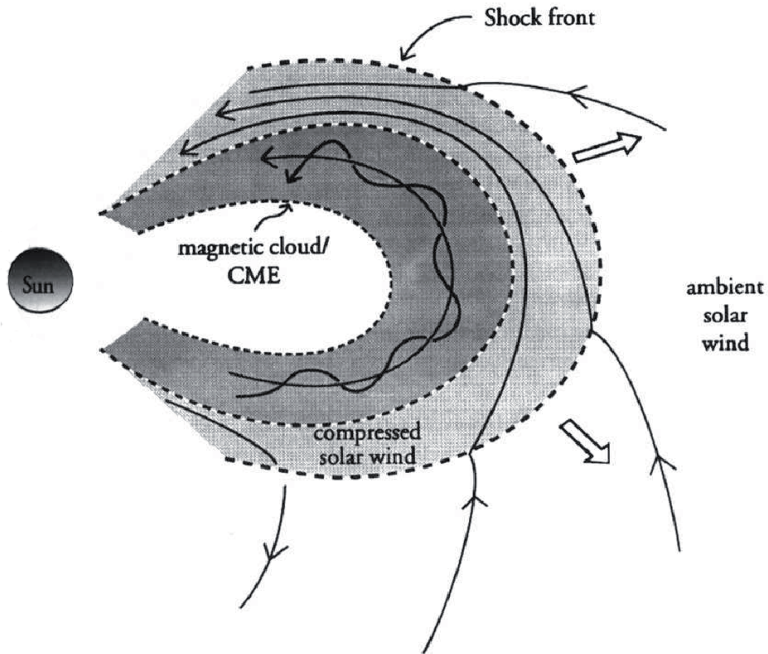


Figure 1.3: Sketch of a CME preceded by a shock. The figure is taken from *Cravens* (1997).

extreme ultraviolet (EUV) radiation (10–100 nm). A moving magnetic field generates currents in such a conductive obstacle (Faraday’s law). The magnetic field produced by these currents diverts the solar wind. The superposition of the induced magnetic field and the IMF corresponds to a magnetic pile-up and results in the creation of the magnetic barrier or the magnetic pile-up region. The IMF thus starts draping around the planet. Magnetic field tubes can penetrate into the topside of the partially conductive ionosphere. These magnetic flux tubes start to drag ionospheric ions with them and thus the flux tubes move slower than their “ends” in the solar wind. This process is called mass loading. Mass-loaded field lines slip over the terminator region and stretch into a magnetotail on the nightside. A boundary analogous to a magnetopause forms in which the magnetic field strength strongly increases and the solar wind flux terminates. This boundary is referred to as the induced magnetosphere boundary (IMB) (see Section 1.3.2). A structure resembling a “common” magnetosphere is formed and is referred to as an induced magnetosphere (see Figure 1.4). The induced magnetosphere is defined by *Zhang et al.* (2008) as the region near a planet and its wake where the magnetic pressure dominates the other pressure contributions.

The interaction of the solar wind with the Martian upper atmosphere leads to the energization of planetary ions (see e.g. *Dubinin et al.*, 2011). These ions flow tailward (they flow away from the Sun) and can escape into space. This mechanism is thought to be responsible for part of the water loss over Martian history. It was probably especially effective in the past when the Sun was young and more active (see e.g. *Terada et al.*, 2009). Extreme solar wind conditions still exist nowadays, such as CIRs and ICMEs, which can significantly increase the atmospheric loss (e.g. *Edberg et al.*, 2010; *Nilsson et al.*, 2011).

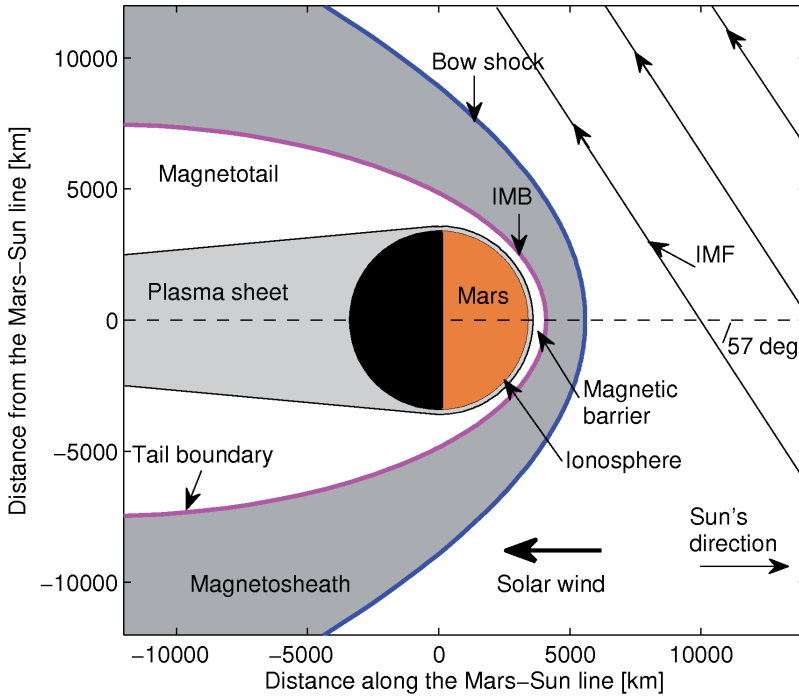


Figure 1.4: The structure of the Martian plasma environment. The Sun is located to the right. The dashed line indicates the Mars-Sun line. IMF is also shown. They make an angle of 57° with the Mars-Sun line.

1.3 The structure of the Martian induced magnetosphere

The Martian plasma environment includes the following domains: the magnetosheath, the magnetic barrier, the magnetotail, the ionosphere and the crustal magnetic

anomalies (Figure 1.4).

1.3.1 The bow shock and the magnetosheath

The conductive ionosphere acts as an obstacle which deviates the solar wind. To enable this, a shock forms in the flow upstream of Mars: the bow shock. At the bow shock, the solar wind flow slows down from supersonic to subsonic speed.

The subsolar bow shock is typically located at a distance of 1.64 Martian radii (R_m) from the center of Mars, i.e., at an altitude of 2200 km (Vignes *et al.*, 2000). At the terminator, the bow shock is located further from Mars in the southern hemisphere than in the northern hemisphere (Edberg *et al.*, 2008). A possible explanation is that in the southern hemisphere, localized magnetic fields are present in the Martian crust, and these fields act as obstacles and may push the bow shock outwards (see Section 1.3.5). At the terminator, the bow shock also moves outwards when the solar EUV flux increases (e.g. Edberg *et al.*, 2009). An increased EUV flux increases the number density of ions produced by the photoionization of the upper neutral atmosphere. These ions add mass to the solar wind and decelerate the solar wind flow due to momentum conservation. The mass loading increases the plasma pressure in the magnetosheath, which pushes the bow shock out. In addition, when the solar wind dynamic pressure increases, the bow shock moves inwards (e.g. Edberg *et al.*, 2009).

At the bow shock, the kinetic energy of the solar wind is converted into thermal energy. The region of heated and turbulent solar wind plasma downstream of the bow shock is called the magnetosheath. The magnetosheath magnetic field is more turbulent and stronger than in the undisturbed solar wind. At the subsolar point, the hot and compressed plasma flows very slowly and stagnates. As the magnetosheath plasma sweeps past the planet, the plasma becomes cooler, less dense and flows faster.

1.3.2 The induced magnetosphere boundary (IMB) and the magnetic barrier

During the early exploration of Mars, different instrument teams using measurements from different instruments gave different names to the boundary where the solar wind flux terminates: the planetopause (Riedler *et al.*, 1989), the magnetopause (e.g. Lundin *et al.*, 1989), the protonopause (Sauer *et al.*, 1994), the ion composition boundary (Breus *et al.*, 1991), the magnetic pile-up boundary (e.g. Vignes *et al.*, 2000) and the IMB (Dubinin *et al.*, 2006a). In later years, all of these boundaries were found to be collocated (Dubinin *et al.*, 2006a) The term induced magnetosphere boundary (IMB) is used in the remainder of this thesis. The IMB separates the magnetosheath from the magnetic barrier. In the magnetic barrier, the solar magnetic field piles up, magnetic turbulence disappears and the solar wind flux vanishes.

The subsolar IMB is typically located at a distance of 1.19 R_m from the center of Mars, i.e. at an altitude of 650 km (Trotignon *et al.*, 1996). The IMB at the terminator seems to move inward when the solar UV flux increases. This may be a result of

increased pressure in the magnetosheath that is caused by the additional mass of ionized ions through the solar wind mass loading (*Edberg et al.*, 2009). The IMB at the terminator is also pushed inwards when dynamic solar wind pressure increases (e.g. *Dubinin et al.*, 2006a).

The magnetic field strength in the magnetic barrier depends on the altitude and the solar zenith angle (SZA). The SZA is the angle of the Sun's direction from the vertical direction. The magnetic field strength increases at altitudes at and below the IMB. The strength decreases when the SZA increases at a fixed altitude. It typically reaches 30–50 nT at the subsolar point (e.g. *Akalın et al.*, 2010). The magnetic field pressure in the magnetic barrier is sufficient for balancing the solar wind dynamic pressure (*Dubinin et al.*, 2008c). Figure 1.5 shows observations of the induced magnetic field strength around Mars. The direction of the magnetic field in the pile-up region is mostly horizontal (parallel to the surface) on the dayside and more vertical (perpendicular to the surface) on the nightside due to stretching (e.g. *Cridner et al.*, 2001).

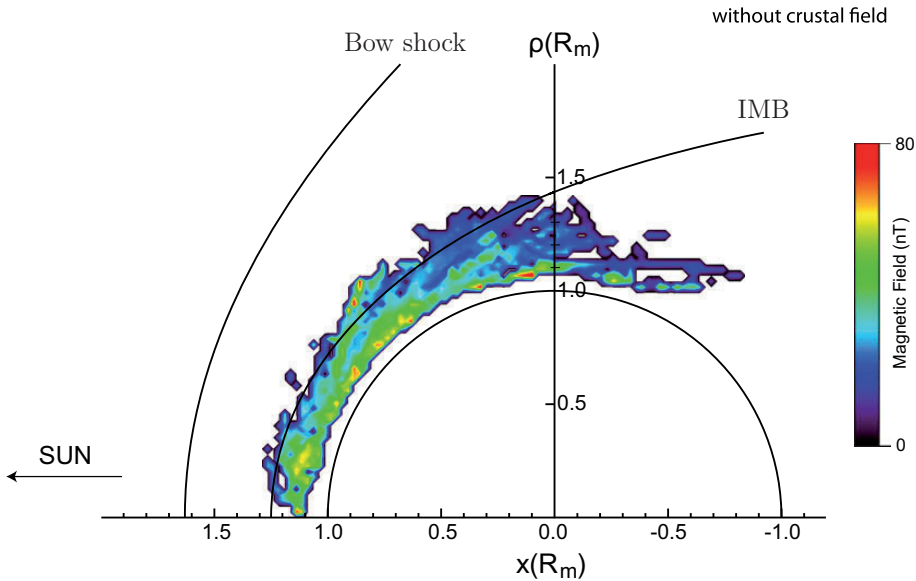


Figure 1.5: The distribution of the magnetic field strength around Mars, with the strong crustal fields removed. The positive horizontal axis points along the Mars-Sun line and the vertical axis is the distance from the Mars-Sun line. The figure is taken from *Akalın et al.* (2010).

1.3.3 The ionosphere and the photoelectron boundary (PEB)

The ionosphere is the ionized region of the atmosphere. Figure 1.6 shows the altitude profile for the number density of O^+ , O_2^+ , NO^+ and CO_2^+ ions. O_2^+ is the main ion species in the ionosphere, and it is formed by the dissociative recombination of CO_2^+ : $CO_2^+ + O \rightarrow O_2^+ + CO$. O^+ is also formed by the dissociative recombination of CO_2^+ : $CO_2^+ + O \rightarrow O^+ + CO_2$. CO_2^+ ions are formed by the photoionization of the major neutral species CO_2 : $CO_2 + h\nu \rightarrow CO_2^+ + e^-$ (see the review by *Nagy et al.* (2004) and the references therein).

The altitude profile of the ion number density is characterized by a main ionospheric peak (the F layer) due to solar EUV. The peak is a result of a balance between the increasing solar EUV flux and the decreasing neutral number density as altitude increases. The altitude of the ionospheric peak increases with the SZA (*Kliore, 1992*). On the dayside, the typical altitude of the ionospheric peak is 135 km. There also exist two other ionospheric peaks: the E layer (110 km altitude on the dayside) due to soft X-rays (1–10 nm) and the D layer (30 km altitude on the dayside) due to galactic cosmic rays.

Even in the absence of solar radiation on the nightside, a weak ionosphere still exists there. Either there is a flow of planetary ions from the dayside supplying new ions to the nightside (*Fränz et al., 2010*) or there is a precipitation of high-energy electrons ionizing the nightside atmosphere (e.g. *Fillingim et al., 2007*).

The topside of the Martian ionosphere is usually permeated by a large-scale IMF. For 85% of the time, the total ionospheric pressure in the Martian ionosphere is insufficient to withstand the solar wind dynamic pressure, which leads to a magnetized ionosphere (*Zhang et al., 1990*).

The photoionization of atmospheric neutrals by solar radiation produces photoelectrons. The ionospheric electron energy spectrum is dominated by two major photoelectron peaks (Figure 1.7), which are produced by the photoionization of CO_2 by the He 304 Å line at the dayside exobase. The exobase is the boundary below which the atmosphere is collisional. The energy of the photoelectron peaks is in the range 21–24 eV and at 27 eV. However, in Figure 1.7, the peaks appear at a lower than predicted energy, because the electrons were decelerated when arriving at the negatively charged spacecraft. The photoelectrons are observed at altitudes from the IMB down to 270 km (the lowest altitude of measurements by Mars Express, see Section 2.1.1) on the dayside and outside the Martian shadow on the nightside (*Frahm et al., 2006*). Nightside photoelectrons are likely to be formed on the dayside and travel to the nightside along magnetic field lines connecting the subsolar ionosphere and the solar wind (*Frahm et al., 2006*).

The PEB is an envelope for the ionospheric plasma, which is characterized by the presence of photoelectrons (*Frahm et al., 2006*). When the PEB is crossed inwards, the ionospheric electron density strongly increases (*Dubinín et al., 2008b*). .

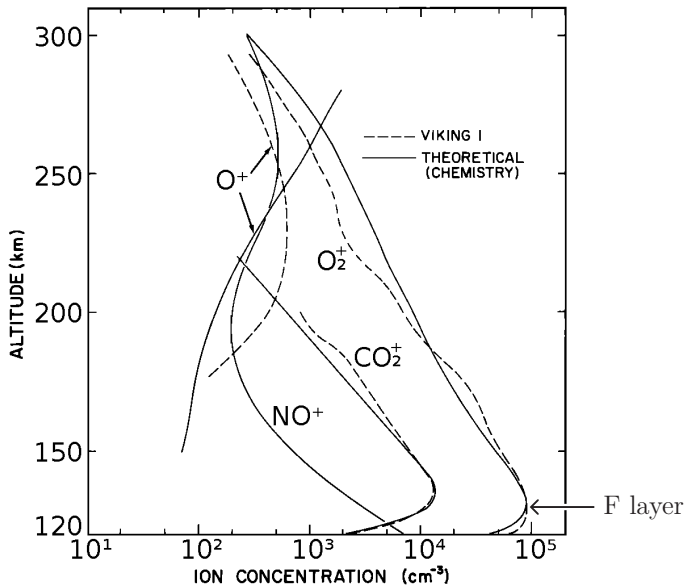


Figure 1.6: The altitude profiles of the ion densities O_2^+ , O^+ , NO^+ and CO_2^+ , observed by the Viking 1 lander (dashed lines) and predicted by a theoretical model (solid lines). The F layer is indicated. The figure is adapted from *Hanson et al.* (1977).

1.3.4 The magnetotail

At low altitudes in the subsolar region, the magnetosheath plasma flows very slowly. However, it accelerates again on the flanks of the planet. The flow carries the IMF past Mars. The magnetic field of the inner magnetosheath drapes over the dayside hemisphere, slips over the terminator region and sinks into the wake behind the planet. The difference in mass-loaded plasma flow between the subsolar region and the flanks of the planet causes a stretching of the magnetic field lines. The region of stretched magnetic field behind the planet is called the magnetotail. The tail boundary is a boundary analogous to the IMB.

A region of hot plasma, known as the plasma sheet, is located at the center of the tail (Figure 1.4). The plasma sheet is dominated by planetary oxygen ions (*Lundin et al.*, 1990) and it divides the magnetotail into two lobes. Field lines are oriented away from the Sun in one lobe and toward the Sun in the other lobe. The magnetic polarity reverses at the center of the tail. Because the magnetic field is the draped IMF, the magnetic polarity in the lobes varies with the IMF direction (*Schwingschuh et al.*, 1992).

The draping of the field lines around Mars is asymmetrical. The upstream IMF makes an angle of 57° on average with the Mars-Sun line: therefore, the IMF lines drape differently around the planet on the dawn and dusk sides (see Figure 1.8).

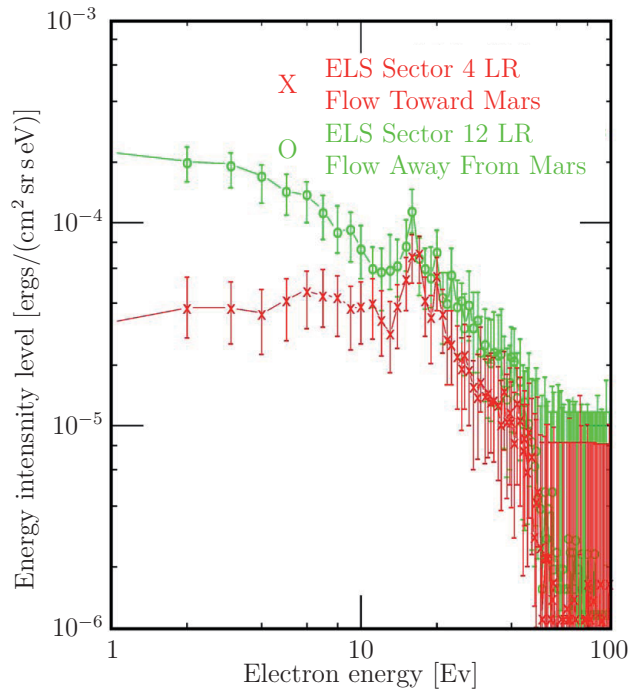


Figure 1.7: Ionospheric electron spectra measured by Mars Express (*Chicarro, 2004*). The red curve corresponds to electrons flowing toward Mars and the green curve corresponds to electrons flowing away from Mars. The figure is adapted from *Frahm et al. (2006)*.

The flaring angle of the magnetotail is the angle between the magnetotail field lines and the Mars-Sun line. This angle defines how much the tail boundary moves away from the Mars-Sun line (see Figure 1.4). *Zhang et al. (1994)* found that the flaring of the magnetotail decreases when the solar wind dynamic pressure increases in a similar way to what is observed at Earth. They reported a median value of 13° for the flaring angle at Mars.

1.3.5 Crustal magnetic fields

Localized magnetic field anomalies whose source is in the crust were discovered by *Acuna et al. (1998, 1999)*. These magnetic anomalies might have been formed during the first few hundred million years of Mars' history (*Connerney et al., 2004*) when iron-rich magma close to the surface cooled in the presence of an ambient primordial Martian magnetic field (*Acuna et al., 1998*). These magnetic anomalies reveal the orientation of the ambient magnetic field at the time when they were formed. The

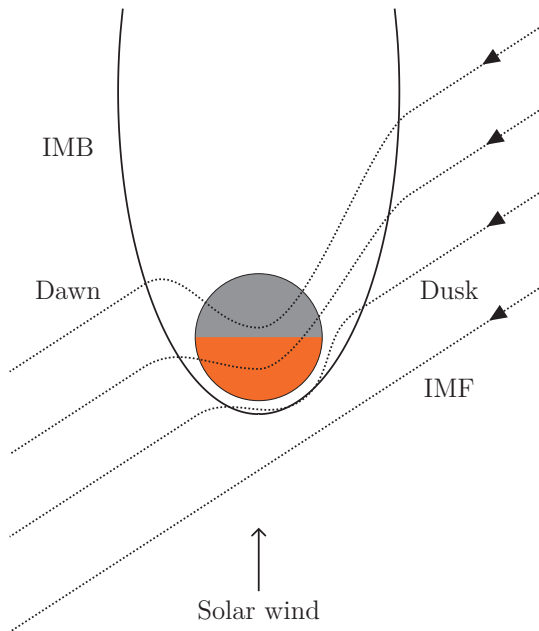


Figure 1.8: Sketch of Mars, IMF lines (dotted lines) and the IMB (solid line). The dawn and dusk sides are indicated. The IMF is carried by the solar wind flow and sweeps past the planet.

age of the cratered terrains suggests that the Martian magnetic field dynamo stopped 3.9×10^9 years ago (*Acuna et al.*, 1999).

Figure 1.9 shows the distribution of the crustal magnetic field strength at an altitude of 400 km. In the northern hemisphere, the crustal field strength is < 50 nT at 400 km altitude. In the southern hemisphere, the crustal field strength can be much larger, extending beyond 100 nT at 400 km altitude in a limited region between 120° and 210° east longitudes and between -30° and -80° latitudes.

The magnetic anomalies affect the position of the Martian plasma boundaries (see Section 1.3.1). The IMB has been suggested to have a corrugated shape (not smooth) due to local crustal fields (*Dubinin et al.*, 2008d). Further, these local magnetic fields are sufficiently strong to increase the total pressure (magnetic plus thermal) and thus to locally increase the altitude where the total pressure balances the solar wind pressure (*Acuna et al.*, 1999).

In some regions, crustal field lines are “open”, i.e., they are connected to both the crust and the solar wind IMF. These regions of predominantly radial fields are called cusps in analogy with the cusps of the Earth’s magnetosphere. Open field lines form when crustal field lines merge (reconnect) with IMF field lines. Solar wind electrons can enter the atmosphere via these cusps, and ionospheric plasma can also escape from these regions (*Acuna et al.*, 1999).

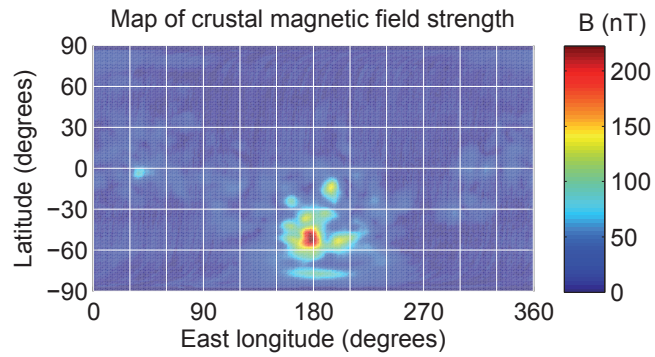


Figure 1.9: A map of the crustal magnetic field strength at an altitude of 400 km (using data from *Connerney et al. (2001)*).

Instrumentation and modeling tools

2.1 Spacecraft and instruments

2.1.1 Mars Express

The Mars Express mission (*Chicarro*, 2004) was designed by the European Space Agency to explore Mars. The spacecraft was launched on 2nd June 2003, and it was inserted into orbit around Mars on 25th December 2003. The spacecraft is in an elliptical polar orbit with an apocenter at an altitude of approximately 10 050 km and a pericenter at an altitude of approximately 270 km. The orbital period is ~ 7 hours. Mars Express has been delivering scientific data since early 2004, and the mission is currently extended to 2014. One of the main scientific objectives of Mars Express is to study the solar wind interaction with Mars. In particular, this thesis addresses the issue of the transfer of mass, energy and momentum from the solar wind into the Martian upper atmosphere.

2.1.1.1 The ASPERA-3 instrument

Most of the data used in this thesis are provided by the ASPERA-3 (Analyzer of Space Plasmas and Energetic Atoms) experiment aboard Mars Express. The ASPERA-3 experiment performs in situ measurements of hot plasma and remote sensing of energetic neutral atoms (ENAs) (*Barabash et al.*, 2006).

The different sensors composing ASPERA-3 are the ELeCtron Spectrometer (ELS), the Ion Mass Analyzer (IMA) and two ENA sensors. The ELS and IMA are the plasma sensors used for the work presented in this thesis.

2.1.1.1.1 ELS Figure 2.1 shows a cross-sectional view of the ELS. The ELS measures electron energy distributions in a two-dimensional (2D) plane with 4 s time resolution. The energy range is 5 eV to 20 keV.

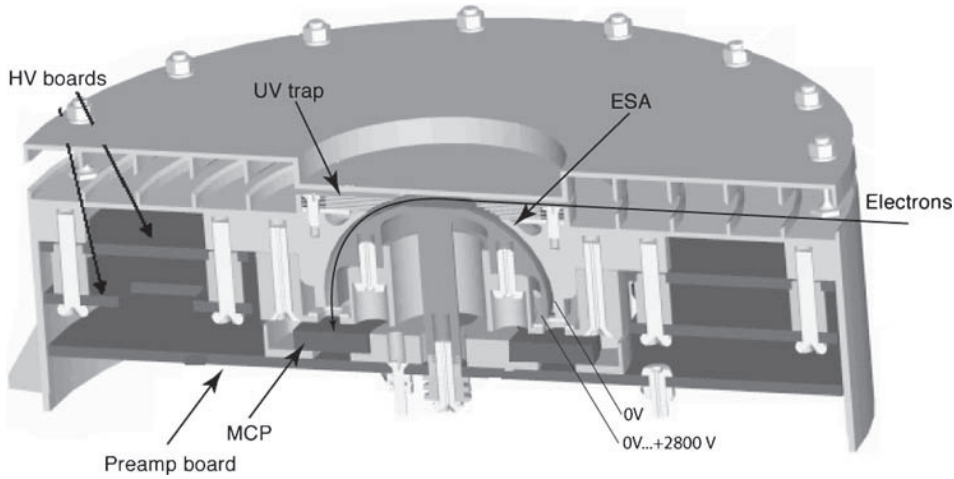


Figure 2.1: A cross-sectional view of the ELS. The black solid line shows the trajectory of an electron entering from the right. ESA = electrostatic analyzer. HV = high voltage. UV = ultraviolet. MCP = micro-channel plate. Preamp board = preamplification board. ESA voltages are also indicated. The figure is taken from *Barabash et al.* (2006).

The sensor consists of a collimator system followed by a top-hat ESA. The electrons enter the aperture at any angle within a plane determined by the collimator to be $4^\circ \times 360^\circ$. The application of a positive voltage to the inner of the two hemispheres in the ESA (Figure 2.1) permits the selection of electrons with a specific energy. By varying the voltage, electrons of different energies are allowed to pass through the system. After exiting the ESA, the electrons hit a MCP. Sixteen anodes are located behind the MCP, and each anode is connected to a preamplifier. Each anode defines a 22.5° sector corresponding to a given looking direction in the aperture plane. The digital processing unit subsequently counts the signals from each preamplifier.

2.1.1.1.2 IMA The ion spectrometer IMA measures ions in the energy range $10 \text{ eV}/q - 36 \text{ keV}/q$ for the main ion components (H^+ , He^{2+} , He^+ and O^+) and the group of molecular ions $20 < m/q < 80$, where m and q are the ion mass and charge, respectively.

The IMA consists of an electrostatic deflection system to provide elevation scanning, a top-hat ESA for the energy per charge selection, a permanent magnet-based velocity analyzer and a MCP detector with a position-sensitive anode (Figure 2.2).

The basic field of view of the IMA is a 2D plane. By varying the voltage between the two deflector plates (in purple in Figure 2.2), ions from different elevation angles are accepted. The electrostatic deflection system increases the instrument field of view

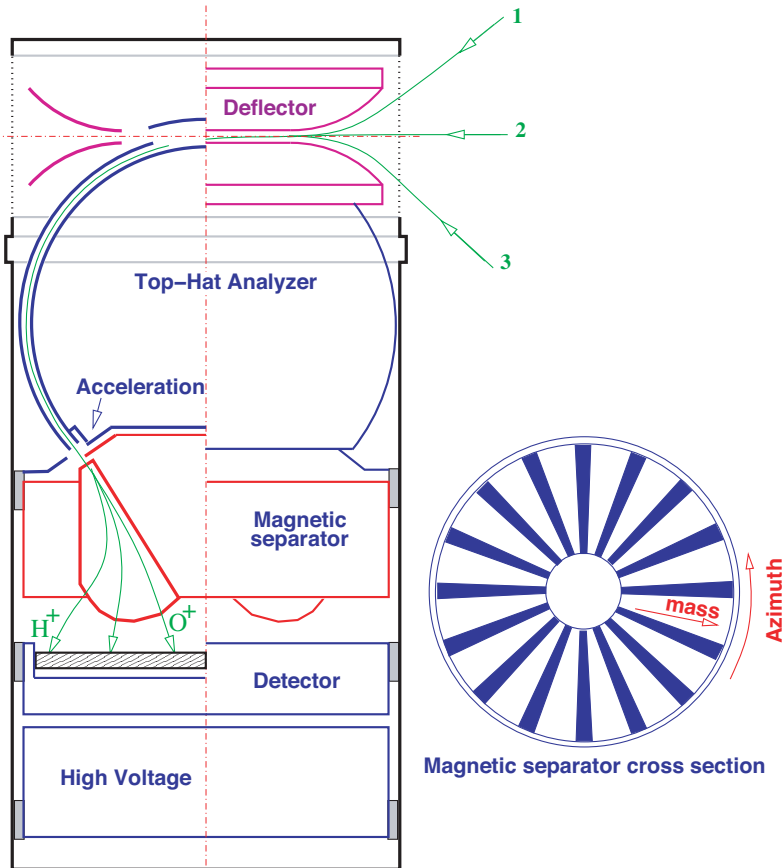


Figure 2.2: A cross-sectional view of the IMA. The solid green lines indicate typical ion trajectories. Sixteen sector anodes measure the ion entrance angles. The figure has been created by A. Fedorov.

to $\pm 45^\circ \times 360^\circ$.

Ions that pass through the deflector system continue to the ESA. In the ESA, the voltage between the two spherical shells is varied, and ions with different energies per charge are allowed through the system.

The mass resolution is obtained by the magnetic velocity analyzer. Particles with the same energy but with different masses are deflected differently in the magnetic field and hit the MCP at different locations. A system of 32 anode rings behind the MCP measures the radial impact position (representing the ion mass), and 16 sector anodes measure the azimuthal impact position (representing the ion entrance angle). The green lines in Figure 2.2 show examples of ion trajectories.

The time for one full energy scan is 12s. To obtain a full distribution (with 16

different elevation angles), a total acquisition time of 192 s is required.

2.1.2 ACE

Mars Express does not enter the upstream solar wind on every orbit. To obtain the solar wind parameters, we used the Advanced Composition Explorer (ACE) (*Stone et al.*, 1990). ACE is a solar wind monitor located upstream of Earth near the L1 Lagrange point (on the Sun-Earth line, 1.5×10^6 km from Earth). ACE is dedicated to the observation of energetic particles within the interplanetary medium. We used data from the MAG magnetometer (*Smith et al.*, 1998) and the Solar Wind Electrons, Protons, and Alpha Particle Monitor (SWEPAM) (*McComas et al.*, 1998). In order to estimate the solar wind parameters at Mars' position, a correction was applied to the solar wind parameters given by ACE, taking into account the positions of Earth and Mars, the solar wind speed and the angular velocity of the Sun's rotation (about $13^\circ/\text{day}$).

2.1.3 MGS

Mars Express does not have a magnetometer. To obtain the magnetic field data at Mars, we relied upon the Mars Global Surveyor (MGS) (*Albee*, 2002). MGS is a Mars orbiter that was in operation until to November 2006. From early 2004 to late 2006, the missions MGS and Mars Express overlapped. During this period, the MGS spacecraft had a near-circular orbit (400 km altitude, two-hour period) fixed at the local time 2 am-2 pm. We used the magnetic field data delivered by the Magnetometer-Electron Reflectometer MAG-ER (*Acuna et al.*, 1992).

2.2 Modeling techniques

2.2.1 Hybrid modeling

A hybrid model is a model in which the ions are treated as particles, while the electrons are treated as a charge-neutralizing (usually mass-less) fluid. Each test particle represents a large group of real ions (typically 10^{20} ions). Hybrid models can be used to simulate the interaction of a plasma flow with a body, for example between the solar wind and Mars (see e.g. *Brecht and Ferrante*, 1991). The most common assumptions of quasi-neutral hybrid models (including the model used in Papers 1 and 3) are listed below:

- The effect of the macroscopic plasma parameters (bulk velocity, charge density...) on the magnetic and electric fields is taken into account.
- The electron pressure is assumed to be isotropic.
- The electron fluid is assumed to be in near thermodynamic equilibrium.

- Relativistic effects and high frequency waves are neglected.
- The plasma is assumed to be quasi neutral: the electron density is equal to the ion density.

The spatial domain of the simulation is divided into cells. Ions of mass m_i , electric charge q_i and velocity \vec{v}_i are placed into these cells (with $i = \text{H}^+, \text{He}^{2+}, \text{O}^+$, etc.). At first, the ions are given an initial velocity and an initial position. They are then moved by the Lorentz force

$$m_i \frac{d\vec{v}_i}{dt} = q_i (\vec{E} + \vec{v}_i \times \vec{B})$$

where \vec{B} is the magnetic field and \vec{E} is the electric field. \vec{E} is calculated as follows:

$$\vec{E} = -\vec{U}_e \times \vec{B} - \frac{\vec{\nabla} (n_e k T_e)}{en_e}$$

where e is the elementary charge, k is the Boltzmann's constant, n_e is the electron density, T_e is the electron temperature and \vec{U}_e is the electron bulk velocity.

$$\frac{\vec{\nabla} (n_e k T_e)}{en_e} = \frac{\vec{\nabla} P_e}{en_e}$$

is the electron pressure gradient and P_e is the electron pressure. If one neglects the electron pressure gradient term, the electric field reduces to $\vec{E} = -\vec{U}_e \times \vec{B}$. This means that the magnetic field is frozen into the electron fluid and the magnetic field is carried by the electron flow. \vec{U}_e is obtained as follows:

$$\vec{U}_e = \frac{(\sum_i en_i \vec{U}_i) - \vec{j}}{en_e}$$

where n_i is the density and \vec{U}_i the bulk velocity of the ion species i , respectively. \vec{j} is the electric current density, which is obtained from Ampère's law, such as:

$$\vec{j} = \frac{\vec{\nabla} \times \vec{B}}{\mu_0}.$$

Faraday's law is used to advance the magnetic field in time.

The size of the spatial domain of the model typically covers a distance of several planetary radii from the center of the planet. The grid size is usually coarse at large distances from the body and is refined at closer distances. Hybrid models are computationally expensive and are preferably used in plasmas where collisions are rare, such as the region above a planetary exobase.

2.2.2 Direct Simulation Monte Carlo (DSMC) modeling

Monte Carlo methods are used to solve complex deterministic problems with a stochastic approach. The DSMC is a probabilistic simulation of a fluid modeled by particles. Each simulated particle represents a large number of real particles. The simulation solves the Boltzmann kinetic equation

$$\frac{\partial f}{\partial t} + \frac{\vec{F}}{m} \frac{\partial f}{\partial \vec{v}} + \vec{v} \frac{\partial f}{\partial \vec{r}} = \left(\frac{\partial f}{\partial t} \right)_{coll}$$

The left-hand term describes the transport of the velocity distribution function $f = f(\vec{r}, \vec{v}, t)$ of the particles, when an external force \vec{F} is present. The function f corresponds to the number of particles (with mass m) which have approximately velocity \vec{v} at time t near position \vec{r} . The right-hand term is a collision term. In DSMC models, ions and electrons are treated as particles; this makes the DSMC highly demanding in terms of computer resources. Papers 2 and 6 use a DSMC model to study the transport of precipitating $\text{H}^+/\text{H}/\text{He}^{2+}$ into the Martian upper atmosphere. In this model, the spatial domain of the simulation extends from 80 km altitude (numerous collisions) to 500 km (rare collisions) and it is divided into vertical cells of size inferior to the mean-free path of the particles. The mean free path depends on the atmospheric density and on the total scattering cross-sections of the different reactions implemented between particles. First, all particles are assigned an initial velocity and an initial position and the simulation spatial domain is divided into cells. Then the following loop is iterated until a predefined number of iterations. At each iteration:

1. Move the particles.
2. Track and index the particles into cells.
3. Select random collision pairs of neighboring particles in a given cell, depending on their relative speeds and total collision cross-sections, and perform the collisions.
4. Calculate the macroscopic properties of the fluid in each cell.

The energy of precipitating particles degrades due to the various collisions with atmospheric particles. The energy loss after the collision is recorded in the cell where it occurs. One can derive altitude profiles of the energy deposition rate from precipitating particles. Paper 2 shows such profiles for protons precipitating into the Martian upper atmosphere.

Solar wind particle precipitation into the Martian ionosphere

Solar wind electrons, protons, hydrogen atoms and alpha particles have been observed at low altitudes around Mars inside the induced magnetosphere (e.g. *Brain et al.*, 2005; *Lundin et al.*, 2004; *Futaana et al.*, 2006; *Stenberg et al.*, 2011). Precipitating particles bring matter, momentum and energy into the Martian upper atmosphere. The energy transfer may cause atmospheric heating. The momentum transfer may cause atmospheric sputtering. The matter transfer may affect the atmospheric composition.

3.1 A mechanism for the solar wind ion precipitation

The gyroradius of a charged particle of mass m and charge q in a background magnetic field strength B is

$$\frac{mv_{\perp}}{qB},$$

where v_{\perp} is the particle's velocity perpendicular to the background magnetic field vector. The gyroradius of an energetic solar wind ion in the magnetosheath can be comparable to the size of the magnetic barrier at the subsolar point. A typical 1-keV solar wind proton has a gyroradius of 152 km for a magnetic field of 30 nT, which is a typical magnetic field strength in the subsolar magnetic barrier. A typical 4-keV solar wind alpha particle subsequently has a gyroradius of ~ 304 km for the same magnetic field. The size of the magnetic barrier is of the order of 300 km at the subsolar point, using the average subsolar IMB altitude of 700 km from *Dubinin et al.* (2006a) and the average PEB altitude of 400 km from *Mitchell et al.* (2001). Therefore, if the particle's energy is high enough, it is possible for it to gyrate through the magnetic pile-up region and to precipitate into the ionosphere below. This example shows that

it is important to consider the motion of individual ions, which can be different from the motion of the bulk plasma. This is referred to as the gyroradius effect.

Another mechanism can also bring solar wind ions to low altitudes. The position of plasma boundaries changes in response to varying solar wind conditions and sometimes the magnetosheath plasma is observed at low altitudes, both ions and electrons at the same time. However, there is no boundary penetration in this case.

3.2 Proton precipitation

3.2.1 Observations

Solar wind protons have been observed at altitudes as low as 270 km in the Martian ionosphere. Low-altitude protons were first reported by *Lundin et al.* (2004). The same event is further analyzed in Paper 1, which suggests that the finite gyroradius effect may cause the observed proton precipitation. The downward proton energy spectra change when moving from the magnetic barrier to the ionosphere: the energy range of the proton populations becomes narrower and restricted to “high” energies (several keV). One explanation is that the gyroradii of low-energy protons are too small to allow the protons to cross the magnetic barrier.

A statistical study of the proton fluxes near Mars showed that solar wind protons penetrate deeper into the magnetosphere on the dawn side than on the dusk side (*Dubinin et al.*, 2008a). These authors attributed the result to the Parker spiral configuration of the IMF. The magnetic tension force of the average Parker IMF is different on the dawn and dusk sides, and the IMF draping presents a dawn-dusk asymmetry (see Figure 1.8). Therefore the magnetic field lines on the dawn side have a small component normal to the IMB. The magnetosheath plasma moving along the magnetic field lines can access low altitudes on the dawn side for the typical (Parker spiral) direction of the IMF (*Dubinin et al.*, 2008d).

Proton precipitation is rare, detected 3% of the dayside observation time and 0.5% of the nightside observation time (Paper 4). On the other hand, ion precipitation is a recurrent phenomenon in hybrid models (*Brecht*, 1997; *Kallio and Janhunen*, 2001; Paper 3). The reason for the infrequent measurements of proton precipitation is not clear. It seems that certain circumstances allow protons to cross the magnetic barrier, perhaps, during transient increases in the proton gyroradius due to transients in the magnetosheath temperature or solar wind speed. When precipitation occurs, it locally brings a particle flux in the range 10^4 – 10^6 cm⁻² s⁻¹, which is a small fraction of the upstream solar wind flux. The magnetic barrier effectively protects the upper atmosphere against proton precipitation. The observed proton precipitation events do not correlate with crustal magnetic anomalies, despite the opposite expectations from modelers (see Section 3.2.2). Proton precipitation is more frequently observed during fast solar wind conditions, likely because of larger mean energies and thus larger gyroradii for magnetosheath protons. The spatial distribution of precipitating fluxes is controlled by the solar wind convective electric field $\vec{E}_{SW} = -\vec{U}_{SW} \times \vec{B}_{SW}$,

where \vec{U}_{SW} is the solar wind velocity and \vec{B}_{SW} is the IMF. This result is consistent with modeling studies (see Section 3.2.2).

The precipitating proton fluxes below the IMB are less frequently observed during solar wind pressure encounters with Mars. A possible mechanism is as follows. During pressure pulses, IMF flux tubes penetrate deep into the ionosphere, where ion densities are high. Ionospheric ions are pulled into the solar wind by the convective electric field reaching low altitudes. The solar wind, loaded with heavy planetary ions, decelerates at low altitudes due to the conservation of momentum. The IMF, carried by the solar wind flow, is convected more slowly and then piles up more on the dayside of Mars. This enhances the total magnetic flux in the magnetic barrier. Under these conditions, the magnetic barrier becomes a bigger obstacle in terms of proton gyroradii. There is a disagreement with modelers (*Brecht, 1997*) which report an increase in the proton precipitation during high dynamic pressure conditions (see Section 3.2.2). The reasons for this are not clear.

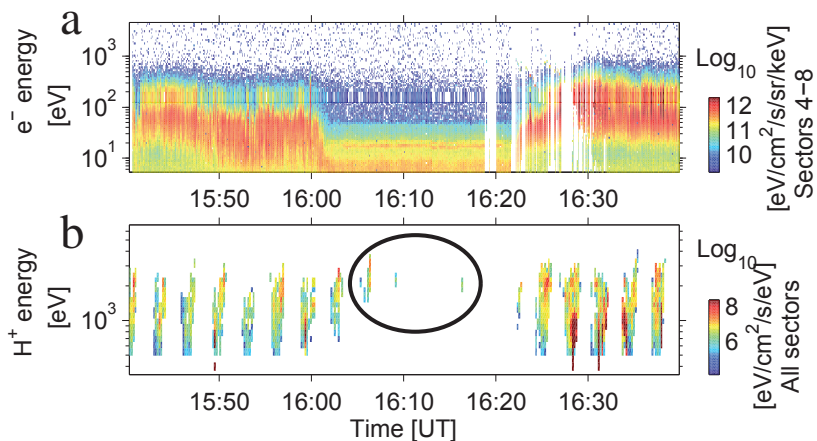


Figure 3.1: An example of proton precipitation in the ionosphere. (a) The electron energy-time spectrum. The vertical axis is electron energy. The sector-averaged differential electron flux is color coded. (b) The proton energy-time spectrum. The vertical axis is proton energy. The downward-integrated proton flux is color coded. The proton fluxes look like blobs repeated every 192 s because the instrument measures protons from different directions at different times at a 192-s time resolution. The pass in the ionosphere is recognized by the presence of photoelectron lines at 20–30 eV in the electron spectrum (horizontal line in (a)) between 1603 UT and 1621 UT. Precipitating protons are marked by a black ellipse in (b).

3.2.2 Modeling

Proton precipitation has also been modeled and studied using hybrid models (*Brecht, 1997; Kallio and Janhunen, 2001*), see Section 2.2.1. Hybrid models are well suited for the study of ion precipitation because they consider the ion gyroradius effect.

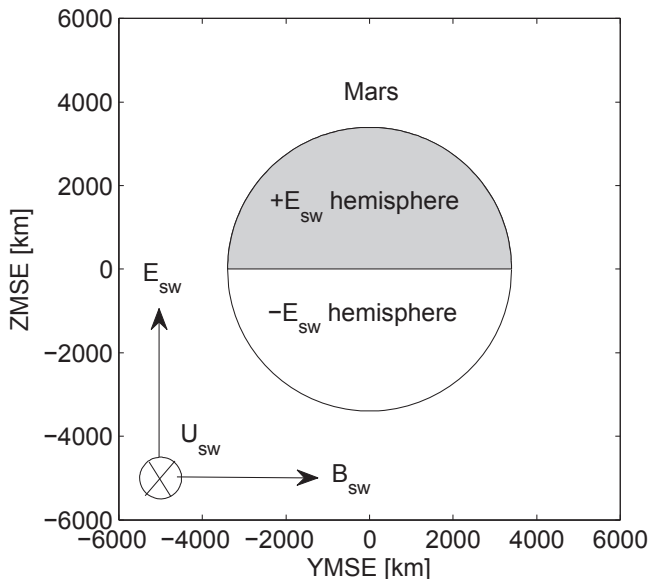


Figure 3.2: The Mars Solar Electric (MSE) coordinate system. The solar wind convective electric field vector, the solar wind bulk velocity vector, the IMF vector and the $\pm \vec{E}_{SW}$ hemispheres are shown. The view is from the Sun.

Modeling results are often shown in the Cartesian MSE coordinate system. In the MSE system, the X_{MSE} axis is directed toward the Sun and is assumed to be antiparallel with the solar wind velocity vector (the solar wind aberration angle is neglected). The Z_{MSE} axis points in the direction of \vec{E}_{SW} . The Y_{MSE} axis completes the right-handed system. In this thesis, the $+\vec{E}_{SW}$ hemisphere is defined as the hemisphere, in which \vec{E}_{SW} points away from Mars ($Z_{MSE} > 0$). The $-\vec{E}_{SW}$ hemisphere is defined as the hemisphere, in which \vec{E}_{SW} points toward Mars ($Z_{MSE} < 0$). Figure 3.2 shows the $\pm \vec{E}_{SW}$ hemispheres.

According to such models, the solar wind proton precipitating flux is largest in the $+\vec{E}_{SW}$ hemisphere (*Brecht, 1997; Kallio and Janhunen, 2001; Paper 3*). This is in agreement with the observations in Paper 4. The solar wind protons in the $-\vec{E}_{SW}$ hemisphere tend to flow downstream without hitting the planet. The proton energy controls towards which hemisphere the protons are accelerated (*Kallio and Janhunen,*

2001).

To explain this phenomenon, one considers that a proton of mass m_i and velocity \vec{v}_i moves according to

$$m_i \frac{d\vec{v}_i}{dt} = q_i \left((\vec{v}_i - \vec{U}_e) \times \vec{B} \right)$$

In the equation above, the electron pressure gradient term is neglected so that $\vec{E} = -\vec{U}_e \times \vec{B}$. The velocity of the ions $|\vec{v}_i|$ can differ from the electron bulk velocity $|\vec{U}_e|$ in regions where mass loading is important (i.e. where heavy planetary ions decelerate the solar wind flow) and where there are strong electric currents. Low-energy protons (velocity $|\vec{v}_i| \ll |\vec{U}_e|$) are accelerated towards Mars in the $-\vec{E}_{SW}$ hemisphere by the $-\vec{U}_e \times \vec{B}$ electric field. High-energy protons (velocity $|\vec{v}_i| \gg |\vec{U}_e|$) instead move toward Mars in the $+\vec{E}_{SW}$ hemisphere due to the $\vec{v}_i \times \vec{B}$ Lorentz force (*Kallio and Janhunen, 2001*). The higher flux in the $+\vec{E}_{SW}$ hemisphere can be explained by the solar wind protons tending to have high energies and thus preferentially precipitating in this hemisphere.

The dependence of proton precipitation on proton energy was investigated in Paper 3. The low-energy precipitating proton population mainly originates from new-born planetary protons created at low altitudes in the neutral hydrogen corona. The high-energy precipitating population originates from solar wind protons and from accelerated planetary protons created at higher altitudes in the corona. Low-energy protons are also more likely to be deflected by the magnetic barrier than high-energy protons because they have smaller gyroradii.

Models predict that the percentage of the solar wind flux that precipitates increases with the upstream solar wind dynamic pressure (e.g. *Brecht, 1997*). The protons in a fast solar wind have a larger gyroradius than the protons in a slow solar wind, and this property increases the chance that they impact Mars.

The deposited flux also depends on IMF orientation (*Brecht, 1997*), i.e., on the Parker angle. Almost 100% of the upstream flux is deposited when the IMF and the solar wind velocity are aligned (the Parker angle is 0°). In this case, the solar wind flows directly into the planet, and no bow shock is formed. For a more realistic Parker angle that is larger than 45° , the percentage of upstream proton flux that is deposited drops to $\sim 4\%$ (*Brecht, 1997*). The nominal Parker angle is 57° at Mars (see Section 1.2).

IMF orientation also determines the width of the precipitating energy spectrum (*Brecht, 1997*). The precipitating spectrum is a monoenergetic beam when the Parker angle is 0° . For larger Parker angles, a bow shock is formed, and the precipitating spectrum is heated.

The precipitating proton energy spectra produced by hybrid models are dominated by protons with energies larger than a few hundred eV (*Brecht, 1997; Kallio and Janhunen, 2001*) and depend on the upstream conditions (*Brecht, 1997*). The spectrum peaks at a higher energy and extends up to higher energies when the upstream solar wind is faster (*Brecht, 1997*).

In a recent study, *Brecht and Ledvina (2012)* included crustal fields in their hybrid model. Large crustal anomalies can focus the solar wind protons into regions of radial field lines connected to the IMF, i.e., into cusps.

There is a large discrepancy between the precipitating proton fluxes reported by modelers (*Brecht, 1997; Kallio and Janhunen, 2001; Paper 3*) and observers (*Paper 4*), see also Section 4.1. The reason for this is not clear and will be investigated in a future analysis. One possible reason is that models do not correctly reproduce the magnetic field configuration in the magnetic barrier due to the use of simplified ionospheric models.

3.3 Alpha particle precipitation

3.3.1 Observations

Solar wind alpha particles He^{2+} have also been observed inside the Martian IMB at altitudes as low as the pericenter of Mars Express (*Stenberg et al., 2011; Paper 5*).

Precipitating alpha particles were observed during 22% of the dayside ionospheric passes investigated by *Stenberg et al. (2011)*. The alpha particles in the ionosphere are often but not always observed together with protons. The downward fluxes of He^{2+} show no correlation with crustal magnetic fields. The spatial deposition of precipitating He^{2+} is asymmetric with respect to \vec{E}_{SW} , as indicated by Figure 3.3.

Precipitating alpha particle fluxes are less frequently detected during disturbed solar wind conditions (*Paper 5*).

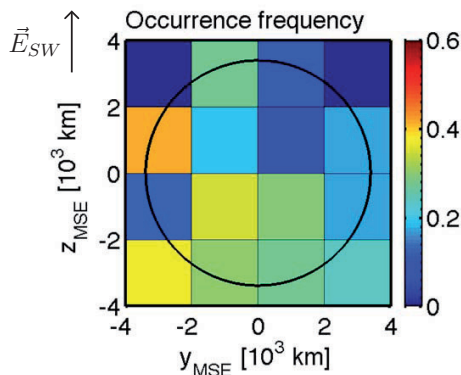


Figure 3.3: View of Mars from the Sun in MSE coordinates. The solar wind convective electric field \vec{E}_{SW} points to the top of the figure. The color represents the occurrence frequency of measuring precipitating alpha particles in each spatial bin. The figure is adapted from *Stenberg et al. (2011)*.

3.3.2 Modeling

Hybrid simulations have also predicted solar wind alpha particle precipitation on Mars (*Brecht, 1997; Modolo et al., 2005; Chanteur et al., 2009*).

According to the modeling study by *Chanteur et al. (2009)*, approximately 30% of the He^{2+} that impacts Mars' cross-section is removed from the solar wind flow. This removal is due to charge exchange reactions with atmospheric neutrals, resulting in the production of He^+ and He. Neutral He atoms hit the upper atmosphere and become trapped (*Chanteur et al., 2009*). *Krasnopolsky and Gladstone (2005)* suggested that the helium supplied by the solar wind is important for the helium balance on Mars (see Section 4.3).

3.4 Electron precipitation

Solar wind electron precipitation is not caused by the gyroradius effect. In the magnetosheath, the electron gyroradius is typically much smaller than the ion gyroradius due to the large mass difference between electrons and ions. The presence of magnetosheath electrons at low altitudes can be attributed to other mechanisms, as described below.

Electron fluxes with magnetosheath-type energy distributions are frequently observed below the IMB (e.g. *Fränz et al., 2006; Soobiah et al., 2006; Dubinin et al., 2006b*). Crustal fields play the determining role in electron precipitation. At an altitude of 400 km, shocked electrons are less likely to be observed in regions with crustal fields than in regions without fields (e.g. *Brain et al., 2005*). The minimum altitude at which magnetosheath electrons are observed increases almost linearly with the crustal field strength (*Fränz et al., 2006; Dubinin et al., 2008d*).

The crustal magnetic field vector has radial and horizontal components. While the horizontal component of crustal fields provides a shielding effect, the merging of the radial component of these fields with the IMF forms cusp-like structures. This merging is called magnetic reconnection. Open field lines are formed which connect the solar wind to the Martian surface. The electrons can follow the open field lines of the cusps (see Section 1.3.5) and travel down to the atmosphere (*Brain et al., 2006*). *Soobiah et al. (2006)* reported solar wind electron spikes (i.e. high fluxes of electrons observed during a short time) associated with radial crustal fields. An example of such an electron spike is shown in Figure 3.4. The crustal field lines reconnect with the IMF lines when the IMF and the crustal field have opposite orientations. This magnetic field configuration permits channelling the magnetosheath electrons into the cusp regions of large magnetic anomalies. Electron spikes are more likely to be observed above large magnetic anomalies when the IMF points toward dawn (*Dubinin et al., 2008d*). Therefore, the orientation and the strength of the crustal field are important for determining electron precipitation at low altitudes (*Brain et al., 2005*).

Statistical studies of electron fluxes near Mars show that the dawn side of the IMB is more permeable to solar wind electron entry (*Dubinin et al., 2008a*) due to the

average Parker configuration of the IMF. The same result has been shown for protons (see Section 3.2.1).

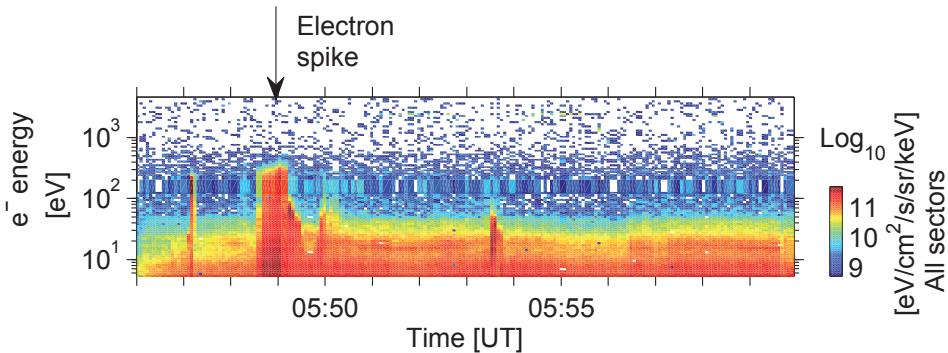


Figure 3.4: The electron energy-time spectrum. The figure shows an example of a solar wind electron spike in the ionosphere.

Magnetosheath electrons are not always observed together with solar wind ions. Instead, *Dubinin et al.* (2006b) reported a narrow plasma structure located along the wake boundary containing a mixture of magnetosheath electrons and planetary oxygen ions. *Dubinin et al.* (2006a) showed that this type of plasma protrusion occurs preferentially in the $+\vec{E}_{SW}$ hemisphere. They suggested two possible mechanisms. One mechanism arises when draped IMF lines sink into the wake, and the associated magnetic tension forces push planetary ions into the wake. The magnetosheath electrons then follow the ions into the wake to maintain quasi neutrality. Another mechanism arises when open crustal field lines are stretched tailward into “auroral field lines” by the solar wind flow. Similar to auroral processes on Earth, currents and electric fields can develop magnetic field-aligned configurations. These electric fields accelerate ions upward and electrons downward. The latter mechanism is observed above strong crustal anomalies in the southern hemisphere (e.g. *Dubinin et al.*, 2008d).

3.5 ENA precipitation

Hydrogen energetic neutral atoms (H ENAs) are produced in the vicinity of Mars when solar wind protons undergo charge exchange reactions with atoms from the exosphere (the upper neutral atmosphere). Owing to their high energy (hundreds of eV), the gravitational effect is negligible. Owing to their neutrality, ENAs are decoupled from electromagnetic fields and are thus not deflected away by the magnetic barrier. The ENA propagates in a straight line in the same direction as the parent ion.

ENAs produced in the magnetosheath and in the solar wind have been observed

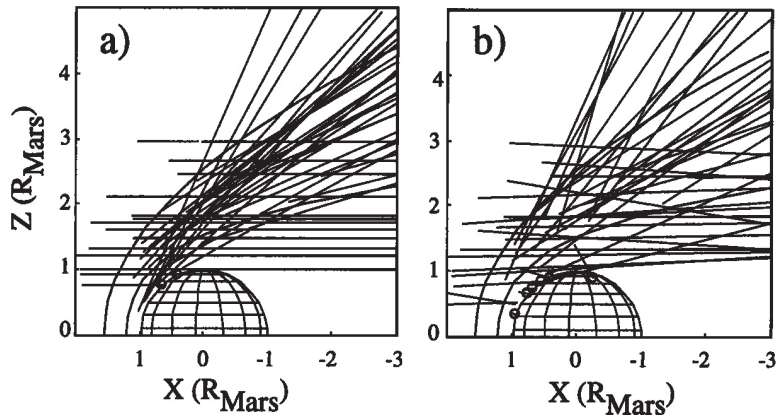


Figure 3.5: Examples of simulated ENA trajectories near Mars. The circles near Mars indicate the locations where precipitating ENAs hit the planetary obstacle. (a) The upstream proton temperature is set to 0. (b) The upstream proton temperature is non null. The figure is taken from *Kallio et al.* (1997).

by ASPERA-3 (*Gunell et al.*, 2006; *Brinkfeldt et al.*, 2006). Observations of ENA fluxes backscattered from the planet have also been reported (*Futaana et al.*, 2006, see also Section 4.2).

Modeling efforts have focused on determining the ENA production rates both upstream of the bow shock and in the magnetosheath and on simulating the expected ENA images (*Holmström et al.*, 2002). According to the simulations by *Kallio et al.* (1997), 1–3% of the solar wind protons are charge-exchanged into ENAs upstream of the bow shock for nominal solar wind conditions (*Kallio et al.*, 1997). The models predict that ENAs can travel to the exobase, where they precipitate. Figure 3.5 illustrates examples of modeled ENA trajectories near Mars. The figure shows that more ENAs can impact the planetary obstacle when the parent proton population is “hot” due to the thermal spread in velocities.

Atmospheric effects of solar wind ion precipitation on Mars

Precipitating ions and neutral atoms react with atmospheric gases via elastic and inelastic collisions. The transport is strongly affected by the presence of the magnetic field.

4.1 Energy deposition of H/H^+ in the atmosphere

Hybrid simulations indicate that the precipitating proton/hydrogen flux is highest at the subsolar point and decreases toward the nightside (*Brecht, 1997; Kallio and Janhunen, 2001; Kallio and Barabash, 2001*). Figures 4.1 and 4.2 show the precipitating proton fluxes and the precipitating hydrogen fluxes respectively, calculated as a function of the SZA at a fixed altitude. The models predict that there are no precipitating ENAs beyond 100° SZA (*Kallio and Barabash, 2001; Holmström et al., 2002*) in contrast to proton precipitation, which also exists on the nightside (*Kallio and Janhunen, 2001*). Therefore, precipitating protons can be an ionization source for the nightside, but hydrogen ENAs cannot.

Table 4.1 compares the energy fluxes of precipitating H^+/H at a fixed altitude at 45° SZA for four different models. There are several orders of magnitude difference between the energy fluxes calculated by *Brecht (1997)*, *Kallio and Janhunen (2001)* and Paper 3. For this reason, it is difficult to directly compare these results with the energy flux of precipitating H ENAs. Nevertheless, *Kallio and Barabash (2001)* and *Kallio and Janhunen (2001)* used the same model to study H/H^+ precipitation. They found that the precipitating H ENA energy flux is two orders of magnitude smaller than the proton energy flux. However, the output is sensitive to the properties of the model.

The energy deposition due to precipitating particles can be compared with the energy flux deposition from the solar radiation. The dayside energy flux of precipitating hydrogen/protons modeled (*Brecht, 1997; Kallio and Janhunen, 2001; Kallio and*

Barabash, 2001; Paper 3), and measured (Paper 4), are two to three orders of magnitude smaller than the energy flux from the solar EUV radiation absorption on Mars for solar minimum conditions (*Kallio et al.*, 1997). Values are given in Table 4.1. For nominal solar wind conditions, the H/H^+ energy flux cannot compete with the solar EUV heating on the dayside but EUV heating does not occur on the nightside and proton precipitation may be a significant heat source there.

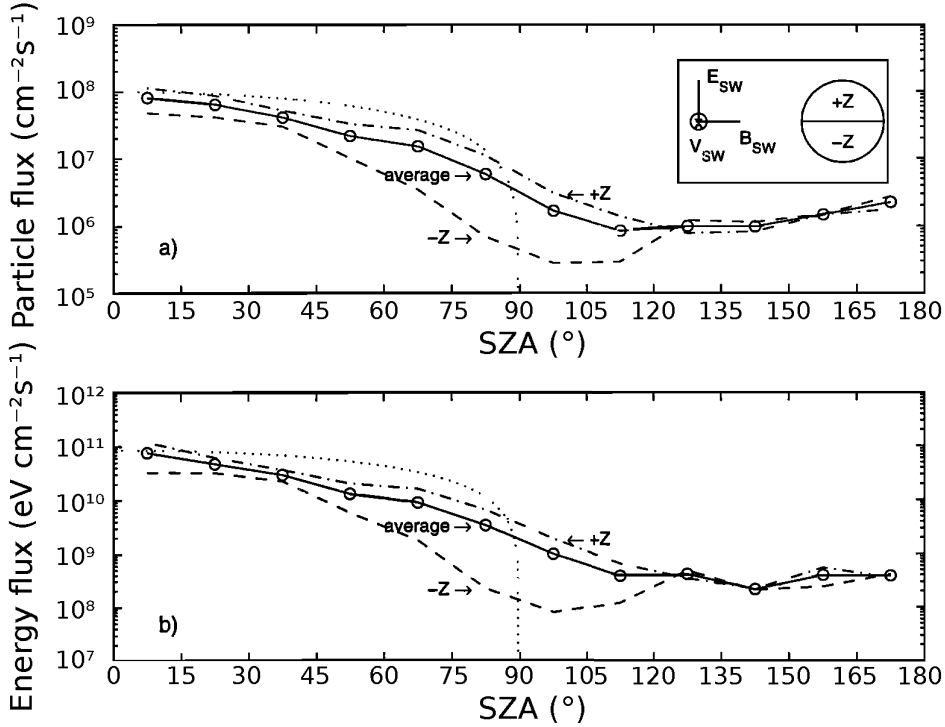


Figure 4.1: The precipitating proton particle flux and energy flux calculated at the exobase (207 km altitude) as a function of the SZA. The flux in the $+\vec{E}_{SW}$ hemisphere is shown with a dotted-dashed curve. The flux in the $-\vec{E}_{SW}$ hemisphere is shown with a dashed curve and the average flux in both hemispheres is shown with a solid curve. The solar wind flux, if the solar wind is able to hit the atmosphere directly, is shown with a dotted curve. The solar wind hits the atmosphere with a dependence of the form $f_0 \cos(SZA)$ where f_0 is the undisturbed solar wind flux. A sketch of the hemispheres is also indicated. The figure is adapted from *Kallio and Janhunen* (2001).

Precipitating solar wind protons and hydrogen ENAs undergo charge exchange/stripping cascading and quickly “forget” their initial charge states (*Kallio and*

Barabash, 2000). Precipitating H/H⁺ particles deposit their energy via collisions with atmospheric neutrals. At the subsolar point, the energy deposition rate for H/H⁺ reaches its maximum at an altitude of 120 km (*Kallio and Janhunen*, 2001; *Kallio and Barabash*, 2001; Paper 2). The maximum energy deposition rate is determined by the balance between decreasing neutral density (and thus fewer collisions) and an increasing amount of precipitating particles as the altitude increases. The magnetic field plays a crucial role in determining the energy deposition from precipitating H⁺ into the upper atmosphere by preventing a significant fraction of these particles from reaching low altitudes (Paper 2).

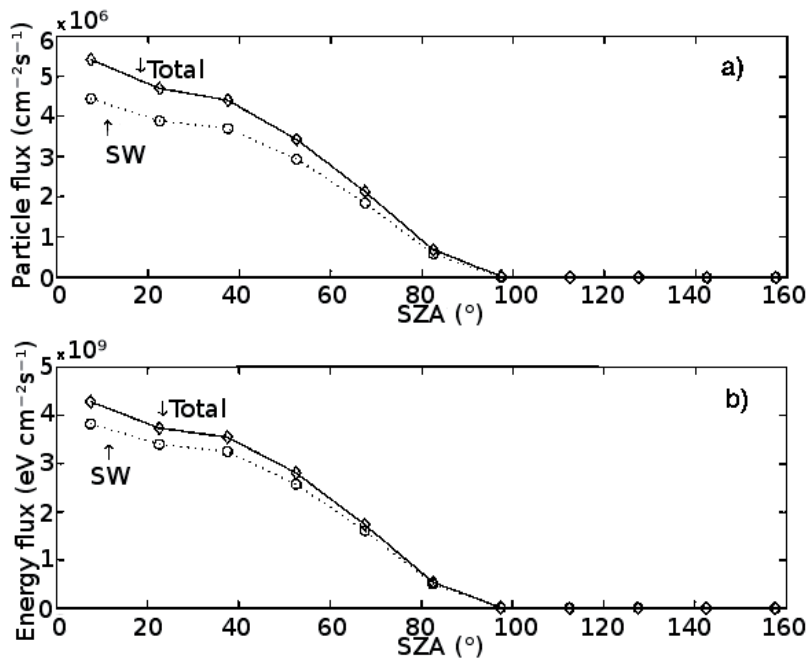


Figure 4.2: The precipitating H ENA particle flux and energy flux at the exobase, as a function of the SZA at an altitude of 260 km. The two curves represent the ENAs produced upstream of the bow shock (dotted curve) and the total amount of ENAs (produced upstream and downstream) (solid line). The figure is adapted from *Kallio and Barabash* (2001).

Precipitating H/H⁺ particles lose energy through elastic and inelastic collisions (*Kallio and Barabash*, 2001). In total, 97% of the energy loss from precipitating H/H⁺ is associated with H ENA-atmospheric neutral collisions. The remainder results from H⁺-atmospheric neutral collisions (*Kallio and Barabash*, 2001). This result means

Study	Energy flux [$\text{eV cm}^{-2} \text{s}^{-1}$]	Altitude [km]
Planetary and solar wind protons (Paper 4)	$\sim 1.2 \times 10^8$	608
Planetary and solar wind protons (Paper 3)	$\sim 1 \times 10^9$	207
Solar wind protons (<i>Kallio and Janhunen, 2001</i>)	$\sim 5 \times 10^{10}$	207
Solar wind protons (<i>Brecht, 1997</i>)	$\sim 1 \times 10^8$	surface (no atmosphere)
Solar wind H ENAs (<i>Kallio and Barabash, 2001</i>)	$\sim 3 \times 10^9$	260
Solar EUV, solar minimum (<i>Kallio et al., 1997</i>)	$\sim 1.35 \times 10^{11}$	100–240

Table 4.1: The modeled energy fluxes at 45° SZA for precipitating protons (Paper 3; *Brecht, 1997*; *Kallio and Janhunen, 2001*). The observed median energy fluxes for precipitating protons below the dayside IMB (Paper 4). The modeled energy fluxes at 45° SZA for precipitating H ENA (*Kallio and Barabash, 2001*). The energy flux from the height-integrated solar radiation absorption at 45° SZA for solar minimum (*Kallio et al., 1997*).

that the projectile is almost always a hydrogen atom.

Table 4.2 presents the contributions of different processes to the total energy loss associated with H ENA-atmospheric neutral collisions (*Kallio and Barabash, 2001*). Inelastic collisions are responsible for 86% of the total energy loss.

	Process	Contribution [%]
	Elastic collision	14
	Lyman α emission	30
Inelastic processes	Ionization	27
	Electron stripping	26
	H α emission	2
	Charge exchange	1

Table 4.2: Contributions from different processes to the total energy loss associated with H ENA-atmospheric neutral collisions (*Kallio and Barabash, 2001*). Inelastic processes are shown in gray shading.

The main ion species produced by H/H⁺ precipitation is CO₂⁺ (*Kallio and Janhunen, 2001*; *Kallio and Barabash, 2001*). The CO₂⁺ production rates generated by hydrogen/proton precipitation (*Kallio and Janhunen, 2001*; *Kallio and Barabash, 2001*) are smaller than the CO₂⁺ production rates due to solar EUV (*Shinagawa and*

Cravens, 1989) on the dayside. Observed precipitating proton fluxes below the dayside IMB (Paper 4) are two orders of magnitude smaller than the dayside precipitating proton fluxes modeled by *Kallio and Janhunen* (2001). The ion production rates associated with the observed proton precipitation are of course even smaller than the modeled ones. Therefore, solar radiation is the main source of ion production on the dayside. However, H^+ precipitation can help to maintain the ionosphere on the nightside (*Kallio and Janhunen*, 2001).

4.2 Backscattering of H from the atmosphere

The numerous collisions at an altitude of 120 km change the trajectory of the precipitating energetic hydrogen atoms such that a fraction of them is scattered back (*Kallio and Barabash*, 2000). Figure 4.3 shows examples of 2D projections of trajectories of H ENA atoms for different collision models. An atom that is not backscattered becomes assimilated with atmospheric gases, where it loses its energy.

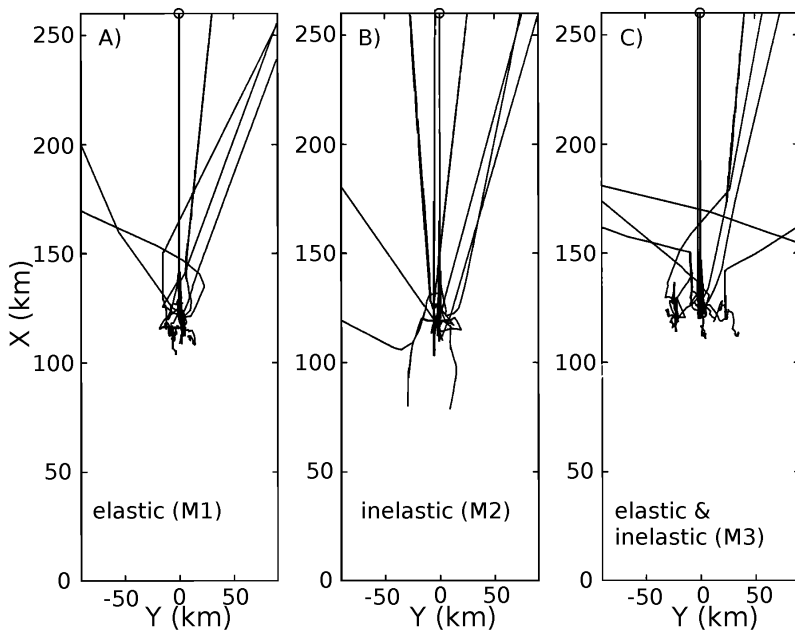


Figure 4.3: Examples of H ENA 2D projection trajectories when elastic collisions are included (a), when inelastic collisions are included (b) and when both inelastic and elastic collisions are included (c). Ten atoms of initial velocity $(V_x, V_y, V_z) = [-400, 0, 0]$ km s⁻¹ are launched from the starting point (marked with an open circle) located at $(x,y,z)=[260,0,0]$ km. The figure is adapted from *Kallio and Barabash* (2000).

The backscattering by the Martian atmosphere of H ENAs produced in the solar wind is referred to as the ENA albedo (*Kallio and Barabash, 2001; Holmström et al., 2002*). According to the model by *Kallio and Barabash (2001)*, the percentage of the precipitating H ENA energy flux that is backscattered is high: 58%. These results are not in agreement with the latest results of the DSMC model reported in Paper 2. The updated backscattering rate is approximately 10%. Paper 2 explains that the reason for the discrepancy may be that *Kallio and Barabash (2001)* used outdated reaction cross-sections and treated collisions as hard sphere collisions, causing an important collisional spreading of particle trajectories.

Hybrid simulations show that proton precipitation increases the dayside ENA albedo. Proton precipitation also creates a nightside ENA albedo. This phenomenon occurs when precipitating protons pass through the IMB and become precipitating H ENAs after charge exchange. The incoming hydrogen atoms can subsequently be backscattered by collisions with atmospheric neutrals. The ENA albedo depends on solar wind conditions (*Holmström et al., 2002*).

There have been observations of H ENA fluxes backscattered by the Martian upper atmosphere (*Futaana et al., 2006*, see also Section 3.5). These observations are consistent with the ENA albedo theory, but the measured energy fluxes ($9.5 \times 10^9 \text{ eV cm}^{-2} \text{ s}^{-1}$) are too high (*Futaana et al., 2006*).

Futaana et al. (2006) suggested that the reason for this may be the IMB altitude, which was lower than on average during the observations. When the IMB altitude is low, the shocked solar wind can reach deeper into the neutral atmosphere: this increases the number of ENAs that are generated and thus backscattered. The backscattered ENAs might be used to estimate proton precipitation fluxes (*Futaana et al., 2006*).

4.3 Helium balance

Helium is formed in the interior of Mars from the radioactive decay of thorium and uranium. This helium then outgasses into the atmosphere. The helium outgassing rate was calculated by *Krasnopolsky et al. (1994)*. The modeled outgassing rate was however much smaller than the outflow rate of helium ions (*Barabash et al., 1995*) estimated from in situ measurements by the Phobos-2 spacecraft in the nineties (*Zaitsev, 1989*). The outgassing of He modeled later by *Krasnopolsky and Gladstone (2005)* accounted for only 10% of the total production rate of He. *Brecht (1997)* and *Krasnopolsky and Gladstone (2005)* suggested that the solar wind He^{2+} ions precipitating into the Martian upper atmosphere could be a major source of helium on Mars. *Stenberg et al. (2011)* confirmed the existence of precipitating He^{2+} from in situ observations. However, the He^{2+} precipitation rate derived from observations does not seem to be a major contributor to the helium in the atmosphere (G. Stenberg, private communication). The helium balance on Mars is still an open question.

CHAPTER 5

Summary of papers

5.1 Paper 1: A case study of proton precipitation at Mars: Mars Express observations and hybrid simulations.

Authors: C. Diéval, E. Kallio, S. Barabash, G. Stenberg, H. Nilsson, Y. Futaana, M. Holmström, A. Fedorov, R. A. Frahm, R. Järvinen and D. A. Brain.

We conducted a detailed study of one orbit of the Mars Express spacecraft, during which downward-moving protons were observed inside the Martian induced magnetosphere. Protons were observed at altitudes less than 700 km and had energies up to 7 keV. A fast solar wind stream is needed to explain the relatively high energies of precipitating protons. When the spacecraft moves from the magnetic barrier to the ionosphere, the energy distribution of downward-moving protons becomes narrower in the energy. Low-energy protons vanish, probably because they are deflected away by the magnetic barrier. Under a stationary assumption, the spatial extent of the proton precipitation region reached several thousand kilometers along the orbit of the spacecraft. The proton precipitation into the upper atmosphere was also simulated using a hybrid code. The simulation indicates that precipitating protons originate partly from the solar wind and partly from the neutral hydrogen corona.

My contribution: I analyzed the observations and the output from the hybrid model. I wrote the text and I made the figures. E. Kallio and R. Järvinen run the hybrid model at the Finnish Institute of Meteorology (Helsinki).

5.2 Paper 2: Protons and hydrogen atoms transport in the Martian upper atmosphere with an induced magnetic field.

Authors: V. I. Shematovich, D. V. Bisikalo, C. Diéval, S. Barabash, G. Stenberg, H. Nilsson, Y. Futaana, M. Holmström and J.-C. Gérard.

We modeled proton precipitation in the Martian upper atmosphere using a DSMC model. The interaction of downward-moving H^+/H with the atmospheric neutrals results in upward fluxes of H and H^+ . The peak in energy deposition is found in the altitude range 100–150 km. The inclusion of a horizontal magnetic field in the model significantly increases the upward fluxes of protons compared with the case without a magnetic field. The model showed that more than 50% of the incoming energy is reflected backwards for a magnetic field of strength 30 nT. The energy deposition from precipitating fast hydrogen atoms is practically not affected by the presence of the magnetic field.

My contribution: I carried out a literature search about the measurements of the induced magnetic field at Mars in the initial phase of the work. The magnetic field values were an essential input to the model runs. I provided the precipitating proton spectra used as inputs to the model and I formulated the conditions for the simulation runs relevant to my work. I wrote a part of the text and I commented on the revision of the text. V. I. Shematovich and D. V. Bisikalo run the DSMC model at the Institute of Astronomy in Moscow.

5.3 Paper 3: Hybrid simulations of proton precipitation patterns in the upper atmosphere of Mars.

Authors: C. Diéval, E. Kallio, G. Stenberg, S. Barabash and R. Järvinen.

We used hybrid simulations to study the spatial pattern of proton precipitation in the Martian upper atmosphere both for solar wind protons and for protons originating from the atmosphere. Solar wind protons and planetary protons contribute 62% and 38% respectively, to the deposition of mass at 207 km altitude for the given input parameters. The precipitation pattern is asymmetric with respect to the direction of the solar wind convective electric field; the asymmetry is more pronounced for the solar wind protons. The precipitation pattern depends on the particle energy. The low-energy part of the precipitating population is dominated by cold newly born planetary protons, while shocked solar wind protons and accelerated picked up planetary protons form the high-energy part. The precipitating flux was found to have a strong dependence on altitude. The flux decreases substantially at low altitudes at the subsolar point, probably due to the backscattering of the incoming protons by the presence of the more intense piled-up magnetic field.

My contribution: I analyzed the output of the hybrid model. I wrote the text and created the figures, except Figure 2. E. Kallio and R. Järvinen run the hybrid model at the Finnish Institute of Meteorology (Helsinki).

5.4 Paper 4: A statistical study of proton precipitation onto the Martian upper atmosphere: Mars Express observations.

Authors: C. Diéval, G. Stenberg, H. Nilsson and S. Barabash.

We conducted a statistical study of downward-moving proton fluxes measured below the Martian IMB by Mars Express. We excluded the intervals where we observed low-altitude magnetosheath electrons to be sure to consider only the ionosphere. We found that proton precipitation is detected 3% of the observation time on the dayside and 0.5% on the nightside. This carries on average 0.2% of the upstream solar wind particle flux. When precipitating proton events occur, they bring energy fluxes in the range 10^7 – 10^9 eV cm⁻² s⁻¹, which are much less than the energy input from solar EUV to the dayside upper atmosphere. Proton precipitation is more frequent during fast solar wind conditions than during slow solar wind conditions. The spatial distribution of precipitating protons is controlled by the solar wind convective electric field. Precipitating fluxes do not correlate with the crustal magnetic anomalies.

My contribution: I collected the events of proton precipitation used in the work and I analyzed the observations. I wrote the text and I created the figures.

5.5 Paper 5: Reduced proton and alpha particle precipitations at Mars during solar wind pressure pulses: Mars Express results.

Authors: C. Diéval, G. Stenberg, H. Nilsson, N. J. T. Edberg and S. Barabash.

We performed a statistical study of proton and alpha particle fluxes precipitating in the Martian dayside ionosphere using observations by Mars Express. We found that the precipitating fluxes of protons and alpha particles are less frequently detected during encounters of solar wind pressure pulses with Mars than the rest of the time. The difference in occurrence frequency is a factor ~ 3 for protons and a factor ~ 2 for alpha particles. This is an unexpected result. One explanation is that during pressure pulses, the IMF penetrates to low altitudes in the ionosphere, where there are high densities of planetary ions. The mass of these additional ions decelerates the solar wind flow. This in turn increases the pile-up of the IMF on the dayside of Mars and the total magnetic flux in the magnetic barrier. The barrier becomes thicker in terms of ion gyroradii, and solar wind ion precipitation decreases.

My contribution: I collected the events of proton and alpha particle precipitations used in the work and I analyzed the observations. N. J. T. Edberg performed an automatic search for intervals of solar wind pressure pulse encounters with Mars, and I checked his list against the data from Mars Express. I wrote the text and I created the figures.

5.6 Paper 6: He^{2+} transport in the Martian upper atmosphere with an induced magnetic field.

Authors: V. I. Shematovich, D. V. Bisikalo, G. Stenberg, S. Barabash, C. Diéval and J.-C. Gérard.

We modeled the transport of precipitating alpha particles in the Martian upper atmosphere using the same DSMC model as in Paper 2. We calculated the upward fluxes of He, He^+ and He^{2+} . Similar to Paper 2, we included in the model a horizontal magnetic field. This magnetic field caused a backscattering of the precipitating alpha particles. The model showed that 30–40% of the incident energy is reflected backwards for a magnetic field of strength 20 nT, depending on the velocity distribution of the precipitating alpha particles. There is no backscattering in the absence of a magnetic field. The magnetic field plays an important role in determining the energy deposition of the solar wind He^{2+} in the upper atmosphere.

My contribution: The paper used the same values of the induced magnetic field as in Paper 2. I participated in the formulation of the task and I contributed to the discussion on the results. Finally, I commented on the text during the revision phase. V. I. Shematovich and D. V. Bisikalo run the DSMC model at the Institute of Astronomy in Moscow.

REFERENCES

- Acuna, M. H., et al., Mars Observer magnetic fields investigation, *J. Geophys. Res.*, *97*, 7799–7814, doi:10.1029/92JE00344, 1992.
- Acuna, M. H., et al., Magnetic Field and Plasma Observations at Mars: Initial Results of, *Science*, *279*, 1676–1680, doi:10.1126/science.279.5357.1676, 1998.
- Acuna, M. H., et al., Global Distribution of Crustal Magnetization Discovered by the Mars Global Surveyor MAG/ER Experiment, *Science*, *284*, 790–793, doi:10.1126/science.284.5415.790, 1999.
- Akalin, F., D. D. Morgan, D. A. Gurnett, D. L. Kirchner, D. A. Brain, R. Modolo, M. H. Acuña, and J. R. Espley, Dayside induced magnetic field in the ionosphere of Mars, *Icarus*, *206*, 104–111, doi:10.1016/j.icarus.2009.03.021, 2010.
- Albee, A., The Mars Global Surveyor mission: description, status, and significant result, *Highlights of Astronomy*, *12*, 631–635, 2002.
- Barabash, S., E. Kallio, R. Lundin, and H. Koskinen, Measurements of the non-thermal helium escape from Mars, *J. Geophys. Res.*, *100*, 21,307–21,316, doi:10.1029/95JA01914, 1995.
- Barabash, S., et al., The Analyzer of Space Plasmas and Energetic Atoms (ASPERA-3) for the Mars Express Mission, *Space Sci. Rev.*, *126*, 113–164, doi:10.1007/s11214-006-9124-8, 2006.
- Brain, D. A., J. S. Halekas, R. Lillis, D. L. Mitchell, R. P. Lin, and D. H. Crider, Variability of the altitude of the Martian sheath, *Geophys. Res. Lett.*, *321*, L18,203, doi:10.1029/2005GL023126, 2005.
- Brain, D. A., D. L. Mitchell, and J. S. Halekas, The magnetic field draping direction at Mars from April 1999 through August 2004, *Icarus*, *182*, 464–473, doi:10.1016/j.icarus.2005.09.023, 2006.
- Brecht, S. H., Solar wind proton deposition into the Martian atmosphere, *J. Geophys. Res.*, *1021*, 11,287–11,294, doi:10.1029/97JA00561, 1997.

- Brecht, S. H., and J. R. Ferrante, Global hybrid simulation of unmagnetized planets – Comparison of Venus and Mars, *J. Geophys. Res.*, *961*, 11,209–11,220, doi:10.1029/91JA00671, 1991.
- Brecht, S. H., and S. A. Ledvina, Control of ion loss from Mars during solar minimum, *Earth, Planets, and Space*, *64*, 165–178, doi:10.5047/eps.2011.05.037, 2012.
- Breus, T. K., E. M. Dubinin, A. M. Krymskii, R. Lundin, and J. G. Luhmann, The solar wind interaction with Mars - Consideration of Phobos 2 mission observations of an ion composition boundary on the dayside, *J. Geophys. Res.*, *961*, 11,165–11,174, doi:10.1029/91JA01131, 1991.
- Brinkfeldt, K., et al., First ENA observations at Mars: Solar-wind ENAs on the nightside, *Icarus*, *182*, 439–447, doi:10.1016/j.icarus.2005.12.023, 2006.
- Chanteur, G. M., E. Dubinin, R. Modolo, and M. Fraenz, Capture of solar wind alpha-particles by the Martian atmosphere, *Geophys. Res. Lett.*, *36*, L23105, doi:10.1029/2009GL040235, 2009.
- Chicarro, A. F., The Mars Express Mission Initial Scientific Results from Orbit, in *Lunar and Planetary Institute Science Conference Abstracts, Lunar and Planetary Inst. Technical Report*, vol. 35, edited by S. Mackwell and E. Stansbery, p. 2174, 2004.
- Connerney, J. E. P., M. H. Acuña, P. J. Wasilewski, G. Kletetschka, N. F. Ness, H. Rème, R. P. Lin, and D. L. Mitchell, The Global Magnetic Field of Mars and Implications for Crustal Evolution, *Geophys. Res. Lett.*, *28*, 4015–4018, doi:10.1029/2001GL013619, 2001.
- Connerney, J. E. P., M. H. Acuña, N. F. Ness, T. Spohn, and G. Schubert, Mars Crustal Magnetism, *Space Sci. Rev.*, *111*, 1–32, doi:10.1023/B:SPAC.0000032719.40094.1d, 2004.
- Cravens, T. E. (Ed.), *Physics of solar system plasmas /Thomas E. Cravens. Cambridge : Cambridge, Cambridge : Cambridge University Press, 1997.*
- Crider, D., et al., Magnetic field draping around Mars: Mars Global Surveyor results, *Adv. Space. Res.*, *27*, 1831–1836, doi:10.1016/S0273-1177(01)00333-7, 2001.
- Diéval, C., The solar wind protons inside the induced magnetosphere of mars, *Tech. rep.*, Luleå University of Technology, Department of Computer Science, Electrical and Space Engineering Division of Space Technology, licentiate thesis, ISBN 978-91-7439-337-8, ISSN 1402-1757, 2011.
- Dolginov, S. S., On the magnetic field of Mars - Mars 5 evidence, *Geophys. Res. Lett.*, *5*, 93–95, doi:10.1029/GL005i001p00093, 1978.

- Dubinin, E., M. Fränz, J. Woch, E. Roussos, S. Barabash, R. Lundin, J. D. Winningham, R. A. Frahm, and M. Acuña, Plasma Morphology at Mars. Aspera-3 Observations, *Space Sci. Rev.*, *126*, 209–238, doi:10.1007/s11214-006-9039-4, 2006a.
- Dubinin, E., G. Chanteur, M. Fraenz, R. Modolo, J. Woch, E. Roussos, S. Barabash, R. Lundin, and J. D. Winningham, Asymmetry of plasma fluxes at Mars. ASPERA-3 observations and hybrid simulations, *Planet Space Sci.*, *56*, 832–835, doi:10.1016/j.pss.2007.12.006, 2008a.
- Dubinin, E., M. Fraenz, A. Fedorov, R. Lundin, N. Edberg, F. Duru, and O. Vaisberg, Ion Energization and Escape on Mars and Venus, *Space Sci. Rev.*, *162*, 173–211, doi:10.1007/s11214-011-9831-7, 2011.
- Dubinin, E., et al., Solar wind plasma protrusion into the martian magnetosphere: ASPERA-3 observations, *Icarus*, *182*, 343–349, doi:10.1016/j.icarus.2005.08.023, 2006b.
- Dubinin, E., et al., Structure and dynamics of the solar wind/ionosphere interface on Mars: MEX-ASPERA-3 and MEX-MARSIS observations, *Geophys. Res. Lett.*, *35*, L11,103, doi:10.1029/2008GL033730, 2008b.
- Dubinin, E., et al., Plasma environment of Mars as observed by simultaneous MEX-ASPERA-3 and MEX-MARSIS observations, *Journal of Geophysical Research (Space Physics)*, *113*, A10217, doi:10.1029/2008JA013355, 2008c.
- Dubinin, E. M., et al., Access of solar wind electrons into the Martian magnetosphere, *Annales Geophysicae*, *26*, 3511–3524, doi:10.5194/angeo-26-3511-2008, 2008d.
- Edberg, N. J. T., M. Lester, S. W. H. Cowley, and A. I. Eriksson, Statistical analysis of the location of the Martian magnetic pileup boundary and bow shock and the influence of crustal magnetic fields, *J. Geophys. Res.*, *113*, A08,206, doi:10.1029/2008JA013096, 2008.
- Edberg, N. J. T., D. A. Brain, M. Lester, S. W. H. Cowley, R. Modolo, M. Fränz, and S. Barabash, Plasma boundary variability at Mars as observed by Mars Global Surveyor and Mars Express, *Ann. Geophys.*, *27*, 3537–3550, doi:10.5194/angeo-27-3537-2009, 2009.
- Edberg, N. J. T., H. Nilsson, A. O. Williams, M. Lester, S. E. Milan, S. W. H. Cowley, M. Fränz, S. Barabash, and Y. Futaana, Pumping out the atmosphere of Mars through solar wind pressure pulses, *Geophys. Res. Lett.*, *37*, L03107, doi:10.1029/2009GL041814, 2010.
- Fillingim, M. O., et al., Model calculations of electron precipitation induced ionization patches on the nightside of Mars, *Geophys. Res. Lett.*, *34*, L12,101, doi:10.1029/2007GL029986, 2007.

- Frahm, R. A., et al., Carbon dioxide photoelectron energy peaks at Mars, *Icarus*, 182, 371–382, doi:10.1016/j.icarus.2006.01.014, 2006.
- Fränz, M., E. Dubinin, E. Nielsen, J. Woch, S. Barabash, R. Lundin, and A. Fedorov, Transterminator ion flow in the Martian ionosphere, *Planet Space Sci.*, 58, 1442–1454, doi:10.1016/j.pss.2010.06.009, 2010.
- Fränz, M., et al., Plasma intrusion above Mars crustal fields—Mars Express ASPERA-3 observations, *Icarus*, 182, 406–412, doi:10.1016/j.icarus.2005.11.016, 2006.
- Futaana, Y., et al., First ENA observations at Mars: ENA emissions from the martian upper atmosphere, *Icarus*, 182, 424–430, doi:10.1016/j.icarus.2005.09.019, 2006.
- Gunell, H., et al., First ENA observations at Mars: Charge exchange ENAs produced in the magnetosheath, *Icarus*, 182, 431–438, doi:10.1016/j.icarus.2005.10.027, 2006.
- Hanson, W. B., S. Sanatani, and D. R. Zuccaro, The Martian ionosphere as observed by the Viking retarding potential analyzers, *J. Geophys. Res.*, 82, 4351–4363, doi:10.1029/JS082i028p04351, 1977.
- Hoffman, N., White Mars: A New Model for Mars' Surface and Atmosphere Based on CO₂, *Icarus*, 146, 326–342, doi:10.1006/icar.2000.6398, 2000.
- Holmström, M., S. Barabash, and E. Kallio, Energetic neutral atoms at Mars 1. Imaging of solar wind protons, *Journal of Geophysical Research (Space Physics)*, 107, 1277, doi:10.1029/2001JA000325, 2002.
- Hundhausen, A. J., Coronal Expansion and Solar Wind, in *Coronal Expansion and Solar Wind, XII, 238 pp. 101 figs.. Also Physics and Chemistry in Space, volume 5*, Springer-Verlag Berlin Heidelberg New York., 1972.
- Jian, L., C. T. Russell, J. G. Luhmann, and R. M. Skoug, Properties of Interplanetary Coronal Mass Ejections at One AU During 1995–2004, *Solar Physics*, 239, 393–436, doi:10.1007/s11207-006-0133-2, 2006.
- Kallio, E., and S. Barabash, On the elastic and inelastic collisions between precipitating energetic hydrogen atoms and Martian atmospheric neutrals, *J. Geophys. Res.*, 105, 24,973–24,996, doi:10.1029/2000JA900077, 2000.
- Kallio, E., and S. Barabash, Atmospheric effects of precipitating energetic hydrogen atoms on the Martian atmosphere, *J. Geophys. Res.*, 106, 165–178, doi:10.1029/2000JA002003, 2001.
- Kallio, E., and P. Janhunen, Atmospheric effects of proton precipitation in the Martian atmosphere and its connection to the Mars-solar wind interaction, *J. Geophys. Res.*, 106, 5617–5634, doi:10.1029/2000JA000239, 2001.

- Kallio, E., J. G. Luhmann, and S. Barabash, Charge exchange near Mars: The solar wind absorption and energetic neutral atom production, *J. Geophys. Res.*, *102*, 22,183–22,198, doi:10.1029/97JA01662, 1997.
- Kliore, A. J., Radio occultation observations of the ionospheres of Mars and Venus, *Washington DC American Geophysical Union Geophysical Monograph Series*, *66*, 265–276, 1992.
- Krasnopolsky, V. A., and G. R. Gladstone, Helium on Mars and Venus: EUVE observations and modeling, *Icarus*, *176*, 395–407, doi:10.1016/j.icarus.2005.02.005, 2005.
- Krasnopolsky, V. A., S. Bowyer, S. Chakrabarti, G. R. Gladstone, and J. S. McDonald, First measurement of helium on Mars: Implications for the problem of radiogenic gases on the terrestrial planets, *Icarus*, *109*, 337–351, doi:10.1006/icar.1994.1098, 1994.
- Lundin, R., H. Borg, B. Hultqvist, A. Zakharov, and R. Pellinen, First measurements of the ionospheric plasma escape from Mars, *Nature*, *341*, 609–612, doi:10.1038/341609a0, 1989.
- Lundin, R., et al., Plasma composition measurements of the Martian magnetosphere morphology, *Geophys. Res. Lett.*, *17*, 877–880, doi:10.1029/GL017i006p00877, 1990.
- Lundin, R., et al., Solar Wind-Induced Atmospheric Erosion at Mars: First Results from ASPERA-3 on Mars Express, *Science*, *305*, 1933–1936, doi:10.1126/science.1101860, 2004.
- McComas, D. J., S. J. Bame, P. Barker, W. C. Feldman, J. L. Phillips, P. Riley, and J. W. Griffee, Solar Wind Electron Proton Alpha Monitor (SWEPAM) for the Advanced Composition Explorer, *Space Sci. Rev.*, *86*, 563–612, doi:10.1023/A:1005040232597, 1998.
- McKay, C. P., and C. R. Stoker, The Early Environment and its Evolution on Mars: Implications for Life, *Reviews of Geophysics*, *27*, 189–214, doi:10.1029/RG027i002p00189, 1989.
- Mitchell, D. L., R. P. Lin, C. Mazelle, H. Rème, P. A. Cloutier, J. E. P. Connerney, M. H. Acuña, and N. F. Ness, Probing Mars' crustal magnetic field and ionosphere with the MGS Electron Reflectometer, *J. Geophys. Res.*, *106*, 23,419–23,428, doi:10.1029/2000JE001435, 2001.
- Modolo, R., G. M. Chanteur, E. Dubinin, and A. P. Matthews, Influence of the solar EUV flux on the Martian plasma environment, *Annales Geophysicae*, *23*, 433–444, doi:10.5194/angeo-23-433-2005, 2005.
- Nagy, A. F., et al., The plasma Environment of Mars, *Space Sci. Rev.*, *111*, 33–114, doi:10.1023/B:SPAC.0000032718.47512.92, 2004.

- Nilsson, H., N. J. T. Edberg, G. Stenberg, S. Barabash, M. Holmström, Y. Futaana, R. Lundin, and A. Fedorov, Heavy ion escape from Mars, influence from solar wind conditions and crustal magnetic fields, *Icarus*, *215*, 475–484, doi:10.1016/j.icarus.2011.08.003, 2011.
- Parker, E. N., *Interplanetary dynamical processes.*, 1963.
- Riedler, W., K. Schwingenschuh, D. Moehlmann, V. N. Oraevskii, E. Eroshenko, and J. Slavin, Magnetic fields near Mars - First results, *Nature*, *341*, 604–607, doi:10.1038/341604a0, 1989.
- Sauer, K., A. Bogdanov, and K. Baumgärtel, Evidence of an ion composition boundary (protonopause) in bi-ion fluid simulations of solar wind mass loading, *Geophys. Res. Lett.*, *21*, 2255–2258, doi:10.1029/94GL01691, 1994.
- Schultz, C., Research Spotlight: Evidence for water ice near the Martian equator, *EOS Transactions*, *92*, 60–60, doi:10.1029/2011EO070014, 2011.
- Schwingenschuh, K., et al., The Martian magnetic field environment - Induced or dominated by an intrinsic magnetic field?, *Adv. Space. Res.*, *12*, 213–219, doi:10.1016/0273-1177(92)90333-S, 1992.
- Shinagawa, H., and T. E. Cravens, A one-dimensional multispecies magnetohydrodynamic model of the dayside ionosphere of Mars, *J. Geophys. Res.*, *94*, 6506–6516, doi:10.1029/JA094iA06p06506, 1989.
- Smith, C. W., J. L'Heureux, N. F. Ness, M. H. Acuña, L. F. Burlaga, and J. Scheifele, The ACE Magnetic Fields Experiment, *Space Sci. Rev.*, *86*, 613–632, doi:10.1023/A:1005092216668, 1998.
- Soobiah, Y., et al., Observations of magnetic anomaly signatures in Mars Express ASPERA-3 ELS data, *Icarus*, *182*, 396–405, doi:10.1016/j.icarus.2005.10.034, 2006.
- Stenberg, G., H. Nilsson, Y. Futaana, S. Barabash, A. Fedorov, and D. Brain, Observational evidence of alpha-particle capture at Mars, *Geophys. Res. Lett.*, *38*, L09101, doi:10.1029/2011GL047155, 2011.
- Stone, E. C., et al., The advanced composition explorer, in *Particle Astrophysics - The NASA Cosmic Ray Program for the 1990s and Beyond*, American Institute of Physics Conference Series, vol. 203, edited by W. V. Jones, F. J. Kerr, and J. F. Ormes, pp. 48–57, doi:10.1063/1.39173, 1990.
- Terada, N., Y. N. Kulikov, H. Lammer, H. I. M. Lichtenegger, T. Tanaka, H. Shinagawa, and T. Zhang, Atmosphere and Water Loss from Early Mars Under Extreme Solar Wind and Extreme Ultraviolet Conditions, *Astrobiology*, *9*, 55–70, doi:10.1089/ast.2008.0250, 2009.

- Trotignon, J. G., E. Dubinin, R. Gérard, S. Barabash, and R. Lundin, Martian planetopause as seen by the plasma wave system onboard Phobos 2, *J. Geophys. Res.*, *1012*, 24,965–24,978, doi:10.1029/96JA01898, 1996.
- Vignes, D., et al., The solar wind interaction with Mars: Locations and shapes of the Bow Shock and the magnetic pile-up boundary from the observations of the MAG/ER experiment onboard Mars Global Surveyor, *Geophys. Res. Lett.*, *27*, 49–52, doi:10.1029/1999GL010703, 2000.
- Zaitsev, I., The successes of Phobos-2, *Spaceflight*, *31*, 374–379, 1989.
- Zhang, M. H. G., J. G. Luhmann, A. J. Kliore, and J. Kim, A post-Pioneer Venus reassessment of the Martian dayside ionosphere as observed by radio occultation methods, *J. Geophys. Res.*, *951*, 14,829–14,839, doi:10.1029/JB095iB09p14829, 1990.
- Zhang, T.-L., K. Schwingenschuh, C. T. Russell, J. G. Luhmann, H. Rosenbauer, M. I. Verigin, and G. Kotova, The flaring of the Martian magnetotail observed by the PHOBOS 2 spacecraft, *Geophys. Res. Lett.*, *21*, 1121–1124, doi:10.1029/94GL01073, 1994.
- Zhang, T. L., et al., Induced magnetosphere and its outer boundary at Venus, *Journal of Geophysical Research (Planets)*, *113*, E00B20, doi:10.1029/2008JE003215, 2008.

PAPER I

A case study of proton precipitation at Mars: Mars Express observations and hybrid simulations

C. Diéval,^{1,2} E. Kallio,³ S. Barabash,¹ G. Stenberg,¹ H. Nilsson,¹ Y. Futaana,¹ M. Holmström,¹ A. Fedorov,⁴ R. A. Frahm,⁵ R. Jarvinen,³ and D. A. Brain⁶

Received 17 January 2012; revised 2 May 2012; accepted 4 May 2012; published 16 June 2012.

[1] Using the data from the Analyzer of Space Plasma and Energetic Atoms (ASPERA-3) experiment on board Mars Express and hybrid simulations, we have investigated the entry of protons into the Martian induced magnetosphere. We discuss one orbit on the dayside with observations of significant proton fluxes at altitudes down to 260 km on 27 February 2004. The protons observed below the induced magnetosphere boundary at an altitude of less than 700 km have energies of a few keV, travel downward, and precipitate onto the atmosphere. The measured energy flux and particle flux are 10^8 – 10^9 eV cm⁻² s⁻¹ and 10^5 – 10^6 H⁺ cm⁻² s⁻¹, respectively. The proton precipitation occurs because the Martian magnetosheath is small with respect to the heated proton gyroradius in the subsolar region. The data suggest that the precipitation is not permanent but may occur when there are transient increases in the magnetosheath proton temperature. The higher-energy protons penetrate deeper because of their larger gyroradii. The proton entry into the induced magnetosphere is simulated using a hybrid code. A simulation using a fast solar wind as input can reproduce the high energies of the observed precipitating protons. The model shows that the precipitating protons originate from both the solar wind and the planetary exosphere. The precipitation extends over a few thousand kilometers along the orbit of the spacecraft. The proton precipitation does not necessarily correlate with the crustal magnetic anomalies.

Citation: Diéval, C., et al. (2012), A case study of proton precipitation at Mars: Mars Express observations and hybrid simulations, *J. Geophys. Res.*, 117, A06222, doi:10.1029/2012JA017537.

1. Introduction

[2] When the supersonic solar wind carrying the interplanetary magnetic field (IMF) flows around a planet such as Mars, which is surrounded by an ionosphere but lacks a global magnetic field, it induces currents in the ionosphere. The associated magnetic field deflects the solar wind flow and results in the formation of an obstacle, the induced magnetosphere. A bow shock and a magnetosheath are also formed similarly to the conventional magnetosphere. The IMF drapes around the conductive ionosphere on the dayside of the planet, and it is stretched into a magnetotail on the nightside. The draping configuration results from

the superposition of the IMF and the magnetic field of the currents induced in the ionosphere. The stretched magnetotail results from mass loading of the magnetic field tubes moving in the upper parts of the ionosphere. If the obstacle was perfectly non-conductive neither draping nor stretching would have occurred. The region of the field draping is called the magnetic pile-up region. It is roughly limited at the upper edge by the induced magnetosphere boundary (IMB), where pressure balance is achieved between the solar wind dynamic pressure and the magnetic pressure [e.g., *Dubinin et al.*, 2008]. At the IMB, the ion composition of the plasma changes from proton-dominated to heavy-ion dominated. The lower boundary of the magnetic pile-up region, referred to as the photoelectron boundary (PEB), is characterized by the appearance of the CO₂ photoelectrons [*Frahm et al.*, 2006] and a sharp increase in the electron number density [*Dubinin et al.*, 2008]. The picture of the Martian magnetosphere is further complicated by the presence of strong crustal magnetic field anomalies in the Southern hemisphere [*Acuña et al.*, 1998, 1999]. Further details of the solar wind interaction with Mars can be found in the review by *Nagy et al.* [2004].

[3] The IMB envelops the solar wind void but is not impenetrable. Due to the small size of the induced magnetosphere, particularly in the subsolar region, the effect of a finite gyroradius becomes important, and the shocked solar

¹Swedish Institute of Space Physics, Kiruna, Sweden.

²Also at Division of Space Technology, Department of Computer Science, Electrical and Space Engineering, Luleå Technical University, Kiruna, Sweden.

³Finnish Meteorological Institute, Helsinki, Finland.

⁴Institut de Recherche en Astrophysique et Planetologie, Toulouse, France.

⁵Southwest Research Institute, San Antonio, Texas, USA.

⁶Laboratory for Atmospheric and Space Physics, University of Colorado, Boulder, Colorado, USA.

Corresponding author: C. Diéval, Swedish Institute of Space Physics, Box 812, SE-98128, Kiruna, Sweden. (catherine@irf.se)

©2012. American Geophysical Union. All Rights Reserved.

wind protons may penetrate through the IMB and precipitate onto the Martian ionosphere. This paper uses data analysis and hybrid modeling to study how the protons penetrate into the ionosphere.

[4] Proton precipitation on Mars has previously been studied by two global hybrid models. In the first model, *Brecht* [1997] simulated the direct impact of the solar wind H^+ ions at the surface of Mars and showed that the rate of deposition of precipitating protons depends on the solar wind dynamic pressure and the angle of the IMF with respect to the solar wind velocity. The energy flux, which is deposited in the upper atmosphere by the precipitating protons, varies spatially, and is controlled by the solar wind convection electric field $\vec{E}_{sw} = -\vec{v}_{sw} \times \vec{B}$, where \vec{B} is the IMF vector and \vec{v}_{sw} is the solar wind velocity vector. In the second model, *Kallio and Janhunen* [2001] studied the solar wind H^+ ion precipitation onto the Martian atmosphere and the related effects on the atmospheric neutrals. They showed that on the dayside, the hemisphere aligned with the convection electric field experiences a higher energy flux of precipitating protons than the opposite hemisphere; and the energy flux is also higher at low solar zenith angle (SZA) than at high SZA.

[5] Some direct and indirect observations are also available. *Lundin et al.* [2004] reported that solar wind protons can reach altitudes as low as 270 km. They used the in situ plasma data of the Analyzer of Space Plasma and Energetic Atoms (ASPERA-3) experiment on board the Mars Express (MEX) mission. The penetration of solar wind alpha particles into the ionosphere of Mars was demonstrated by *Stenberg et al.* [2011]. The entry of the solar wind electrons into the Martian atmosphere has also been studied extensively [see, e.g., *Brain et al.*, 2005; *Fränz et al.*, 2006].

[6] This paper provides ASPERA-3 measurements of energy/particle fluxes of the downward-moving protons into the Martian atmosphere in the subsolar region and proposes a mechanism to explain the proton precipitation. The paper also investigates the origin of the proton fluxes using hybrid modeling, and suggests that the precipitation is a transient phenomenon. Section 2 presents the instruments that provide the data used in this study. Section 3 describes the observations of proton precipitation fluxes. In section 4, the hybrid code used in this study and the modeling results are briefly presented. Finally, the results are discussed in section 5.

2. Instrumentation

[7] ASPERA-3 is an instrument package designed to study the interaction between the solar wind and the Martian atmosphere [*Barabash et al.*, 2006]. It comprises the Electron Spectrometer (ELS), the Ion Mass Analyzer (IMA) and two energetic neutral atom sensors.

[8] For this study, the ELS instrument measures the two-dimensional distributions of the electron flux in the energy range 5 eV–15 keV ($\Delta E/E = 8\%$) with a field of view (FOV) of $4^\circ \times 360^\circ$ divided into 16 azimuth sectors. The time resolution used in this study is 4 s. Observation of very low-energy electrons is prohibited by a repelling grid voltage of -5 V.

[9] The IMA instrument consists of an electrostatic deflection system followed by a top-hat electrostatic energy analyzer

and a magnetic mass analyzer. The IMA sensor measures the fluxes of different ion species with m/q resolution (m and q are the ion mass and charge, respectively) in the energy range of 200 eV/ q –36 keV/ q . The measured ions include H^+ , He^{2+} , O^+ and molecular ions with $20 < m/q < 80$. With a time resolution of 12 s, IMA gives a two-dimensional measurement of the ion fluxes (16 azimuth sectors) for all energies. Electrostatic sweeping provides $\pm 45^\circ$ coverage out of the plane of the aperture, and a complete distribution with a FOV of $90^\circ \times 360^\circ$ is produced in 192 s (one elevation scan).

[10] Both ELS and IMA have other operational modes that are not used in this paper.

3. Observations

[11] We present a detailed analysis of one event from the subsolar region (within 0 – 45° SZA) where the proton fluxes are observed below the IMB. The event is recorded by Mars Express/ASPERA-3 on 27 February 2004 (orbit 154). This orbit was chosen because the protons were observed during several consecutive IMA scans down to the pericenter and because the protons had energies up to 7 keV. The present paper contains a deeper analysis of the proton penetration reported by *Lundin et al.* [2004], which briefly considered the same orbit.

[12] Figure 1 presents the data from the event. Figure 1a shows the altitude and the SZA of the spacecraft, and Figure 1b shows the magnitude and the angle of the crustal magnetic field vector relative to the local zenith. The magnetic field vector is derived at the spacecraft position from the Cain model [*Cain et al.*, 2003]. Figure 1c shows the electron energy-time spectrogram (averaged over sectors 4–8).

[13] The pass through the dayside ionosphere is visible in the electron data as a thin horizontal, the so-called photoelectron line, at ~ 20 eV. These electrons are produced by photoionization of the atmospheric CO_2 [*Frahm et al.*, 2006]. The pericenter altitude of ~ 260 km is reached at $\sim 19:40$ UT. The outbound crossings of the photoelectron boundary (PEB) at $\sim 19:46:30$ UT and the induced magnetosphere boundary (IMB) at $\sim 19:47:30$ UT are indicated with vertical lines. The decrease of the high-energy electron flux (>80 eV) is used to identify the inbound IMB crossing. The disappearance of the ionospheric electrons indicates that MEX made an incursion into the magnetosheath between $\sim 19:25:30$ UT and $19:27:00$ UT. At that time, MEX had an altitude of 900–1000 km near the terminator. The inward motion of IMB and the appearance of the magnetosheath plasma likely result from a pulse of increased solar wind dynamic pressure which occurred between $19:25:30$ UT and $19:27:00$ UT, pushing the shocked electrons closer to Mars.

[14] Figure 1c shows that the high-energy electron flux (with energy up to 400 eV) gradually decreases from $19:27$ UT until $19:41$ UT as MEX approaches the planet. The electron entries are intermittent. Similar entries of high-energy electrons were previously observed by ASPERA-3 [e.g., *Lundin et al.*, 2004; *Soobiah et al.*, 2006] and the Mars Global Surveyor (MGS) electron reflectometer [e.g., *Mitchell et al.*, 2001]. The flux of shocked electrons is decreased compared to the flux in the magnetosheath proper and becomes less energetic. Furthermore, the photoelectrons become more visible when the magnetosheath flux weakens. The intermittent penetration of shocked electrons may be

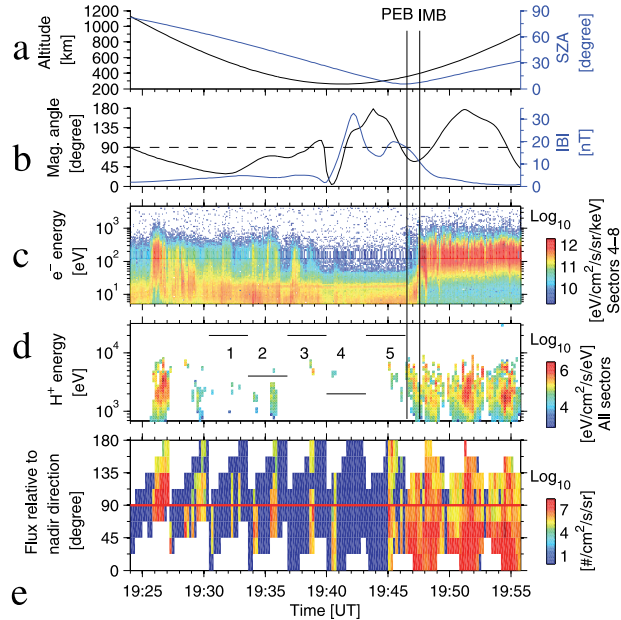


Figure 1. Observations made on 27 February 2004 (19:24 UT–19:56 UT). (a) Altitude (left axis, black solid curve) and solar zenith angle (SZAs) (right axis, blue solid curve). (b) Magnitude of the crustal magnetic field (left axis, black solid curve) and angle of the crustal magnetic field vector relative to the local zenith from the Cain model (left axis, black solid curve) at the spacecraft position. The direction of the modeled magnetic field vector is shown relative to the zenith. Hence, 0° and 180° correspond to the locally upward and downward vertical magnetic fields, respectively; 90° corresponds to a locally horizontal magnetic field. (c) Electron energy-time spectrogram averaged over the azimuth sectors 4–8. The unit is $\log_{10}(\text{eV cm}^{-2} \text{s}^{-1} \text{sr}^{-1} \text{keV}^{-1})$. (d) Proton energy-time spectrogram averaged over all azimuth sectors. The unit is $\log_{10}(\text{eV cm}^{-2} \text{s}^{-1} \text{eV}^{-1})$. (e) Observed direction of the proton fluxes relative to nadir for the energy range 1.1–10.5 keV. The unit is $\log_{10}(\text{H}^+ \text{cm}^{-2} \text{s}^{-1} \text{sr}^{-1})$. Hence, 0° and 180° correspond to the fluxes directed toward the nadir and the zenith, respectively. A horizontal solid red line is drawn at 90° to separate the downgoing flux (below the line) from the upgoing flux (above the line). The black vertical solid lines indicate the plasma boundaries.

caused by the rapid and small-amplitude back-and-forth motions of the IMB above MEX while MEX is located in the magnetic pile-up region. Note, however, that MEX is always below the IMB during this period. Between 19:41 UT and 19:46 UT, the spacecraft is located in the ionosphere and no sheath electron entries are observed.

[15] The protons are shown in Figures 1d and 1e. Figure 1d shows the proton energy-time spectrogram (averaged over all azimuth sectors) and Figure 1e presents the direction of the observed proton fluxes relative to nadir, binned in 22.5° bins. In Figure 1d, only the fluxes above the (one-count) background level are shown. Each time interval of 12 s corresponds to measurements at a fixed elevation angle over 360° azimuths. After 12 s, the voltage settings of the deflector system are changed to measure at the next elevation angle. In 192 s, we observe 16 different elevations (a full elevation scan), giving a coverage of ± 45 degrees out of the plane of the aperture. The “blob” shape of the

proton flux is due to this elevation sweep. Each elevation scan of interest is given a number and is indicated by a horizontal solid line in Figure 1d. The white areas in Figure 1e are the directions not covered by the measurement or the directions blocked by the spacecraft. The flux in Figure 1e is integrated over the energy range 1.1–10.5 keV.

[16] There are five elevation scans with significant proton fluxes (compared to the background level) at altitudes below 700 km: 19:31–19:33 UT (scan 1), 19:34–19:36 UT (2), 19:38–19:39 UT (3), 19:40–19:41 UT (4) and 19:45–19:46 UT (5). The proton flux in scans 1 to 5 drops by a factor of ~ 10 –100 compared to the values in the magnetosheath. We notice that the protons are accompanied by shocked electrons, between 19:27 UT and 19:41 UT (including scans 1–4), while we see protons without shocked electrons in scan 5. The protons are relatively abundant below the IMB during the inbound pass (scans 1–4), and only sporadic fluxes are seen during the outbound pass (scan 5). The orbit

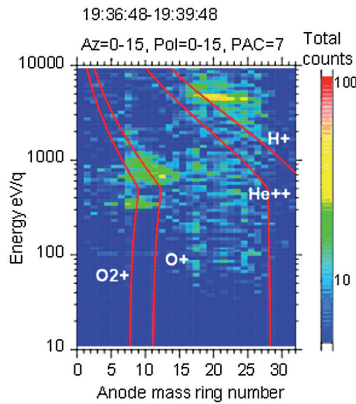


Figure 2. Plasma composition during scan 3. The ion fluxes are shown as a function of energy and radial position on the Ion Mass Analyzer (IMA) detection plate. The skewed red lines are curves of constant m/q for H^+ , He^{2+} , O^+ and O_2^+ . The counts shown are integrated over all azimuth sectors and all elevations.

geometry during the inbound pass is such that MEX skims the IMB; therefore the orbit geometry is favorable to an extended period where protons are observed below the IMB. On the outbound pass, the orbit geometry is different and we observe a narrow region of proton precipitation (scan 5) and a sharp IMB crossing (at $\sim 19:47:30$ UT). Within one given scan, the protons are not continuously observed, which might be because the looking directions of the instrument do not match the proton flux.

[17] From Figure 1e, we find that on average, 81% of the total proton particle flux (total = upward + downward) measured during these 5 scans is moving downward (angle to nadir $< 90^\circ$), and it can be considered as a precipitating flux. The protons below the IMB flow both toward and away from Mars, and the angle distribution is broad, covering several angular bins within a downgoing hemisphere.

[18] However we cannot be sure that the protons will actually reach the exobase (the measurements are made down to only 260 km in altitude). The exobase altitude is ~ 180 km at solar minimum. Regardless, we assume that this event shows a clear case of proton precipitation.

[19] Mars Express does not carry a magnetometer: to relate the observed precipitation event to the crustal magnetic field, we use the Cain model [Cain *et al.*, 2003]. We note that the magnetic field predicted by the Cain model is not likely the field experienced by MEX because the draped induced magnetic field, which is typically ≥ 30 nT at low SZA, is expected to dominate [Brain *et al.*, 2005]. In Figure 1b, we see that the spacecraft is passing above weak crustal field regions $|B| < 35$ nT and that the magnetic zenith angle varies between different proton flux observations. For comparison, the magnitude of the draped magnetic field in the subsolar region during this orbit is ~ 50 nT [Brain *et al.*, 2005]. Downgoing proton fluxes are observed regardless

of the crustal magnetic field direction: horizontal (scan 3), vertical (scans 1 and 4), or intermediate (scans 2 and 5). The crustal magnetic field strength is >10 T during 19:41 UT–19:47 UT, while proton fluxes are still sporadically detected during this period. Therefore, we argue that neither the orientation nor the strength of the crustal field influence the proton precipitation in the ionosphere.

[20] Figure 2 shows the plasma composition of scan 3. The ion fluxes are presented as a function of the energy and the radial position on the detection plate in the IMA detector. The red lines are curves of constant m/q corresponding to H^+ , He^{2+} , O^+ and O_2^+ . The counts shown are integrated over all azimuth sectors and all elevations, during ~ 3 min.

[21] In this study heavy planetary ions (O^+ , O_2^+) were recorded during scans 1, 3, 4 and 5. However, before May 2007, the instrumental energy cut-off for heavy ions was 200 eV [Lundin *et al.*, 2008], which explains why the heavy ions are not detected during all scans. Additionally, alpha particles were only observed during scan 2. The protons can sometimes be observed together with the alpha particles at low altitudes [Stenberg *et al.*, 2011].

[22] To verify our assumption that the proton fluxes have a magnetosheath origin, in Figure 3, we plot the energy spectrum of the scans 1–5 together with a magnetosheath energy spectrum from the same orbit (taken at SZA $\sim 20^\circ$).

[23] The black vertical dashed line indicates the instrumental energy cutoff for the respective mode of IMA, and the blue dashed line represents the one-count level. Due to the decrease of the detection efficiency with the energy,

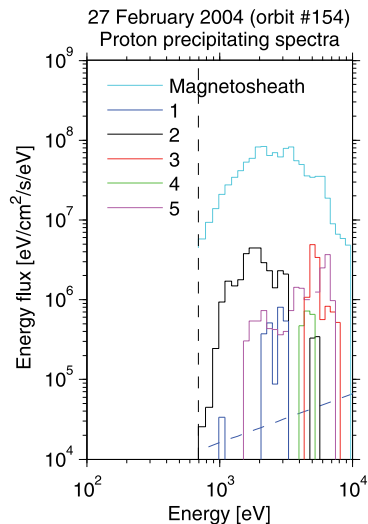


Figure 3. Energy flux of precipitating protons for scans 1–5. A magnetosheath energy spectrum obtained during the same orbit is also shown. The unit is $eV\ cm^{-2}\ s^{-1}\ eV^{-1}$. See text for details.

which is an inherent feature of the IMA detector geometry, the fluxes corresponding to the one-count level increase with the energy. However, the observed fluxes are well above the one-count level for the shown energy range.

[24] The maximum magnetosheath flux is approximately 2 orders of magnitude higher than the maximum precipitating proton flux. The magnetosheath energy spectrum peaks at ~ 2 keV, which indicates that the upstream solar wind must be fast and may explain the observation of protons with energies up to 7 keV close to Mars during the investigated period. Overall, the proton fluxes recorded below the IMB are not more energetic than the magnetosheath protons. The hypothesis of a magnetosheath origin of the penetrating protons is further examined in section 4.

[25] All scans with recorded proton fluxes that are discussed in the paper are summarized in Table 1. The energy range and the peak energy of the proton energy spectra are given with an indicator of whether the shocked electrons were observed during the scan. The table gives the spacecraft altitude, the SZA, the crustal magnetic field magnitude and the crustal magnetic zenith angle for each scan. In the table, the maximum values of the energy flux ($7 \cdot 10^9$ eV cm $^{-2}$ s $^{-1}$) and the particle flux ($3 \cdot 10^6$ H $^+$ cm $^{-2}$ s $^{-1}$) are shown in boldface. In summary, the precipitating proton fluxes of 10^5 – 10^6 H $^+$ cm $^{-2}$ s $^{-1}$ (and energy fluxes of 10^8 – 10^9 eV cm $^{-2}$ s $^{-1}$) are observed in the altitude range of ~ 260 – 630 km for SZA between 7° – 60° . The precipitating protons seem unrelated to the location and the topology of the crustal magnetic fields.

[26] In order to investigate effects of the different upstream conditions, we used the MGS proxy defined by *Crider et al.* [2003] to derive the solar wind dynamic pressure, and we used the MGS magnetic field data to derive the IMF direction following the approach described by *Fedorov et al.* [2006]. The upstream dynamic pressure proxy value was nominal: 0.99 nPa (close to the average value = 1.06 nPa [*Crider et al.*, 2003]). This value may not represent the sudden pulse of increased dynamic pressure (19:25:30 UT–19:27:00 UT), but it may correspond to a period of more quiet solar wind conditions following the increased pressure pulse. Nevertheless, the IMB crossing with altitude of ~ 393 km at 7° SZA at 19:47:30 UT is lower than average. This suggests that the overall solar wind dynamic pressure remains high during our observations. Thus, we believe that the case of proton precipitation presented here is associated with high dynamic pressure conditions.

[27] In MSO (Mars Solar Orbital) coordinates, the y and z components of the IMF are estimated to be $[-1.6, -2.5]$ nT for the analyzed case. In MSO, the x axis points from the center of Mars toward the Sun, the z axis points toward the orbital north and the y axis completes the right hand system. Assuming a Parker spiral shape for the IMF, we conclude that the IMF points dawnward and the solar wind convection electric field points southward. The hybrid modeling studies [*Brecht*, 1997; *Kallio and Janhunen*, 2001] predict that the proton precipitation would be more intensive in the hemisphere where \vec{E}_{sw} points away from the planet. In our case, this hemisphere is the southern hemisphere, where the proton precipitation is indeed observed. However, no further conclusion could be drawn without a statistical study.

[28] In section 4, we use hybrid modeling to interpret the observational data. The input to the model is the upstream IMF that we just discussed.

4. Hybrid Simulations

[29] We use the HYB-Mars model, a 3-D quasi-neutral hybrid model, and we will compare the modeling results with the observations of proton precipitation found on 27 February 2004. The HYB-Mars model is described in detail by *Kallio et al.* [2010] and the references therein. Here, we briefly discuss the fundamental parts of the model and the new features added since the work by *Kallio et al.* [2010].

[30] HYB-Mars is a particle-in-cloud model [*Kallio and Janhunen*, 2003]. The plasma ions are treated as macroparticles, which correspond to groups of real plasma ions, and the electrons are treated as a massless charge-neutralizing fluid. The code includes finite gyroradius effects, which makes it suitable to study ion precipitation.

[31] The ions are accelerated by the Lorentz force:

$$m_i \frac{d\vec{v}_i}{dt} = q_i (\vec{E} + \vec{v}_i \times \vec{B}) \quad (1)$$

where \vec{E} and \vec{B} are the electric field and the magnetic field, and m_i , \vec{v}_i and q_i are the mass, velocity and electric charge of an ion i , respectively. The electric field is calculated from the electron momentum equation:

$$\vec{E} = -\vec{U}_e \times \vec{B} - \frac{\vec{\nabla}(n_e k T_e)}{en_e} \quad (2)$$

where k is the Boltzmann's constant, e is the unit electron charge, and n_e , T_e and \vec{U}_e are the electron density, temperature and bulk velocity, respectively. The gradient term in equation (2) is the electron gradient pressure, which is also called the ambipolar electric field.

[32] The model uses the MSO Cartesian coordinate system. The aberration angle of the solar wind direction, caused by the Martian orbital motion, is neglected in this study. The size of the simulation box is $-4.2 R_m < x, y, z < 4.2 R_m$, where $R_m = 3393$ km is the radius of Mars. In the simulation, the grid size depends on the distance, r , from the center of Mars: the grid size is 720 km where $r > 3 R_m$, 360 km where $2 R_m < r < 3 R_m$ and 180 km where $r < 2 R_m$. The observations were made at $r < 1.32 R_m$. The total running time was 585 s with a time step of 0.02 s. The average number of ions per cell is significant: ~ 30 . The model does not include the crustal magnetic anomalies.

[33] The model contains two spherically symmetric exospheres (oxygen and hydrogen) surrounding Mars. They are sources of H $^+$ and O $^+$ ions. We use the models of the respective coronae adopted by the Solar Wind Interaction with Mars (SWIM) modeling comparison team [see *Braim et al.*, 2010].

[34] The hydrogen neutral profile used is

$$n(H[m^{-3}]) = N_1 \cdot \exp(A_1 \cdot (1/R_1 - 1/r)) + N_2 \cdot \exp(A_2 \cdot (1/R_2 - 1/r)) \quad (3)$$

where $N_1 = 1.5 \cdot 10^{11}$, $N_2 = 1.9 \cdot 10^{10}$, $A_1 = -25965 \cdot 10^3$, $A_2 = -10365 \cdot 10^3$, $R_1 = 3593.5 \cdot 10^3$, $R_2 = 3593.5 \cdot 10^3$, r is the distance from the center of Mars (in meters) and the indices

Table 1. Summary of Proton Precipitation Fluxes^a

Scans, 27 February 2004	Energy Range (keV)	Energy Peak (keV)	Shocked Electrons	Altitude (km)	Solar Zenith Angle (°)	Crustal B (nT)	Magnetic Zenith Angle (°)	Particle Flux (cm ⁻² s ⁻¹)	Energy Flux (eV cm ⁻² s ⁻¹)
1	1.-4.	2.5	yes	627	61.7	3.7	32	2·10 ⁵	6·10 ⁸
2	1.-4.	2.	yes	437	49.4	4.5	54	3·10⁶	6·10 ⁹
3	4.-7.	5.	yes	281	30.7	4.6	94	1·10 ⁶	6·10 ⁹
4	4.5-5.	5.	yes	262	23.5	7.8	7	2·10 ⁵	8·10 ⁸
5	1.5-7.	7.	no	310	7.6	17.8	149	2·10 ⁶	7·10⁹

^aBoldface indicates the maximum values of the energy flux (7·10⁹ eV cm⁻² s⁻¹) and the particle flux (3·10⁶ H⁺ cm⁻² s⁻¹).

1 and 2 refer to the thermal and hot hydrogen profiles, respectively. The thermal component is taken from *Chaufray et al.* [2008]. We take the photoionization rate as 5.58·10⁻⁸ s⁻¹, which is also used by *Ma et al.* [2004] and *Fulle et al.* [2007].

[35] The neutral hot oxygen profile is modeled as

$$n(O[m^{-3}]) = N_1 \cdot \exp(-(r - R_0)/B_1) + N_2 \cdot \exp(-(r - R_0)/B_2) + N_3 \cdot \exp(-(r - R_0)/B_3) \quad (4)$$

where $N_1 = 5.23 \cdot 10^9$, $N_2 = 9.76 \cdot 10^8$, $N_3 = 3.71 \cdot 10^{10}$, $B_1 = 626.2 \cdot 10^3$, $B_2 = 2790 \cdot 10^3$, $B_3 = 88.47 \cdot 10^3$, $R_0 = 3393.5 \cdot 10^3$, and r is the distance from the center of Mars (in meters). We take the photoionization rate as 8.89·10⁻⁸ s⁻¹, which is also used by *Ma et al.* [2004]. The values of the density and the photoionization rates for the neutral profiles correspond to the solar minimum conditions.

[36] The ionosphere is not self-consistently modeled. O⁺ and O₂⁺ ions are emitted from the inner boundary of the model. The inner boundary is a spherical shell at 207 km altitude, which mimics the exobase. The emission of ionospheric oxygen ions is proportional to 0.1 + 0.9·cos(SZA) on the dayside, and it is constant (0.1) on the nightside [*Kallio et al.*, 2010].

[37] The hybrid model implements the electron impact ionization reactions, and the charge-exchange (CX) reactions between the planetary atoms and the planetary/solar wind protons. Details of the reactions are given by *Kallio et al.* [2010].

[38] In our model, the solar wind contains protons and alpha particles. We have conducted two simulations with different input parameters. For both simulations, we use a solar wind density of 2.5 cm⁻³ (the nominal value at Earth scaled to the heliocentric distance of Mars) and a solar wind temperature of 1.5·10⁵ K. In both simulations, the IMF vector is chosen as [0, -1.6, -2.5] nT. The y and z components were estimated from the MGS data (see section 3). For simplicity, the x component has been assumed to be zero, which means that the IMF is perpendicular to the Mars-Sun line. The simulations differ only by the solar wind velocity. The simulations, called “nominal SW” and “fast SW,” use a solar wind velocity of 487 km⁻¹ and 1028 km⁻¹, respectively. These values correspond to dynamic pressures of 1.0 nPa and 4.4 nPa, respectively. The solar wind velocity is taken opposite to the x axis in both simulations.

[39] Two different dynamic pressure values are used to look at the precipitation dynamics. The “fast SW” simulation corresponds to the observations on 27 February 2004 (proton energy up to 7 keV in Figure 1d) being discussed here. We chose the upstream solar wind velocity for the “fast SW” run somewhat arbitrary just requiring that the energy

peak of the input upstream solar wind must be larger than that of the measured magnetosheath energy spectrum (cyan curve in Figure 3). Note that the angular separation between Mars and the Earth during the time of observations was too great (77°) to allow a reliable extrapolation of the solar wind conditions from the WIND or ACE spacecraft.

[40] The code uses an absorbing boundary condition for the ions on the inner boundary. An ion is removed from the simulation if it hits this boundary. In reality, the ions would not be immediately neutralized, but they would be scattered via the collisions with the atmospheric neutrals [*Kallio and Barabash*, 2001, Figure 2].

[41] In this study, we consider two proton populations: the solar wind protons and the exospheric protons. The exospheric protons originate from the hydrogen corona and include photoions, protons created by electron impact ionization and protons created by the CX reactions between the planetary neutral hydrogen and the protons of solar wind/planetary origin. To compare the observations with the simulations, we place a virtual tube detector of radius 170 km along the spacecraft orbit. During 435 s, the position \vec{r}_i , the velocity \vec{v}_i , and the weight w_i of an ion i are recorded when the ion enters the tube detector at the time t_i . The ion weight tells the number of real ions to which a macroparticle corresponds. The radius of the tube detector is on the order of the smallest cell size. This type of detector allows one to make simulated energy time spectrograms along the orbit [*Kallio et al.*, 2008]. The collected ions are binned logarithmically in 52 energy steps from 0.1 to 32 keV using the IMA energy table. The tube detector is divided into small cylindrical elements, where the length of a segment is equal to the distance covered by the spacecraft during 12 s. Hence, the length corresponds to the IMA time resolution for a 2-D measurement at a fixed elevation. We have used the surface of each cylindrical element (the wall of the cylinder) as the collecting surface for the particles. The FOV of a cylindrical element is 360° × 180°. The wall of each cylindrical element is divided into 16 individual azimuth sectors. The proton flux is calculated relative to the normal vector to the surface of each azimuth sector and summed up over all sectors. Figure 4 shows a cylindrical element of the tube detector, together with the velocity vector of an ion hitting the element, the normal vector to an azimuth sector, and a segment along the orbit (thick line).

[42] The particle flux (in units of H⁺ cm⁻² s⁻¹ eV⁻¹) through a cylindrical surface element of radius R and length L is given by the following:

$$F = \frac{1}{2 \cdot \pi \cdot R \cdot L \cdot \Delta t} \sum_{i,j,k} \frac{w_k \cdot \cos(\alpha_{jk})}{\Delta E_i} \quad (5)$$

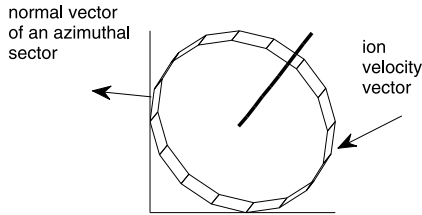


Figure 4. Schema of a cylindrical element of the tube detector, divided into 16 azimuthal sectors. The velocity vector of an ion hitting the element, the normal vector of an azimuthal sector, and a segment along the orbit (the thick line) are also shown.

where α_{jk} is the angle between the velocity of an ion k and the normal vector of an azimuthal sector j and w_k is the weight of an ion k recorded at the energy step E_i of width ΔE_i in the azimuthal sector j .

[43] The central plane of the FOV of the cylindrical element always points perpendicular to the velocity vector of the spacecraft, which gives an ideal orientation to detect particles coming from different directions relative to the local nadir. However, the simulated energy-time spectrograms are not meant to be compared in great detail with the data but to give a qualitative picture of the simulated proton distributions along the orbit.

[44] Figure 5 presents the simulated energy-time spectrograms from the tube detector and compares them with the observations. Shown are the “fast SW” simulation and the “nominal SW” simulation. In both simulations, we distinguish between the planetary protons (Figures 5b and 5g) and the solar wind protons (Figures 5c and 5h). Figures 5d and 5i include all protons. Figures 5a and 5f have the same format as Figure 1a. Figures 5e and 5j have the same format as Figure 1d. The simulated energy-time spectrograms show the first “entry point” of the ions into the tube (each ion can enter the tube several times while gyrating).

[45] The simulations (Figures 5d and 5i) indicate that the proton flux is significant at high altitudes, which is

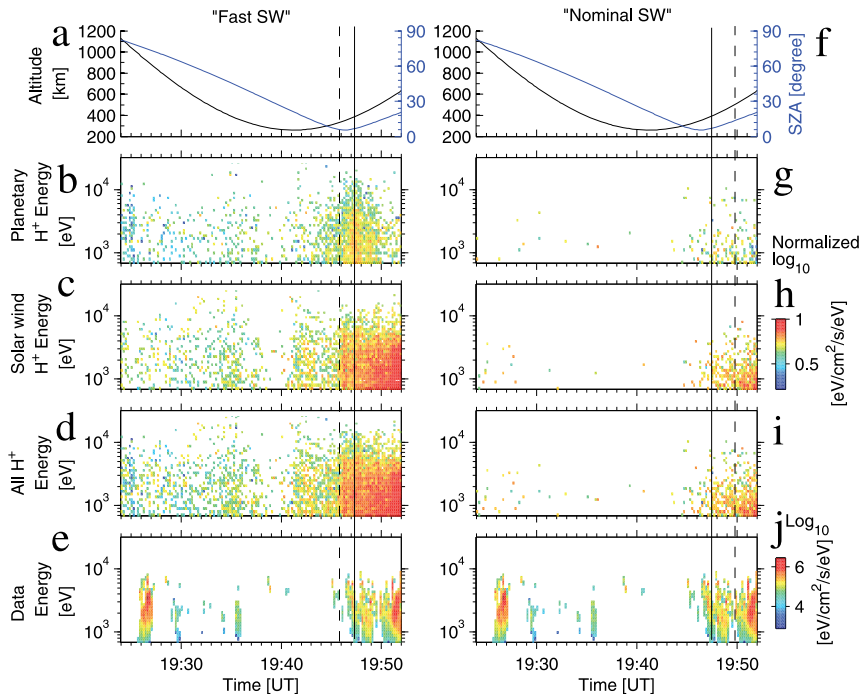


Figure 5. Results from the “fast SW” simulation and the “nominal SW” simulation. (a and f) Same format as Figure 1a. Simulated energy-time spectrogram for (b and g) the planetary protons, (c and h) the solar wind protons and (d and i) all proton populations. In each simulated spectrogram, the unit is $\log_{10}(\text{eV cm}^{-2} \text{s}^{-1} \text{eV}^{-1})$, normalized to the maximum value from Figure 5d. (e and j) Data (Figure 1d) reprinted for ease of comparison. In the simulation, we use a field of view (FOV) of 4π sr, but the FOV of the IMA instrument is narrower. The induced magnetosphere boundary (IMB) crossings determined from observations and from simulations are shown by a vertical solid line and a dashed line, respectively.

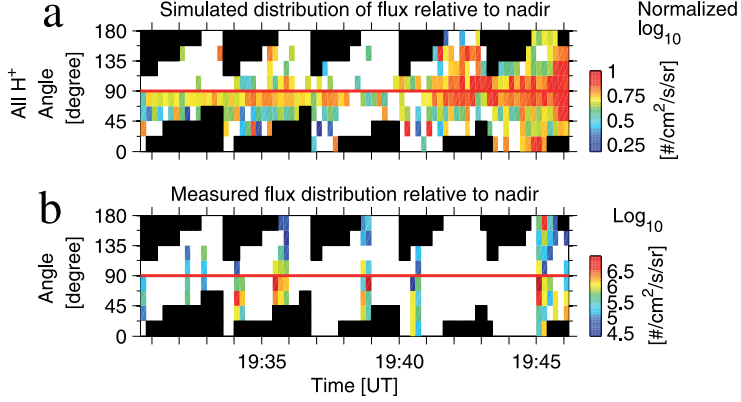


Figure 6. (a) Simulated distribution of flux directions relative to the nadir for all proton populations in the “fast SW” simulation. The flux in units of $\log_{10}(\text{H}^+ \text{ cm}^{-2} \text{ s}^{-1} \text{ sr}^{-1})$ is normalized to the maximum value, and the white color indicates no particles. (b) Distribution of flux directions relative to nadir, in the same format as Figure 1e; the white color indicates no flux. The black shaded area shows angles excluded from IMA’s field of view.

consistent with the observations (Figures 5e and 5j). However, both simulations indicate that the proton flux is the lowest near the pericenter, whereas the observations show that the proton flux is still significant. The simulations also indicate both low- and high-energy particles near the pericenter, whereas there are only protons with energies above 4 keV in the IMA data there. These two issues will be examined further in section 5. When comparing the two simulations, there are more proton entries in the “fast SW” run than in the “nominal SW” run. Assuming that the magnetic pressure balances the solar wind dynamic pressure in the pile-up region ($v^2 \sim B^2$), we get $v \sim B$ and thus the gyroradius ($\sim v/B$) may not change much between the two runs. On the other hand, the pile-up region gets more compressed in the “fast SW” run, and becomes a smaller obstacle to the heated proton.

[46] The vertical solid line in Figure 5 indicates the time of the measured IMB crossing. The vertical dashed line indicates the time of a plasma boundary crossing in the simulation (we call it IMB crossing). In the “fast SW” simulation, there is a sharp IMB crossing at $\sim 19:46$ UT at ~ 339 km altitude. In the “nominal SW” simulation, there is a smooth IMB crossing at $\sim 19:50$ UT at ~ 516 km altitude. Thus, the sharp low-altitude IMB crossing of the high dynamic pressure case matches the measured IMB crossing ($19:47:30$ UT at ~ 393 km altitude) better than the IMB crossing of the nominal pressure case does. The “fast SW” simulation indicates a significant proton flux below the IMB crossing, while the “nominal SW” simulation shows significantly less particles penetrating the IMB. The “fast SW” simulation reproduces the high proton flux before $19:41$ UT, as seen in the data, while the “nominal SW” simulation does not. On the other hand, the “fast SW” simulation overestimates the flux between $19:41$ UT and $19:45$ UT. This disagreement may be due to the low spatial resolution of the model (180 km size grid at low altitudes).

[47] Naturally the protons entering the induced magnetosphere in the “fast SW” run have higher energies than in the “nominal SW” run. The high solar wind speed also leads to a more efficient acceleration by $\vec{E}_{sw} = -\vec{v}_{sw} \times \vec{B}$. The proton energy in the “nominal SW” simulation is too low compared to the observations, while the “fast SW” simulation can reproduce the high energies of the observed protons.

[48] The model permits to distinguish between planetary and solar wind protons. Comparing the protons of planetary and solar wind origins, we see that according to the model both populations are present below the IMB. We have integrated the particle flux of protons (total = upward + downward) over the energy range shown in Figure 5 and the period $19:24$ UT– $19:46$ UT (interval in the ionosphere). We have done so for each proton population separately. For the “fast SW” simulation, 73% of the total proton flux below the IMB has a solar wind origin. For the “nominal SW” simulation, this number is 63%. The exospheric protons account for the rest. Therefore, the most important contribution comes from the shocked solar wind protons (Figures 5c and 5h). The high-energy planetary protons seen in Figures 5b and 5g are picked up and accelerated by the convection electric field.

[49] Figure 6 shows the simulated distribution of the flux direction relative to the nadir for all proton populations recorded in the tube detector, from the “fast SW” simulation (Figure 6a). The time interval is from $19:30$ UT to $19:46$ UT, which corresponds to the scans 1–5. The flowing directions of the particles are binned in 22.5° bins, and the flux in each bin is integrated over the energy range 1.1 – 10.5 keV. The observed flux distribution is shown in Figure 6b, which has the same format as Figure 1e, except that the bins with no flux are shown in white. A horizontal solid red line is drawn at 90° in both plots to separate the downgoing flux (below the line) from the upgoing flux (above the line).

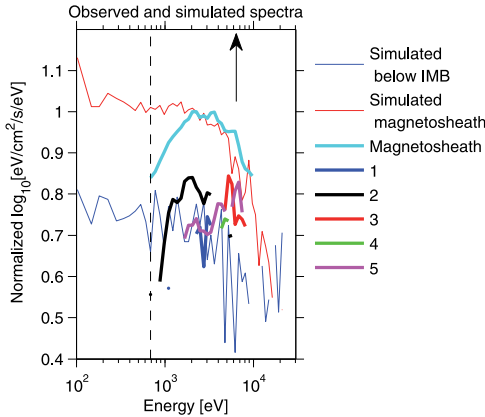


Figure 7. Comparison of the observed energy spectra of precipitating protons (scans 1–5 and magnetosheath, shown as thick lines) with the simulated energy spectra of magnetosheath protons (thin red line) and precipitating protons below the IMB (thin blue line). The vertical dashed black line shows the energy cutoff of IMA. For all energy spectra, the decimal logarithm of the flux (unit: $\text{eV cm}^{-2} \text{s}^{-1} \text{eV}^{-1}$) is normalized, so that the height of the simulated magnetosheath energy spectrum at ~ 2 keV is equal to the height of the measured magnetosheath energy spectrum. The arrow indicates the energy peak (5.5 keV) of the simulated upstream solar wind energy spectrum (a Maxwellian distribution).

[50] The simulated angular distribution peaks at 90° relative to the nadir, which means that the flow is mainly horizontal relative to Mars. The simulated distribution also indicates that more particles move downward (precipitating) than upward between 19:30 UT and 19:41 UT, which is in reasonable agreement with the observations. After 19:41 UT, the agreement is worse. On average 87% of the measured total proton flux is moving downward during 19:30 UT–19:41 UT (angle to nadir $< 90^\circ$). By comparison, if we do the same calculation for the simulated flux (not including the black area in Figure 6b), we find that 79% of the simulated total flux is downward, which agrees reasonably with the data. This result suggests that the absorbing inner boundary can mimic reasonably well the analyzed case. Finally, the model qualitatively confirms that proton precipitation can indeed occur at low altitudes on a large spatial scale. This issue is discussed further in section 5.

[51] Figure 7 shows the observed energy spectra of precipitating protons for scans 1–5 and a magnetosheath energy spectrum (with the same format as in Figure 3, but shown with thick lines). Two simulated energy spectra of downgoing protons from all proton populations are also represented for comparison. We have used the “fast SW” simulation. To obtain the simulated energy spectra, the proton fluxes were averaged over time for two time intervals to obtain a magnetosheath energy spectrum (from 19:45 UT to 19:49 UT, thin red line) and a precipitating proton energy spectrum “below the IMB” (from 19:36 UT to 19:41 UT, thin blue line).

[52] The simulated energy spectra are thermalized and heated. There is no evident energy peak in both simulated spectra. According to the simulation, the overall flux in the magnetosheath is larger than the flux below the IMB. The flux difference is larger at 100 eV than at 10 keV because the magnetic field in the pile-up region deflects low energy protons more effectively.

[53] The observed and simulated spectra in the magnetosheath agree well for energies > 2 keV. The energy ranges of the observed and simulated precipitating protons below the IMB also reasonably agree between 1 and 3 keV, although the observations show higher fluxes beyond 3 keV. The absence of low energy protons in the observed spectra is an instrumental effect. As noted above, in the operation mode in question the IMA low energy cutoff was 700 eV (see the dashed vertical line). Since May 2007, the energy range of IMA is extended down to 10 eV, which enables the observations of low-energy (< 50 eV) protons when the instrument is run in the high post-acceleration mode [Lundin *et al.*, 2009].

5. Discussion and Conclusion

[54] The main reason for proton precipitation is the large gyroradius of the hot magnetosheath protons relative to the size of the induced magnetosphere in the subsolar region. The temperature of the shocked plasma near the subsolar point is 400–600 eV [Lundin *et al.*, 1993]. Therefore, fluxes of protons with energy up to a few keV are still significant. The gyroradius of the 1–5 keV heated protons in a magnetic field of 50 nT (value in the subsolar magnetic pile-up region) is ~ 100 –200 km. The height of the IMB is ~ 393 km at 7° SZA and the height of the PEB is ~ 352 km at 6° SZA (Figure 1). This result implies that the thickness of the subsolar magnetic pile-up region is about 40 km between 6° – 7° SZA during the time of our observations. This thickness is smaller than the proton gyroradius previously calculated. Therefore, protons of a few keV may reach altitudes down to 200–300 km between 6° – 7° SZA. This result is in reasonable agreement with the observations (scan 5 in the same SZA range).

[55] Figure 1 indicates a change in the proton energy spectrum when altitude decreases. When the IMB is crossed inward, the proton energy spectrum becomes narrower in energy, the fluxes decrease, and the low-energy component of the energy spectrum disappears: the original magnetosheath energy spectrum is strongly disturbed by the penetration through the IMB. For instance, in scans 1 and 2, the energy range is 1–4 keV, while for scan 4 (at pericenter), the protons have higher energies: 4–5 keV. The same change in the energy spectrum is also visible when comparing the proton energy distribution in scan 5 to the distribution during 19:46 UT–19:49 UT. The high-energy protons penetrate deeper than the low-energy protons due to a larger gyroradius in the pile-up region.

[56] The proton fluxes in scan 3–4 have a very narrow energy distribution, which suggests they may be pick-up protons precipitating. On the other hand, the solar wind alpha particles are observed to precipitate into the Martian atmosphere with narrow energy distributions [Stenberg *et al.*, 2011], like the precipitating protons. Hence, we argue that the observed protons can be of solar wind origin.

The observation cannot separate between the planetary protons and the solar wind protons but the model suggests that the observed precipitating protons originate both from the exosphere and the solar wind.

[57] In addition, one might remark that the high energy component in the last proton scan in Figure 1d (the red spot at energy ≥ 5 keV at 19:54 UT–19:55 UT) looks like the fluxes in scans 3–4. This red spot corresponds to alpha particles contaminating the measurement.

[58] The simulations (see Figure 7) indicate that the precipitating proton flux decreases more at lower energies than at higher energies when the altitude decreases. However, the decrease at low energies is not as sharp as in the observations: we measure only protons with energies ≥ 4 keV in scans 3 and 4 around the pericenter. It is possible that the protons are observed at the lowest altitude with a significant flux because of a transient increase in the magnetosheath proton temperature. A higher proton temperature can result in protons with higher energies and larger gyroradii. These protons with large gyroradii would pass through the IMB and penetrate deep into the atmosphere, which is consistent with the observations in scans 3–4.

[59] When searching for an orbit suitable for a case study of the proton precipitation, we noticed that the precipitation was not observed for all orbits investigated. This suggests that the precipitation is a transient phenomenon. It is possible that no proton penetration would have been measured at the pericenter if the precipitation was not enhanced by a change in the magnetosheath conditions.

[60] When the precipitating protons reach the exobase, the cascade of CX reactions and elastic and non-elastic collisions occurs, and a fraction of the precipitating proton flux may be backscattered and leave the system as energetic hydrogen atoms (ENAs) [Kallio and Barabash, 2001; Shematovich et al., 2011]. Shematovich et al. [2011] investigated the transport of precipitating protons into the Martian atmosphere using a Direct Monte Carlo (DMC) model, and showed that, when no magnetic field is present, 8% of the incident energy proton flux is backscattered by the Martian atmosphere as upgoing hydrogen energy flux. If the measured precipitating protons (10^8 – 10^9 eV cm $^{-2}$ s $^{-1}$) are reflected back as ENAs, an ENA flux of 10^7 – 10^8 eV cm $^{-2}$ s $^{-1}$ is expected. Futaana et al. [2006] observed hydrogen ENAs emitted from the dayside of Mars at low (~ 600 km) altitude on the same day (27 February 2004) as the proton observations considered in this paper. They reported fluxes of ~ 1 keV hydrogen atoms to be 10^7 H $^+$ cm $^{-2}$ s $^{-1}$, corresponding to energy fluxes of 10^{10} eV cm $^{-2}$ s $^{-1}$, i.e., 100–1000 times higher than the backscattered ENA energy flux that might have been associated with the proton precipitation. Therefore, the main source of the dayside ENAs is unlikely to be the precipitating protons.

[61] To understand the gross effect of proton precipitation onto the atmosphere we first estimate the maximal horizontal extent of proton precipitation along the orbit. The spacecraft velocity close to the pericenter is ~ 4 km s $^{-1}$. With the elevation scans 1–5 (192 s each), we obtain a spatial extent of ~ 4000 km along the orbit if we assume a stationary precipitation during this orbit.

[62] The heating due to proton precipitation can be compared to solar heating. The energy flux associated with the solar Extreme Ultraviolet (EUV) radiation absorption for the

altitude range of 100–240 km is $1.4 \cdot 10^{11}$ eV cm $^{-2}$ s $^{-1}$ [Kallio et al., 1997], which is ~ 20 times greater than the observed maximal precipitation energy flux value ($7 \cdot 10^9$ eV cm $^{-2}$ s $^{-1}$, in bold in Table 1), i.e., proton precipitation is not a significant heating source for the dayside atmosphere.

[63] In summary, due to the small size of the subsolar magnetosheath and the high plasma temperature, protons with a few keV energies and large gyroradius may reach the upper atmosphere. The hybrid simulation shows that both the shocked solar wind protons and the planetary picked-up protons contribute to the observed precipitation, with a larger contribution coming from the solar wind protons. The observations indicate that the flux of the low-energy protons is more reduced than the flux of the higher-energy protons when the altitude decreases, which is consistent with the gyroradius effect. Nevertheless, this result is less evident in the model. A fast solar wind stream can explain the high energies of the precipitating protons observed on 27 February 2004. Proton precipitation can occur on a scale of few thousands kilometers along the orbit. The precipitation occurs intermittently and it may be triggered by the transient changes in the magnetosheath temperature. The study of more precipitation events is needed to clarify the relationship between the magnetic anomalies and the precipitation. The energy flux of the precipitating protons (10^8 – 10^9 eV cm $^{-2}$ s $^{-1}$) is much smaller than the solar UV energy flux onto the upper atmosphere.

[64] Future work will be a statistical study of the observed proton fluxes to investigate the influence of the solar wind conditions, the solar wind convection electric field and the magnetic anomalies on proton precipitation.

[65] **Acknowledgments.** C. Diéval acknowledges funding from the Kungliga Vetenskapsakademien. C. Diéval and G. Stenborg were supported by the National Graduate School of Space Technology of the Luleå Technical University. The Swedish contribution to the ASPERA-3 experiment was supported by the Swedish National Space Board. The authors acknowledge E. Penou at the Centre d'Etude Spatiale des Rayonnements (France) for providing the data analysis software CL and D. H. Hurley at the Johns Hopkins University Applied Physics Laboratory (USA) for providing upstream dynamic pressure proxy data. The authors also acknowledge Arnaud Valeille, University of Michigan, for providing the hot hydrogen and hot oxygen profiles used in the hybrid model. The authors thank the anonymous reviewers for their help in improving the paper.

[66] Masaki Fujimoto thanks the reviewers for their assistance in evaluating this paper.

References

- Acuña, M. H., et al. (1998), Magnetic field and plasma observations at Mars: Preliminary results of the Mars Global Surveyor Mission, *Science*, 279(5357), 1676–1680, doi:10.1126/science.279.5357.1676.
- Acuña, M. H., et al. (1999), Global distribution of crustal magnetization discovered by the Mars Global Surveyor MAG/ER experiment, *Science*, 284(5415), 790–793, doi:10.1126/science.284.5415.790.
- Barabash, S., et al. (2006), The Analyzer of Space Plasmas and Energetic Atoms (ASPERA-3) for the Mars Express mission, *Space Sci. Rev.*, 126(1–4), 113–164, doi:10.1007/s11214-006-9124-8.
- Brain, D. A., et al. (2005), Variability of the altitude of the Martian sheath, *Geophys. Res. Lett.*, 32, L18203, doi:10.1029/2005GL023126.
- Brain, D. A., et al. (2010), A comparison of global models for the solar wind interaction with Mars, *Icarus*, 206(1), 139–151, doi:10.1016/j.icarus.2009.06.030.
- Brecht, S. H. (1997), Solar wind proton deposition into the Martian atmosphere, *J. Geophys. Res.*, 102(A6), 11,287–11,294, doi:10.1029/97JA00561.
- Cain, J. C., et al. (2003), An $n = 90$ internal potential function of the Martian crustal magnetic field, *J. Geophys. Res.*, 108(E2), 5008, doi:10.1029/2000JE001487.

- Chaufray, J. Y., et al. (2008), Observation of the hydrogen corona with SPICAM on Mars Express, *Icarus*, *195*(2), 598–613, doi:10.1016/j.icarus.2008.01.009.
- Cridder, D. H., et al. (2003), A proxy for determining solar wind dynamic pressure at Mars using Mars Global Surveyor data, *J. Geophys. Res.*, *108*(A12), 1461, doi:10.1029/2003JA009875.
- Dubinin, E., et al. (2008), Structure and dynamics of the solar wind/ionosphere interface on Mars: MEX-ASPERA-3 and MEX-MARSIS observations, *Geophys. Res. Lett.*, *35*, L11103, doi:10.1029/2008GL033730.
- Fedorov, A., et al. (2006), Structure of the Martian wake, *Icarus*, *182*(2), 329–336, doi:10.1016/j.icarus.2005.09.021.
- Frahm, R. A., et al. (2006), Carbon dioxide photoelectron energy peaks at Mars, *Icarus*, *182*(2), 371–382, doi:10.1016/j.icarus.2006.01.014.
- Fränz, M., et al. (2006), Plasma intrusion above Mars crustal fields—Mars Express ASPERA-3 observations, *Icarus*, *182*(2), 406–412, doi:10.1016/j.icarus.2005.11.016.
- Fulle, M., et al. (2007), Discovery of the atomic iron tail of comet McNaught using the heliospheric imager on STEREO, *Astrophys. J.*, *661*, L93–L96, doi:10.1086/518719.
- Futaana, Y., et al. (2006), First ENA observations at Mars: ENA emissions from the Martian upper atmosphere, *Icarus*, *182*(2), 424–430, doi:10.1016/j.icarus.2005.09.019.
- Kallio, E., and S. Barabash (2001), Atmospheric effects of precipitation energetic hydrogen atoms on the Martian atmosphere, *J. Geophys. Res.*, *106*(A1), 165–177, doi:10.1029/2000JA002003.
- Kallio, E., and P. Janhunen (2001), Atmospheric effects of proton precipitation in the Martian atmosphere and its connection to the Mars-solar wind interaction, *J. Geophys. Res.*, *106*(A4), 5617–5634, doi:10.1029/2000JA000239.
- Kallio, E., and P. Janhunen (2003), Modeling the solar wind interaction with Mercury by a quasineutral hybrid model, *Ann. Geophys.*, *21*(11), 2133–2145, doi:10.5194/angeo-21-2133-2003.
- Kallio, E., et al. (1997), Charge exchange near Mars: The solar wind absorption and energetic neutral atom production, *J. Geophys. Res.*, *102*(A10), 22,183–22,197, doi:10.1029/97JA01662.
- Kallio, E., et al. (2008), On the properties of O⁺ and O₂⁺ ions in a hybrid model and in Mars Express IMA/ASPERA-3 data: A case study, *Planet. Space Sci.*, *56*, 1204–1213, doi:10.1016/j.pss.2008.03.007.
- Kallio, E., et al. (2010), Oxygen ion escape at Mars in a hybrid model: High energy and low energy ions, *Icarus*, *206*, 152–163, doi:10.1016/j.icarus.2009.05.015.
- Lundin, R., et al. (1993), *Plasma Environment of Non-Magnetic Planets*, edited by T. Gombosi, 311 pp., Pergamon, New York.
- Lundin, R., et al. (2004), Solar wind-induced atmospheric erosion at Mars: First results from ASPERA-3 on Mars Express, *Science*, *305*(5692), 1933–1936, doi:10.1126/science.1101860.
- Lundin, R., et al. (2008), A comet-like escape of ionospheric plasma from Mars, *Geophys. Res. Lett.*, *35*, L18203, doi:10.1029/2008GL034811.
- Lundin, R., et al. (2009), Atmospheric origin of cold ion escape from Mars, *Geophys. Res. Lett.*, *36*, L17202, doi:10.1029/2009GL039341.
- Ma, Y., et al. (2004), Three-dimensional, multispecies, high spatial resolution MHD studies of the solar wind interaction with Mars, *J. Geophys. Res.*, *109*, A07211, doi:10.1029/2003JA010367.
- Mitchell, D. L., et al. (2001), Probing Mars' crustal magnetic field and ionosphere with the MGS Electron Reflectometer, *J. Geophys. Res.*, *106*(E10), 23,419–23,427, doi:10.1029/2000JE001435.
- Nagy, A. F., et al. (2004), The plasma environment of Mars, *Space Sci. Rev.*, *111*, 33–114, doi:10.1023/B:SPAC.0000032718.47512.92.
- Shematovich, V. I., et al. (2011), Protons and hydrogen atoms transport in the Martian upper atmosphere with an induced magnetic field, *J. Geophys. Res.*, *116*, A11320, doi:10.1029/2011JA017007.
- Soobiah, Y., et al. (2006), Observations of magnetic anomaly signatures in Mars Express ASPERA-3 ELS data, *Icarus*, *182*(2), 396–405, doi:10.1016/j.icarus.2005.10.034.
- Stenberg, G., et al. (2011), Observational evidence of alpha particle capture at Mars, *Geophys. Res. Lett.*, *38*, L09101, doi:10.1029/2011GL047155.

PAPER II

Proton and hydrogen atom transport in the Martian upper atmosphere with an induced magnetic field

V. I. Shematovich,¹ D. V. Bisikalo,¹ C. Diéval,² S. Barabash,² G. Stenberg,² H. Nilsson,² Y. Futaana,² M. Holmstrom,² and J.-C. Gérard³

Received 14 July 2011; revised 9 September 2011; accepted 10 September 2011; published 17 November 2011.

[1] We have applied the Direct Simulation Monte Carlo method to solve the kinetic equation for the H/H⁺ transport in the upper Martian atmosphere. We calculate the upward H and H⁺ fluxes, values that can be measured, and the altitude profile of the energy deposition to be used to understand the energy balance in the Martian atmosphere. The calculations of the upward flux have been made for the Martian atmosphere during solar minimum. We use an energy spectrum of the down moving protons in the altitude range 355–437 km adopted from the Mars Express Analyzer of Space Plasma and Energetic Atoms measurements in the range 700 eV–20 keV. The particle and energy fluxes of the downward moving protons were equal to $3.0 \times 10^6 \text{ cm}^{-2} \text{ s}^{-1}$ and $1.4 \times 10^{-2} \text{ erg cm}^{-2} \text{ s}^{-1}$. It was found that 22% of particle flux and 12% of the energy flux of the precipitating protons is backscattered by the Martian upper atmosphere, if no induced magnetic field is taken into account in the simulations. If we include a 20 nT horizontal magnetic field, a typical field measured by Mars Global Surveyor in the altitude range of 85–500 km, we find that up to 40%–50% of the energy flux of the precipitating protons is backscattered depending on the velocity distribution of the precipitating protons. We thus conclude that the induced magnetic field plays a crucial role in the transport of charged particles in the upper atmosphere of Mars and, therefore, that it determines the energy deposition of the solar wind.

Citation: Shematovich, V. I., D. V. Bisikalo, C. Diéval, S. Barabash, G. Stenberg, H. Nilsson, Y. Futaana, M. Holmstrom, and J.-C. Gérard (2011), Proton and hydrogen atom transport in the Martian upper atmosphere with an induced magnetic field, *J. Geophys. Res.*, 116, A11320, doi:10.1029/2011JA017007.

1. Introduction

[2] Mars differs from the Earth in what concerns the atom and ion precipitation onto the atmosphere. At the Earth a strong intrinsic magnetic field diverts the solar wind flow around the planet far above the neutral atmosphere and only the magnetic cusps can channel the particles and energy down to the atmosphere. Instead, on Mars the boundary between the solar wind and the obstacle, the induced magnetosphere boundary (IMB), is located so close to the planet that the solar wind particles penetrating IMB can directly interact with the upper atmosphere. These differences between the solar wind interaction at Earth and Mars result in different characteristics of the precipitating particles. The terrestrial ring current protons and heavier ions accelerated up to energies of tens keV in the magnetosphere are guided by the strong global intrinsic magnetic field and reach the upper atmosphere at high altitudes [Moore and Horwitz, 2007]. In

contrast, Mars has no ring current and the proton energies near the planet do not exceed a few keV. The induced magnetic field near the planets is typically weak, only several tens of nT. The relative importance of different collision processes between protons and atmospheric neutrals is also expected to be different at Mars and at the Earth because of the different precipitating energies and the different neutral compositions [Kallio and Barabash, 2001]. Therefore, studying the H/H⁺ transport in the upper Martian atmosphere presents a new scientific challenge.

[3] Lundin *et al.* [2004] used the in situ plasma data of the Analyzer of Space Plasma and Energetic Atoms (ASPERA-3) experiment on board the Mars Express mission to show that solar wind protons can reach altitudes as low as 270 km at Mars. Futaana *et al.* [2006] reported energetic neutral atom (ENA) fluxes from the Martian dayside at low altitudes. They interpreted the ENA flux as a result of the backscattering of neutralized solar wind protons from the atmosphere and charge-exchanged neutral hydrogen of solar wind proton origin, the so-called ENA albedo [Kallio and Barabash, 2001]. The Martian upper atmosphere is also a subject of the solar wind ENAs precipitation originated from the charge exchange reaction between the solar wind protons outside the IMB and the extended hydrogen corona. The total energy flux

¹Institute of Astronomy, Russian Academy of Sciences, Moscow, Russia.

²Swedish Institute of Space Physics, Kiruna, Sweden.

³LPAP, Université de Liège, Liège, Belgium.

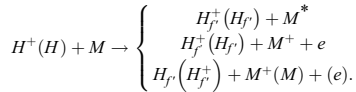
associated to the precipitating (≤ 1 keV) hydrogen atoms can be substantial $\sim 10^9$ eV cm⁻² s⁻¹ [Kallio *et al.*, 1997]. Therefore, the atmospheric effects caused by these precipitating atoms and protons should be also investigated.

[4] To investigate the transport of protons and hydrogen ENAs through the upper Martian atmosphere we developed the Direct Simulation Monte Carlo (DSMC) model. The main features of the model are discussed in section 2. In section 3 results of simulations are presented. Section 4 summarizes the results and conclusions.

2. The Model Description

2.1. Proton/Hydrogen Precipitation

[5] Interactions of precipitating energetic hydrogen atoms and protons with the main atmospheric constituents include the momentum and energy transfer in elastic and inelastic collisions, ionization of target atmospheric molecules/atoms, charge transfer and electron capture collisions. Energetic H atoms (or protons) produced by proton (or hydrogen) impact further collide with the main atmosphere constituents, transferring their momentum and kinetic energy to atmospheric particles by elastic and inelastic collisions, ionization and stripping processes. The collisional processes describing the penetration of the energetic H⁺/H through the ambient atmospheric gas can be written as:



Here, M denotes the major atmospheric constituents – CO₂, N₂, and O included in the model. Secondary fast H_p atoms and H_p⁺ protons produced by momentum transfer and stripping reactions loop the reaction set shown above. Consequently, the interaction of the precipitating hydrogen atoms (protons) with the main neutral constituents of the thermosphere must be considered as a cascade process producing a growing set of translationally and internally excited particles M* of the ambient atmospheric gas.

2.2. Mathematical Description

[6] To analyze the penetration of energetic H/H⁺ into the atmospheric gas, we use the kinetic Boltzmann equations [Gérard *et al.*, 2000] with the collision term:

$$\mathbf{v} \cdot \frac{\partial}{\partial \mathbf{r}} f_{H/H^+} + \left(\mathbf{g} + \frac{e}{m_{H^+}} \mathbf{v} \times \mathbf{B} \right) \cdot \frac{\partial}{\partial \mathbf{v}} f_{H/H^+} = Q_{H/H^+}(\mathbf{v}) + \sum_{M=O, N_2, CO_2} J_{m(H/H^+, f_M)}, \quad (1)$$

where $f_{H/H^+}(\mathbf{r}, \mathbf{v})$ and $f_M(\mathbf{r}, \mathbf{v})$ are the velocity distribution functions for hydrogen atoms or protons, and components of ambient gas, respectively, e the electron charge, and m_{H^+} the proton mass. The left side of the kinetic equation describes the transport of particles in the planetary gravitational and induced magnetic fields. The right-hand side term Q_{H/H^+} is the production rate of respective particles in charge exchange and stripping collisions. The elastic and inelastic scattering terms J_m for H/H⁺ collisions with the ambient atmospheric

species are written in the standard form [Shematovich *et al.*, 1994]. It is assumed that the ambient atmospheric gas is characterized by local Maxwellian velocity distribution functions.

2.3. Stochastic Approach

[7] The DSMC method used to solve the kinetic equation (1) implies generation of a sample of paths for the state of the physical system under study – H/H⁺ thermalization and transport in the transition region of the upper atmosphere. It is an efficient tool for studying such complex kinetic systems in the stochastic approximation [Shematovich *et al.*, 1994; Bisikalo *et al.*, 1995; Gérard *et al.*, 2000]. The details of the algorithmic realization of this numeric model were given earlier [Shematovich *et al.*, 1994; Bisikalo *et al.*, 1995]. The statistics in the DSMC model is controlled using the standard procedures [Shematovich, 2008]. When the steady state is reached then it is possible to accumulate the statistics with the needed accuracy. In the calculations presented below the fluxes and other characteristics were calculated with the variation below 10%. The low-energy parts of proton and hydrogen fluxes were calculated with the sufficient accuracy because these particles were slowed down due to the wealth of collisions with the ambient atmospheric gas.

[8] The energy deposition rate of H/H⁺ flux is determined by the cross sections of the collisions with the ambient gas. The energy lost by the H/H⁺ in a collision is determined by the scattering angle χ

$$\Delta E = E_{H/H^+} \times \left(\frac{2m_M m_{H/H^+}}{(m_M + m_{H/H^+})^2} \right) \times (1 - \cos \chi),$$

where E_{H/H^+} is the initial energy of the impacting proton or hydrogen atom. It is apparent that the energy loss for collisions in forward direction (for $\chi < 90^\circ$) at small scattering angles χ is less than that for larger scattering angles. The key point of this model is the stochastic treatment of the scattering angle distribution. This distribution influences both the energy degradation rate through the losses of energy in the momentum transfer collisions that are proportional to the sine of the scattering angle, and the angle redistribution of the precipitating protons.

2.4. Numerical Model

[9] We consider the H/H⁺ transport between altitudes where H/H⁺ are efficiently thermalized and atmospheric gas becomes practically collisionless. For the Martian atmosphere, the lower boundary is placed at 80 km. The 80 km altitude is well below the exobase placed near 180 km with low solar activity conditions. To link our model with the actual measurements we chose the upper boundary in the altitude range 355–437 km, where measurements of the precipitating protons were made by the ASPERA-3 instrument (see Table 1 for details). The region of the atmosphere under the study was divided into 49 vertical cells, and the altitude-dependent cell size is chosen according to the condition that it must be equal to or smaller than the free path length. In model the radial position and 3 velocity components for each modeling particle are kept. The modeling particle trajectory is calculated in 3-D space for each time step and after that the new radial position is kept. Therefore, protons launched at given angle

Table 1. Input Data for the DSMC Model

Run	B, Horizontal (nT)	Precipitating H ⁺ or H Distribution Versus Nadir	Precipitating H ⁺ Spectrum Measured by ASPERA-3 at Altitude h_{ub}	Precipitating H Spectrum
1	0	Isotropic, 0°–90°	Spectrum 1, $h_{ub} = 437$ km	None
2	10	Isotropic, 0°–90°	Spectrum 1, $h_{ub} = 437$ km	None
3a	20	Isotropic, 0°–90°	Spectrum 1, $h_{ub} = 355$ km	None
3b	20	Isotropic, 0°–90°	Spectrum 1, $h_{ub} = 437$ km	None
4	30	Isotropic, 0°–90°	Spectrum 1, $h_{ub} = 437$ km	None
5	50	Isotropic, 0°–90°	Spectrum 1, $h_{ub} = 437$ km	None
6a	20	Isotropic, 0°–90°	Spectrum 2, $h_{ub} = 387$ km	None
6b	20	Isotropic, 0°–90°	Spectrum 2, $h_{ub} = 435$ km	None
7	20	Isotropic, 0°–90°	None, $h_{ub} = 500$ km	MS H ⁺ [Kallio et al., 1997]
8	20	Isotropic, 0°–90°	None, $h_{ub} = 500$ km	SW H ⁺ [Kallio et al., 1997]

^aHydrogen energetic neutral atoms (ENAs) originating in the Martian magnetosheath.

^bHydrogen ENAs originating in undisturbed solar wind.

versus nadir direction can move to different angles and planet curvature is also taken into account.

[10] The altitude distributions of the main neutral species, CO₂, N₂, O, H₂, and He, were adopted from [Fox and Hac, 2009] for a low level of solar activity corresponding to the ASPERA-3 observations. The altitude profiles of the main neutral species adopted in the model are shown in Figure 1. Efficiency of the collisional thermalization and energy deposition of high-energy protons is determined by the elastic, ionization, and charge transfer collisions. If we suggest that

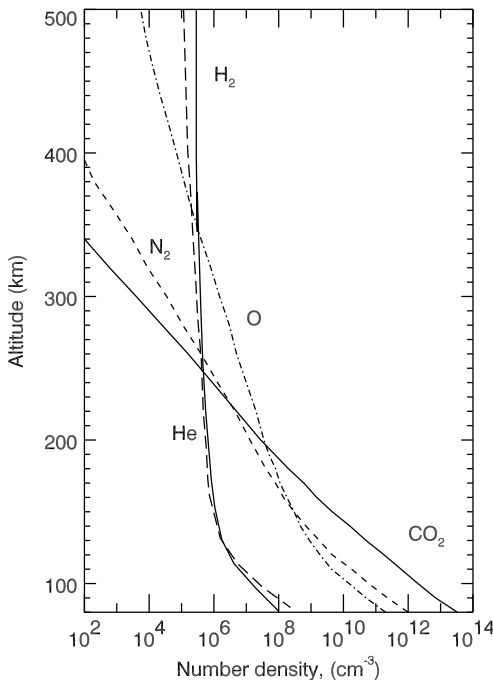


Figure 1. The altitude distributions of the main neutral species, CO₂, N₂, O, H₂, and He, adopted from Fox and Hac [2009].

characteristic value of total cross sections for collisions of all neutral species with protons at energy 1 keV is about value of 10^{-15} cm² (see, for example, Figure 2 for H⁺ collisions with CO₂) then the collisional frequencies below exobase will be proportional to the number densities of neutral species under consideration. From Figure 1 it is seen that at altitudes below

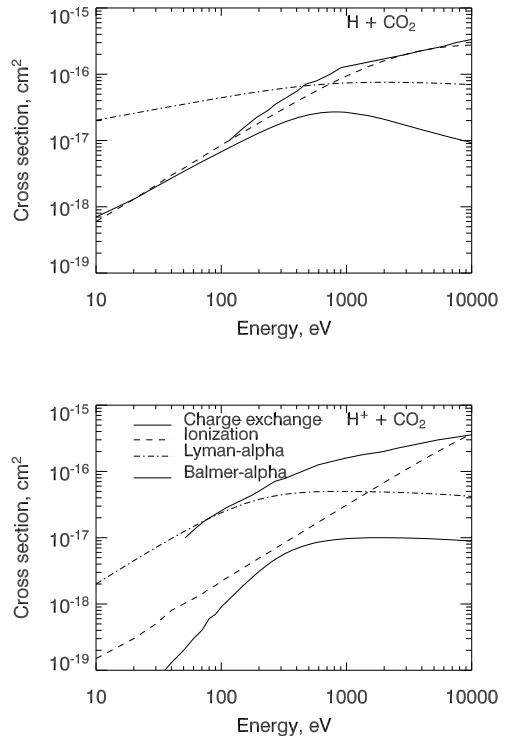


Figure 2. Cross sections for (top) H and (bottom) H⁺ collisions with CO₂. Processes are marked in the legend of Figure 2 (bottom). The solid line in Figure 2 (top) shows the stripping process.

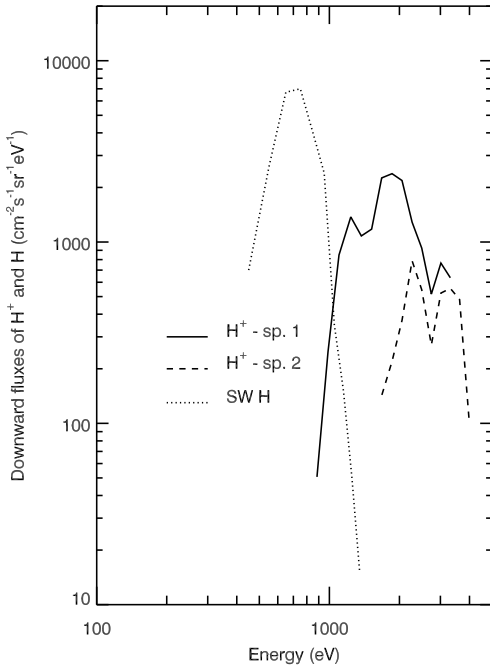


Figure 3. Energy spectra of the downward moving protons (H^+) measured by ASPERA-3 and solar wind hydrogen atoms (SW H) calculated by *Kallio et al.* [1997], used as an input to the model at the upper boundary.

200 km the number densities of light species H_2 and He are more than 2 orders of magnitude lower than ones of heavy particles, therefore collisions with CO_2 , N_2 , and O only were taken into account in the current version of the model aimed to calculate the proton energy deposition in the Martian upper atmosphere. Moreover, the cross sections of elastic collisions between protons and atmospheric species decrease with the proton energy, and are lower for the collisions with light (H_2 and He) particles. The temperature in the considered domain changes from 150 K at lower boundary up to 170 K at the upper boundary.

[11] In the model, the most recent measurements or calculations of the required cross sections were adopted. The cross sections and scattering angle distributions for H/H^+ interactions with N_2 and O are from the model of the proton aurora at Earth [*Gérard et al.*, 2000]. The cross sections and scattering angle distributions for H/H^+ collisions with CO_2 are taken from *Nakai et al.* [1987] for charge exchange and stripping collisions, from *Haider et al.* [2002] for ionization, Lyman alpha and Balmer alpha excitation, and from *Lindsay et al.* [2005] for scattering angle distributions. The elastic and other inelastic collisions cross sections for H/H^+ collisions with CO_2 are assumed to be the same as for O_2 . The compiled cross sections for H/H^+ collisions with CO_2 are shown in Figure 2.

[12] The Monte Carlo code to model the penetration of high-energy protons and hydrogen atoms into the planetary atmosphere [*Gérard et al.*, 2000] was modified to take into account the effect of the horizontal magnetic field on the proton trajectories. The induced magnetic field has been measured at Mars by the Mars Global Surveyor orbiter [*Brain et al.*, 2003] and the Mars Express orbiter [*Akalin et al.*, 2010]. These authors show that the induced magnetic field is mainly horizontal; its strength decreases with increasing altitude and with increasing solar zenith angle. The induced magnetic field strength is typically the strongest near the subsolar point (about 40 nT) and reaches a value of 20 nT at the terminator, in the altitude range 360–440 km [*Akalin et al.*, 2010]. Following these measurements we assume the constant in time and uniform in space horizontal magnetic field $B = 10, 20, 30, 40,$ and 50 nT for the different runs.

3. Results of Calculations

[13] The most interesting effects of H/H^+ penetration into the Mars upper atmosphere to investigate are heating of the neutral gas due to momentum transfer collisions, excitation of the precipitating hydrogen atoms and ambient gas emissions, and formation of the backscattered flux of the energetic hydrogen atoms and protons.

[14] The photon emissions and particle backscattered fluxes can be observed by the Spectroscopy for the Investigation of the Characteristics of the Atmosphere of Mars (SPICAM) and ASPERA-3 instruments orbiting Mars onboard the Mars Express mission. In this work, we use a spectrum of the downward moving protons, measured by the Mars Express ASPERA-3 [*Barabash et al.*, 2006] in the energy range 700 eV to 20 keV, and in altitude range 355–437 km at solar zenith angles 42° – 49° on 27 February 2004, at around 19:35 UT. For this particular operational mode 700 eV was the lower energy threshold. For this case, referred to as spectrum 1 (see Figure 3, solid line), the particle and energy fluxes of the incident protons were equal to $3.0 \times 10^6 \text{ cm}^{-2} \text{ s}^{-1}$ and $1.4 \times 10^{-2} \text{ erg cm}^{-2} \text{ s}^{-1}$. To study the dependence on the input spectrum we also use another spectrum of downward moving protons measured by ASPERA-3, referred to as spectrum 2 (see Figure 3, dashed line). Spectrum 2 was measured in altitude range 387–435 km at solar zenith angles 30° – 33° on 4 October 2005 at around 16:06 UT. Spectrum 2 is narrower in energy and the corresponding incident fluxes are of the same order of magnitude as those of spectrum 1. A case study analysis of these proton spectra was reported by C. Diéval et al. (A case study of proton precipitation at Mars: Mars Express observations and hybrid simulation, submitted to *Journal of Geophysical Research*, 2011). It is necessary to point out that these proton spectra have been recorded when Mars Express spacecraft was in the ionosphere, thus below the IMB; that is, they are not magnetosheath spectra. The shapes of both spectra used in the calculations are typical as it follows from the statistical analysis of all proton precipitation events observed by Mars Express when the spacecraft was below the IMB, over a period of 1.5 years (C. Diéval, private communication, 2011). The proton events are rare: they are measured out of 1% of the observation time. The ASPERA ion instrument performs a full angular

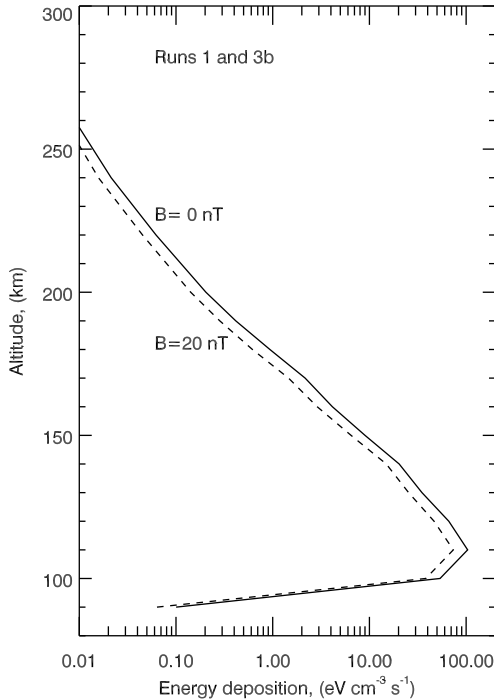


Figure 4. Energy deposition rates of precipitating protons for run without magnetic field (run 1 from Table 1) (solid line) and for run where $B = 20$ nT (run 3b from Table 1) (dashed line).

scan in 192 s, 16 angular steps. The proton flux inside the IMB is usually observed for shorter periods than this. We can therefore not obtain the full distribution. Assuming it to be isotropic is then a reasonable compromise, and we did try other distributions as well.

[15] We have conducted a set of runs to estimate the magnitudes of the H/H⁺ backscattered fluxes from the Martian atmosphere. The model input parameters are: energy spectrum and angle distribution versus nadir of the incident protons (or hydrogen atoms); magnitude of the parallel (horizontal to the surface of Mars) component of the induced magnetic field. The angle θ distribution is isotropic in the sense of the uniform distribution of $\cos \theta$. Such isotropic distribution is routinely used to study the proton precipitation in the Earth's polar atmosphere [Decker *et al.*, 1996; Gérard *et al.*, 2000]. We have conducted 8 runs, 6 for proton and 2 for hydrogen precipitation, which are listed in Table 1. The upper boundary was taken at altitudes 355 km and 437 km for runs 3a and 3b with spectrum 1, and 387 km and 435 km for runs 6a and 6b with spectrum 2. For all other runs 1–6 the upper boundary was assigned at 437 km just to exclude the influence of the neutral Martian corona on the precipitating flux of protons.

3.1. Run Without Induced Magnetic Field

[16] To validate the developed DSMC model and to compare its outputs with previous studies [Kallio *et al.*, 1997; Kallio and Barabash, 2001], we first have run the model for the case without an induced magnetic field in the Martian upper atmosphere. Figure 4 shows the energy deposition rate for the H/H⁺ flux penetrating through the Martian atmosphere. It is seen that in run 1 (without induced magnetic field) (Figure 4, solid line) the incident protons and hydrogen atoms penetrate rather deep into the thermosphere of Mars down to 100–150 km where the maximum of the energy deposition is reached.

[17] The calculated energy spectra of the protons and hydrogen atoms moving upward at the model upper boundary $h_{ub} = 437$ km are given in Figure 5. In the calculations with the DSMC model it was found that the interaction of the precipitating protons with the upper atmosphere results in the formation of an upward moving particle flux of 2.0×10^5 cm⁻² s⁻¹ and 7.0×10^5 cm⁻² s⁻¹ (protons and hydrogen atoms, respectively) and an energy flux of 5.7×10^{-4} erg cm⁻² s⁻¹ and 1.3×10^{-3} erg cm⁻² s⁻¹ (protons and hydrogen atoms, respectively) at the altitude 437 km. In the “nonmagnetic” case 22% of the particle flux and 12% of the energy flux of the precipitating protons are backscattered as upward moving protons and hydrogen atoms by the Martian upper atmosphere. The energy spectrum of the up going protons follows

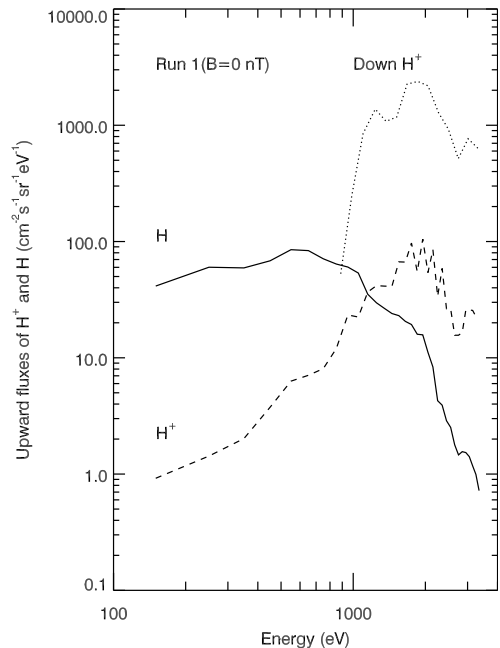


Figure 5. Energy spectra of the downward (spectrum 1 marked by dotted line) and upward (dashed line) moving protons and upward moving hydrogen atoms (solid line) for the run without induced magnetic field.

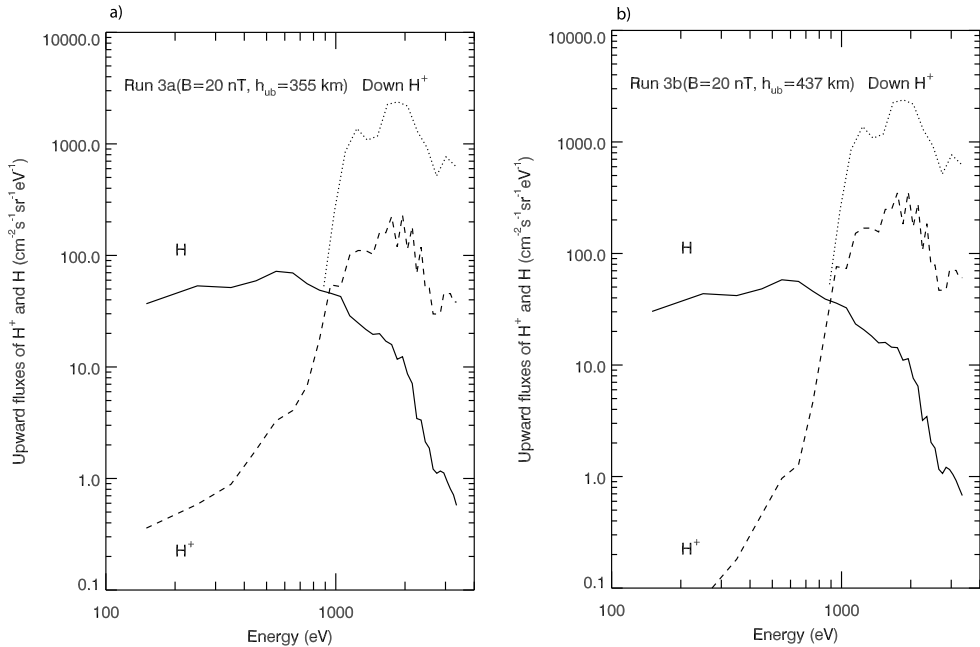


Figure 6. (a) Energy spectra of the downward (spectrum 1 at $h_{ub} = 355$ km marked by dotted line) and upward (dashed line) moving protons and upward moving hydrogen atoms (solid line) for the run with the 20 nT horizontal component of the induced magnetic field. (b) Energy spectra of the downward (spectrum 1 at $h_{ub} = 437$ km marked by dotted line) and upward (dashed line) moving protons and upward moving hydrogen atoms (solid line) for the run with the 20 nT horizontal component of the induced magnetic field.

well the spectrum of the precipitating protons due to the single backward scattering at large angles (reflection) in the nadir direction which almost conserves energy due to large difference in masses for protons and atmospheric gas components. The low-energy part of spectrum (<700 eV) is formed by the collisional spreading in the thermosphere due to multiple collisions. The spectrum of the up moving hydrogen atoms has a significantly stronger low-energy component also formed by collisional spreading due to multiple collisions in the altitude range of the maximum energy deposition rate (Figure 4, solid line).

[18] These estimates of the backscattered energy flux of the precipitating protons are lower than the values calculated by *Kallio and Barabash* [2001] for the precipitation of high-energy hydrogen atoms into the Martian upper atmosphere. *Kallio and Barabash* [2001] found that the up going hydrogen particle and energy fluxes constitute 58% and 33% of the impinging particle and energy fluxes, respectively. The difference could be explained by the fact that in the present model we use the updated set of cross sections and scattering angle distributions for each collisional process instead of the hard sphere approximation used in the previous models. It is well known that the hard sphere approximation based on the isotropic scattering angle distribution results in a very high rate of collisional spreading of the penetrating flux of protons

and hydrogen atoms in a planetary atmosphere [*Gérard et al.*, 2000, 2005].

3.2. Runs With the Induced Magnetic Field

[19] For the incident proton spectrum 1 we conducted two runs 3a and 3b with the most probable value of the horizontal component $B = 20$ nT of the induced magnetic field. In these runs the model upper boundary was changed in accordance with the altitude range of the spectrum 1 measurements by ASPERA-3 instrument; that is, h_{ub} was taken equal to 355 km in run 3a, and h_{ub} was taken equal to 437 km in run 3b. Figures 6a and 6b show the energy spectra of the incident and backscattered protons and upward moving hydrogen atoms at the altitudes $h_{ub} = 355$ km (run 3a) and altitudes $h_{ub} = 437$ km (run 3b). It is necessary to point out that the value of 82 km altitude range during the measurement of spectrum 1 by the ASPERA-3 instrument is approaching the value of gyroradius for the precipitating protons (~125 km for 2 keV protons for conditions of run 3). Therefore, precipitating protons in run 3a have a higher probability to reach a collision-dominated region and deposit practically all their kinetic energy in this region. We have obtained the following estimates of the relative back-scattered (upward) energy fluxes (EBF) for protons and hydrogen atoms: $EBF_p = 16$, and 30% and $EBF_H = 7$, and

Table 2. Calculated Values of the Backscattered Energy Fluxes of H/H⁺

Run	B, Horizontal (nT)	Precipitating Spectra, H ⁺ and H at Altitude h_{ub}	Energy Up, H (%)	Energy Up, H ⁺ (%)	Energy Up, Total (%)	H/H ⁺ Flux Up, Total (%)
1	0	Spectrum 1, none, $h_{ub} = 437$ km	8	4	12	22
2	10	Spectrum 1, none, $h_{ub} = 437$ km	7	11	18	27
3a	20	Spectrum 1, none, $h_{ub} = 355$ km	7	16	23	33
3b	20	Spectrum 1, none, $h_{ub} = 437$ km	6	30	36	45
4	30	Spectrum 1, none, $h_{ub} = 437$ km	5	53	58	66
5	50	Spectrum 1, none, $h_{ub} = 437$ km	3	89	92	95
6a	20	Spectrum 2, none, $h_{ub} = 387$ km	4	16	20	26
6b	20	Spectrum 2, none, $h_{ub} = 435$ km	4	24	28	34
7	20	None, MS H, $h_{ub} = 500$ km	12	0.3	12	19
8	20	None, SW H, $h_{ub} = 500$ km	10	0.3	10	15

6% for runs 3a and 3b with the horizontal magnetic field $B = 20$, correspondingly (see Table 2). It is seen that a value of EBF_p strongly depends on the selected value of the model upper boundary h_{ub} , but EBF_H practically does not change in runs 3a and 3b. Therefore, to exclude the direct influence of the neutral atmosphere on the flux of precipitating protons we used the value $h_{ub} = 437$ km as an upper boundary for our model.

[20] For the incident proton spectrum 1 and for the different magnitudes of the horizontal component of the induced magnetic field B we have obtained the following estimates of the relative backscattered (upward) energy fluxes for protons and hydrogen atoms: $EBF_p = 11\%$, 30% , 53% , and 89% and $EBF_H = 7\%$, 6% , 5% , and 3% for the horizontal magnetic field $B = 10$, 20 , 30 , and 50 nT, correspondingly (see Table 2).

[21] The shapes of the upward spectra are similar to the case without magnetic field except the low-energy proton component is gone but the absolute fluxes are substantially higher. For the measured spectrum of the incident protons and the relatively high magnitude of the horizontal (parallel) magnetic field $B = 50$ nT the thermosphere of Mars is practically shielded from proton precipitation (the up going flux reaches 95% of the down going flux). Indeed, in this case the gyroradius for precipitating protons (~ 125 km for 2 keV protons) is smaller than the distance between the top boundary and the collision dominated region (420 km). Therefore, all protons return back even before they reach altitudes where collisions start playing role. The up going neutral flux is due to small amount of high-energy protons which managed penetrate through the magnetic field. The cases with moderate magnitudes of the horizontal magnetic field result in values of the backscattered fluxes of protons and hydrogen atoms that are comparable with the previous estimates based on the ASPERA-3 measurements. The dependence of the upward flux energy spectra on the value of the horizontal magnetic field is presented in Figure 7.

[22] The presence of the magnetic field changes not only the upward flux but also the energy deposition rate and the excitation of gas emissions. Figure 4 shows the changes in the energy deposition rate due to the presence of the magnetic field. For the case with the magnetic field $B = 20$ nT the heating of the neutral gas due to momentum transfer collisions decreases (37% at the peak) due to significant increase of the proton albedo.

[23] We have also conducted two sensitivity runs. Two runs were conducted for the reference case 3b but the cross sections of the CO₂ collisions with protons and hydrogen

atoms were enlarged and decreased by a factor of 10. In the reference case the elastic and inelastic cross sections for CO₂ collisions with H/H⁺ are taken to be the same as for O₂ molecule and are thus uncertain. The following values of the upward energy flux of $EBF_H = 13\%$ cross sections (CSs) enlarged by 10, and 3% (CSs decreased by 10) and $EBF_p = 30\%$ and 30% were obtained. It is seen that difference with the reference run 3b is about a factor of 2 for the value of EBF_H and is practically negligible for EBF_p . In the other sensitivity run the dependence on the angle distribution of the

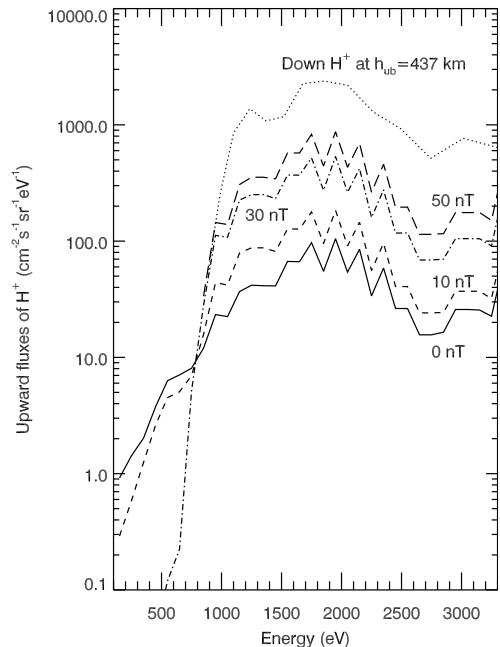


Figure 7. Energy spectra of the upward proton fluxes for different values of the horizontal magnetic field B . Solid line denotes the run for $B = 0$, short-dashed line denotes the run for $B = 10$, dashed-dotted line denotes the run for $B = 30$, long-dashed line denotes the run for $B = 50$, and the dotted line shows the downward spectrum 1.

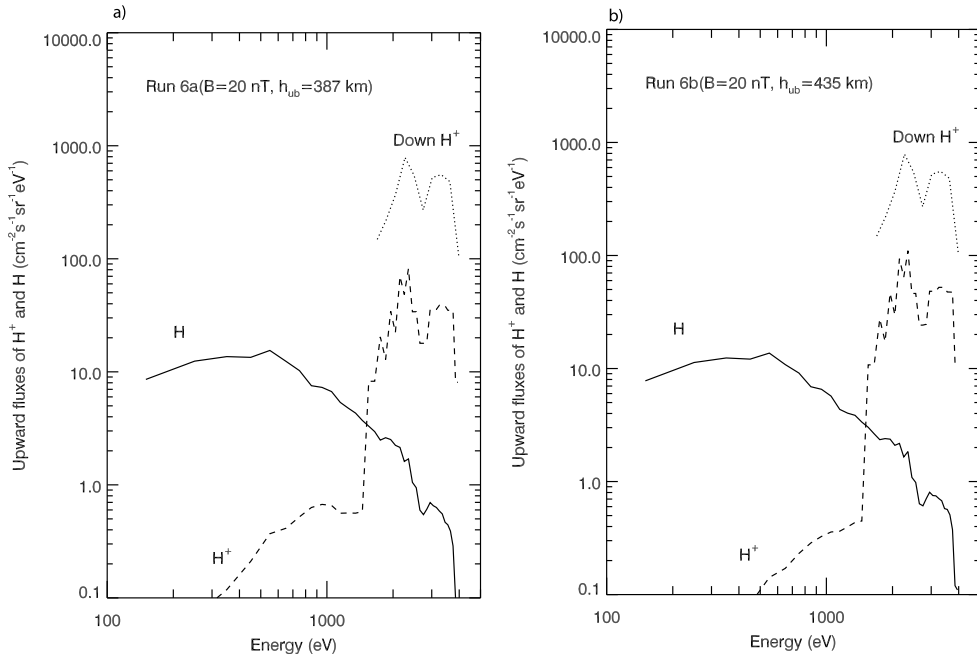


Figure 8. (a) Energy spectra of the downward (spectrum 2 at $h_{ub} = 387$ km marked by dotted line) and upward (dashed line) moving protons and upward moving hydrogen atoms (solid line) for the run with the 20 nT horizontal component of the induced magnetic field. (b) Energy spectra of the downward (spectrum 2 at $h_{ub} = 435$ km marked by dotted line) and upward (dashed line) moving protons and upward moving hydrogen atoms (solid line) for the run with the 20 nT horizontal component of the induced magnetic field.

incident protons was investigated. In this run a nonisotropic distribution (the angle to the nadir direction was limited to the range $\pm 45^\circ$) for the precipitating flux of protons was considered. The upward energy flux was for H = 6%, and P = 25.5%. Again, it was found that the difference is not large. There is a small reduction for protons due to additional collisions, but the backscattered fluxes of protons and hydrogen atoms due to gyromotion are practically the same. This is caused by the deeper penetration of the H/H⁺ flux into the Martian thermosphere and, as a consequence, a more efficient collisional thermalization of the incident particles.

[24] For the incident proton spectrum 2 we also conducted two runs 6a and 6b with the most probable value of the horizontal component $B = 20$ nT of the induced magnetic field. In these runs the model upper boundary was changed in accordance with the altitude range of the spectrum 2 measurements by ASPERA-3 instrument; that is, h_{ub} was taken equal to 387 km in run 6a, and h_{ub} was taken equal to 435 km in run 6b. Figures 8a and 8b show the energy spectra of the incident and backscattered protons and upward moving hydrogen atoms at the altitudes $h_{ub} = 387$ km (run 6a) and altitudes $h_{ub} = 435$ km (run 6b). For the incident proton spectrum 2 (run 6 with $B = 20$ nT) the upward fluxes for protons and hydrogen are $EBF_H = 4\%$, and 4% and $EBF_P =$

16%, and 24% for runs 6a and 6b, correspondingly. The relative upward energy fluxes were 20% and 28%, and upward particle fluxes 34% and 40% for runs 6a and 6b. The calculated energy spectra of the protons and hydrogen atoms moving upward at the model upper boundary are shown in Figure 8. Comparison of Figures 6 and 8 shows that the overall pattern qualitatively remains the same. The mean energy of the spectrum 2 is higher (see Figure 3), therefore the low-energy upward proton flux is more developed, and the hydrogen up going flux is shifted toward lower energies because of collisional spreading in the altitude range of maximum energy deposition.

[25] The Martian upper atmosphere is under the influence of an intense flux of hydrogen atoms of the solar wind energy [Kallio and Barabash, 2001]. In the solar wind and in the magnetosheath, hydrogen ENAs are produced in the charge exchange between solar wind protons and the hydrogen corona either beyond the bow shock (undisturbed solar wind) or in the magnetosheath. Two runs were conducted for fluxes of hydrogen ENAs precipitating onto the Martian atmosphere at a height of 500 km. The respective spectra were taken from Kallio *et al.* [1997, Figure 10]. In run 7 the incident H spectrum corresponds to the magnetosheath (MS) energetic neutral atoms (ENAs) and in run 8 it corresponds to the solar

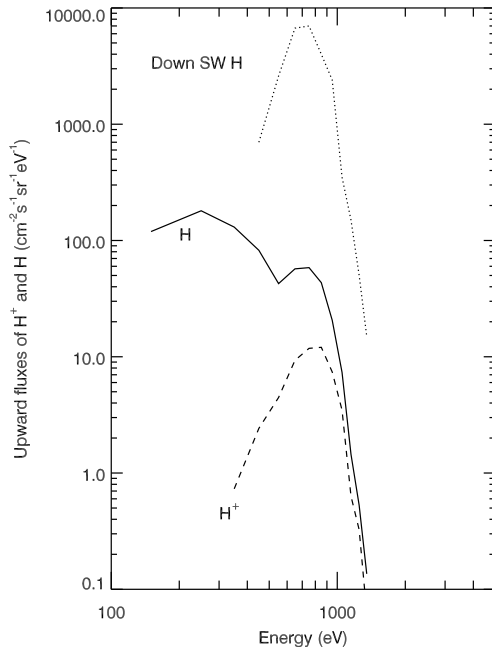


Figure 9. Energy spectra of the downward (dotted line) and upward (dashed line) moving hydrogen atoms and upward moving protons (solid line) for run 8.

wind (SW) ENAs (Figure 3, dotted line). In run 7 the spectrum of MS H ENAs was approximated by a flat distribution with a value of $3 \times 10^6 \text{ cm}^{-2} \text{ s}^{-1} \text{ eV}^{-1}$ for the energy interval from 100 to 900 eV. In run 7 the upward energy flux of hydrogen was 12%, and protons 0.3%. For run 8 the upward energy flux of hydrogen was 10%, and of protons 0.3%. The calculated energy spectra of the protons and hydrogen atoms moving upward at the model upper boundary are given in Figure 9. An additional run, identical to run 8 but without induced magnetic field, was conducted. For this run the upward energy fluxes of hydrogen atoms and protons were found to be practically the same as in run 8. Again, the backscattered flux of H is formed mainly due to the collisional spreading in the Martian thermosphere, while the upward moving flux of protons is formed due to the stripping in the upper layers of the atmosphere and therefore it follows the energy spectrum of the incident hydrogen atoms at altitude 500 km.

[26] The calculated estimates of the energy and particle fluxes of backscattered protons and hydrogen atoms obtained in runs 1–8 are summed in Table 2.

[27] The total amount of up going particles (H and H⁺) is about the same in runs 1, 7, and 8. This indicates the down going flux reaches the exobase unaffected either due to neutrality (run 7 and 8) or the absence of the magnetic field (run 1). Runs 7 and 8 show that very few protons leave the system. As it can be seen in Figure 2 (top) the cross section

for stripping is comparable to the ionization cross section. This leads to the formation of protons in the collision dominated region, and as a consequence to the reduction of the backscattered flux.

4. Summary and Conclusions

[28] A DSMC model for the calculations of the transport of high-energy proton and hydrogen atoms in the Martian upper atmosphere has been developed. It takes into account all physical processes of the H/H⁺ penetration through the atmosphere. The important features of the elaborated model are: the detailed consideration of the scattering angle in each collision and utilization of the most recent set of cross sections.

[29] This code is used to calculate the backscattered flux of energetic hydrogen atoms and protons and the total energy deposition rates. The calculations have been performed for the Martian atmosphere during the solar minimum. We use a spectrum of the incident protons in the altitude range 355–437 km measured by the Mars Express ASPERA-3 in the energy range 700 eV to 20 keV. The particle and energy fluxes of the incident protons were equal to $3.0 \times 10^6 \text{ cm}^{-2} \text{ s}^{-1}$ and $1.4 \times 10^{-2} \text{ erg cm}^{-2} \text{ s}^{-1}$. It was found that 22% of particle flux and 12% of the energy flux of the precipitating protons were backscattered by the Martian upper atmosphere if no magnetic field is taken into account.

[30] The horizontal magnetic field induced by solar wind leads to an increase of the H⁺ upward flux because of the proton gyromotion. Including a 20 nT horizontal magnetic field in the altitude range of 85–500 km in the model increases the backscattered up to 40%–50%. The 50 nT field almost completely screen off the precipitating flux. The magnetic field plays a crucial role in the transport of charged particles and determines the energy deposition of the solar wind protons in the upper atmosphere of Mars.

[31] **Acknowledgments.** The contribution by V.S. and D.B. was supported by the Swedish Research Council via grant “Physics of induced magnetospheres” to the Swedish Institute of Space Physics and the Basic Research Program of the Presidium of the Russian Academy of Sciences, Russian Foundation for Basic Research (project 11-02-00479a), and the Federal Targeted Program “Science and Science Education for Innovation in Russia 2009–2013.” This study was also supported by the Belgium National Found for Scientific Research (FNRS). C.D. was supported by the National Graduate School of Space Technology of Luleå Technical University.

[32] Masaki Fujimoto thanks the reviewers for their assistance in evaluating this paper.

References

- Akalin, F., D. D. Morgan, D. A. Gurnett, D. L. Kirchner, D. A. Brain, R. Modolo, M. H. Acuna, and J. R. Espley (2010), Dayside induced magnetic field in the ionosphere of Mars, *Icarus*, *206*, 104–111, doi:10.1016/j.icarus.2009.03.021.
- Barabash, S., et al. (2006), The analyzer of space plasmas and energetic atoms (ASPERA-3) for the Mars Express mission, *Space Sci. Rev.*, *126*(1–4), 113–164.
- Bisikalo, D. V., V. I. Shematovich, and J.-C. Gérard (1995), Kinetic model of the formation of the hot oxygen geocorona: 2. Influence of O⁺ ion precipitation, *J. Geophys. Res.*, *100*, 3715–3720, doi:10.1029/94JA03196.
- Brain, D. A., F. Bagenal, M. H. Acuna, and J. E. P. Connerney (2003), Martian magnetic morphology: Contributions from the solar wind and crust, *J. Geophys. Res.*, *108*(A12), 1424, doi:10.1029/2002JA009482.
- Decker, D. T., B. V. Kozelov, B. Basu, J. R. Jasperse, and V. E. Ivanov (1996), Collisional degradation of the proton-H atom fluxes in the atmosphere: A comparison of theoretical techniques, *J. Geophys. Res.*, *101*, 26,947–26,960, doi:10.1029/96JA02679.

- Fox, J. L., and A. B. Hac (2009), Photochemical escape of oxygen from Mars: A comparison of the exobase approximation to a Monte Carlo method, *Icarus*, *204*, 527–544, doi:10.1016/j.icarus.2009.07.005.
- Futaana, Y., et al. (2006), First ENA observations at Mars: ENA emissions from the Martian upper atmosphere, *Icarus*, *182*, 424–430, doi:10.1016/j.icarus.2005.09.019.
- Gérard, J.-C., B. Hubert, D. V. Bisikalo, and V. I. Shematovich (2000), A model of the Lyman- α line profile in the proton aurora, *J. Geophys. Res.*, *105*, 15,795–15,806, doi:10.1029/1999JA002002.
- Gérard, J.-C., V. I. Shematovich, D. V. Bisikalo, and D. Lummerzheim (2005), A Monte Carlo model of auroral hydrogen emission line profiles, *Ann. Geophys.*, *23*, 1473–1480, doi:10.5194/angeo-23-1473-2005.
- Haider, S. A., S. P. Seth, E. Kallio, and K. I. Oyama (2002), Solar EUV and electron-proton-hydrogen atom-produced ionosphere on Mars: Comparative studies of particle fluxes and ion production rates due to different processes, *Icarus*, *159*, 18–30, doi:10.1006/icar.2002.6919.
- Kallio, E., and S. Barabash (2001), Atmospheric effects of precipitating energetic hydrogen atoms on the Martian atmosphere, *J. Geophys. Res.*, *106*, 165–177, doi:10.1029/2000JA002003.
- Kallio, E., J. G. Luhmann, and S. Barabash (1997), Charge exchange near Mars: The solar wind absorption and neutral atom production, *J. Geophys. Res.*, *102*, 22,183–22,197, doi:10.1029/97JA01662.
- Lindsay, B. G., W. S. Yu, and R. F. Stebbings (2005), Cross sections for electron capture and loss by keV oxygen atoms in collisions with CO and CO₂, *J. Geophys. Res.*, *110*, A02302, doi:10.1029/2004JA010854.
- Lundin, R., et al. (2004), Solar wind-induced atmospheric erosion at Mars: First results from ASPERA-3 on Mars Express, *Science*, *305*(5692), 1933–1936, doi:10.1126/science.1101860.
- Moore, T. E., and J. L. Horwitz (2007), Stellar ablation of planetary atmospheres, *Rev. Geophys.*, *45*, RG3002, doi:10.1029/2005RG000194.
- Nakai, Y., T. Shirai, T. Tabata, and R. Ito (1987), Cross sections for charge transfer of hydrogen atoms and ions colliding with gaseous atoms and molecules, *At. Data Nucl. Data Tables*, *37*, 69–101, doi:10.1016/0092-640X(87)90005-2.
- Shematovich, V. I. (2008), Kinetics of suprathermal atoms and molecules in the rarefied planetary atmospheres, in *Rarified Gas Dynamics*, edited by T. Abe et al., *AIP Conf. Proc.*, *1084*, 1047–1054, doi:10.1063/1.3076436.
- Shematovich, V. I., D. V. Bisikalo, and J.-C. Gérard (1994), A kinetic model of the formation of the hot oxygen geocorona: 1. Quiet geomagnetic conditions, *J. Geophys. Res.*, *99*, 23,217–23,228, doi:10.1029/94JA01769.

S. Barabash, C. Diéval, Y. Futaana, M. Holmstrom, H. Nilsson, and G. Stenberg, Swedish Institute of Space Physics, SE-98128 Kiruna, Sweden. (stas@irf.se; catherine@irf.se; futaana@irf.se; matsh@irf.se; hans.nilsson@irf.se; gabriella@irf.se)

D. V. Bisikalo and V. I. Shematovich, Institute of Astronomy, Russian Academy of Sciences, 48 Pyatnitskaya str., Moscow 119017, Russia. (bisikalo@inasan.rssi.ru; shematov@inasan.ru)

J.-C. Gérard, LPAP, Université de Liège, B-4000 Liège, Belgium. (jc.gerard@ulg.ac.be)

PAPER III

Hybrid simulations of proton precipitation patterns onto the upper atmosphere of Mars

Catherine Diéval¹, Esa Kallio², Gabriella Stenberg¹, Stas Barabash¹, and Riku Jarvinen²

¹Swedish Institute of Space Physics, SE-98128, Kiruna, Sweden

²Finnish Meteorological Institute, FIN-00101, Helsinki, Finland

(Received February 16, 2011; Revised June 11, 2011; Accepted August 20, 2011; Online published March 8, 2012)

We study the dependence of proton precipitation patterns onto the Martian upper atmosphere on altitude, proton energy, proton origin, and in a lesser extent, solar zenith angle, using the HYB-Mars model, a 3D quasi-neutral hybrid model. We find that the flux of precipitating protons has a strong altitude dependence: on the dayside, the flux of precipitating protons decreases substantially when the altitude over Mars decreases. We also find that the contribution of exospheric protons to the deposition is significant and its spatial distribution is not identical to that of the solar wind protons. In addition, the low energy proton population comes mainly from the newborn planetary protons. The energized pick-up protons and solar wind protons contribute to the higher energy proton population. The study also confirms that the proton precipitation is highly asymmetric with respect to the direction of the convection electric field in the solar wind. The study implies that the Martian induced magnetosphere protects the upper atmosphere effectively against proton precipitation.

Key words: Solar wind, Mars, proton precipitation, Martian atmosphere, magnetospheres.

1. Introduction

The interaction of the supersonic solar wind with an unmagnetized planet like Mars leads to the formation of an induced magnetosphere: the flow is decelerated and diverted around the conductive ionosphere due to the magnetic field associated with the induced currents, and the interplanetary magnetic field (IMF) frozen into the flow drapes around the obstacle, forming a magnetic barrier on the dayside and a magnetotail on the nightside (e.g. Nagy *et al.*, 2004). The induced magnetospheric boundary separates the magnetosheath, dominated by solar wind protons, from the ionosphere, dominated by heavy ions (O^+ , O_2^+). However, the gyroradius of some solar wind protons may be large enough due to their high energy, so that they can penetrate the magnetic barrier and reach the upper atmosphere, carrying energy, matter and momentum.

The solar wind proton precipitation on Mars has been studied with hybrid models (Brecht, 1997; Kallio and Janhunen, 2001). Since the hybrid models treat the protons as individual gyrating particles, they are well suited to study proton precipitation. Brecht (1997) has shown that the precipitation is sensitive to upstream solar wind conditions, that is, the solar wind bulk velocity \vec{U}_{sw} , and the direction of the interplanetary magnetic field \vec{B}_{sw} . Results from Brecht (1997) and Kallio and Janhunen (2001) also show an asymmetry in the proton precipitation associated with the direction of the solar wind convection electric field $\vec{E}_{sw} = -\vec{U}_{sw} \times \vec{B}_{sw}$. More H^+ ions are deposited on the

hemisphere where the electric field points away from the planet ($+\vec{E}_{sw}$ hemisphere) than on the opposite hemisphere ($-\vec{E}_{sw}$ hemisphere).

The purpose of the present paper is to study the proton precipitation on Mars and its dependence on altitude, energy and origin of the particles, using the HYB-Mars model (Kallio *et al.*, 2010, and references therein), a 3D quasi-neutral hybrid model. Although proton precipitation has already been modeled with hybrid simulations, this is the first study which examines the spatial precipitation patterns given by the solar wind protons and the protons of planetary origin, at different altitudes, for different energy ranges of precipitating protons.

The current paper is an attempt to better understand measurements of downgoing proton flux in the Martian ionosphere made by Mars Express. Observations of solar wind protons in the Martian ionosphere down to 260 km altitude (the pericenter of the orbit of Mars Express, slightly above the exobase) have been reported by Lundin *et al.* (2004). A case study by Diéval *et al.* (submitted, 2011) compared Mars Express observations of downgoing proton flux in the ionosphere to simulated proton energy spectra derived from a hybrid simulation, in a similar way as was done by Kallio *et al.* (2008). The current study is a further step. We want to get a global view of the proton precipitation, using nominal solar wind conditions, to guide the interpretation of future observational statistical studies of proton precipitation onto the Martian atmosphere.

In the present study we keep the solar wind conditions and the solar activity constant: we use an average solar wind speed and minimum solar activity. This choice is motivated by the fact that the operation period of Mars Express (since 2004) coincides with low solar activity. The

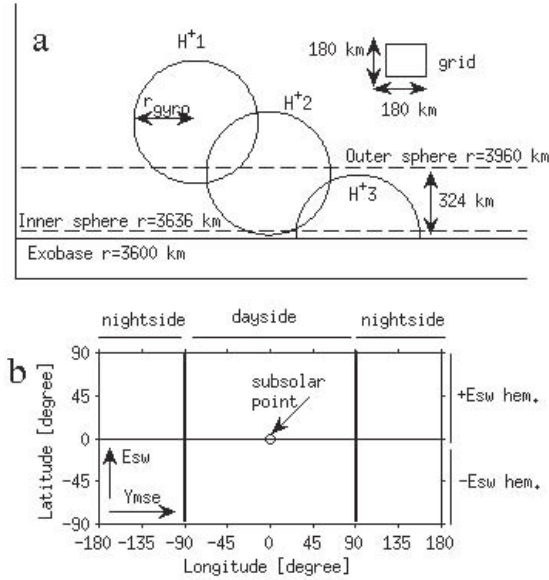


Fig. 1. (a) Sketch showing a grid cell (rectangle on the top right), the altitudes of the exobase (solid line), inner sphere and outer sphere (dashed lines), and gyrations of protons (black circles). (b) Longitude-latitude map. The solar wind convection electric field points to the top and the component of IMF transverse to the flow \vec{v}_{mse} points to the right. The two thick vertical black lines at longitude = $\pm 90^\circ$ indicate the terminator. The horizontal black line at latitude = 0° separates the $\pm E_{sw}$ hemispheres.

effect of the oxygen corona on the proton precipitation, the proton backscattering and the energetic neutral atoms production are beyond the scope of this study.

The basic characteristics of the model and the needed inputs are described in Section 2. The results are presented in Section 3 and discussed in Section 4.

2. Model

The HYB-Mars model is described in detail in the paper by Kallio *et al.* (2010) and references therein. Here we do not explain the details of the code but repeat the basics and describe what is new compared to the work by Kallio *et al.* (2010). HYB-Mars is a Particle-in-Cloud (PIC) model where an ion is a cloud (macroparticle), which has the same size as the cell, in which the center of cloud is located (see Kallio and Janhunen, 2003, for details). The macroparticle corresponds to w real particles. The weight w depends on the ion specie and its value is typically 10^{20} – 10^{22} .

In the model, the plasma ions are treated as particles and the electrons are treated as a massless charge-neutralizing fluid. The ions are accelerated by the Lorentz force:

$$m_i \frac{d\vec{v}_i}{dt} = q_i (\vec{E} + \vec{v}_i \times \vec{B}) \quad (1)$$

where \vec{E} and \vec{B} are the electromagnetic fields, m_i the mass of an ion i , \vec{v}_i the velocity of an ion i and q_i the electric charge of an ion i . The electric field is calculated from the electron momentum equation:

$$\vec{E} = -\vec{U}_e \times \vec{B} - \frac{\nabla(n_e k T_e)}{en_e} \quad (2)$$

where n_e is the electron density, T_e the electron temperature, \vec{U}_e the electron bulk velocity, e the unit electron charge and k Boltzmann's constant. The last term in Eq. (2) is the electron gradient pressure, also referred to the ambipolar electric field.

The coordinate system used is the Mars Solar Orbital (MSO) Cartesian coordinate system. The x -axis points from the center of Mars towards the Sun, the z -axis points towards the orbital North and the y -axis completes the right-handed system. The size of the simulation box is $-4.2 R_m < x, y, z < 4.2 R_m$, where $R_m = 3393$ km is the Martian radius. The simulation uses three different grid sizes, depending on the distance r from the center of Mars: 720 km for $r > 3 R_m$, 360 km for $2 R_m < r < 3 R_m$ and 180 km for $r < 2 R_m$. The time step is 0.02 s, and the average number of particles per grid cell is ~ 30 , which is significant. The total running time was ~ 700 s.

It is noteworthy that the crustal magnetic anomalies (Acuña *et al.*, 1998, 1999) are not included into the model because the grid size is too coarse to model the intrinsic magnetic field accurately. The magnetic field is saved on the face of the cells and even the smallest grid size (180 km) would be too large to model the crustal magnetic anomalies accurately enough. The large grid size may, therefore, reduce the gradients of the electric and magnetic fields of the model and can result in a smoothed electromagnetic field. Ions within the grid cell are, however, subject to gyromotion caused by the Lorentz force (Eq. (1)) within a grid cell, also in the situation where the grid size is larger than the ion gyroradius. In general, the smallest grid size in the sim-

ulation, 180 km, is still relative large compared with the interaction region. How the grid size affects the solution is an issue which should be studied in the future with hybrid model simulations with a finer grid size than in the present study.

We believe that the crustal magnetic anomalies may inhibit the downward proton flux to the atmosphere, at least in regions where the field is not radial. We base this hypothesis on the work of Shematovich *et al.* (2011), who used a Monte Carlo simulation of the interaction between the solar wind protons and the Martian atmospheric neutrals, and showed that the presence of an induced horizontal magnetic field increases the backscattering of incoming protons. This means that the downward proton flux is reduced by the magnetic field. As an example, the gyro-radius of a 2 keV proton is 1300 km in a 5 nT magnetic field (typical value at 400 km altitude in a region of weak crustal field), and becomes ~ 30 km in a 200 nT magnetic field (typical value at 400 km altitude in the region of the strongest anomalies). However, the magnetic field configuration, not only its magnitude, is important in determining plasma motion. In a recent study using a hybrid simulation, Brecht and Ledvina (this issue, 2012) showed that magnetic anomalies can locally focus solar wind protons into cusps. On the observational side, there is on one hand no clear evidence that magnetic anomalies actually have a significant influence on the solar wind ion dynamics in the near-Mars environment (Diéval *et al.*, submitted, 2011; Stenberg *et al.*, 2011). On the other hand, there is evidence that in the Southern hemisphere, the strong magnetic anomalies reduce the ionospheric ion outflow (Nilsson *et al.*, 2011) and affect the flow pattern of escaping O^+ ions (Lundin *et al.*, 2011). The possible effect of the magnetic anomalies on proton precipitation will be investigated in a future statistical study using Mars Express observations. Although the magnetic anomalies might change the precipitation pattern, we believe that the direction of the convection electric field \vec{E}_{sw} is a much more important parameter.

2.1 Input parameters: Solar wind

In our model, the solar wind contains H^+ and He^{++} ions. Two simulations are conducted in this study. The upstream solar wind parameters are the same in both: the density is 2.5 cm^{-3} , the bulk velocity vector is $[-487, 0, 0] \text{ km s}^{-1}$ and the temperature is $1.5 \cdot 10^5 \text{ K}$. This corresponds to average solar wind conditions. The aberration angle of the solar wind direction, due to the Martian orbital motion, is excluded in our study, which means that the solar wind direction is assumed to be along the Mars-Sun line. We use two different interplanetary magnetic fields (IMF). In one case, the IMF vector is $[1.9, -1.6, -2.5] \text{ nT}$ with a Parker spiral angle of 57° (Parker IMF simulation). In the second case, it is $[0, 3, 0] \text{ nT}$ ($B_x = 0$ simulation), which means that the IMF is perpendicular to the solar wind flow. The $B_x = 0$ case results in a symmetric draping of the IMF, which helps us to study the precipitation patterns, particularly the asymmetries with respect to the direction of the convection electric field, as will be seen later in Section 3. In the Parker spiral case, the Parker spiral leads to a draping asymmetry, which affects the plasma environment, including the precipitation patterns. This situation is more

realistic. The IMF y and z components of the Parker IMF case were derived from Mars Global Surveyor (MGS) data, recorded on February 27, 2004, with the method used by Fedorov *et al.* (2006). The draped IMF measured by MGS is expected to have the same orientation in the y - z plane as the upstream IMF (Brain *et al.*, 2006; Fedorov *et al.*, 2006). This IMF data has also been used as input to the hybrid simulation performed in Diéval *et al.* (submitted, 2011).

2.2 Input parameters: Neutral corona

Two spherically symmetric neutral coronae (oxygen and hydrogen) around Mars are included. The hydrogen corona is a source of H^+ ions and the oxygen corona is a source of O^+ ions. We use the same hot hydrogen and oxygen exospheres as the ones used in the community coordinated Solar Wind Interaction with Mars (SWIM) modeling comparison team. The hydrogen neutral profile adopted into the present paper is

$$n(H[\text{m}^{-3}]) = N_1 \cdot \exp(A_1 \cdot (1/R_0 - 1/r)) + N_2 \cdot \exp(A_2 \cdot (1/R_0 - 1/r)) \quad (3)$$

where $N_1 = 1.5 \cdot 10^{11}$, $N_2 = 1.9 \cdot 10^{10}$, $A_1 = -25965 \cdot 10^3$, $A_2 = -10365 \cdot 10^3$, $R_0 = 3593.5 \cdot 10^3$, r is the distance from the center of Mars (in meters) and the subscript 1 and 2 refers to the thermal and hot hydrogen profiles, respectively. The cold component is from Chaufray *et al.* (2008). The photoionization rate is $5.58 \cdot 10^{-8} \text{ s}^{-1}$ from Ma *et al.* (2004) (see also Fulle *et al.*, 2007, for hydrogen photoionization rates), and it corresponds to solar minimum conditions.

The neutral hot oxygen profile is modeled as Eq. (4)

$$n(O[\text{m}^{-3}]) = N_1 \cdot \exp(-(r - R_0)/B_1) + N_2 \cdot \exp(-(r - R_0)/B_2) + N_3 \cdot \exp(-(r - R_0)/B_3) \quad (4)$$

where $N_1 = 5.23 \cdot 10^9$, $N_2 = 9.76 \cdot 10^8$, $N_3 = 3.71 \cdot 10^{10}$, $B_1 = 626.2 \cdot 10^3$, $B_2 = 2790 \cdot 10^3$, $B_3 = 88.47 \cdot 10^3$, $R_0 = 3393.5 \cdot 10^3$, and r is the distance from the center of Mars (in meters). The photoionization rate is $8.89 \cdot 10^{-8} \text{ s}^{-1}$ from Ma *et al.* (2004) (their table 1). The values of the density and photoionization rate correspond to solar minimum conditions.

2.3 Input parameters: Ionospheric ions

The HYB-Mars model does not contain self-consistent ionosphere because of the coarse grid size (minimum grid size is 180 km). Therefore, the role of ions originating from below the exobase is taken into account by emitting O^+ and O_2^+ ions from the model inner boundary. The inner boundary, which mimics the exobase, is a spherical shell at 207 km altitude. The model also contains a background electron density, which mimics the role of the density of planetary ions. Ionospheric oxygen ions are created in the model with a dependence of the form $0.1 + 0.9 \cdot \cos(\text{SZA})$ on dayside, while the emission is equal to 0.1 on nightside. Radio occultation studies have shown that the peak in the electron density profiles at Mars has this SZA dependence (e.g. Zhang *et al.*, 1990).

2.4 Input parameters: Chemical reactions

In addition to photoionization, the hybrid model also implements electron impact ionization reactions, and charge-exchange (CX) reactions between the neutral corona atoms

and exospheric/solar wind protons. As in our previous study (Kallio *et al.*, 2010), constant cross sections were used in the CX processes: $2.5 \cdot 10^{-19} \text{ m}^2$ for the two $\text{H}^+ - \text{H}_{\text{exosphere}}$ CX processes ($\text{H}_{\text{SW}}^+ + \text{H}_{\text{exosphere}}$, $\text{H}_{\text{exosphere}}^+ + \text{H}_{\text{exosphere}}$) and $1 \cdot 10^{-19} \text{ m}^2$ for the two $\text{H}^+ - \text{O}_{\text{exosphere}}$ CX processes ($\text{H}_{\text{SW}}^+ + \text{O}_{\text{exosphere}}$, $\text{H}_{\text{exosphere}}^+ + \text{O}_{\text{exosphere}}$). Also, constant electron impact ionization frequencies were used for simplicity: $1.5 \cdot 10^{-14} \text{ m}^3 \text{ s}^{-1}$ for $e^- + \text{H}$ and $5.0 \cdot 10^{-14} \text{ m}^3 \text{ s}^{-1}$ for $e^- + \text{O}$ processes (see Cravens *et al.*, 1987, their figure 2, for detailed temperature-dependent electron impact ionization frequencies).

2.5 Ion precipitation

In this paper, we record the position \vec{r}_i , the velocity \vec{v}_i , the weight w_i and the time t_i of the hit of an ion i during a period $\Delta t \sim 500 \text{ s}$. The particles are recorded on spheres (shells) of different altitudes centered at the center of Mars. For the $B_x = 0$ simulation, the ions were collected on two shells: the inner sphere and the outer sphere (distance from the center of Mars $r = 3636 \text{ km}$ and 3960 km , respectively). They correspond respectively to altitudes $\sim 240 \text{ km}$ and 560 km . For the Parker IMF simulation, the ions were collected at the exobase (distance $r = 3600 \text{ km}$). This choice of the exobase for the Parker IMF case and the choice of the two other shells for the $B_x = 0$ case, are made for practical reasons: the $B_x = 0$ simulation was realized first, to study the dependence of the precipitation pattern on altitude. The Parker IMF simulation was realized afterwards, and then the protons were collected directly at the exobase, to study the proton population actually entering the atmosphere.

The HYB-Mars model uses an absorbing boundary condition for ions on the inner boundary. Only the ions with a downward velocity are considered in this paper. An ion hitting the exobase is immediately “removed” and really precipitates. The ions hitting the shells above are gyrating and can hit these shells several times. Then the hits on these shells with a downward velocity are used to derive a downward flux in number of hits $\text{cm}^{-2} \text{ s}^{-1}$. This flux is not a net flux but simply the downward flux of gyrating particles. In this study, we use the term “precipitation” in a general meaning of downgoing flux in the atmosphere. This is fine in the sense that we have used the same terminology for ion measurements as in the work of Diéval *et al.* (submitted, 2011). We can not know whether the ions recorded by Mars Express (down to $\sim 260 \text{ km}$ altitude) actually enter the exobase. It was assumed that these measured ions precipitate. Note that any estimate of the precipitating flux above the exobase (either measured or simulated) may lead to strong overestimate of the real flux precipitating into the atmosphere.

A schematic sketch is shown in panel 1(a): the exobase, the inner and outer spheres, a grid cell and some ion gyrations. The distance between the inner shell and the exobase is negligible, 36 km , and then the precipitation patterns will be qualitatively the same for one set of inputs. The distance between the inner and outer spheres is 324 km , which is twice the grid size (180 km , at $r < 2 R_m$). The grid size is thus fine enough to capture the behaviour of the precipitating particles as they go from the outer sphere down to the exobase. An ion with energy 2 keV in a 20 nT mag-

netic field has a gyroradius of $\sim 324 \text{ km}$. Hence, in this case, the distance between the shells is 1 gyroradius ~ 2 grid cells. The ion $\text{H}^+ 1$ has the center of gyration above the outer sphere and impacts it several times. The ion $\text{H}^+ 2$ can hit the outer and inner spheres one time. The ion $\text{H}^+ 3$ hits the inner boundary one time and is absorbed. When an ion hits the inner sphere, it has practically reached the exobase, as one can see on the figure. An ion with a small gyroradius under the same magnetic field (lower energy) can gyrate during a longer time from the outer sphere to the exobase before it is taken away. In the same manner, if the magnetic field increases, the ion gyroradius becomes smaller and the particle hits the spheres more times while gyrating. On the other hand, particles with a small gyroradius tend to be backscattered at high altitude by the magnetic field. It means that the height of the depletion layer (height from which the ions have no room to gyrate because they are taken away) depends on the particle energy and on the magnetic field. In reality, the ions are not immediately lost, but scattered back by the atmosphere after ion-neutral collisions (see Kallio and Barabash, 2001, their figure 2).

For this study, the flux is binned in longitude/latitude. We use a 10° resolution. To calculate the particle flux [$\text{cm}^{-2} \text{ s}^{-1}$] of all precipitating protons i on a shell of radius R over all energies between longitudes long1 and long2 , and between latitudes lat1 and lat2 (longitudes and latitudes in degrees), we use the formula:

$$F_{\text{P}}^{\text{long/lat}} = \frac{\sum_i w_i}{\Delta t \cdot \pi / 180 \cdot R^2 \cdot |\sin(\text{lat1}) - \sin(\text{lat2})| \cdot |\text{long1} - \text{long2}|} \quad (5)$$

and the corresponding formula for the energy flux [$\text{eV cm}^{-2} \text{ s}^{-1}$]:

$$F_{\text{E}}^{\text{long/lat}} = \frac{\sum_i w_i \cdot 1/2 m_i \cdot v_i^2}{\Delta t \cdot \pi / 180 \cdot R^2 \cdot |\sin(\text{lat1}) - \sin(\text{lat2})| \cdot |\text{long1} - \text{long2}|} \quad (6)$$

A sketch, which represents a longitude-latitude map is shown in panel 1(b). The solar wind convection electric field \vec{E}_{sw} points to the top and the component of IMF perpendicular to the flow \vec{Y}_{mse} points to the right. We point out that we do not use the geographic longitude and latitude, but “magnetic” longitude/latitude coordinates related to the so-called Mars Solar Electric field (MSE) Cartesian system. In this system \vec{X}_{mse} points from the center of Mars toward the Sun, along (0° longitude, 0° latitude), \vec{Y}_{mse} points along (90° , 0°) and \vec{Z}_{mse} completes the right-handed system and points along (0° , 90°). The subsolar point (0° , 0°), dayside, nightside and $\pm \vec{E}_{\text{sw}}$ hemispheres are indicated in the figure. We also define the 90° latitude point as the $+\vec{E}_{\text{sw}}$ pole, and the -90° latitude point as the $-\vec{E}_{\text{sw}}$ pole. The $\pm \vec{E}_{\text{sw}}$ poles correspond to horizontal lines at the top and at the bottom in panel (b).

We will also present our results in a SZA form, to simplify comparison with the figure 6 from Kallio and Janhunen (2001). To calculate the particle flux [$\text{cm}^{-2} \text{ s}^{-1}$] of all precipitating protons i on a shell of radius R over all

energies for a band of SZA ($SZA1 < SZA2$), we use the formula

$$F_P^{SZA} = \frac{\sum_i w_i}{\Delta t \cdot 2 \cdot \pi \cdot R^2 \cdot (\cos(SZA1) - \cos(SZA2))}. \quad (7)$$

The corresponding formula for the energy flux [$\text{eV cm}^{-2} \text{s}^{-1}$] is

$$F_E^{SZA} = \frac{\sum_i w_i \cdot 1/2 m_i \cdot v_i^2}{\Delta t \cdot 2 \cdot \pi \cdot R^2 \cdot (\cos(SZA1) - \cos(SZA2))}. \quad (8)$$

3. Results

We first look at an overview of how the Martian environment looks for the Parker IMF case. Figure 2 shows the proton density and the magnetic field strength from the Parker IMF simulation (panels (a) and (b), respectively), in the x - z plane ($y = 0$). The exobase is shown as a sphere originating from the center of Mars. The black shading serves to see the exobase better. The ripples at the center of the spheres occur because the grid is cubic and the quantities are derived on a sphere. Panel (a) contains contributions from all proton populations.

The density of the solar wind increases at the bow shock and decreases close to Mars on the dayside and behind Mars on the nightside (panel (a)). We see that at the exobase, the proton density is asymmetric in z on the dayside. This is related to the direction of the solar wind convection electric field, which points predominantly toward the $z < 0$ region (the y component of the IMF is negative) for this simulation. The magnetic field increases first at the bow shock, and continues to increase closer to the planet, forming the magnetic barrier (panel (b)). The magnetic barrier is stronger in the $z < 0$ region, and the maximum magnetic field is not at subsolar point. It was shown in hybrid simulations (e.g. Brecht, 1990) that the magnetic pile-up in the magnetic barrier is stronger on the hemisphere where the solar wind convection electric field points away from the planet. We can also see that the plasma boundaries are asymmetric with respect to the x -axis, especially in the tail.

3.1 Precipitation map on the outer sphere: Perpendicular IMF case

We will now focus on the proton precipitation patterns resulting from the two simulations. We first consider the $B_x = 0$ simulation since it is the simplest case and we investigate how the precipitation pattern changes with distance to Mars. We start with the pattern recorded on the outer sphere at $r = 3960$ km, which is shown in Fig. 3 (panel (a)), in unit of $\log_{10}(\text{hits cm}^{-2} \text{s}^{-1})$. The white color indicates no particles. Panel (a) shows the downgoing protons of both exospheric and solar wind origins. The pattern is symmetric about the line at 0° longitude, which separates the magnetic dawn and dusk sides. The flux is the most intense at subsolar point. The well known asymmetry related to \vec{E}_{sw} is visible, with a more intense flux in the direction aligned with the convection electric field ($+\vec{E}_{sw}$ hemisphere) than in the opposite direction ($-\vec{E}_{sw}$ hemisphere). Precipitation also exists on the nightside. All these features are in agreement with Brecht (1997) and Kallio and Janhunen (2001). The reader can find the values of energy and particle fluxes in Section 4, where the results from the different altitudes are summarized.

We are also interested to separate the contribution from solar wind and planetary origins (panels 3(b) and (c)). In the simulation we record different planetary proton species on the shells: photoions, protons created by electron impact ionization, and protons created by a CX reaction between a solar wind proton and a neutral hydrogen atom. In our analysis, we group them together into one exospheric population. We see that for both solar wind and planetary protons (panels (b) and (c)), the most intense flux is at the subsolar point, and the flux onto the $+\vec{E}_{sw}$ hemisphere is larger than in the $-\vec{E}_{sw}$ hemisphere. The planetary proton flux is more intense than the solar wind flux on the $-\vec{E}_{sw}$ hemisphere. On the $+\vec{E}_{sw}$ hemisphere, there are several interesting features. One is that the exospheric proton flux is higher on the flanks of the region of major deposition, than in the center (it makes an orange “V” shape in panel (c)). Another thing to note is that around the $+\vec{E}_{sw}$ pole ($\sim 90^\circ$ latitude), the solar wind flux is higher than the exospheric flux. However, the planetary flux is higher than the solar wind flux away from the $+\vec{E}_{sw}$ pole, on the nightside along a curve (yellow-green on panel (c)) starting at the terminator and arriving at the antisub solar point ($-180^\circ/180^\circ, 0^\circ$). Finally, there are two “patches” on the nightside flanks, touching both the $\pm\vec{E}_{sw}$ hemispheres, symmetric relative to the 0° longitude line, where the flux is quite high: one region from -135° to -90° longitude and from -45° to 45° latitude (magnetic dawn), the other is on the other side (magnetic dusk). In these two regions (blue-green in panel (b)), the planetary protons also dominate. These “patches” correspond to the regions where the transverse component of the IMF \vec{V}_{mse} points toward/away from Mars. Generally, on the nightside and away from the convection electric field direction, the planetary protons dominate the solar wind protons. The flux differences between different regions are smaller, i.e. the pattern is more uniform, for planetary protons than for solar wind protons. The incoming solar wind protons have a strongly asymmetric deposition pattern and precipitate intensively in the region aligned with $+\vec{E}_{sw}$ direction and in the subsolar point.

Now we instead divide the protons into different energy ranges (panels (d)–(f)). It is seen that the high energy protons avoid the $-\vec{E}_{sw}$ hemisphere (panel (d)). In the region of major deposition, in the $+\vec{E}_{sw}$ hemisphere, the contribution from protons of intermediate energy (panel (e)) is the most important, particularly around the $+\vec{E}_{sw}$ pole and at the subsolar point. We observe that the $-\vec{E}_{sw}$ hemisphere is dominated by low energy particles (panel (f)). Brecht (1997) showed that the precipitation of slow solar wind streams, i.e. low energy protons, is favored in the $-\vec{E}_{sw}$ hemisphere; this is in agreement with our results. The symmetric “curves” and the magnetic dawn/dusk “patches” noted previously on the nightside flanks are dominated by low energy protons (panel (f)). The low energy proton flux (panel (f)) is higher than the high energy proton flux (panel (d)) in the $+\vec{E}_{sw}$ direction. In that respect, the low energy proton contribution to the region of major deposition is significant. According to Kallio and Janhunen (2001), the $-\vec{E}_{sw}$ hemisphere favors the precipitation of low energy solar wind protons, while the $+\vec{E}_{sw}$ hemisphere favors the precipitation of solar wind protons of higher energy; this is

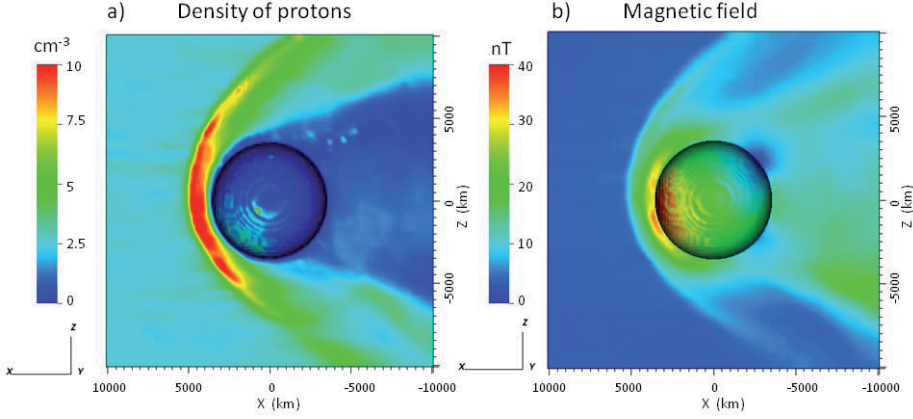


Fig. 2. Overview of the Martian plasma environment in the Parker IMF simulation. (a) Proton density. (b) Magnitude of the magnetic field. The color plane is at $y = 0$. The exobase is represented as a sphere originating at the center of Mars.

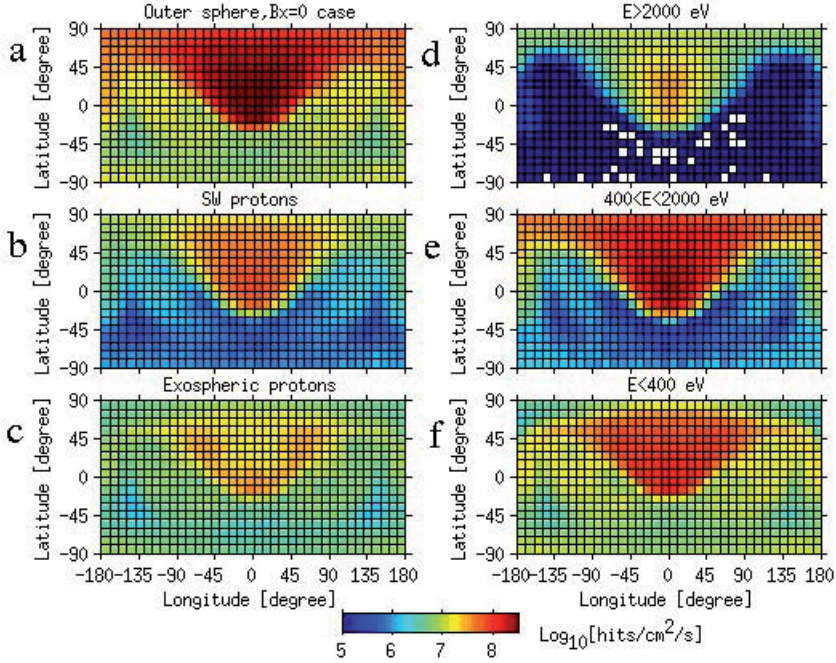


Fig. 3. Longitude-latitude maps of downgoing protons on the outer sphere at $r = 3960$ km for the $B_x = 0$ simulation. (a) All protons. (b) Solar wind protons. (c) Exospheric protons. (d) Protons with energies >2000 eV. (e) Protons with energies between 400 and 2000 eV. (f) Protons with energies <400 eV.

in agreement with our results. It seems that the low energy features are associated with the exospheric protons. This hypothesis is verified later in Fig. 6.

3.2 Precipitation map on the inner sphere: Perpendicular IMF case

Next, we study the downgoing particles at a lower altitude. Figure 4 presents the precipitation patterns on the

inner sphere at $r = 3636$ km. Compared to Fig. 3, the deposited flux has decreased everywhere. In panel 4(a), compared to panel 3(a), the flux is decreased by 2–3 orders of magnitude at subsolar point ($0^\circ, 0^\circ$) and by less than one order of magnitude at the $+\vec{E}_{sw}$ and $-\vec{E}_{sw}$ poles and at the anti-subsolar point. The region of major deposition shrinks and becomes narrower. The flux is still more intense in the

$+\vec{E}_{sw}$ direction and around the $+\vec{E}_{sw}$ pole (panel (a)). The flux at the subsolar point is now smaller than at the $+\vec{E}_{sw}$ pole, and is comparable to the flux at the $-\vec{E}_{sw}$ pole.

Next we compare the different proton species (panels (b) and (c)). We see that, again, the solar wind protons dominate the $+\vec{E}_{sw}$ pole and the rest of the major deposition region (panel (b)), while the exospheric protons dominate the $-\vec{E}_{sw}$ hemisphere (panel (c)). The symmetric “curves” on the nightside flanks, noted in panel 3(c), disappear in panel 4(c). But the magnetic dawn/dusk “patches” are still visible.

The contribution of protons of different energies is shown in panels (d)–(f). We see that the flux of the low energy protons now concentrates at the $+\vec{E}_{sw}$ pole and has decreased significantly in the rest of the region of major deposition, especially at the subsolar point (panel (f)). The region of major deposition is again dominated by the protons of intermediate energies (panel (c)). The $-\vec{E}_{sw}$ hemisphere is favored by the low energy protons (panel (f)) and avoided by the high energy protons (panel (d)). Thus, when looking closer to Mars (here, only 36 km above the exobase) the region of major deposition tends to shrink, becoming more strongly aligned with the convection electric field direction and moves away from the subsolar point, to favor the $+\vec{E}_{sw}$ pole.

The precipitation pattern on the inner sphere differs from the results of Brecht (1997) and Kallio and Janhunen (2001). Indeed, they show that the precipitating flux is largest at low SZA. In the former study, the flux was derived at the surface of Mars. Unfortunately, the latter study does not mention the altitude at which the fluxes were calculated, but it is probably the exobase. A comparison will be made in Section 4. The dramatic change of the precipitation pattern when approaching Mars, suggests that the subsolar region may be strongly affected by some process, which reduces the downward flux in that region. The nature of this process will be examined in Section 4.

3.3 Precipitation map on the exobase: Parker spiral case

Moving further down, we get to the exobase. The ions which have reached this altitude (207 km) will hit the inner boundary once, be absorbed in the atmosphere and not gyrate out again. The corresponding flux is thus the particle precipitation in its original meaning. The altitude difference between the exobase and the inner sphere is small. The two patterns will thus be qualitatively similar for a given set of inputs.

Next, we will look at the effect of the Parker spiral on the precipitation patterns. We show the precipitation map at the exobase in Fig. 5. The main features found in the $B_x = 0$ case are also visible in Fig. 5. But the details in the patterns differ. The $\pm\vec{E}_{sw}$ poles, the major deposition region, and the magnetic dawn/dusk patches on the nightside flanks are now asymmetric about the 0° longitude line. The flux is more intense on the magnetic dawn patch from -135° to -90° longitude (orange) than on the magnetic dusk patch from 90° to 135° longitude (green) in panel (a). In other words, the flux is higher in the region where \vec{Y}_{mse} points toward Mars, than in the region where it points away. This is consistent with the work of Dubinin *et al.* (2008). They in-

deed show that the induced magnetosphere of Mars is more exposed to solar wind protons on the side where the upstream IMF vector points toward the planet than on the opposite side. Around the $+\vec{E}_{sw}$ pole, the pattern is irregular on the dawn side, and more regular on the dusk side, and the flux is higher on the dusk side of the $+\vec{E}_{sw}$ pole than on the dawn side (panel (a)). Around the $-\vec{E}_{sw}$ pole, the opposite is true: the pattern is more regular on the dawn side, and irregular on the dusk side. These dawn-dusk asymmetries are seen in the two maps of solar wind protons and planetary protons as well (panel (b) and (c)), and also for different energy ranges (panels (d)–(f)). Thus, the Parker spiral makes the precipitation pattern more complicated. Finally, when looking at the subsolar point (0° , 0°) at different altitudes, we see that the solar wind protons dominate the precipitating flux at high altitude (Fig. 3), while the exospheric protons become significant at lower altitude (Fig. 5).

3.4 Precipitating proton spectra

We have also derived precipitating proton spectra on the outer and inner spheres, to check the altitude dependence. We return to the simple $B_x = 0$ case. The spectra are shown in Fig. 6. The energy flux is plotted for three SZA ranges: 0° – 60° (subsolar region), 60° – 120° (terminator region) and 120° – 180° (nightside). The dashed lines correspond to the outer sphere (560 km altitude) and the solid lines to the inner sphere (240 km altitude). The thick black curve is the upstream solar wind spectrum used as input: a Maxwellian distribution which peaks at ~ 1.2 keV.

3.4.1 Solar wind and planetary protons contributions In the first row we compare the contribution from the solar wind protons (black) and planetary protons (grey) to the precipitating spectra. The spectra are averaged over the $\pm\vec{E}_{sw}$ hemispheres.

The energy fluxes decrease as we go from the outer sphere to the inner sphere. It drops more drastically at low energy ($E < 100$ eV) than at higher energy, when the altitude decreases. One can also see that the decrease at $E < 100$ eV is larger in the subsolar region (panel (a)) than at higher SZA. The peak in the energy spectra is well pronounced in the subsolar region (panel (a)), and vanishes as we go to the terminator (panel (b)) and the nightside (panel (c)). The energy peak is also more pronounced at low altitude than at high altitude, for a given spatial region. The energy peak also shifts to higher energy as we go down in altitude on dayside (panel (a)). One can see that the low energy part ($E < 100$ eV) is dominated by cold new-born planetary protons. The domination of the low energy population by the planetary protons becomes more evident as the altitude decreases in the subsolar region (panel (a)). By contrast, the domination of the low energy population by the planetary protons becomes less evident as the altitude decreases for the terminator and nightside (panels (b) and (c)). On the outer sphere, indeed, the exospheric proton peak level is by contrast higher than the solar wind peak on nightside (panel (c)). The higher energy part ($E > 400$ eV) is dominated by solar wind protons until 4–5 keV; above this energy, the spectrum becomes dominated again by the planetary protons, accelerated by the convection electric field. The solar wind spectrum peaks at a higher energy and at a higher level than the planetary proton spectrum, on the dayside and at

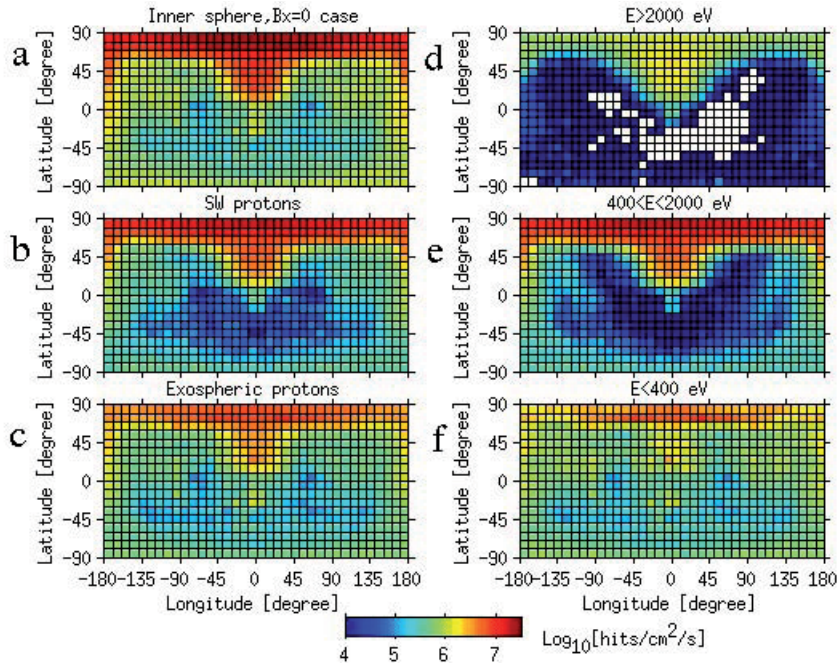


Fig. 4. Same format as Fig. 3. Inner sphere at $r = 3636$ km for the $B_x = 0$ simulation.

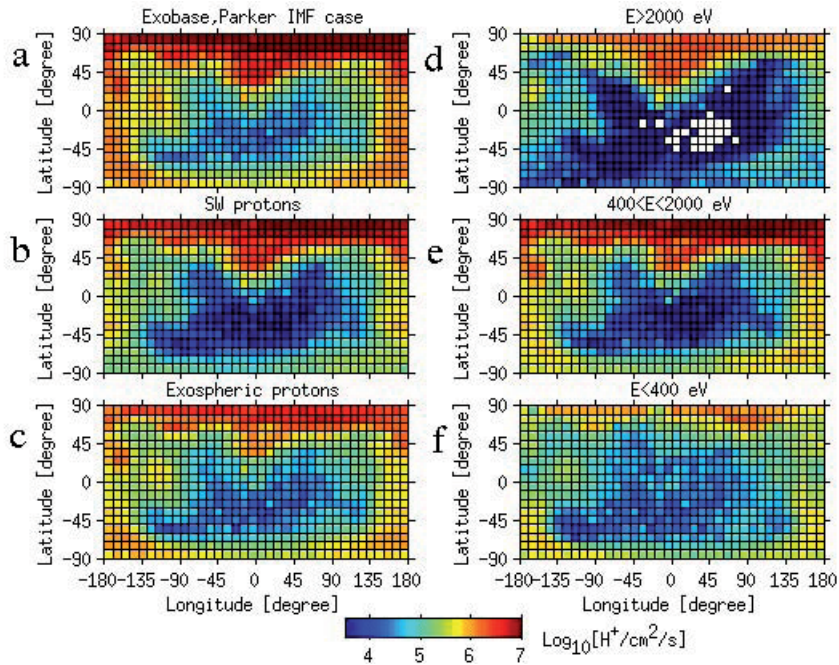


Fig. 5. Same format as Fig. 3. Exobase at $r = 3600$ km for the Parker IMF simulation.

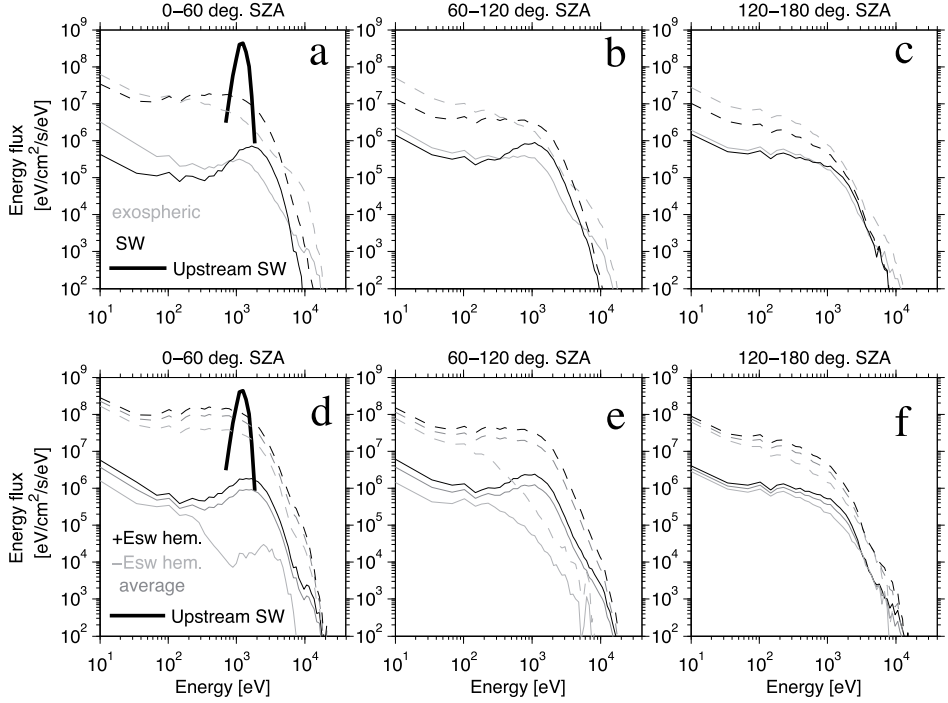


Fig. 6. Energy spectra of downgoing protons. The dashed lines and solid lines correspond to the outer sphere at $r = 3960$ km and inner sphere at $r = 3636$ km, respectively. The spectra are averaged in different solar zenith angle intervals. In panels (a)–(c), the black and grey lines correspond to the solar wind protons and exospheric protons, respectively, and the curves are averages over the $\pm E_{sw}$ hemispheres. In panels (d)–(f), the black, light grey and dark grey lines correspond to the $+E_{sw}$, $-E_{sw}$ hemispheres and the average of both hemispheres, respectively, for all protons. The upstream solar wind spectrum is shown as a thick black line in panel (a).

the terminator (panels (a) and (b)).

On the outer sphere, the spectrum of solar wind protons peaks at a lower energy than the upstream solar wind, but on the inner sphere, it peaks at a higher energy than the upstream solar wind (panels (a) and (b)). On the outer sphere, the exospheric proton spectrum also peaks at an energy lower than the upstream solar wind, but on the inner sphere, it peaks at the same energy as the upstream solar wind (panels (a) and (b)). On the dayside, the precipitating solar wind spectrum energy peak is at $\sim 2 \cdot 10^7$ eV $\text{cm}^{-2} \text{s}^{-1} \text{eV}^{-1}$ on the outer sphere and is $\sim 1 \cdot 10^6$ eV $\text{cm}^{-2} \text{s}^{-1} \text{eV}^{-1}$ on the inner sphere (panel (a)), respectively 1 and 2 orders of magnitude lower than the upstream solar wind energy flux ($4 \cdot 10^8$ eV $\text{cm}^{-2} \text{s}^{-1} \text{eV}^{-1}$). The precipitating solar wind spectrum, averaged over a given sphere, would peak at the mean energy of the upstream solar wind.

The flux decrease seen at low energy is more drastic in the subsolar region when the altitude decreases. On the dayside, the high energy population accelerates as we approach Mars. This can be related to the removal of the low energy population. The low energy population tends to be dominated by planetary protons. On the dayside, the contribution of the planetary protons to the low energy population is, relatively to the solar wind, larger at lower altitudes than at high altitudes, because new-born planetary protons

are massively created at lower altitudes in the corona on the dayside. At the terminator and on the nightside, the reverse is true: the contribution of the planetary protons to the low energy population is, relatively to the solar wind, lower at low altitudes than at high altitudes. This is because it is difficult to create planetary protons at low altitude in Mars's shadow. At very high energies (above 4–5 keV), the contribution of planetary protons to the precipitation becomes more important than that of the solar wind. The planetary population has been accelerated by the convection electric field. The maximum energy gain is $4E_{sw}(\sin(\theta))^2$, where E_{sw} is the upstream solar wind bulk energy and θ is the angle between the solar wind velocity and the IMF. For this simulation, $\theta = 90^\circ$ and $E_{sw} \sim 1.2$ keV, so the maximum energy gain is ~ 5 keV. Planetary protons are also seen with even higher energies (bump around 10 keV). We interpret these exospheric protons with energies more than $4E_{sw}$ as protons picked up upstream of the bow shock and accelerated by reflections at the Martian bow shock (Dubinin *et al.*, 2006). Test-particle simulations (e.g. Dubinin *et al.*, 1994), which follow the ions motion under electromagnetic fields, have shown that exospheric picked up protons are reflected by the bow shock potential. In principle, hybrid simulations, which also treat ions as particles, can model how some of the ions are accelerated and scattered at the

bow shock back to the upstream solar wind.

3.4.2 Energy spectra organized by the convection electric field In the second row of Fig. 6, we investigate the relationships between the precipitating proton spectra and the $\pm \vec{E}_{sw}$ hemispheres. The panels (d), (e) and (f) show the energy spectra, in the same format as in panels (a)–(c), but for the $+\vec{E}_{sw}$ hemisphere (black), the $-\vec{E}_{sw}$ hemisphere (light grey) and the average (dark grey). These spectra correspond to all protons (solar wind and exospheric origins).

The two populations together cause the average spectrum on the outer sphere to peak at an energy flux comparable ($1 \cdot 10^8 \text{ eV cm}^{-2} \text{ s}^{-1} \text{ eV}^{-1}$) to the solar wind energy peak on dayside (panel (d)). At the terminator and on the nightside (panels (e) and (f)), the peak is lower. On the inner shell, the \vec{E}_{sw} asymmetry is the most pronounced on the dayside (panel (d)), and least pronounced on the nightside (panel (f)). On the outer shell, the \vec{E}_{sw} asymmetry is most pronounced at the terminator (panel (e)). This is consistent with the strong \vec{E}_{sw} hemisphere asymmetry noticed in Fig. 3. On the inner shell, the peak of the energy spectrum on the $-\vec{E}_{sw}$ hemisphere exists on dayside (panel (d)), but disappears at the terminator and on the nightside (panels (e) and (f)). On the inner shell, the peak in the $+\vec{E}_{sw}$ hemisphere spectrum persists on the dayside and the terminator (panels (d) and (e)).

On the inner shell, the low energy population plays a dominant role in the $-\vec{E}_{sw}$ hemisphere spectrum. Also, on the inner shell on the dayside and at the terminator (panels (d) and (e)), the $+\vec{E}_{sw}$ hemisphere spectrum gets a significant contribution from both the low energy population and the higher energy population, which have their own preferred area of deposition (see panels 4(d)–(f)).

The average precipitating spectrum is dominated by protons of energy greater than a few hundred eV, in qualitative agreement with studies of Brecht (1997) and Kallio and Janhunen (2001).

4. Discussion

The analysis shows that the energy and particle proton fluxes (solar wind and exospheric origins together), which reach the exobase on the dayside are $\sim 9.3 \cdot 10^{26} \text{ eV s}^{-1}$ and $\sim 6.4 \cdot 10^{23} \text{ H}^+ \text{ s}^{-1}$, respectively. If only solar wind protons are taken into account, the energy flux is $\sim 7.7 \cdot 10^{26} \text{ eV s}^{-1}$ and the particle flux is $\sim 4.0 \cdot 10^{23} \text{ H}^+ \text{ s}^{-1}$. Thus, the solar wind protons account for 62% of the precipitating proton flux on dayside on the inner boundary. We can consider separately the low energy and the higher energy populations. Taking all protons with energies below the solar wind bulk energy, the planetary protons account for 55% and the solar wind protons for 45% of the precipitating population at the inner boundary. When taking all protons with energies above the solar wind bulk energy, the two populations account for 27% and 73% of the population, respectively.

These precipitating energy and particle fluxes of solar wind protons correspond respectively to $\sim 1\%$ of the energy flux and $\sim 1\%$ of the particle flux of the upstream solar wind protons (if the upstream solar wind could directly hit the exobase).

Now, we compare our results expressed in a SZA form,

with the figure 6 from Kallio and Janhunen (2001). We use a 15° resolution. The precipitating proton flux, averaged over the $\pm \vec{E}_{sw}$ hemispheres, is shown as a function of SZA in Fig. 7. All protons are considered: solar wind and exospheric origins. The particle flux (panel (a)) and energy flux (panel (b)) are summarized at the exobase in the Parker spiral case at 207 km altitude (solid line with crosses), the inner sphere at 240 km altitude (solid line) and outer sphere at 560 km altitude (dashed line) in the $B_x = 0$ case. This way of presenting the precipitating flux washes out the eventual dawn-dusk asymmetries. The reader has to keep in mind that the flux that would be derived at the exobase for the $B_x = 0$ case would be slightly different from the flux shown by the solid-and-crosses line, because of different IMF magnitudes (3 nT and 3.5 nT for the $B_x = 0$ and Parker IMF cases respectively).

On the outer sphere, the flux is largest at subsolar point ($\sim 3 \cdot 10^8 \text{ hits cm}^{-2} \text{ s}^{-1}$ and $\sim 3 \cdot 10^{11} \text{ eV cm}^{-2} \text{ s}^{-1}$) and decreases toward the nightside. On the outer sphere, at the terminator, the fluxes are $\sim 3 \cdot 10^7 \text{ hits cm}^{-2} \text{ s}^{-1}$ and $\sim 2 \cdot 10^{10} \text{ eV cm}^{-2} \text{ s}^{-1}$. The flux values at subsolar point on the outer sphere are larger than the upstream solar wind particle flux ($\sim 1 \cdot 10^8 \text{ H}^+ \text{ cm}^{-2} \text{ s}^{-1}$) and energy flux ($\sim 2 \cdot 10^{11} \text{ eV cm}^{-2} \text{ s}^{-1}$). However, this is not a problem since the flux on the outer sphere contains contributions from both the solar wind and the planetary protons. It implies that the exospheric proton production is significant at low SZA, and that it locally contributes to the precipitation.

The overall flux has decreased, by one order of magnitude at the terminator and nightside and by 2 orders of magnitude on the dayside when we reach the inner sphere. On the inner sphere, the particle flux is $\sim 1 \cdot 10^6 \text{ hits cm}^{-2} \text{ s}^{-1}$ and the energy flux is $\sim 1 \cdot 10^9 \text{ eV cm}^{-2} \text{ s}^{-1}$ at the subsolar point, while they reach $\sim 2 \cdot 10^6 \text{ hits cm}^{-2} \text{ s}^{-1}$ and $\sim 2 \cdot 10^9 \text{ eV cm}^{-2} \text{ s}^{-1}$ respectively at the terminator.

At the exobase, there is a small change in flux compared to the inner sphere on the nightside and at the terminator, but on the dayside, the flux again decreases by one order of magnitude. At the exobase, the fluxes become $\sim 1 \cdot 10^5 \text{ H}^+ \text{ cm}^{-2} \text{ s}^{-1}$ and $\sim 1 \cdot 10^8 \text{ eV cm}^{-2} \text{ s}^{-1}$ at the subsolar point, and $\sim 1 \cdot 10^6 \text{ H}^+ \text{ cm}^{-2} \text{ s}^{-1}$ and $\sim 1 \cdot 10^9 \text{ eV cm}^{-2} \text{ s}^{-1}$ at the terminator. Hence, at the inner boundary, the fluxes (solar wind and planetary protons combined) have decreased by 3 orders of magnitude compared to the upstream solar wind.

Our results show differences compared to the work by Kallio and Janhunen (2001). Our integrated precipitating proton particle flux at the exobase is about 1% of the total solar wind flux, while they get almost 50%. In contrast to their paper, our proton fluxes are also severely reduced at the subsolar point close to Mars. At the subsolar point our precipitating particle fluxes are up to 3 orders of magnitude lower than the fluxes shown by Kallio and Janhunen (2001). Finally, we note that our energy fluxes on the dayside are comparable to what is obtained by Brecht (1997), except in the subsolar region where he gets an energy flux value of $\sim 1 \cdot 10^9 \text{ eV cm}^{-2} \text{ s}^{-1}$ for nominal solar wind conditions.

There are several possible reasons for these differences. The solar wind input parameters are not a likely reason, because Kallio and Janhunen (2001) used a solar wind bulk velocity quite similar to ours (they used $[-400, 0, 0]$

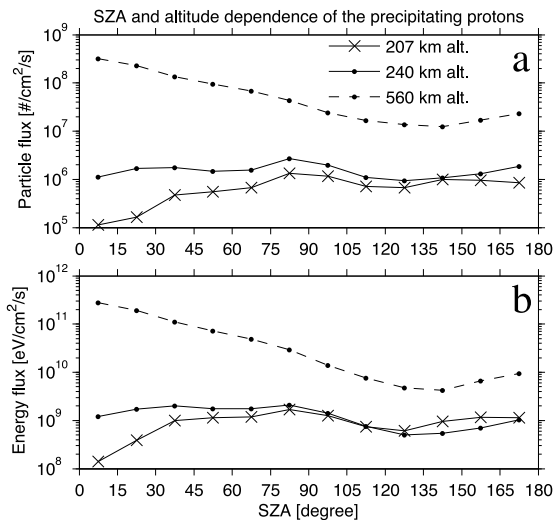


Fig. 7. Precipitating proton particle flux (panel (a)) and energy flux (panel (b)) function of SZA. The fluxes are averaged over the $\pm \bar{E}_{sw}$ hemispheres. The outer sphere at $r = 3960$ km (dashed line), the inner sphere at $r = 3636$ km (solid line) for the $B_x = 0$ case are shown, as well as the exobase at $r = 3600$ km for the Parker IMF case (solid line and crosses).

km s^{-1}), while the solar wind density and the IMF were identical to ours for the $B_x = 0$ simulation. In the previous work, the neutral oxygen corona was spherically symmetric like ours, but had a scale height of 1100 km and a manually given O^+ photoionization production rate within the simulation box of $\sim 6 \cdot 10^{23} s^{-1}$. In the present work, the oxygen corona is modeled by three scale heights and the ion production rate is derived by using a photoionization rate (see Section 2). Planetary ions, which are originating from the ionosphere, are also modeled in a more realistic way than by Kallio and Janhunen (2001). In our study, the emission has a $\cos(SZA)$ dependence while in their study the ions were emitted homogeneously on the dayside. The $\cos(SZA)$ dependence increases the relative density of planetary ions near the subsolar point compared to the previous study, which may also affect the strength of the magnetic barrier and the properties of the ion composition boundary, which separates the solar wind and planetary ions. In this study, the model also contains background electron density, which mimics the role of the density of planetary ions that are not included in the hybrid model.

We note that neither the current model nor the 2001 study contain a self-consistent ionosphere, but they both have a changing grid size as the altitude decreases (with similar grid sizes in both codes). Hence, these two features do not explain the differences in the results for low altitude.

The number of particles per cell is increased in the present study. In addition, the numerical code used in the present work gives a much less disturbed magnetic barrier near the grid refined boundaries and a more clearly defined bow shock (see Fig. 2) than in the old numerical code used by Kallio and Janhunen (2001). We also note that the size of the region where the magnetic field magnitude is high (>20 nT) is larger and the proton density near Mars is

smaller, compared with the previous work. The reduced proton density, resulting from a stronger magnetic barrier and a stronger bow shock, should result in fewer protons reaching the exobase.

The new model also includes processes that were not included in the previous work: charge exchange reactions between protons and neutral atoms, and electron impact ionization. The electron impact ionization reactions and the charge exchange reactions between the neutral exospheric atoms and the solar wind plasma play in an important role in the formation of the Martian plasma boundaries, in particular the magnetic barrier (Jin *et al.*, 2006). This shows the necessity to implement exospheric processes.

It is said before that 62% of the proton deposition on dayside comes from the solar wind; the rest comes from the exosphere. The photoionization and the electron impact ionization create additional exospheric protons, but do not necessarily result in an increased precipitation since these ions are created with low energies and small gyroradii. The charge exchange of the solar wind protons with neutral hydrogen does not change the number of protons. It replaces relatively high energy solar wind protons by new-born cold exospheric ions which are less likely to pass the magnetic barrier on dayside. These cold ions are then picked up and accelerated by the solar wind convection electric field, and may again charge exchange with the neutral coronae, giving either new-born exospheric protons or O^+ ions. The same reasoning applies to the charge exchange of the exospheric protons with the coronae.

The charge exchange of the incoming protons with the neutral atoms of the oxygen corona accounts for a part of the removal of the proton population at low SZA. For example, if the density of the neutral coronae is high, then the charge exchange of the solar wind with the low altitude oxy-

gen corona can attenuate the proton density by a few tens of percent in the subsolar region close to the obstacle (Kallio *et al.*, 1997). In the model, the high production rate of oxygen ions at low SZA leads to a region dominated by planetary ions. A so-called Ion Composition Boundary forms, which separates the oxygen plasma and the incoming protons. Note that the mass loading of the solar wind flow by the O^+ ions from the oxygen corona will also push the bow shock further from Mars, reducing the proton precipitation (Kallio and Janhunen, 2001). It is noted that only an oxygen corona was present in the study by Kallio and Janhunen (2001), while the present study uses both oxygen and hydrogen coronae. The presence of both exospheres in the new model may slow down the solar wind more strongly. One consequence is that the decelerated solar wind protons have smaller gyroradii and do not penetrate the magnetic barrier as effectively.

Both our model and the model used by Kallio and Janhunen (2001) have an absorbing boundary condition for the inner boundary. Thus, the incoming protons are not reflected, but absorbed. In the paper by Kallio and Janhunen (2001), a hybrid code is used above the exobase, and a Monte Carlo simulation is used below. This means that in their model, the protons are not artificially cut away from the whole simulation, but are treated as particles colliding with atmospheric neutrals. These collisions backscatter the ions (Kallio and Barabash, 2001). The ions may hit the inner boundary a few times more, instead of being immediately removed after one hit on the inner boundary. We cannot completely exclude the effect of the particle removal introduced by our inner boundary (see Fig. 1) on the precipitation pattern at altitudes lower than the outer sphere. However, this removal should be in proportion to the number of particle hits onto the exobase. In the case where the ions are taken away when hitting the inner boundary, one would expect that if the number of incoming particles to the exobase is larger on the dayside than elsewhere, the inner boundary will remove the hits in the same proportion all over the planet. On the other hand, if ion-neutral collisions are implemented at the exobase, one would also expect that if the incoming proton flux is largest on dayside, the proton flux at the exobase will be still largest in that region, after particle backscattering.

Our analysis suggests that a process is removing protons at low altitude on the dayside, between the outer sphere and the exobase. This geographically localized removal of protons cannot be explained by the way the protons are treated at the exobase (either cut away from the simulation or scattered by collisions). We think that this process is due to the finite gyroradius effect.

The strong magnetic field in the magnetic barrier, especially at low SZA, can deflect H^+ ions with a small gyroradius, preventing them from reaching the exobase. For instance, at the altitude of the exobase, the magnetic field from the simulation has a value of ~ 45 nT at low SZA. In this field, a 100 eV proton has a gyroradius of 32 km, while a 5000 eV proton has a gyroradius of 227 km. This can be compared to the size of the region where the magnetic field magnitude is largest: ~ 500 km at low SZA (panel 2(b)). It is noted that the inner sphere (240 km altitude) is

located inside the magnetic barrier, while the outer sphere is located slightly above (560 km altitude). The low energy protons, which have passed the altitude of the outer sphere will thus enter the magnetic barrier, where they can be deflected and only a few reach this region. As the SZA increases, the magnetic field magnitude decreases and the access becomes easier for low energy protons, as seen in the proton maps. This interpretation is supported by the work of Shematovich *et al.* (2011). As said in Section 2, they showed that the stronger the induced magnetic field in the Martian atmosphere, the more incoming solar wind protons is backscattered. They found that a 50 nT horizontal magnetic field (typical value measured in the magnetic barrier) shields almost completely the atmosphere from downward proton fluxes. In addition, the morphology of the magnetic field on the dayside and on the nightside is not similar. On the dayside there is an horizontal magnetic field in a wide altitude range (the magnetic barrier) while on the nightside the magnetic field starts to form the magnetic tail lobes where the B_z -component (and, consequently, vertical \vec{B}) is important. Therefore, the motion of ions toward Mars (easily along \vec{B} and difficult perpendicular to \vec{B}) is not identical at the dayside and nightside.

Now, we discuss the effect of the energy of the precipitating protons on the \vec{E}_{sw} asymmetry. It is seen from the proton maps that at low altitude on the dayside, the low energy protons dominate the precipitation onto the $-\vec{E}_{sw}$ hemisphere while the precipitation onto the $+\vec{E}_{sw}$ hemisphere is dominated by protons with higher energies. This can be explained by the Lorentz force. In Eq. (2), the pressure gradient term is of minor importance for the precipitating protons in the energy range analyzed in this study. Only the $\vec{v} \times \vec{B}$ and $-\vec{U}_e \times \vec{B}$ terms need to be considered. The proton velocity $|\vec{v}_i|$ can differ from the electrons bulk velocity \vec{U}_e in all regions where there is a substantial amount of oxygen ions (i.e. where the mass loading is important) and where there are strong electric currents (like in the cross tail current sheet). The low energy protons (velocity $|\vec{v}_i| \ll |\vec{U}_e|$) are affected by the $-\vec{U}_e \times \vec{B}$ electric field which accelerates them toward Mars on the $-\vec{E}_{sw}$ hemisphere. The higher energy protons (velocity $|\vec{v}_i| \gg |\vec{U}_e|$) are affected by the $\vec{v} \times \vec{B}$ electric field which accelerates them toward Mars on the $+\vec{E}_{sw}$ hemisphere (Kallio and Janhunen, 2001). Recalling that the draped magnetic field is stronger on the side of the planet aligned with the solar wind convection electric field ($+\vec{E}_{sw}$ hemisphere), one may think that it is difficult for low energy protons to be deposited on the $+\vec{E}_{sw}$ hemisphere, because of their small gyroradius.

The low energy population is dominated by the pickup planetary protons. Ions created very close to the exobase will have not much room to be accelerated until they reach the inner boundary. These ions are recorded as a very low energy population at the exobase. They precipitate locally, close to their place of production. On the other hand, planetary protons created upstream from the bow shock have space to gyrate. They will be accelerated and produce a more asymmetric precipitation pattern. As a consequence, the \vec{E}_{sw} asymmetry on dayside is reduced for the low energy population, but enhanced for the higher energy population.

On the nightside, the magnetic field is weaker and the

field lines extend vertically (tailward), such that the low energy protons can propagate more easily to low altitude. The low values of $|\vec{B}|$ and $|\vec{U}_c|$, and the situation of a bulk velocity parallel with the magnetic field lines $\vec{U}_c//\vec{B}$, decrease the convection electric field $|\vec{U}_c \times \vec{B}|$ on the nightside (e.g. Kallio *et al.*, 2010). This allows the protons to move more freely, and that may be the reason for the reduction of the \vec{E}_{sw} asymmetry on the inner sphere on the nightside.

The precipitating protons deposit energy into the atmosphere, but the atmosphere also absorbs energy from the solar radiation. To compare the two energy sources, we note that the solar radiation absorption at Mars for solar minimum conditions (height-integrated in the altitude range 100–240 km) is $1.35 \cdot 10^{11}$ eV cm⁻² s⁻¹ (Kallio *et al.*, 1997). The average precipitating energy flux from our model is $\sim 1 \cdot 10^8$ eV cm⁻² s⁻¹ at subsolar point at the exobase. Hence, we conclude that the energy transfer to the dayside exobase from the precipitating protons is up to 3 orders of magnitude less than the energy transfer from solar radiation absorption. Under the conditions specified for the simulation, the precipitating proton energy flux can not compete with the energy flux from the solar radiation on the dayside. On the nightside, the atmosphere is in the shadow and the proton precipitation heating becomes more important than the solar heating, in agreement with Brecht (1997) and Kallio and Janhunen (2001).

In the future, the present results should be compared to an observational statistical study of proton precipitation, which is now in progress, but this comparison is saved for a future publication.

5. Summary and Conclusions

This paper reports the first investigation of the altitude dependence of the pattern of proton precipitation onto the Martian atmosphere, using the HYB-Mars hybrid code. We also report the first study of the relative importance of solar wind versus planetary protons in term of proton precipitation, and emphasize the role of the proton energy to determine the precipitation pattern.

Overall, our study confirms the asymmetry of the proton precipitation due to the convection electric field, and its role in the energy balance compared to the UV flux, shown by Brecht (1997) and Kallio and Janhunen (2001). An important new finding is the strong altitude dependence of the proton precipitation: the flux of precipitating protons is reduced substantially when crossing the magnetic barrier near Mars. The study suggests that the Martian induced magnetosphere protects the upper atmosphere effectively against proton precipitation. Finally, we find that the solar wind protons contribute to 62% of the proton precipitation on the dayside exobase in our simulation, which means that the hydrogen exosphere can be a significant source of precipitating protons.

Concerning the atmospheric energy balance, we note that on the dayside the energy transfer to the Martian atmosphere from proton precipitation is up to 3 orders of magnitude lower than the contribution from solar radiation. On the nightside, however, precipitating protons are a significant heat source compared to the solar radiation.

Future modeling work would be to study solar wind

He⁺⁺ precipitation patterns on Mars. The analysis also implies that new high spatial resolution 3D hybrid simulations with a self-consistent ionosphere should be performed in the future in order to resolve accurately the region near the Martian exobase. The inclusion of the crustal magnetic anomalies would be also of interest because of the possible screening of the Martian atmosphere by the mini-magnetospheres.

Acknowledgments. C. D. and G. S. are supported by the National Graduate School of Space Technology of the Luleå Technical University. Figure 2 is made using the VisIt open source visualization tool. The authors thank Arnaud Valeille, University of Michigan, for providing the hot hydrogen and hot oxygen profiles used in the hybrid model.

References

- Acuña, M. H. *et al.*, Magnetic field and plasma observations at Mars: Preliminary Results of the Mars Global Surveyor Mission, *Science*, **279**, 5357, 1676–1680, 1998.
- Acuña, M. H. *et al.*, Global distribution of crustal magnetization discovered by the Mars Global Surveyor MAG/ER experiment, *Science*, **284**, 5415, 790–793, 1999.
- Brain, D. A. *et al.*, The magnetic field draping direction at Mars from April 1999 through August 2004, *Icarus*, **182**(2), 464–473, 2006.
- Brecht, S. H., Magnetic asymmetries of unmagnetized planets, *Geophys. Res. Lett.*, **17**(9), 1243–1246, 1990.
- Brecht, S. H., Solar wind proton deposition into the Martian atmosphere, *J. Geophys. Res.*, **102**(A6), 11,287–11,294, 1997.
- Brecht, S. H. and S. A. Ledvina, Control of ion loss from Mars during solar minimum, *Earth Planets Space*, **64**, this issue, 165–178, 2012.
- Chaufray, J. Y. *et al.*, Observation of the hydrogen corona with SPICAM on Mars Express, *Icarus*, **195**(2), 598–613, 2008.
- Cravens, T. E. *et al.*, Electron Impact Ionization in the vicinity of Comets, *J. Geophys. Res.*, **92**(A7), 7341–7353, 1987.
- Diéval, C. *et al.*, A case study of proton precipitation at Mars: Mars Express observations and hybrid simulation, *J. Geophys. Res.*, 2011 (submitted).
- Dubinin, E. *et al.*, Mass-loading asymmetry in upstream region near Mars, *Geophys. Res. Lett.*, **21**(24), 2769–2772, 1994.
- Dubinin, E. *et al.*, Hydrogen exosphere at Mars: Pick-up protons and their acceleration at the bow shock, *Geophys. Res. Lett.*, **33**, L22103, 2006.
- Dubinin, E. *et al.*, Asymmetry of plasma fluxes at Mars: ASPERA-3 observations and hybrid simulations, *Planet. Space Sci.*, **56**, 832–835, 2008.
- Fedorov, A. *et al.*, Structure of the martian wake, *Icarus*, **182**(2), 329–326, 2006.
- Fulle, M. *et al.*, Discovery of the atomic iron tail of comet McNaught using the heliospheric imager on STEREO, *Astrophys. J.*, **661**, 93–96, 2007.
- Jin, H. *et al.*, Effects of charge exchange and electron impact ionization on the formation of the magnetic pileup boundary at Mars, *J. Geophys. Res.*, **111**, A05306, 2006.
- Kallio, E. and S. Barabash, On the elastic and inelastic collisions between the precipitating hydrogen atoms and Martian atmospheric neutrals, *J. Geophys. Res.*, **105**(A11), 24,973–24,996, 2001.
- Kallio, E. and P. Janhunen, Atmospheric effects of proton precipitation in the Martian atmosphere and its connection to the Mars-solar wind interaction, *J. Geophys. Res.*, **106**(A4), 5617–5634, 2001.
- Kallio, E. and P. Janhunen, Modelling the solar wind interaction with Mercury by a quasineutral hybrid model, *Ann. Geophys.*, **21**(11), 2133–2145, 2003.
- Kallio, E. *et al.*, Charge exchange near Mars: The solar wind absorption and energetic neutral atom production, *J. Geophys. Res.*, **102**(A10), 22,183–22,197, 1997.
- Kallio, E. *et al.*, On the properties of O⁺ and O₂⁺ ions in a hybrid model and in Mars Express IMA/ASPERA-3 data: A case study, *Planet. Space Sci.*, **56**, 1204–1213, 2008.
- Kallio, E. *et al.*, Oxygen ion escape at Mars in a hybrid model: High energy and low energy ions, *Icarus*, **206**, 152–163, 2010.
- Lundin, R. *et al.*, Solar wind-induced atmospheric erosion at Mars: First results from ASPERA-3 on Mars Express, *Science*, **305**, 5692, 1933–1936, 2004.
- Lundin, R. *et al.*, On the relation between plasma escape and the Martian crustal magnetic field, *Geophys. Res. Lett.*, **38**, L02102, 2011.
- Ma, Y. *et al.*, Three-dimensional, multispecies, high spatial resolution

- MHD studies of the solar wind interaction with Mars, *J. Geophys. Res.*, **109**, A07211, 2004.
- Nagy, A. F. *et al.*, The plasma environment of Mars, *Space Sci. Rev.*, **111**, 33–114, 2004.
- Nilsson, H. *et al.*, Heavy ion escape from Mars, influence from solar wind conditions and crustal magnetic fields, *Icarus*, **215**(2), 475–484, 2011.
- Shematovich, V. I. *et al.*, Protons and hydrogen atoms transport in the Martian upper atmosphere with an induced magnetic field, *J. Geophys. Res.*, **116**, A11320, 2011.
- Stenberg, G. *et al.*, Observational evidence of alpha particle capture at Mars, *Geophys. Res. Lett.*, **38**, L09101, 2011.
- Zhang, M. H. G., J. G. Luhmann, and A. J. Kliore, An Observational Study of the Nightside Ionospheres of Mars and Venus with Radio Occultation Methods, *J. Geophys. Res.*, **95**(A10), 17095–17102, 1990.

C. Diéval (e-mail: catherine@ifr.se), E. Kallio, G. Stenberg, S. Barabash, and R. Jarvinen

PAPER IV

A statistical study of proton precipitation onto the Martian upper atmosphere: Mars Express observations

C. Diéval^{1,2}, G. Stenberg¹, H. Nilsson¹ and S. Barabash¹

¹Swedish Institute of Space Physics, Box 812, SE-98128, Kiruna, Sweden

²Division of Space Technology, Department of Computer Science, Electrical and Space Engineering, Luleå University of Technology, SE-91187, Luleå, Sweden

Author for correspondence: catherine@irf.se

Abstract. Due to the small size of the Martian magnetic pile-up region, especially at the subsolar point, heated protons with high enough energy can penetrate the induced magnetosphere boundary (IMB) without being backscattered, i.e., they precipitate. We present a statistical study of the downgoing proton fluxes measured in the Martian ionosphere by the Analyzer of Space Plasma and Energetic Atoms (ASPERA-3) experiment onboard the Mars Express spacecraft. We find that on the dayside, the events of proton penetration occur during 3% of the observation time: the precipitation is an intermittent phenomenon. The proton events carry on average ~0.2% of the incident solar wind flux. Therefore, the induced magnetosphere is an effective shield against the magnetosheath protons. The events are more frequent during fast solar wind conditions than during slow solar wind conditions. The sporadic proton penetration is thought to be caused by transients in the magnetosheath/solar wind. The precipitating flux is higher on the dayside than on the nightside, and its spatial deposition is controlled by the solar wind convective electric field. The events seem not to be correlated to the crustal magnetic anomalies. The particle and energy fluxes vary in the range 10^4 - 10^6 $\text{cm}^{-2}\text{s}^{-1}$ and 10^7 - 10^9 $\text{eVcm}^{-2}\text{s}^{-1}$, respectively. The corresponding heating for the dayside atmosphere is on average negligible compared to the solar extreme ultraviolet heating, although the intermittent penetration may cause local ionization. The median net precipitating proton particle flux to the dayside ionosphere, corrected by the occurrence frequency, is estimated as $1.2 \cdot 10^{21} \text{ s}^{-1}$.

1 Introduction

Mars does not have a global planetary magnetic field. As a consequence, the solar wind flow, carrying the interplanetary magnetic field (IMF), can directly encounter the Martian ionosphere. The moving IMF generates currents in this conductive obstacle. The magnetic field associated with the currents, diverts the solar wind. A magnetic barrier (magnetic pile-up region) is formed through the superposition of the induced magnetic fields and the partial diffusion of the IMF lines into the ionosphere. The IMF lines drape around the dayside of the planet, slip over the terminator and extend into a magnetotail on

the nightside. An induced magnetosphere forms. Localized crustal magnetic anomalies, mainly present in the Southern hemisphere, locally modify the Mars-solar wind interaction [e.g. *Acuña et al.*, 1998; 1999]. The reader can refer to for example the review paper of *Nagy et al.* [2004].

The magnetic barrier is limited from below by the photoelectron boundary (PEB) and from above by the induced magnetosphere boundary (IMB). The PEB marks the presence of ionospheric photoelectron with energy peaks at 20-30 eV [*Frahm et al.*, 2006], generated by photoionization of atmospheric CO_2 by the

solar 304 Å He line. The IMB is a boundary that is analogous to a magnetopause where the magnetic field strongly increases and the solar wind flux terminates.

However, hybrid models (which treat the ions as particles and the electrons as a massless charge-neutralizing fluid) predict that the IMB is permeable to heated solar wind protons with high enough energies [Brecht, 1997; Kallio and Janhunen, 2001; Diéval et al., 2012a, 2012b]. This situation arises because in the subsolar magnetosheath, the hot plasma (proton temperature of 40-60 eV [Fränz et al., 2006]) includes populations of protons with high energies and large gyroradii mv/qB . B is the magnetic field strength, m , v and q are respectively the mass, velocity and charge of the proton. These high energy protons can thus penetrate the magnetic barrier without being deflected away and can enter the upper atmosphere. Modeling studies demonstrate that the precipitating solar wind protons contribute to ionizing and heating the atmosphere, and they are neutralized by charge exchange reactions with the atmospheric neutrals [Kallio and Barabash, 2001; Kallio and Janhunen, 2001; Shematovich et al.; 2011]. The incident flux adds mass and energy to the atmosphere.

Observations of solar wind proton entries into the dayside Martian atmosphere have been reported in the literature [Lundin et al., 2004; Diéval et al., 2012b]. The study of Diéval et al. [2012b] is a detailed analysis of the data from one orbit of the Mars Express (MEX) spacecraft, with observations of downgoing proton fluxes in the dayside ionosphere. Using hybrid simulations, the authors have determined that the measured protons originate both from the solar wind and the upper neutral hydrogen atmosphere. They attributed the observed proton precipitation to the gyroradius effect.

However, there is no statistical study available so far providing observation of proton precipitation or any investigation of proton precipitation on the nightside. Hybrid models predict proton precipitation on the

nightside and show significant atmospheric effects there in the absence of solar radiation [Brecht, 1997; Kallio and Janhunen, 2001; Diéval et al., 2012a]. The purpose of this paper is to make an observational statistical study of the downgoing protons fluxes at low altitude around Mars, both on the dayside and on the nightside. We use data from the Analyzer of Space Plasma and Energetic Atoms (ASPERA-3) experiment onboard MEX. The paper compares the observations with model predictions.

Section 2 describes the instruments used in this study and the data selection, and it presents an example of proton penetration. Section 3 presents the spatial distribution and characteristics of the precipitating protons. Section 4 investigates the dependence of the precipitation on the solar wind conditions, the IMF direction and the crustal magnetic anomalies. Section 5 treats the net flux of the precipitation. Finally, Section 6 discusses the results.

2 Instrumentation, data selection and methods

ASPERA-3 is an instrument package designed to study the interaction between the solar wind and the Martian atmosphere [Barabash et al., 2006]. It includes the ELectron Spectrometer (ELS), the Ion Mass Analyzer (IMA) and two energetic neutral atom sensors. We used data from the ELS and IMA sensors, which are described in more detail below.

The ELS instrument measures the two-dimensional distributions of the electron flux in the energy range of 5 eV-15 keV ($\Delta E/E=8\%$) with a field of view of $4^\circ \times 360^\circ$ divided into 16 azimuth sectors. The time resolution used in this study is 4 s. The IMA instrument consists of an electrostatic deflection system, followed by a top-hat electrostatic energy analyzer and a magnetic mass analyzer. The IMA sensor measures the fluxes of different ion species with m/q resolution (m and q being the ion mass and charge), including H^+ , He^{2+} , O^+ and molecular ions with $20 < m/q < 80$. The

measurements are in the energy range 10 eV/q-36 keV/q for all ion species except H⁺, where the lower energy limit is ~1.2 keV for the intermediate post-acceleration level (PAC). The PAC voltage serves to vary the mass resolution of the instrument. With a time resolution of 12 s, IMA gives a two-dimensional measurement of the ion fluxes (16 azimuth sectors) for all energies. For this study, electrostatic sweeping provides $\pm 45^\circ$ coverage out of the plane of the aperture (scanning in elevation angle) and a complete distribution with a field of view of $90^\circ \times 360^\circ$ is produced in 192 s (an IMA scan).

Both ELS and IMA have other operational modes that are not used in this study. For our statistical study we use electron and ion data taken from February 2004 to April 2011. The analysis was conducted for the solar minimum. Two new energy tables were uploaded for IMA, one in May 2007 and the other in November 2009. We have not used data from these two months. In addition, we have excluded data from periods when the elevation scanning was off.

The analysis covers altitudes ≤ 2000 km. The electron data are used to identify the plasma regions. An inbound IMB crossing is identified by a sharp decrease in suprathermal (i.e., 40-300 eV in energy) electron fluxes. An inbound PEB crossing is identified by the appearance of the CO₂ photoelectrons [Frahm *et al.*, 2006]. This feature marks the entry into the ionosphere. On the dayside, we have manually searched for proton fluxes in the presence of the photoelectrons that are not accompanied by magnetosheath-like electrons to ensure that the spacecraft is in the dayside ionosphere. On the nightside, the photoelectrons are less frequently observed, and there we just require the proton fluxes to be located below the IMB. We have checked that there is a non-null flux in downgoing directions during these IMA scans (we want precipitating particles). Then, we have integrated the downward proton flux from a 3-D distribution (of time resolution = 192 s), to

obtain a total downward flux of the “event” of proton precipitation. We have finally discarded cases where the proton mass channel of IMA is severely contaminated by ultraviolet (UV) radiation and alpha particles; these cases are referred to as invalid data.

All measurements by Mars Express are made above the exobase, which is located at approximately 180 km altitude at the solar minimum. Incoming protons that arrive at the exobase undergo collisions with the atmospheric neutrals and lose energy. These protons are neutralized by charge exchange reactions at lower altitude and are considered lost in the atmosphere [Kallio and Barabash, 2000]. In this study, we have assumed that all precipitating proton fluxes reach the exobase and deposit their mass and energy further down.

Figure 1 gives an example of the precipitating protons observed by MEX on 4 October 2005 in the subsolar region at solar zenith angles (SZA) $< 50^\circ$. The time interval is 1540 UT-1640 UT. The pericenter is reached at 1612 UT at ~270 km altitude (panel a). The magnetosheath is recognized by the high fluxes of 40-300 eV electrons (panel b). The dayside ionosphere is identified by the CO₂ photoelectrons (horizontal line at 20-30 eV) between 1603 UT and 1621 UT. The “blob” shape of the proton energy distributions in panel c is the result of the scanning in elevation angle of IMA. Several proton fluxes are observed within the ionosphere, at 1604 UT-1607 UT, 1609 UT-1610 UT and 1616 UT-1617 UT, and marked by arrows. During these three IMA scans, a part of the distribution is moving downward, i.e., precipitating. These three scans correspond to three events according to our definition of an event.

3 Spatial distribution and characteristics of the events

Figure 2 (panel a) shows the IMA data coverage below the IMB, excluding invalid data, in the X_{M_{SO}}-R_{M_{SO}} plane. In the Mars Solar Orbital (MSO) Cartesian coordinate

system, the X_{MSO} axis points from the center of Mars toward the Sun, the Y_{MSO} axis points opposite to the Martian orbital velocity vector and the Z_{MSO} axis completes the right-handed system. The total number of IMA scans (of 192 s time resolution) is 44731. The coverage below the IMB is best at low altitudes around the terminator, away from the subsolar point and from the shadow. The altitude of the IMB changes with varying solar wind conditions, and it can be located above the nominal position of the IMB. The IMB model of *Dubinin et al.* [2006] is shown in the figure. In the other panels of the figure, b, c and d, we show only the spatial bins where the data coverage below the IMB is at least 30 scans.

Panel b shows the occurrence frequency of the observed events. We have found 524 events in total. The events are observed on the dayside ($X_{\text{MSO}} > 0$) and on the nightside ($X_{\text{MSO}} < 0$). The events extend from the subsolar region up to 150° SZA. The solar wind void in the shadow of Mars is visible. The altitude spans from the pericenter (~ 260 km) up to the altitude limit that we have used of 2000 km. For the altitude distribution of the events, the mean and median values are 700 km and 608 km on the dayside, respectively; the mean and median values are 881 and 782 km on the nightside, respectively.

Some events are found outside the nominal position of the IMB. These events are located in regions where the spacecraft is seldom below the IMB so that the data coverage below the IMB consists of less than 30 scans (which are thus not shown in the figure). From panel b, the occurrence frequency of observing the events is on average 3.2% on the dayside and 0.5% on the nightside outside the shadow. The relatively high occurrence frequency bins at low altitude on the dayside are significant, due to the good data coverage. The low occurrence frequency in general indicates that the events are sporadic [see also *Diéval et al.*, 2012b] and rare.

Panels c and d show the average values of the downward particle fluxes and

energy fluxes of the events. Here and in the rest of the paper, we will consider the fluxes of the events when they occur and no occurrence frequency is taken into account, except when mentioned. Additionally, for all values of mean flux, we will use a log average. The particle and energy fluxes vary in the range 10^4 - 10^6 $\text{cm}^{-2}\text{s}^{-1}$ and 10^7 - 10^9 $\text{eVcm}^{-2}\text{s}^{-1}$, respectively. The particle flux is higher on the dayside (median value $1.2 \cdot 10^5$ $\text{cm}^{-2}\text{s}^{-1}$, mean value $7.7 \cdot 10^5$ $\text{cm}^{-2}\text{s}^{-1}$) than on the nightside (median value $3.8 \cdot 10^4$ $\text{cm}^{-2}\text{s}^{-1}$, mean value $6.0 \cdot 10^5$ $\text{cm}^{-2}\text{s}^{-1}$). The flux decreases with increasing SZA. This trend is consistent with the results of hybrid modeling studies [*Kallio and Janhunen*, 2001; *Diéval et al.*, 2012a]

Diéval et al. [2012a] reported that the modeled precipitating flux decreases with altitude, especially in the subsolar region. We note that the data coverage below the IMB is rather poor at low altitudes in the subsolar region (panel c). The situation is better on the dayside flanks and there we see no altitude dependence of the downward flux of events. However, the figure presents all solar wind conditions mixed (the effect of which will be investigated in Section 4), which makes the comparison difficult with a simulation that uses one set of solar wind parameters.

Figure 3 (panel a) shows a histogram of the downward particle fluxes of events. The mean and median values of the distribution are $7.4 \cdot 10^5$ $\text{cm}^{-2}\text{s}^{-1}$ and $9.8 \cdot 10^4$ $\text{cm}^{-2}\text{s}^{-1}$, respectively. Panel b shows a histogram of the peak energy of the events. We define the peak energy as the energy bin with the maximum differential flux in the energy spectrum. The events tend to have peak energies ≥ 1 keV. The mean and median values of the distribution are 2.1 keV and 1.7 keV, respectively. The distribution has a tail at high energies. The highest peak energy recorded is ~ 7.9 keV. However, the proton measurements are limited by an instrumental energy threshold depending on the PAC level in which IMA is run [*Barabash et al.*, 2006]. The protons with energies < 1 keV require the highest PAC

level to reach the detector. These low energy protons are not detected for the lowest PAC level. Therefore, the number of events with peak energies < 1 keV may be underestimated, and the determination of their peak energies may be less reliable, as the low-energy part of the energy spectrum would be cut-off. On the other hand, the events with peak energies ≥ 1 keV usually have their maximum fluxes at energies well above the energy threshold: their peak energies are reliable.

As we have determined the peak energy of the events, we now look at the characteristics of the energy spectra. The energy spectra of the protons, integrated over downgoing angles, are sometimes broad in energy (several keV), but they typically have an energy width of ~ 0.5 keV.

To obtain an average shape of the precipitating proton energy spectrum, we first shift the individual spectra to the mean peak energy of the events, 2.1 keV, and interpolate these spectra onto a linearly spaced energy grid between 0.6 and 10.0 keV with an energy step of 100 eV prior to averaging over the logarithm of the flux of all spectra. The resulting average spectrum is shown in Figure 4. The spectrum is narrow in energy, in contrast to simulation results that show a broad energy range [Brecht, 1997; Kallio and Janhunen, 2001; Diéval *et al.*, 2012a]. In addition, simulations by Diéval *et al.* [2012a] predict a low energy component (energy < 1 keV) in the precipitating proton spectrum, which we do not measure. One reason is that the instrumental energy cut-off of IMA, ~ 1.2 keV in the intermediate PAC level limits the detection of the low-energy protons.

Diéval *et al.* [2012b] noted that the spectra of downgoing protons measured below the IMB become narrower in energy as the particles move through the pile-up region and enter the ionosphere. These authors report that the high-energy component of the original magnetosheath spectrum reaches low altitudes, while the low energy component vanishes at a higher altitude, likely due to deflection by the

draped magnetic field. Thus, the statistical analysis confirms the tendency of the events to have narrow energy distributions peaking at high energies ≥ 1 keV (Figures 3b and 4).

4 Influence of solar wind parameters, IMF orientation and magnetic anomalies

4.1 Influence of the solar wind parameters

We have investigated how the proton precipitation is affected by the solar wind proton bulk velocity and by the magnetosheath proton temperature. For the solar wind velocity, we use moments taken when MEX is upstream of the bow shock model of Vignes *et al.* [2000]. For the magnetosheath temperature, we use moments taken when MEX is located between the previous bow shock model and the IMB model of Dubinin *et al.* [2006]. An averaged-over-time value of the solar wind bulk velocity and magnetosheath temperature is attributed to each event provided that MEX spends some time in the magnetosheath and in the upstream solar wind on the inbound leg of the same orbit and that reliable moments are available. This procedure is not possible for all events because MEX does not enter the solar wind on every orbit. The magnetosheath temperature and the solar wind bulk velocity have been determined for 466 events and 271 events, respectively.

Figure 5 (panels a and c, left column) shows histograms of the magnetosheath temperature and the solar wind bulk velocity, respectively. The grey shaded distribution and the black shaded distribution correspond to all the data from the studied period and the events, respectively. One sees that the distribution of the magnetosheath temperature of the events does not differ from the data of the studied period (panel a). This indicates that the occurrence frequency of the events does not depend on the magnetosheath temperature. The mean and median values of the magnetosheath temperature associated with the events are

56 eV and 50 eV, respectively. On the other hand, panel c indicates that the events occur relatively more often during fast solar wind conditions (450-600 kms^{-1} bins) and less often during slow solar wind conditions (350 kms^{-1} bin), compared to the overall data from the studied period. The mean and median values of the solar wind bulk velocity associated with the events are 443 kms^{-1} and 434 kms^{-1} , respectively.

Figures 5 (panels b and d, right column) shows the downward particle flux of the events versus the magnetosheath temperature and the solar wind bulk velocity, respectively. The plots indicate a large scatter of points. The downward flux has no clear correlation with either the solar wind velocity (panel d) or the magnetosheath temperature (panel b). There is a slight increase of the event flux with the magnetosheath temperature and with the solar wind velocity, but this trend is weak in relation to the significant scatter of the data points.

Hybrid simulations predict an increase of the precipitating solar wind flux for increasing solar wind speed V and density n [Brecht, 1997]. It is generally assumed that the magnetic pressure $\sim B^2$ in the pile-up region counterbalances the upstream solar wind dynamic pressure $\sim nV^2$ (B = magnetic field strength). The magnetic pressure thus increases in the compressed pile-up region when Mars encounters a fast solar wind stream. In addition, a high-speed solar wind leads to shocked protons with high velocities v . In this case, the proton gyroradius mv/qB may not change much as both B and v have high values, while the size of the pile-up region is reduced. As a consequence, these protons are more likely to penetrate the thinner magnetic barrier without being backscattered: the fast solar wind can in principle enhance precipitation. The observed higher occurrence frequency of events for high solar wind speeds is consistent with this view. However, there is no clear correlation between the downward flux and the solar wind speed.

In hot magnetosheath plasma,

protons with large gyroradii may possibly pass through the magnetic barrier and precipitate due to a finite gyro radius effect. Thus one can expect to obtain larger or more frequent downward flux when the magnetosheath plasma is hotter. However, there is no preferred occurrence of the events for a high magnetosheath temperature. This result may be due to the use of all upstream conditions, which may have different effects on the proton precipitation. For example, hot magnetosheath plasma can be caused by either a dense solar wind or a fast solar wind (high upstream dynamic pressure in both cases). The effect of the solar wind pressure pulses on the proton precipitation is left for a future study.

Diéval et al. [2012b] suggested that a transient increase of the magnetosheath temperature could cause the sporadic observations of downward proton flux. In the present statistical study, we take time-averaged magnetosheath (and upstream) conditions along the orbit and thus we cannot capture any rapid change in the magnetosheath (and upstream) conditions that could happen before the precipitation event. This may explain why we do not observe any good correlation between the downward flux and the magnetosheath/upstream parameters.

High solar wind speeds and high magnetosheath temperatures are associated to populations of energetic protons. How does this relate to the peak energies of the events? Figure 6 shows the peak energy of the events versus the magnetosheath proton temperature (panel a) and versus the solar wind bulk velocity (panel b). We see that the peak energy range broadens toward higher energies both when the magnetosheath temperature increases and when the solar wind speed increases. This means that we find events that are more energetic when these parameters increase.

Figure 7 (panel a) shows the ratio of the downward particle flux of the events to the solar wind particle flux. The solar wind flux is calculated using the solar wind density and bulk velocity. From the figure,

we see that some events (7 out of 271) have $\log_{10}(\text{ratio}) > 0$ (that is event flux > solar wind flux), which is due to an underestimation of the upstream flux. The flux of the cold solar wind beam can be underestimated due to field-of-view limitations, and also due to the energy cut-off of IMA. When ignoring these outliers, we obtain the mean and median value of the distribution as 0.002 and 0.002, respectively. Assuming that the precipitating protons come from the solar wind, this means that only very little of the solar wind flux is transmitted through the IMB when the precipitation occurs (0.2% on average). Considering that the events are observed during only ~3% of the observation time in the dayside ionosphere, we conclude that the particle input from the solar wind to the ionosphere, averaged over time, is not significant. Therefore, the Martian atmosphere is well protected by the magnetic barrier against the proton precipitation. For a comparison, [Diéval *et al.*, 2012a] find that 1% of the solar wind proton particle flux reaches 207 km altitude on the dayside of Mars, using a hybrid model. However, the proton precipitation is a recurrent phenomenon in such simulations [Brecht, 1997; Kallio and Janhunen, 2001; Diéval *et al.*, 2012a]. Therefore, the previous modeling studies drastically overestimate the solar wind input to the atmosphere because they do not take into account any occurrence frequency of the precipitation.

It is also interesting to know how the peak energy of the events relates to the upstream peak energy. Panel b shows the ratio of peak energies between the events and the solar wind. The mean and median value of the distribution is 1.4 and 1.2, respectively. The events tend to have their peak energy close to the upstream peak energy. The distribution has a tail toward ratios >1 and up to ~3.5. It is known that protons picked up from the Martian corona have energies up to 4 times the solar wind energy. Nevertheless, we cannot conclude whether the observed events have a solar wind origin or a planetary origin. Diéval *et*

al. [2012b] reported that in their hybrid simulations the precipitating protons have both origins, with a larger proportion from the solar wind.

4.2 Influence of the IMF orientation

The solar wind convective electric field $\vec{E}_{sw} = -\vec{V} \times \vec{B}$ controls the spatial deposition of the solar wind protons in hybrid simulations [Brecht, 1997; Kallio and Janhunen, 2001; Diéval *et al.*, 2012a]. We will check this prediction by using our data.

To determine the direction of \vec{E}_{sw} for the identified events, we use the magnetic field data from the MAG-ER instrument [Acuña *et al.*, 1992] onboard the Mars Global Surveyor (MGS) spacecraft. The draped IMF orientation is assumed to be the same as in the upstream solar wind [Brain *et al.*, 2006; Fedorov *et al.*, 2006]. For minimizing the influence of the crustal fields we only use magnetic field data recorded when MGS is on the dayside, between +50° and +60° latitudes [Brain *et al.*, 2006]. For each event, we search whether there are data corresponding to this criterion in a time interval of 2h before and after the event, and we average the direction of the magnetic field over time. The analysis of the effect of the IMF direction is possible until November 2006 (the end of the MGS mission). The IMF direction has been determined for 84 events.

To study the effect of \vec{E}_{sw} , we present the results in the Mars Solar Electric (MSE) frame. The MSE coordinate system is Cartesian: the X_{MSE} axis points from the center of Mars to the Sun, the Z_{MSE} axis is aligned with \vec{E}_{sw} and the Y_{MSE} axis completes the right-handed system. We define the $+\vec{E}_{sw}$ hemisphere as the hemisphere where \vec{E}_{sw} points away from Mars ($Z_{MSE} > 0$) and the $-\vec{E}_{sw}$ hemisphere as the hemisphere where \vec{E}_{sw} points toward Mars ($Z_{MSE} < 0$).

Figure 8 shows a view from the Sun

in the MSE frame. Panel a shows the data coverage below the IMB, excluding the invalid data. The coverage is best around the terminator (where the black circle is located). In the other panels of the figure, b, c and d, only the spatial bins where there are at least 30 IMA scans are used. The occurrence frequency for observing the events is shown in panel b. The occurrence frequency is higher in the $-\bar{E}_{sw}$ hemisphere than in the $+\bar{E}_{sw}$ hemisphere. In total, 34 events are found in the $+\bar{E}_{sw}$ hemisphere, and 50 events are found in the $-\bar{E}_{sw}$ hemisphere. *Stenberg et al.* [2011] also find that solar wind origin alpha particles precipitating into the Martian ionosphere are detected more frequently in the $-\bar{E}_{sw}$ hemisphere than in the $+\bar{E}_{sw}$ hemisphere.

The downward particle flux of the events, averaged in each bin where the events occur, is shown in panel c. The fluxes are higher in the $+\bar{E}_{sw}$ hemisphere (median value $5.6 \cdot 10^5 \text{ cm}^{-2}\text{s}^{-1}$, average value $1.2 \cdot 10^6 \text{ cm}^{-2}\text{s}^{-1}$) than in the $-\bar{E}_{sw}$ hemisphere (median value $2.0 \cdot 10^5 \text{ cm}^{-2}\text{s}^{-1}$, average value $1.9 \cdot 10^5 \text{ cm}^{-2}\text{s}^{-1}$). The asymmetry is consistent with simulation studies [*Brecht, 1997; Kallio and Janhunen, 2001; Diéval et al., 2012a*]. Panel c considers the average fluxes when they occur. Panel d uses data from panels b and c to show the averaged downward particle flux of the events multiplied by the occurrence frequency. This flux corrected by occurrence varies in the range 10^2 - $10^4 \text{ cm}^{-2}\text{s}^{-1}$.

Hybrid simulations predict that high-energy protons are deposited preferentially on the $+\bar{E}_{sw}$ hemisphere [*Brecht, 1997; Kallio and Janhunen, 2001; Diéval et al., 2012a*]. Figure 9 shows a histogram of the peak energy of the events measured in the $+\bar{E}_{sw}$ hemisphere (black shaded distribution) and in the $-\bar{E}_{sw}$ hemisphere (grey shaded distribution). The mean and median value of the distribution are ~ 2.6

keV and ~ 1.9 keV, respectively, in the $+\bar{E}_{sw}$ hemisphere. The mean and median value of the distribution are ~ 1.9 keV and ~ 1.5 keV in the $-\bar{E}_{sw}$ hemisphere, respectively.

Therefore, the events measured in the $+\bar{E}_{sw}$ hemisphere tend to be more energetic than in the $-\bar{E}_{sw}$ hemisphere, in reasonable agreement with the previous modeling studies. This result does not permit us to deduce the origin of the events. Indeed, hybrid simulations of precipitating proton patterns by *Diéval et al.* [2012a] show that both planetary proton and solar wind proton precipitation fluxes are larger in the $+\bar{E}_{sw}$ hemisphere than in the $-\bar{E}_{sw}$ hemisphere, although the asymmetry is less pronounced for the planetary protons.

4.3 Influence of the crustal magnetic anomalies

The crustal magnetic anomalies were discovered by MGS [*Acuña et al., 1998; 1999*]. At 400 km altitude, the crustal magnetic field strength is < 50 nT in the Northern hemisphere, while the strongest magnetic anomaly (field strength > 100 nT) is located in the Southern hemisphere from 120° to 240° East longitude and from -30° to -80° latitude.

Simulation studies report that the solar wind protons may reach the Martian upper atmosphere in regions of strong radial fields [*Harnett and Winglee, 2006; Brecht and Ledvina, 2012*]. Our data cover several Martian years; all solar effects (Martian season, solar wind and extreme ultraviolet (EUV) conditions, IMF orientation) should be eliminated when looking at the events in a longitude-latitude frame. Then, we can investigate the effect of the planetary crustal magnetic field on the events. We consider only observations below 500 km altitude because we expect that the crustal fields have a stronger effect on the events at low altitudes, if they have any. Unfortunately the data coverage is not even when comparing the Northern and Southern hemispheres due

to the orbit geometry. Therefore, we restrict the analysis to the latitude band where the largest magnetic anomaly is located and search for a longitudinal dependence of the events.

In Figure 10 (panel a), we show the data coverage below the IMB for altitudes below 500 km in a latitude band between -30° and -90° , excluding the invalid data. We use the latitude and East longitude of the footprint of MEX. The data coverage is relatively even in this latitude band.

Panel b shows the occurrence frequency of observed events and panel c shows the average downward particle flux of the events where they occur, in spatial bins of longitude and latitude, below 500 km altitude. We see no longitudinal dependence of either the occurrence frequency or the downward flux of the events, meaning that the magnetic anomalies seem to have no effect on the proton precipitation. This result is also consistent with the absence of a longitudinal correlation reported by *Stenberg et al.* [2011] for the observed precipitation of solar wind alpha particles, but it disagrees with the previous modeling work [*Harnett and Winglee*, 2006; *Brecht and Ledvina*, 2012].

We find that the location of the magnetic anomalies is not important for the observed proton precipitation, as suggested by *Diéval et al.* [2012b].

5 Net particle input

It is interesting to know whether the proton events have downward or upward net fluxes and how these fluxes are distributed in space. In this section, we calculate the net fluxes of the events through a spherical surface centered at Mars. For each event, the particle flux measured by a given energy channel, elevation angle and azimuth angle is multiplied by $\vec{s} \cdot \vec{a}$, where \vec{s} is the nadir direction unit vector and \vec{a} is the unit vector opposite to the viewing direction. This flux is then summed over all energy channels, elevation and azimuth angles for the corresponding IMA scan. The net downward flux is positive, and the net upward flux is

negative. We find that 136 events and 388 events have a net upward flux and net downward flux, respectively.

Figure 11 (panel a) represents the median net flux of the events in the $X_{\text{MSO}}-R_{\text{MSO}}$ plane for the regions where the coverage (below the IMB and excluding invalid data) comprises at least 30 scans. We see that the net flux is rather downward close to Mars (red color) and rather upward or tailward further from Mars (blue color). This is particularly visible on the nightside. On the dayside, the events with a net upward flux are not obvious in the figure because they tend to be located at high altitudes in regions where the data coverage is seldom below the IMB (they are not shown in the figure). On the dayside, the median altitudes of the downward and upward net fluxes are 578 km and 783 km, respectively. On the nightside, the median altitudes of the downward and upward net fluxes are 516 km and 971 km, respectively. We will obtain a similar picture if we plot each event as an individual point colored by the net flux. The pattern is consistent with protons moving more toward the planet on the dayside and more tailward on the nightside, as the solar wind flows past the obstacle.

Now, we will focus on the events that have a net downward flux. Panel b shows the median net downward flux multiplied by the occurrence frequency of these events. The flux tends to be larger on the dayside ($10^2-10^4 \text{ cm}^{-2}\text{s}^{-1}$) than on the nightside ($10^1-10^3 \text{ cm}^{-2}\text{s}^{-1}$).

Then, we estimate the total net downward particle flux input through a half sphere of radius R_m+578 km on the dayside of Mars. $R_m=3397$ km is the radius of Mars. We use the events having a net downward flux on the dayside; their median values of flux and altitude are $\sim 1.2 \cdot 10^3 \text{ cm}^{-2}\text{s}^{-1}$ and 578 km, respectively. We calculate the total net downward flux through the half sphere as follows:

$$1.2 \cdot 10^3 \cdot 2 \cdot \pi \cdot ((R_m + 578) \cdot 10^5)^2 = 1.2 \cdot 10^{21} \text{ s}^{-1}$$

This is two orders of magnitude less than the number of solar wind protons precipitating at 207 km altitude on the

dayside of Mars in the hybrid simulations by *Diéval et al.* [2012a]: $4.0 \cdot 10^{23} \text{ s}^{-1}$. For a comparison, we can calculate from the measurements, the median solar wind particle flux input through a disc of cross section $\pi \cdot ((R_m + 578) \cdot 10^5)^2 \text{ cm}^2$. We use the median solar wind particle flux associated with the events: $4.1 \cdot 10^7 \text{ cm}^{-2} \text{ s}^{-1}$. We obtain

$$4.1 \cdot 10^7 \cdot \pi \cdot ((R_m + 578) \cdot 10^5)^2 = 2.0 \cdot 10^{25} \text{ s}^{-1}.$$

Thus the total net downward flux input from the events ($1.2 \cdot 10^{21} \text{ s}^{-1}$) corresponds to 0.006% of the upstream solar wind flux input.

6 Discussion and conclusion

We have conducted a statistical study of precipitating protons measured below the Martian IMB using Mars Express/ASPHERA-3 data collected from February 2004 to April 2011, during the solar minimum.

The observations of the downward proton events show an asymmetry relative to the solar wind convective electric field direction in terms of fluxes and peak energies, which is predicted by hybrid modeling studies [*Brecht, 1997; Kallio and Jahnunen, 2001; Diéval et al., 2012a*]. *Diéval et al.* [2012a] predicted fine spatial details in simulated proton precipitation maps. These details are not resolved by the observations of the events shown in MSE coordinates (Figure 8) for several reasons. First, the number of events must be high enough to provide good statistics everywhere around Mars. Additionally, there are not enough statistics to look at the events at different altitudes in the MSE system. We also need to know the orientation of the upstream IMF to organize the events according to the \vec{E}_{sw} , but Mars Express does not have a magnetometer. As mentioned above, we rely on MGS data to determine the IMF orientation. The operation of this mission ended in late 2006, reducing the number of events for which the IMF can be found.

Proton precipitation events are

observed during ~3% of the observation time when MEX is below the dayside IMB. This is in contrast to hybrid models, which predict that the proton precipitation occurs permanently. Why do we then observe so few events? Several reasons may lead to an underestimation of the number of events, and therefore of the occurrence frequency.

The efficiency of the proton detection decreases below the IMA energy threshold: only the most energetic events can be detected when IMA is run in the lowest post-acceleration level (this level was used for 5% of our data coverage). Furthermore, solar UV contamination was quite frequent during the ionospheric passes. The proton flux can be hard to separate from the instrumental noise, such that the events can be missed. Additionally, alpha particles can be detected in the proton channel if their flux is intense, leading to an overestimation of the proton fluxes: the corresponding events were discarded. We have removed 9058 invalid scans corresponding to 17% of the initial data coverage below the IMB (53789 scans). In addition, the region of major deposition of precipitating protons (where the precipitating flux is the highest) will change position as the upstream IMF direction changes. However, this seems not to be important for the probability of detecting the events because we see the events in both $\pm \vec{E}_{sw}$ hemispheres. Furthermore, the ion observations are made in situ, in only one location at a time. So it is possible that we miss events because we do not measure at the right place at the right time. This would be the case if the precipitation is a time-dependent process as well as if it occurs in spatially limited regions. Indeed, the observations of *Diéval et al.* [2012b] suggest that the precipitation is a dynamic phenomenon, which occurs only at times, most likely due to transients in the magnetosheath. The preferred occurrence frequency of the events for periods of fast solar wind indicates that transients in the upstream solar wind may also trig the intermittent proton precipitation. In the case of sporadic heating/acceleration of the

proton population, these protons with large gyroradii could in turn pass the magnetic barrier, as observed.

A question which remains is what is the typical size of a region of proton precipitation? Hybrid modeling studies [Brecht, 1997; Kallio and Janhunen, 2001; Diéval *et al.*, 2012a] predict that the protons precipitate over large area of the planet. A case study by Diéval *et al.* [2012b] reports that precipitating protons have been measured below the IMB over a distance of ~4000 km along an orbit of MEX. In our statistical analysis, precipitation events were detected on 363 MEX orbits out of 4707 orbits (8% of the orbits). On one hand, 256 out of 363 orbits counted just one event, suggesting a small precipitation area. On the other hand, 2 out of 363 orbits counted 6 events, suggesting a rather large precipitation area. There is in any case a trend to see the precipitation only for a short time.

Figure 12 proposes a sketch of the sporadic precipitation, as it could be observed by MEX at two times t_1 and t_2 (left and right columns, respectively). Figure 12 (panels a, b) illustrates a local precipitation in a small area, which will be detected if MEX is at the right place at the right time. Figure 12 (panels c, d) illustrates a global precipitation in an extended area, which will appear as local if it is intermittent. The question of the size of the precipitation region could be solved with two hypothetical orbiters flying over the same region. The imaging of the spatial distribution of hydrogen energetic neutral atoms (H ENAs), backscattered by the atmosphere, would also help to obtain a picture of the proton precipitation [Futaana *et al.*, 2006]. These H ENAs are generated through charge exchange reactions between cold planetary atoms and solar wind protons in the vicinity of Mars [Kallio *et al.*, 1997; Kallio and Barabash, 2001; Holmström *et al.*, 2002].

The events intermittently bring particle fluxes in the range 10^4 - 10^6 $\text{cm}^{-2}\text{s}^{-1}$ into the atmosphere. These fluxes are two

orders of magnitude lower than the modeled precipitating fluxes calculated by Kallio and Janhunen [2001]. In contrast, the measured fluxes vary within the range of the modeled precipitating fluxes calculated at 260 km altitude by Diéval *et al.* [2012a], but they are one order of magnitude lower than the modeled fluxes calculated at 540 km altitude. Therefore, the quantitative comparison with the models is not simple, as the different models have different input parameters and set ups.

Does the precipitating proton energy flux play any role in the heating of the upper atmosphere? The energy fluxes measured on the dayside (10^8 - 10^9 $\text{eVcm}^{-2}\text{s}^{-1}$) are much lower than the heat input from the solar radiation absorption at Mars for solar minimum conditions (height-integrated between 100-240 km) from Kallio *et al.* [1997]: $1.35 \cdot 10^{11}$ $\text{eVcm}^{-2}\text{s}^{-1}$. The proton precipitation thus has a minor role in the heat balance on the dayside, compared to the solar EUV. On the other hand, precipitation events have been measured also on the nightside in the absence of solar radiation. Although they are even less frequent than the dayside events, they carry an energy flux of 10^7 - 10^8 $\text{eVcm}^{-2}\text{s}^{-1}$, which is significant in the absence of EUV.

The precipitating proton fluxes can also be compared to the fluxes of penetrating solar wind electrons observed by Dubinin *et al.* [2008] in the energy range 40-80 eV. Dubinin *et al.* [2008] reported that the maximum solar wind electron particle flux can reach 10^{10} $\text{cm}^{-2}\text{s}^{-1}$ on the dayside and can reach $>10^9$ $\text{cm}^{-2}\text{s}^{-1}$ as spikes on the nightside. This gives an order of magnitude for the energy flux, 10^{11} $\text{eVcm}^{-2}\text{s}^{-1}$ on the dayside and $>10^{10}$ $\text{eVcm}^{-2}\text{s}^{-1}$ as spikes on the nightside. Dubinin *et al.* [2008] estimated that these electron spikes increase the ionization and are needed for causing aurora on the nightside. For comparison with the solar wind electrons, our maximum proton energy fluxes are 2 orders of magnitude lower on the dayside and the nightside. Thus, the local ionization effect of the proton events is negligible compared to the

ionization due to the solar wind electrons. It is also unlikely that the proton events are a driver for aurora, in contrast with estimations of *Kallio and Janhunen* [2001].

In conclusion, the statistical study of the precipitating proton events confirms that the proton precipitation, likely driven by the gyroradius effect, does exist on Mars, on the dayside and the nightside. The energy distributions of the events correspond to the high-energy part of the magnetosheath proton distribution, which is able to penetrate the magnetic barrier due to large gyroradii. The events are rare (~3% of the observation time on the dayside). The precipitation is more frequent during periods of fast solar wind than during periods of slow solar wind. Transients in the magnetosheath/upstream solar wind may explain the intermittence of the events. The study confirms the asymmetry related to the solar wind convective electric field reported by hybrid models. The precipitating protons do not correlate with the magnetic anomalies. The events carry ~0.2% of the upstream solar wind flux on average when they occur, which indicates that the magnetic barrier effectively shields the upper atmosphere against the incident magnetosheath protons. On the dayside, the resulting heating and ionization of the upper atmosphere are insignificant compared to the solar EUV flux. On the nightside, the heating and ionization are minor compared to the effects of the solar wind electron on the ionosphere. The median net input of the precipitating proton particle flux to the dayside ionosphere, corrected by occurrence frequency, is estimated as $1.2 \cdot 10^{21} \text{ s}^{-1}$.

The present study covers the solar minimum. A future goal would be to study the proton precipitation during the coming solar maximum and to compare these data with those obtained during the solar minimum. The production rate of planetary O^+ ions is expected to be more important during the solar maximum than the solar minimum because of increased neutral oxygen densities and because of increased UV radiation. According to hybrid

simulations [*Kallio and Janhunen*, 2001], the proton precipitation decreases when the O^+ production rate increases. This result shall be compared with the observations.

Acknowledgements.

C. D. and G. S. are supported by the National Graduate School of Space Technology of the Luleå Technical University. C. D. acknowledges funding from the Kungliga Vetenskapsakademien. The Swedish contribution to the ASPERA-3 experiment is supported by the Swedish National Space Board. C.D. thanks Markus Fränz from the Max-Planck Institut für Sonnensystemforschung (Katlenburg-Lindau) for providing the IMA moments used in this study.

References.

- Acuña, M. H., et al. (1992), Mars Observer magnetic field investigations, *J. of Geophys. Res.*, 97(E5), 7799-7814.
- Acuña, M. H., et al. (1998), Magnetic field and plasma observations at Mars: Preliminary Results of the Mars Global Surveyor Mission, *Science*, 279, 5357, 1676-1680, doi:10.1126/science.279.5357.1676.
- Acuña, M. H., et al. (1999), Global distribution of crustal magnetization discovered by the Mars Global Surveyor MAG/ER experiment, *Science*, 284, 5415, 790-793, doi:10.1126/science.284.5415.790.
- Barabash, S., et al. (2006), The Analyzer of Space Plasmas and Energetic Atoms (ASPERA-3) for the Mars Express Mission, *Space Sci. Rev.*, 126(1-4), 113-164, doi:10.1007/s11214-006-9124-8.
- Brain, D. A., et al. (2006), Magnetic field draping direction at Mars from April 1999 through August 2004, *Icarus*, 182, 464-473, doi: 10.1016/j.icarus.2005.09.023.
- Brecht, S. H., (1997), Solar wind proton deposition into the Martian atmosphere, *J.*

- Geophys. Res.*, 102(A6), 11,287-11,294, doi: 10.1029/97JA00561.
- Brecht, S. H., and Ledvina, S. A. (2012), Control of ion loss from Mars during solar minimum, *Earth Planets and Space*, 64, 165-178, doi: 10.5047/eps.2011.05.037.
- Diéval, C., et al. (2012a), Hybrid simulations of proton precipitation patterns onto the upper atmosphere of Mars, *Earth Planets Space*, 64, 121-134, doi: 10.5047/eps.2011.08.015.
- Diéval, C., et al. (2012b), A case study of proton precipitation at Mars: Mars Express observations and hybrid simulations, *J. of Geophys. Res.*, 117, A06222, doi: 10.1029/2012JA017537.
- Dubinin, E., et al. (2006), Plasma Morphology at Mars. Aspera-3 Observations, *Space Sci. Rev.*, 126, 209-238, doi: 10.1007/s.11214-006-9039-4.
- Dubinin, E., et al. (2008), Access of solar wind electrons into the Martian magnetosphere, *Ann. Geophys.*, 26, 3511-3524, doi: 10.5194/angeo-26-3511-2008.
- Fedorov, A., et al. (2006), Structure of the martian wake, *Icarus*, 182(2), 329-326, doi: 10.1016/j.icarus.2005.09.021.
- Frahm, R. A., et al. (2006), Carbon dioxide photoelectron energy peaks at Mars, *Icarus*, 182(2), 371-382, doi: 10.1016/j.icarus.2006.01.014.
- Fränz, M., et al. (2006), Plasma moments in the environment of Mars: Mars Express ASPERA-3 observations, *Space Sci. Rev.*, 126, 165-207, doi: 10.1007/s11214-006-9115-9.
- Harnett, E. M., and Winglee, R. M. (2006), Three-dimensional multifluid simulations of ionospheric loss at Mars from nominal solar wind conditions to magnetic cloud events, *J. of Geophys. Res.*, 111(A9), A09213, doi: 10.1029/2006JA011724.
- Holmström, M., et al. (2002), Energetic neutral atoms at Mars 1 Imaging of solar wind protons, *J. of Geophys. Res.*, 107(A10), 1277, doi: 10.1029/2001JA000325.
- Kallio, E., et al. (1997), Charge exchange near Mars: the solar wind absorption and energetic neutral atom production, *J. Geophys. Res.*, 102(A10), 22,183-22,197, doi: 10.1029/97JA01662.
- Kallio, E., and Barabash, S. (2000), On the elastic and inelastic collisions between precipitating energetic hydrogen atoms and Martian atmospheric neutrals, *J. of Geophys. Res.*, 105(A11), 24973-24996, doi: 10.1029/2000JA900077.
- Kallio, E., and S. Barabash (2001), Atmospheric effects of precipitation energetic hydrogen atoms on the martian atmosphere, *J. Geophys. Res.*, 106(A1), 165-177, doi: 10.1029/2000JA002003.
- Kallio, E., and P. Janhunen (2001), Atmospheric effects of proton precipitation in the Martian atmosphere and its connection to the Mars-solar wind interaction, *J. Geophys. Res.*, 106(A4), 5617-5634, doi: 10.1029/2000JA239.
- Lundin, R., et al. (2004), Solar wind-induced atmospheric erosion at Mars: first results from ASPERA-3 on Mars Express, *Science*, 305, 5692, 1933-1936, doi:10.1126/science.1101860.
- Nagy, A. F., et al. (2004), The plasma environment of Mars, *Space Sci. Rev.*, 111, 33-114, doi: 10.1023/B:SPAC.0000032718.47512.92.
- Shematovich, V.I., et al. (2011), Protons and hydrogen atoms transport in the Martian upper atmosphere with an induced magnetic field, *J. Geophys. Res.*, 116, A11320, doi: 10.1029/2011JA017007.
- Stenberg, G., et al. (2011), Observational evidence of alpha particle capture at Mars,

Geophys. Res. Letters, 38, L09101, doi: 10.1029/2011GL047155.

Vignes, D., et al. (2000), The solar wind interaction with Mars: Locations and shapes of the Bow Shock and the magnetic pile-up

boundary from the observations of the MAG/ER experiment onboard Mars Global Surveyor, *Geophys. Res. Lett.*, 27, 49-52, doi: 10.1029/1999GL010703.

Figures.

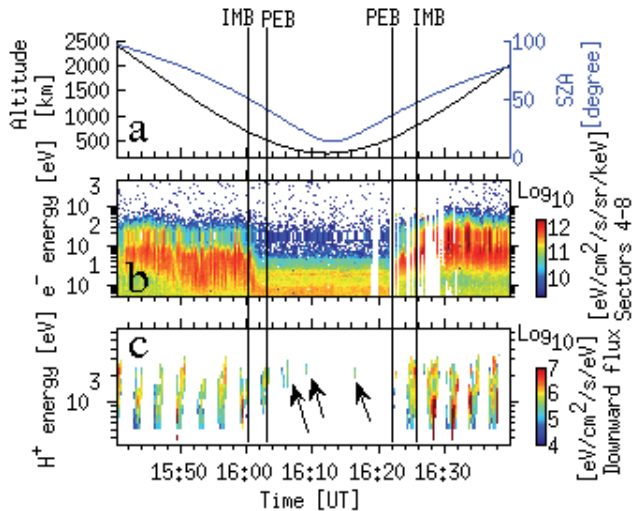


Figure 1. An example of proton penetration into the ionosphere. (a) Altitude (black solid line) and SZA (blue solid line) of Mars Express. (b) Electron energy-time spectrogram (the energy flux is averaged over sectors 4-8). The data gaps (white vertical bands) are an instrumental artifact. (c) Proton energy-time spectrogram (the energy flux is integrated over downgoing angles). The proton fluxes measured in the ionosphere are marked by arrows; they are referred to as “events”. The vertical black lines indicate the PEB and IMB crossings.

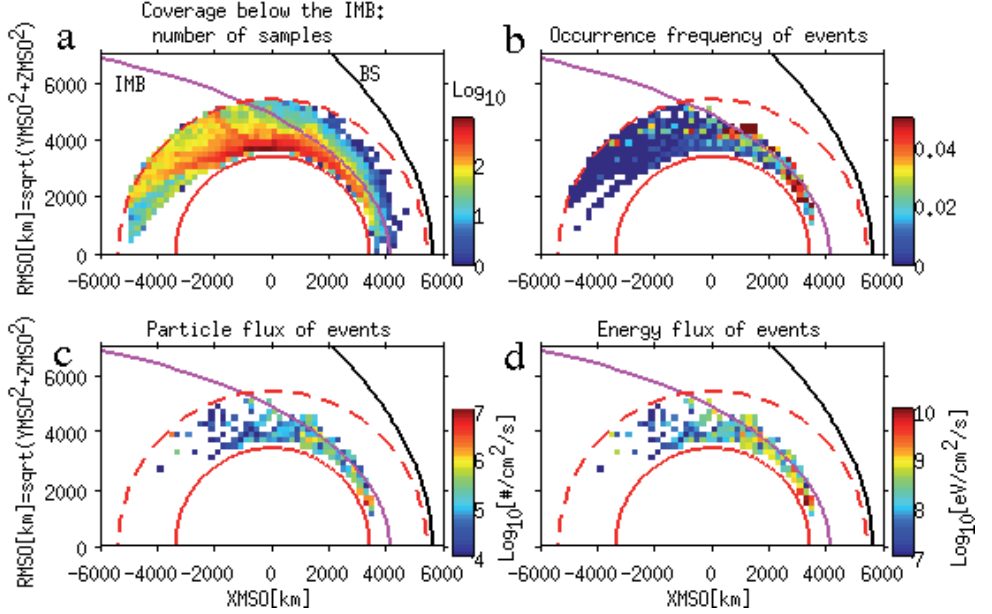


Figure 2: Each panel shows the X_{MSO} - R_{MSO} plane. The vertical axis is the distance $R_{MSO} = \sqrt{Y_{MSO}^2 + Z_{MSO}^2}$ from the Mars-Sun line. The spatial bin size is $200 \text{ km} \times 200 \text{ km}$. The red solid curve, the black solid curve and the pink solid curve indicate Mars, the bow shock model of Vignes et al. [2000] and the IMB model of Dubinin et al. [2006], respectively. The red dashed curve shows the altitude limit of 2000 km, under which the data were taken. (a) Data coverage below the IMB, excluding the invalid scans (contamination by alpha particles and UV). The colorbar indicates the number of IMA scans obtained in each spatial bin. In the following panels b, c and d only the spatial bins where the data coverage below the IMB comprises at least 30 scans are used. (b) Occurrence frequency of observing the events. The colorbar shows the number of events divided by the total number of IMA scans from panel (a) in each spatial bin. (c) Average downward particle fluxes and (d) average downward energy fluxes of the events. The colorbar shows the average flux in each spatial bin where the events occur.

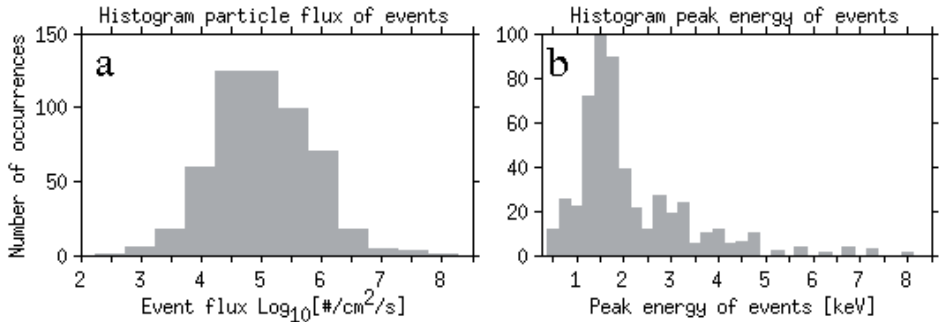


Figure 3: (a) Histogram of the downward particle flux of the events. (b) Histogram of

the peak energy of the events.

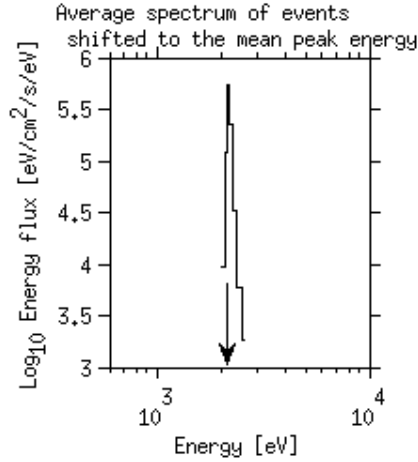


Figure 4: Spectrum of precipitating protons averaged over all individual event spectra, shifted to the mean peak energy of the events. Fluxes $<10^3$ $\text{eVcm}^{-2}\text{s}^{-1}\text{eV}^{-1}$ are not shown. The arrow indicates the mean peak energy of the events.

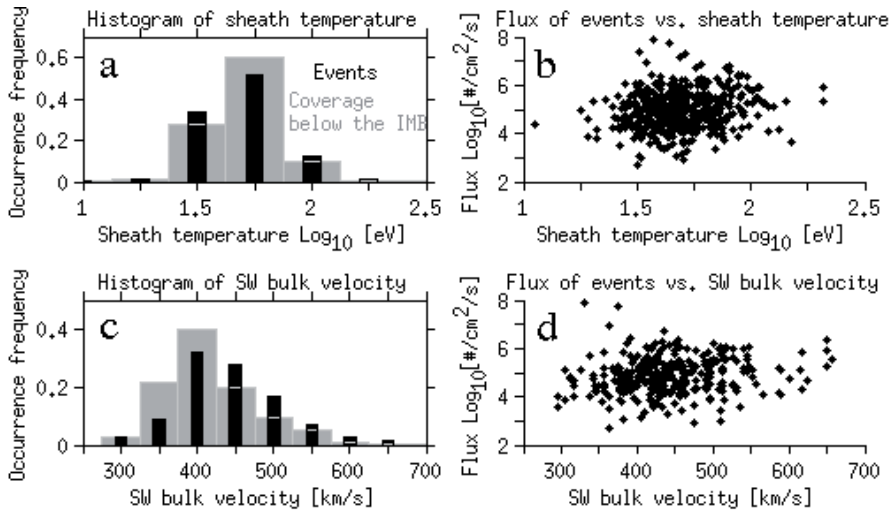


Figure 5: (a) Histogram of the magnetosheath proton temperature for the studied period (grey shading) and the events (black shading). (b) Downward event flux versus magnetosheath temperature. (c) Histogram of the solar wind bulk velocity for the studied period and the events. (d) Downward event flux versus solar wind proton bulk velocity. In panels a and c, each distribution is normalized by the total number of samples of the population.

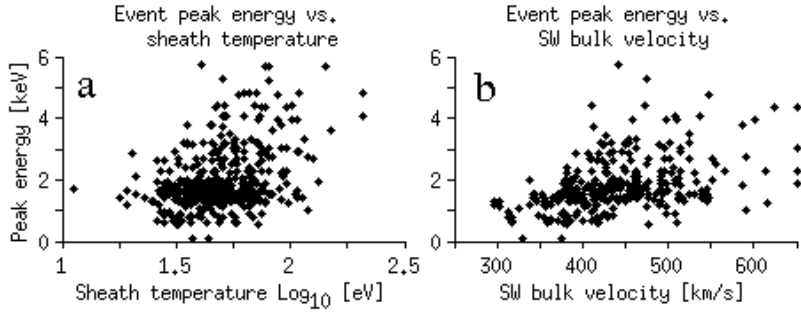


Figure 6: (a) Peak energy of the events versus magnetosheath proton temperature. (b) Peak energy of the events versus solar wind proton bulk velocity.

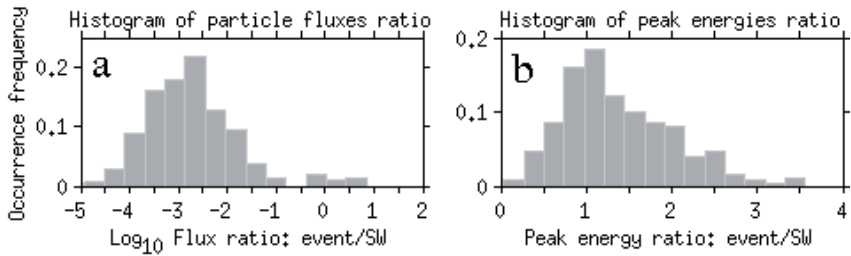


Figure 7: (a) Histogram of the downward proton particle flux ratio: event/solar wind. (b) Histogram of the proton peak energy ratio: event/solar wind. In both panels, each distribution is normalized by the total number of samples of the population.

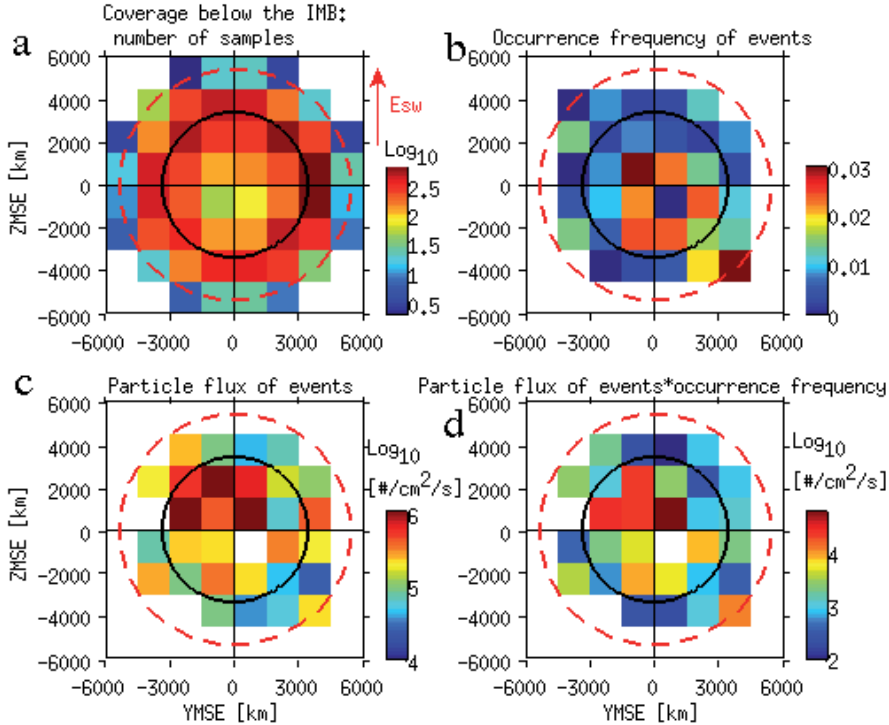


Figure 8: Each panel shows the Y_{MSE} - Z_{MSE} plane viewed from the Sun. The vertical axis points along the direction of the solar wind convective electric field. The spatial bin size is $1500 \text{ km} \times 1500 \text{ km}$. The solid black line indicates Mars, and the dashed red line indicates the altitude limit at 2000 km under which the data are taken. (a) Data coverage below the IMB, excluding invalid data. The colorbar indicates the number of IMA scans in each spatial bin. In the following panels b, c and d, only the spatial bins where the data coverage below the IMB is at least 30 scans are used. (b) Occurrence frequency of observing the events. The colorbar shows the number of events divided by the total number of IMA scans (from panel a) in each spatial bin. (c) Average downward particle flux of the events. The colorbar shows the average flux in each spatial bin where the events occur. The average is made along the Mars-Sun line axis and includes both dayside and nightside. (d) Average downward particle flux of the events multiplied by the occurrence frequency of the events.

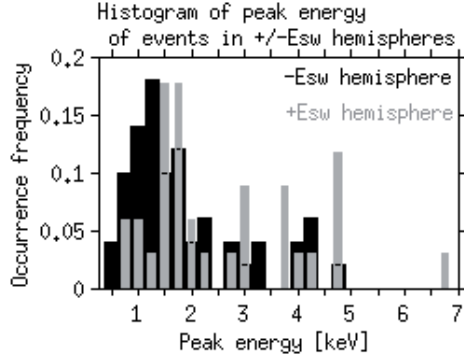


Figure 9: Histogram of the peak energies of the events in the $+\bar{E}_{sw}$ hemisphere (grey) and in the $-\bar{E}_{sw}$ hemisphere (black). Each distribution is normalized by the total number of samples of the population.

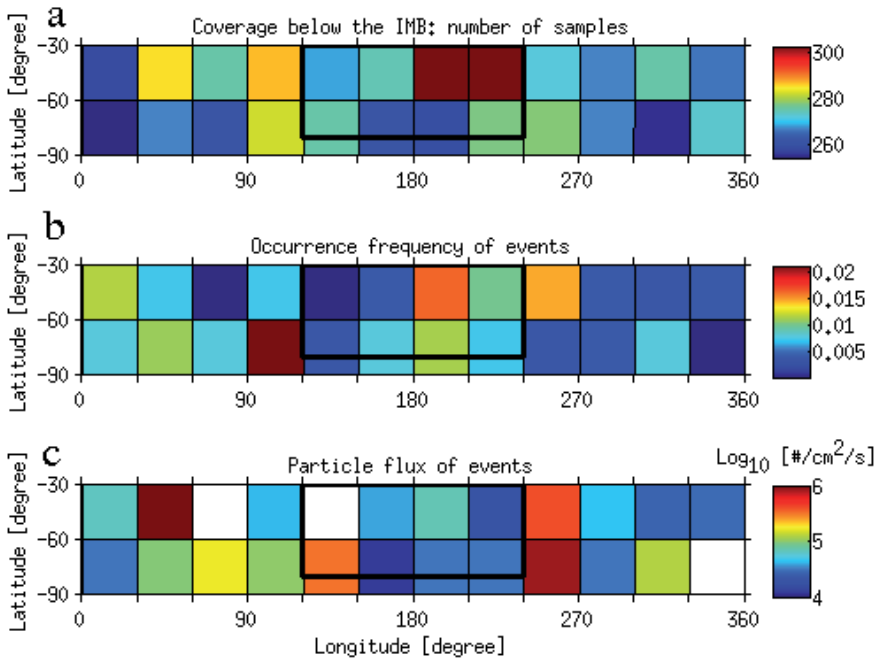


Figure 10: Each panel shows a latitude band in the Southern hemisphere, between -30° and -90° latitude. The bin size is $30^\circ \times 30^\circ$. The location of the strongest magnetic anomalies is delimited inside the thick black solid line. All panels use the latitude and longitude of MEX's footprint, when MEX is located below 500 km altitude. (a) Data coverage below the IMB, excluding invalid data. The colorbar indicates the number of IMA scans in each spatial bin. (b) Occurrence frequency of observing the events. The colorbar indicates the number of events divided by the total number of IMA scans (from panel a) in each spatial bin. (c) Average downward particle flux of the events. The colorbar shows the average flux in each spatial bin where the events occur. The

white color means no event.

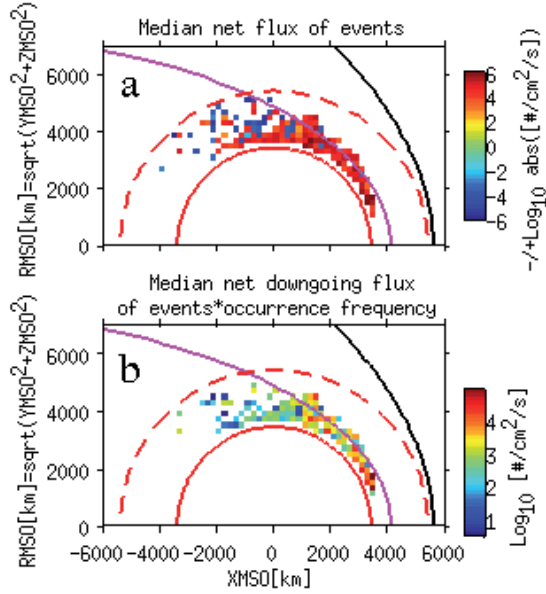


Figure 11: Each panel shows the $X_{\text{MSO}}\text{-}R_{\text{MSO}}$ plane. The spatial bin size is $200\text{ km}\times 200\text{ km}$. The lines have the same format as in Figure 2. Only the spatial bins where the data coverage below the IMB comprises at least 30 scans are used. (a) $\text{Log}_{10}(\text{abs}(\text{median net flux of the events}))$, multiplied with a “-“ (“+”) sign for negative (positive) values of the median net flux. An upward (downward) net flux is negative (positive). (b) Median net particle flux of the events multiplied by their occurrence frequency, calculated only from the events with a net downward flux.

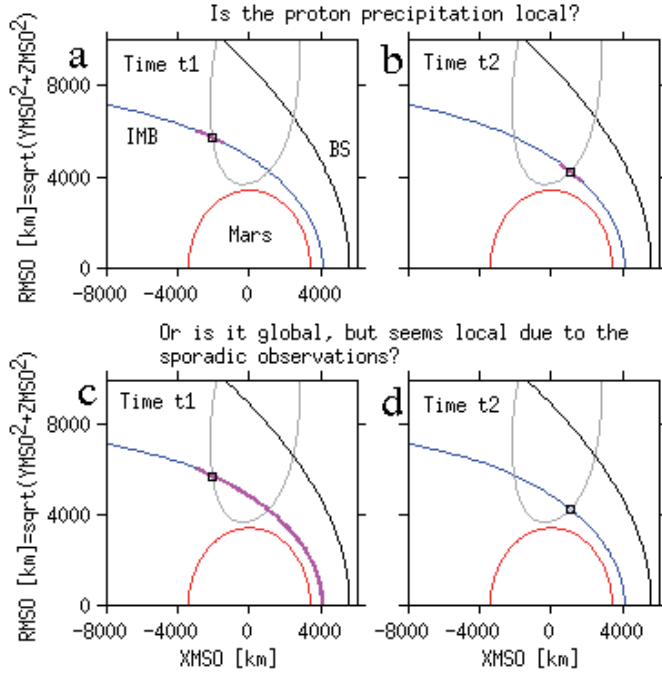


Figure 12: Each panel shows the $X_{M_{SO}}-R_{M_{SO}}$ plane. The red, black and blue solid line represent Mars, the bow shock model of *Vignes et al.* [2000] and the IMB model of *Dubinin et al.* [2006], respectively. The grey solid line and the black square represent an orbit of MEX and the position of MEX at a given time, respectively. The thick pink solid line indicates a zone of proton precipitation. (a) and (b) Sketch proposed for a local precipitation, at times t1 and t2, respectively. (c) and (d) Sketch proposed for a global precipitation, at times t1 and t2, respectively.

PAPER V

Reduced proton and alpha particle precipitations at Mars during solar wind pressure pulses: Mars Express results

C. Diéval^{1,2}, G. Stenberg¹, H. Nilsson^{1,2}, N. J. T. Edberg³ and S. Barabash¹

¹Swedish Institute of Space Physics, Box 812, SE-98128, Kiruna, Sweden

²Division of Space Technology, Department of Computer Science, Electrical and Space Engineering, Luleå University of Technology, SE-91187, Kiruna, Sweden

³Swedish Institute of Space Physics, Box 537, SE-75121, Uppsala, Sweden

Author for correspondence: catherine@irf.se

Abstract.

We performed a statistical study of downward moving solar wind protons and alpha particles of \sim keV energy, inside the Martian induced magnetosphere from July 2006 to July 2010. Ion and electron data are from the Analyzer of Space Plasma and Energetic Atoms (ASPERA-3) package onboard Mars Express. We investigated the solar wind ion entry into the ionosphere, excluding intervals of low altitude magnetosheath encounters. The study compares periods of quiet solar wind conditions and periods of solar wind pressure pulses, including interplanetary coronal mass ejections and corotating interaction regions. Precipitation events are less frequent and the precipitating fluxes do not increase during pressure pulse encounters. During pressure pulses the occurrence frequency of observed proton precipitation events is reduced by a factor \sim 3 and for He^{2+} events the occurrence frequency is reduced by a factor \sim 2. One explanation is that during pressure pulse periods, the mass loading of the solar wind plasma increases due to a deeper penetration of the interplanetary magnetic flux tubes into the ionosphere. The associated decrease of the solar wind speed thus increases the pile-up of the interplanetary magnetic field on the dayside of the planet. The magnetic barrier becomes thicker in terms of solar wind ion gyroradii, causing the observed reduction of $\text{H}^+/\text{He}^{2+}$ precipitations.

1 Introduction

The Martian ionosphere presents a partially conductive obstacle to the solar wind. When flowing around Mars, the solar wind, which carries the frozen-in interplanetary magnetic field (IMF), induces currents in the ionosphere. At the same time, the IMF diffuses into the ionosphere. There is a superposition of the magnetic fields from the induced currents, and the IMF partially diffused into the ionosphere. This superposition creates a region of an increased magnetic field above the ionosphere, the so-called magnetic barrier.

The inner edge of the magnetic barrier corresponds to the photoelectron boundary (PEB), below which the ionosphere starts, and where the ionospheric electron density steeply increases [Frahm et

al., 2006; Dubinin et al., 2008]. The outer edge of the magnetic barrier is referred to as the induced magnetospheric boundary (IMB) [Dubinin et al., 2006]. There is a pressure balance at the IMB between the upstream dynamic pressure and the magnetic pressure of the pile-up region. The IMB also separates the solar wind ions (mainly H^+ , He^{2+}) from the planetary ionospheric ions (mainly O^+ , O_2^+ , CO_2^+) [e.g. Breus et al., 1991].

However, in some circumstances, solar wind ions are able to pass from the magnetosheath to the ionosphere. In the hot magnetosheath plasma, there are solar wind ions with a gyroradius comparable to the size of the subsolar magnetic barrier. For example, the gyroradius for a typical 1 keV solar wind proton H^+ and for a typical 4 keV

solar wind alpha particle He^{2+} are 152 km and 306 km, respectively, for a background magnetic field strength of 30 nT (a typical strength of the dayside piled up magnetic field). These gyroradii are close to the nominal size of the subsolar magnetic barrier, estimated to be 300 km, using the mean altitude of the PEB at 400 km from *Mitchell et al.* [2001] and the mean altitude of the subsolar IMB at 700 km from *Dubinin et al.* [2006]. Modeling studies predict that solar wind ions with relatively high energies (large gyroradii) can cross the IMB without being deflected away and that they finally travel down, i.e., precipitate to low altitudes [*Brecht*, 1997; *Kallio and Janhunen*, 2001]. The precipitating protons and alpha particles then deposit their energy into the Martian upper atmosphere, causing charge exchange reactions, ionization and heating of the planetary neutral atoms [*Kallio and Janhunen*, 2001; *Shematovich et al.*, 2011; 2012]. Downgoing protons and alpha particles with solar wind energies are regularly observed in the Martian ionosphere [*Lundin et al.*, 2004; *Stenberg et al.*, 2011; *Diéval et al.*, 2012a; 2012b].

There are two main types of solar disturbance of the interplanetary medium associated with high dynamic pressures: the Corotating Interaction Regions (CIR) and the Interplanetary Coronal Mass Ejections (ICME).

CIRs are recurrent structures of the interplanetary medium [see e.g. *Hundhausen*, 1972]. The rotating and tilted Sun emits fast plasma at the poles and slow plasma near the equator. The fast solar wind stream overtakes the slow solar wind stream, forming the CIR. The CIR is a spiral structure which rotates with the Sun.

Coronal Mass Ejections (CME) are sporadic ejections of huge amounts of plasma and twisted magnetic field lines from the Sun. ICMEs correspond to the propagation of this material in the interplanetary medium [see e.g. *Jian et al.*, 2006].

When a solar wind pressure pulse impacts Mars, the resulting intense solar

wind fluxes move closer to the planet, tailward fluxes of accelerated planetary ions are enhanced and atmospheric escape increases [e.g. *Dubinin et al.*, 2009; *Edberg et al.*, 2010; *Nilsson et al.*, 2011]. Modeling studies also indicate increased atmospheric escape during high dynamic pressure conditions compared to quiet conditions [e.g. *Harnett and Winglee*, 2006; *Kaneda et al.*, 2009].

Hara et al. [2011] reported observations of enhanced fluxes of O^+ ions picked up by the solar wind, precipitating at the Martian terminator, during solar wind pressure pulses. Under normal solar conditions, the picked up O^+ ions have gyroradii larger than the planet (Martian radius = 3397 km) and are quickly swept away by the solar wind. However, during conditions of high upstream dynamic pressure and/or high IMF strength, the magnetic pressure increases in the Martian pile-up region and the gyroradii of the picked up ions decrease [*Hara et al.*, 2011], so that these ions are more likely to impact the planet along their trajectory.

In this paper we investigate how the precipitating H^+ and He^{2+} ions react to pressure pulses. Section 2 presents the instrumentation and the methodology. Section 3 describes the results. Section 4 discusses the results in relation to previous work. Section 5 concludes the paper.

2 Instrumentation and data selection

We use in situ ion and electron measurements from the Analyzer of Space Plasma and Energetic Atoms (ASPERA-3) package [*Barabash et al.*, 2006] onboard the Mars Express (MEX) spacecraft. We use the ELeCtron Spectrometer (ELS) and the Ion Mass Analyzer (IMA). ELS measures 2-D distributions of the electron flux in the energy range 5 eV–15 keV with a field of view of $4^\circ \times 360^\circ$ divided into 16 azimuth sectors, and a time resolution of 4 s. IMA measures distributions of the fluxes of different ion species, including H^+ , He^{2+} ,

O^+ , with m/q resolution in the energy range 200 eV/ q –36 keV/ q . In practice, the lower energy limit to detect protons is ~ 1.2 keV for the intermediate post-acceleration level. IMA gives a 2-D measurement of the ion fluxes (16 azimuth sectors), for all energies, at a time resolution of 12 s. A full distribution with a field of view of $90^\circ \times 360^\circ$ is obtained in 192 s (one IMA scan), using electrostatic sweeping to get $\pm 45^\circ$ coverage out of the plane of the aperture (sweep over elevation angles). We use data from July 2006 to July 2010 (during the solar minimum), except May 2007 and November 2009 when new IMA energy tables were uploaded. We consider altitudes from ~ 260 km (pericenter) up to 2000 km, in the region $X_{\text{MSO}} > 0$ (dayside). In the Mars Solar Orbital (MSO) Cartesian coordinate system, the X_{MSO} axis points from the center of Mars toward the Sun, the Y_{MSO} axis points opposite to the Martian orbital velocity vector and the Z_{MSO} axis completes the right-handed system.

We are only interested in precipitation events observed inside the ionosphere. We have manually identified and selected proton and alpha particle fluxes (with \sim keV energy) in the presence of ionospheric photoelectrons and in the absence of magnetosheath electrons. The method is the same as used by *Diéval et al.* [2012b]. There is a precipitating flux during an IMA scan if the downward-integrated flux is non-zero. When an IMA scan meets such requirements, we say we have found an “event” of proton precipitation or an “event” of alpha particle precipitation. We exclude from the consideration time periods when the data were regarded invalid (instrumental effects, etc.). To separate solar wind alpha-particles from low energy planetary H_2^+ (both have $m/q=2$, where m is the ion mass and q the elementary charge), we consider the mass channel $m/q=2$ for energies above 200 eV only.

We treat proton events and alpha particle events independently, and we do not attempt to examine the differences in solar

wind ion composition during different sets of external conditions.

We use an extended version of the list of solar wind pressure pulse encounters with Mars (ICMEs and CIRs) determined by *Edberg et al.* [2010]. *Edberg et al.* [2010] describes in detail the automatic selection of solar wind pressure pulse intervals from the magnetic field and ion data measured by the Advanced Composition Explorer (ACE) spacecraft, which monitors the solar wind upstream of the Earth. The arrival time at Mars of such solar wind pressure pulse is calculated following the method of *Vennerstrom et al.* [2003] [see *Edberg et al.*, 2010]. This calculated time is then compared with the electron observations from MEX, to get a more accurate arrival time, as well as an end time of the pressure pulse encounter, which we use in this work. During the observation period, 121 automatically selected ICMEs/CIRs had counterparts in the MEX data at Mars (no large gap in MEX data). To this list, we add 72 intervals manually selected in the MEX data, suggesting an ICME/CIR passage. For these 72 intervals, we manually check for counterparts in the ACE data: either no counterpart can be found (cases of an ICME hitting only MEX but not ACE) or a counterpart is identified by eye in the ACE data but does not meet the automatic selection criterion. The full list contains 193 intervals of solar wind pressure pulse encounters at Mars. Finally, we check the intervals for valid dayside IMA data below the local IMB. The final numbers of pressure pulse intervals are 150 for the proton study and 149 for the alpha particle study, respectively.

3 Observations

Examples of precipitating H^+ and He^{2+} are shown in Figure 1. The left column shows a proton event (panels a, b, and c) on 11 August 2007 from 0715 to 0730 UT, during orbit # 4627. The dayside ionosphere electron spectra are characterized by narrow photoelectron peaks (horizontal lines

between 20–30 eV, *Frahm et al.*, 2006) between 0715 and ~0723 UT in panel b. The proton precipitation event is detected in the ionosphere at 0722 UT (altitude ~1000 km, SZA = 29°, energy range 1.1–1.7 keV). The PEB is crossed outbound at ~0723 UT. The IMB is crossed outbound at 0724 UT (solar zenith angle SZA = 28°, altitude ~1100 km). Afterwards, the magnetosheath plasma is recognized by high fluxes of electrons at suprathermal energies (40–300 eV). This case shows clear crossings of the plasma boundaries, suggesting quiet solar wind conditions.

The right column of Figure 1 shows an alpha particle event (panels d, e, and f), on 13 August 2007 from 1930 to 1950 UT, during orbit # 4636. The dayside ionosphere is visible from 1930 to ~1937 UT (panel e). The precipitating He²⁺ event is detected at 1935–1936 UT in the ionosphere (altitude ~580–620 km, SZA ~43–44°, energy = 3 keV/q). Between ~1937 and ~1943 UT, there are multiple crossings of the ionosphere/magnetosheath interface, where we see both ionospheric photoelectrons and reduced fluxes of shocked electrons: this is the magnetic pile-up region. This result suggests unsteady solar wind conditions and makes the identification of plasma boundary crossings difficult. We choose to place the outbound PEB crossing at ~1937 UT and the outbound IMB crossing at ~1943 UT (SZA = 52°, altitude = 440 km). The IMB crossing occurs at low altitude on 13 August, compared to the crossing on 11 August: the magnetosphere was more compressed than usual. The magnetosheath is present from ~1943 UT. There is a dip in the suprathermal electron flux between 1944 and 1945 UT, indicating that the plasma boundaries moved to higher altitudes during this interval, likely because of a short-duration decrease of the upstream dynamic pressure. The disturbed solar wind conditions shown by the MEX data on 13 August 2007 are the results of a CIR encounter with Mars. The same CIR front reached the ACE spacecraft earlier on 6 August 2007.

Figure 2 gives an overview of the passage of this CIR at Earth and then at Mars. Panels a, b, c, and d are time series of ACE data showing the IMF strength, the density, the bulk velocity and the dynamic pressure of the solar wind protons, respectively, from 6 August 2007 (0000 UT) to 9 August 2007 (0000 UT). The magnetic field is given by the MAGnetometer MAG [*Smith et al.*, 1998] and the solar wind parameters are given by the Solar Wind Electrons, Protons, and Alpha Particle Monitor SWEPAM [*McComas et al.*, 1998]. At the beginning of the interval, the solar wind conditions are quiet: IMF strength = 4 nT, solar wind bulk velocity = 290 km s⁻¹. On 6 August 2007 at 0400 UT, the spacecraft meets the CIR front. During the passage of the CIR, there are increases of the solar wind density (up to 26 cm⁻³), of the IMF strength (up to 18 nT), and of the dynamic pressure (up to 8 nPa), followed by a decline of these parameters down to their nominal values at the end of the CIR encounter, on 7 August 2007 at 0830 UT. CIRs are indeed characterized by high values of the magnetic field strength, plasma density and dynamic pressure. Inside the CIR, the solar wind bulk speed increases more gradually to finally reach a maximum value of ~690 km s⁻¹ (panel c). After the passage of the CIR, the bulk velocity slowly decreases during several days.

Panel e is an electron energy time spectrogram measured by MEX, from 11 August 2007 (0350 UT) to 14 August 2007 (2332 UT). The panel shows low altitude data intervals measured during 14 consecutive orbits (the orbit is elliptical). The estimated period of the impact of the pressure pulse is indicated by a horizontal black bar from 11 August 2007 (~0930 UT) to 13 August 2007 (~2300 UT), by visual identification. Indeed, the electron flux is hotter and more intense during this period, compared to the periods before and after the CIR passage. The times of the two precipitation events previously discussed are marked by arrows. The proton event on

11 August 2007 occurred during the quiet upstream conditions which preceded the impact of the CIR front at Mars. The He^{2+} event occurred on 13 August 2007 when the upstream conditions were still disturbed at the end of the passage of the CIR.

Next, we compare the H^+ and He^{2+} precipitation events during the two regimes of upstream conditions. Figure 3 shows the IMA data coverage below the local dayside IMB, in the $X_{\text{MISO}}\text{-}R_{\text{MISO}}$ plane, for the proton study. Panel a shows the data during quiet conditions and panel d shows the data during pressure pulses. The data coverage for the alpha particle study is similar and is not shown. The ICMEs/CIRs represent 22.6% of the data coverage and the quiet upstream conditions represent the rest. *Edberg et al.* [2010] estimated that pressure pulses impacted Mars during ~15% of the time. However, we also include pressure pulse intervals at Mars which were not identified by the automatic selection used by *Edberg et al.* [2010], thus increasing our proportion of pressure pulse periods. Table 1 summarizes the data coverage during both sets of solar wind conditions, for the proton and alpha particle studies.

As seen from Fig. 3 (panels a and d), the coverage below the IMB is best at low altitudes around the terminator, away from the subsolar point. The blue pixels above the IMB model of *Dubin et al.* [2006] (the magenta curve in the figure) indicate that the spacecraft sometimes samples the ionosphere at altitudes above the model, because the altitude of the IMB changes with varying solar wind conditions.

The spatial location of the precipitation events in the $X_{\text{MISO}}\text{-}R_{\text{MISO}}$ plane during quiet solar wind conditions is shown in the top row (panel b: protons, panel c: alpha particles) and during pressure pulses in the bottom row (panel e: protons, panel f: alpha particles). Most of the proton and alpha particle events are located below the position of the IMB model, while a few events can also be found above the model, since we consider all observations below the locally observed IMB. The events are found

at both low altitudes and high altitudes during quiet external conditions. The altitude range of the events is restricted to low altitudes during pressure pulse encounters because the induced magnetosphere is compressed. Fewer events are detected during periods of disturbed external conditions.

We have examined the distribution of downward particle fluxes for the proton events and for the alpha particle events, comparing periods of quiet external conditions with periods of disturbed external conditions. Figure 4 shows histograms of the particle flux for the proton events (panel a) and for the alpha particle events (panel b). The black shaded distribution corresponds to the quiet upstream conditions and the grey shaded distribution corresponds to the CIR/ICME passages.

Panel a shows that the shape of the distribution of fluxes of the proton precipitation events is similar during quiet external conditions and during pressure pulses, both ranging from 10^4 to 10^6 $\text{cm}^{-2}\text{s}^{-1}$, although the statistics are poorer in the case of the pressure pulse periods due to the small number of events. During quiet and disturbed upstream conditions, the median values of the proton event flux are $1.2 \cdot 10^5$ $\text{cm}^{-2}\text{s}^{-1}$ and $8.6 \cdot 10^4$ $\text{cm}^{-2}\text{s}^{-1}$, respectively. Panel b in Fig. 4 shows that the distributions of the fluxes of the alpha particle events have a similar shape during quiet external conditions and during pressure pulses, and both range from 10^3 $\text{cm}^{-2}\text{s}^{-1}$ to 10^6 $\text{cm}^{-2}\text{s}^{-1}$. The statistics are again poorer in the case of the pressure pulse periods. During quiet and disturbed upstream conditions, the median values of the alpha particle event flux are $8.8 \cdot 10^4$ $\text{cm}^{-2}\text{s}^{-1}$ and $4.3 \cdot 10^4$ $\text{cm}^{-2}\text{s}^{-1}$, respectively. We conclude that the H^+ and He^{2+} event fluxes do not increase during solar wind disturbances.

We also calculate the occurrence frequency of detecting H^+ and He^{2+} events during quiet solar wind conditions and during ICME/CIR passages. Tables 2, 3a-b and 4 summarize the occurrence frequency

and typical fluxes of the proton events and alpha particle events during both sets of upstream conditions.

For the protons the occurrence frequencies are 1.01% during ICMEs/CIRs encounters and 3.39% during quiet conditions (Table 3a). The occurrence frequency is a factor ~ 3 lower during disturbed solar wind conditions. The majority of pressure pulses contains no proton event while the pressure pulse intervals represent on average $\sim 23\%$ of the data coverage (Table 2).

For the alpha particles the occurrence frequencies are 1.30% during ICMEs/CIRs encounters and 2.75% during quiet conditions (Table 3b). The occurrence frequency is a factor ~ 2 lower during disturbed solar wind conditions. Here again, the majority of the pressure pulses contains no alpha particle event (Table 2).

The dataset during disturbed conditions is roughly 4 times smaller than the dataset during quiet conditions. We thus need to check whether the difference in occurrence frequency is significant. For this purpose, we compare the results during pressure pulses with intervals of similar number of IMA scans drawn from the period of quiet conditions. We take 4 intervals of 2000 scans each. The occurrence frequency calculated from chronological intervals is biased by the orbit geometry, which evolves over time. Instead, we take random intervals, and we calculate the median occurrence frequency of detecting the precipitation events in these intervals. When comparing the results, we assume that the CIR/ICMEs regularly impact Mars during short periods of arbitrary orbital geometry, and that this dataset can be considered as a random group.

The median occurrence frequency for the proton events during quiet conditions is 3.45: this is a factor ~ 3 larger than the occurrence frequency of 1.01 during pressure pulses. The median occurrence frequency for the alpha particle events during quiet conditions is 2.70: this is a

factor ~ 2 larger than the occurrence frequency of 1.30 during pressure pulses. Therefore, there is a significant difference in the occurrence frequency of measuring the H^+ and He^{2+} events during quiet solar wind conditions and during ICME/CIR passages. The results are summarized in Table 4.

4 Discussion

The occurrence frequency of detecting the precipitating solar wind ions is significantly lower during pressure pulses than during quiet conditions. Although the magnetosheath flux is observed to be larger and to reach lower altitudes during the passage of pressure pulses [e.g. *Dubin et al.*, 2009], we find that the precipitating flux itself does not increase. This result means that a smaller fraction of the upstream solar wind flux can precipitate under these conditions, contrary to modelers' expectations [*Brecht*, 1997; *Harnett and Winglee*, 2006], and suggests that the magnetic barrier is a more effective obstacle to the H^+ and He^{2+} precipitation during pressure pulses. We recall that we take the H^+ and He^{2+} events within the ionosphere, clearly below the IMB. The precipitation events we are looking for are thus not related to the motion of plasma boundaries, but to the crossing of boundaries by some precipitating ions.

The effectiveness of the magnetic barrier as an obstacle to the H^+ and He^{2+} precipitation is determined by the thickness of the magnetic barrier in terms of H^+ gyroradii and He^{2+} gyroradii. The thickness in terms of ion gyroradii depends on the total magnetic flux in the magnetic barrier. If the total magnetic flux is constant in the magnetic barrier, then a thinner magnetic barrier leads to a higher magnetic field strength and to smaller ion gyroradii, but the thickness of the obstacle in term of ion gyroradii remains approximately the same.

The total magnetic flux should increase with respect to quiet upstream conditions in the magnetic barrier during a pressure pulse, to explain the lesser solar wind ion precipitation. We suggest that this

is possible when the magnetosheath flow is decelerated by a stronger mass loading under these conditions. The increased magnetic field in the magnetic barrier region penetrates deeper into the ionosphere (we assume no change in the ionosphere conductivity during the pressure pulse events). Therefore, the magnetic field tubes are dragged through the ionosphere layers with higher ion density and, thus, get more loaded by the planetary ions, mostly O^+ . This results in the increase of the ionospheric erosion and the total ion escape, indeed, reported by modelers [e.g. *Kaneda et al.*, 2009] and observers [e.g. *Edberg et al.*, 2010; 2011]. The additional mass of planetary ions into the solar wind causes a deceleration of the solar wind at low altitudes, due to the conservation of momentum [e.g. *Dubinin et al.*, 2000]. The solar wind magnetic field, frozen-in into the plasma flow, takes a longer time to sweep past the planet. The IMF piles up even more on the dayside before it is convected to the nightside, leading to a larger total magnetic flux in the magnetic barrier. Furthermore, the IMF strength in the upstream solar wind is typically larger than usual (several tens of nT), and this also can contribute to increase the total magnetic flux in the magnetic barrier. Measurements by the Mars Global Surveyor orbiter indeed showed an enhanced magnetic field strength in the magnetic barrier during solar wind disturbances [e.g. *Crider et al.*, 2005]. Also, models indicate that the magnetic barrier is more developed during conditions of high IMF strength and high dynamic pressure, [e.g. *McKenna-Lawlor*, 2012]. The magnetic barrier becomes a thicker obstacle in terms of solar wind ion gyroradii, and the solar wind precipitation decreases.

We can compare the results for the precipitation events with the modeling results by *Brecht* [1997] and *Harnett and Winglee* [2006]. They performed simulations with nominal and high values of solar wind density, speed and IMF strength and they found that the solar wind precipitation is largest for extreme upstream

conditions. These results are consistent with the more frequent observations of solar wind plasma at low altitudes reported during high dynamic pressure conditions [e.g. *Brain et al.*, 2005]. However, the models predict that the solar wind precipitation occurs all the time and for any set of upstream conditions. The models and their stationary inputs do not reproduce the intermittent solar wind ion precipitation as it is observed [*Diéval et al.*, 2012a, 2012b; *Stenberg et al.*, 2011]. Furthermore, the modelers may simply consider the altitude of the IMB as an indicator of the depth reached by the magnetosheath plasma. In contrast, we made our analysis for intervals of ionosphere without magnetosheath electron spikes, because we want to be sure not to include any low altitude magnetosheath encounters. Finally, *Kallio and Janhunen* [2001] reported a decrease of the solar wind proton precipitation rate in their model when taking into account the planetary O^+ production rate from the ionosphere and from the oxygen corona.

5 Conclusion

We performed a statistical study of precipitating proton and alpha particle events with \sim keV energy measured in the Martian dayside ionosphere by Mars Express. We found that the solar wind ion precipitation is less frequent during ICME/CIR encounters: a factor \sim 3 for the H^+ precipitation and a factor \sim 2 for the He^{2+} precipitation. In addition, the precipitating flux does not increase during pressure pulses.

The total magnetic flux in the magnetic barrier determines the thickness of the magnetic barrier in terms of ion gyroradii, and thus the effectiveness of the obstacle to the solar wind ion precipitation. We suggest that the total magnetic flux can increase in the magnetic barrier during the impact of a pressure pulse. This is possible since the mass loading of the solar wind by planetary O^+ ions is expected to be stronger during pressure pulses, due to the penetration of the IMF to lower altitudes.

The more effective mass loading decelerates the solar wind flow close to Mars. This in turn increases the pile up of the magnetic field on the dayside of Mars, and thus the total magnetic flux increases in the magnetic barrier. The magnetic barrier becomes thicker in terms of solar wind ion gyroradii, which causes the reduction of the H^+ and He^{2+} precipitation during pressure pulses.

Acknowledgements.

C. D. and G. S. are supported by the Swedish National Graduate School of Space Technology of the Luleå University of Technology. C. D. acknowledges funding from Kungliga Vetenskapsakademien. N. J. T. E. is supported by the Swedish National Space Board. The Swedish contribution to the ASPERA-3 experiment is supported by the Swedish National Space Board.

References.

- Barabash, S., et al. (2006), The Analyzer of Space Plasmas and Energetic Atoms (ASPERA-3) for the Mars Express Mission, *Space Sci. Rev.*, 126(1-4), 113-164, doi:10.1007/s11214-006-9124-8.
- Brain, D. A., et al. (2005), Variability of the altitude of the Martian sheath, *Geophys. Res. Lett.*, 32, L18203, doi:10.1029/2005GL023126.
- Breus, T. K., et al. (1991), The solar wind interaction with Mars - Consideration of Phobos 2 mission observations of an ion composition boundary on the dayside, *J. of Geophys. Res.*, 96, 11165-11174, doi: 10.1029/91JA01131.
- Crider, D. H., et al. (2005), Mars global surveyor observations of the halloween 2003 solar superstorm's encounter with Mars, *J. of Geophys. Res.*, 110, A09251, doi: 10.1029/2004JA010881.
- Diéval, C., et al. (2012a), A case study of proton precipitation at Mars: Mars Express observations and hybrid simulations, *J. of Geophys. Res.*, 117, A06222, doi: 10.1029/2012JA017537.
- Diéval, C., et al. (2012b), A statistical study of proton precipitation onto the Martian upper atmosphere: Mars Express observations, under revision for *J. of Geophys. Res.*.
- Dubinin, E., et al. (2000), Multi-instrument study of the upstream region near Mars: The Phobos 2 observations, *J. of Geophys. Res.*, 105, (A4), 7557-7572, doi: 10.1029/1999JA900400.
- Dubinin, E., et al. (2006), Plasma Morphology at Mars. Aspera-3 Observations, *Space Sci. Rev.*, 126, 209-238, doi: 10.1007/s.11214-006-9039-4.
- Dubinin, E., et al. (2008), Structure and dynamics of the solar wind/ionosphere interface on Mars: MEX-ASPERA-3 and MEX-MARSIS observations, *Geophys. Res. Lett.*, 35, L11103, doi: 10.1029/2008GL033730.
- Dubinin, E., et al. (2009), Ionospheric storms on Mars: Impact of the corotating interaction region, *Geophys. Res. Lett.*, 36, L01105, doi:10.1029/2008GL036559.
- Edberg, N. J. T., et al. (2010), Pumping out the atmosphere of Mars through solar wind pressure pulses, *Geophys. Res. Lett.*, 37, L03107, doi:10.1029/2009GL041814.
- Edberg, N. J. T., et al. (2011), Atmospheric erosion of Venus during stormy space weather, *J. of Geophys. Res.*, 116, A09308, doi:10.1029/2011JA016749.
- Frahm, R. A., et al. (2006), Carbon dioxide photoelectron energy peaks at Mars, *Icarus*, 182(2), 371-382, doi: 10.1016/j.icarus.2006.01.014.
- Hara, T., et al. (2011), Heavy - ion flux enhancement in the vicinity of the Martian ionosphere during CIR passage: Mars

- Express ASPERA - 3 observations, *J. of Geophys. Res.*, 116, A02309, doi:10.1029/2010JA015778.
- Harnett, E. M., and R. M. Winglee (2006), Three dimensional multifluid simulations of ionospheric loss at Mars from nominal solar wind conditions to magnetic cloud events, *J. of Geophys. Res.*, 111, A09213, doi: 10.1029/2006JA011724.
- Hundhausen, A. J. (1972), Coronal Expansion and Solar Wind, Phys. Chem. Space, vol. 5, Springer, New York.
- Jian, L., et al. (2006), Properties of coronal mass ejections at one AU during 1995-2004, *Sol. Phys.*, 239, 393-436, doi: 10.1007/s11207-006-0133-2.
- Kallio, E., and P. Janhunen (2001), Atmospheric effects of proton precipitation in the Martian atmosphere and its connection to the Mars-solar wind interaction, *J. Geophys. Res.*, 106(A4), 5617-5634, doi: 10.1029/2000JA239.
- Kaneda, K., et al. (2009), Solar wind control of the hot oxygen corona around Mars, *J. Geophys. Res.*, 114, E02007, doi: 10.1029/2008JE003234.
- Lundin, R., et al. (2004), Solar wind-induced atmospheric erosion at Mars: first results from ASPERA-3 on Mars Express, *Science*, 305, 5692, 1933-1936, doi:10.1126/science.1101860.
- McComas, D., et al. (1998), Solar Wind Electron Proton Alpha Particle Monitor (SWEPAM), *Space Sci. Rev.*, 86(1-4), 563-612, doi: 10.1023/A:1005040232597.
- McKenna-Lawlor, S., et al. (2012), Magnetic shadowing of high energy ions at Mars and how this effect can be simulated using a hybrid model, *Earth Planets Space*, 64, 247-256, doi: 10.5047/eps.2011.06.039.
- Mitchell, D. L., et al. (2001), Probing Mars' crustal magnetic field and ionosphere with the MGS Electron Reflectometer, *J. Geophys. Res.*, 106(E10), 23,419-23,427, doi: 10.1029/2000JE001435.
- Nilsson, H., et al. (2011), Heavy ion escape from Mars, influence from solar wind conditions and crustal magnetic fields, *Icarus*, 215, 475-484, doi: 10.1016/j.icarus.2011.08.003.
- Shematovich, V.I., et al. (2011), Protons and hydrogen atoms transport in the Martian upper atmosphere with an induced magnetic field, *J. Geophys. Res.*, 116, A11320, doi: 10.1029/2011JA017007.
- Shematovich, V.I., et al. (2012), He²⁺ transport in the Martian upper atmosphere with an induced magnetic field, submitted to *J. Geophys. Res.*.
- Smith, C. W., et al. (1998), The ACE magnetic fields experiment, *Space Sci. Rev.*, 86(1-4), 613-632, doi: 10.1023/A:1005092216668.
- Stenberg, G., et al. (2011), Observational evidence of alpha particle capture at Mars, *Geophys. Res. Letters*, 38, L09101, doi: 10.1029/2011GL047155.
- Vennerstrom, S., et al. (2003), The magnetic field in the pile-up region of Mars, and its variation with the solar wind, *Geophys. Res. Lett.*, 30(7), 1369, doi: 10.1029/2003GL016883.
- Vignes, D., et al. (2000), The solar wind interaction with Mars: Locations and shapes of the Bow Shock and the magnetic pile-up boundary from the observations of the MAG/ER experiment onboard Mars Global Surveyor, *Geophys. Res. Lett.*, 27, 49-52, doi: 10.1029/1999GL010703.

Tables

Table 1: IMA data coverage below the local IMB and excluding invalid scans ^a.

Proton study	During quiet conditions	During pressure pulses	Total
Number of scans	8452	2474	10926
% of scans	77.4	22.6	100.0
Alpha particle study	During quiet conditions	During pressure pulses	Total
Number of scans	8348	2466	10814
% of scans	77.2	22.8	100.0

^a The data coverage during quiet solar wind conditions and during ICMEs/CIRs passages is given separately for the H⁺ study and the He²⁺ study.

Table 2: Distribution of solar wind pressure pulses according to the presence or absence of precipitating H⁺ events and He²⁺ events.

	With H ⁺ events	No H ⁺ events	Total
Number of pressure pulses	17	133	150
% of pressure pulses	11.3	86.7	100.0
	With He ²⁺ events	No He ²⁺ events	Total
Number of pressure pulses	21	128	149
% of pressure pulses	14.0	86.0	100.0

Table 3a: Distribution of precipitating proton events during pressure pulses and during quiet solar wind conditions.

	Number of events	% of events	Occurrence frequency relative to the period ^a (%)	Average particle flux ^b (cm ⁻² s ⁻¹)	25 th percentile particle flux (cm ⁻² s ⁻¹)	Median particle flux (cm ⁻² s ⁻¹)	75 th percentile particle flux (cm ⁻² s ⁻¹)
ICMEs/CIRs	25	8.0	1.01	1.1·10 ⁵	2.6·10 ⁴	8.6·10 ⁴	2.7·10 ⁵
Quiet conditions	287	92.0	3.39	1.3·10 ⁵	4.0·10 ⁴	1.2·10 ⁵	4.2·10 ⁵
Total events	312	100.0	2.85	1.3·10 ⁵	3.8·10 ⁴	1.2·10 ⁵	4.0·10 ⁵

^aThe occurrence frequency of detecting the proton events is calculated for each period using the number of events divided by the number of IMA scans of the data coverage.

^bThe mean values of the downward particle flux of the proton events are calculated as 10^{^(mean(log₁₀(fluxes)))}.

Table 3b: Distribution of precipitating alpha particle events during pressure pulses and during quiet solar wind conditions ^a.

	Number of events	% of events	Occurrence frequency relative to the period (%)	Mean particle flux ($\text{cm}^{-2}\text{s}^{-1}$)	25 th percentile particle flux ($\text{cm}^{-2}\text{s}^{-1}$)	Median particle flux ($\text{cm}^{-2}\text{s}^{-1}$)	75 th percentile particle flux ($\text{cm}^{-2}\text{s}^{-1}$)
ICMEs/CIRs	32	12.3	1.30	$4.1 \cdot 10^4$	$1.5 \cdot 10^4$	$4.3 \cdot 10^4$	$1.6 \cdot 10^5$
Quiet conditions	229	87.7	2.74	$7.4 \cdot 10^4$	$2.5 \cdot 10^4$	$8.7 \cdot 10^4$	$2.1 \cdot 10^5$
Total events	261	100.0	2.41	$6.9 \cdot 10^4$	$2.3 \cdot 10^4$	$8.0 \cdot 10^4$	$2.0 \cdot 10^5$

^a Same format as in Table 3a.

Table 4: Median occurrence frequency of measuring precipitating H^+ and He^{2+} events during periods of quiet solar wind, calculated from 4 random groups of scans drawn from the dataset, as explained in the text.

	No pressure pulses	Pressure pulses ^a
Occurrence frequency of H^+ events (%)	3.45	1.01
Occurrence frequency of He^{2+} events (%)	2.70	1.30

^a The occurrence frequency of measuring the events during pressure pulses is also repeated from Tables 3a-b.

Figures.

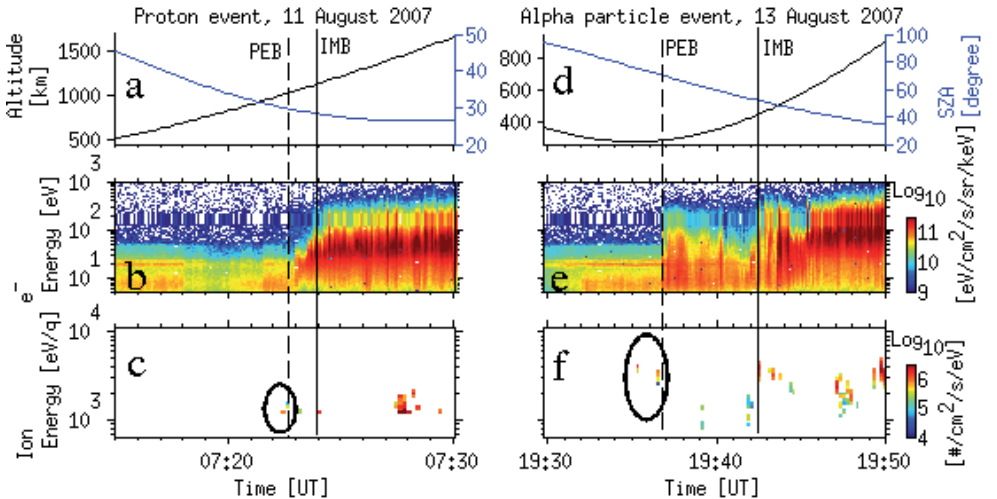


Figure 1. Left column (a, b, and c): A proton precipitation event on 11 August 2007. The vertical solid line marks the IMB crossing and the vertical dashed line marks the PEB crossing. (a): altitude of MEX (black curve, left axis) and SZA of MEX (blue curve, right axis). (b): energy time spectrogram of electrons measured by ELS (averaged over all sectors). (c): energy time spectrogram of protons measured by IMA

(downward flux summed over sectors). Right column (d, e, and f): an alpha particle precipitation event on 13 August 2007. The format is the same as for the left column, except that panel f shows alpha particles.

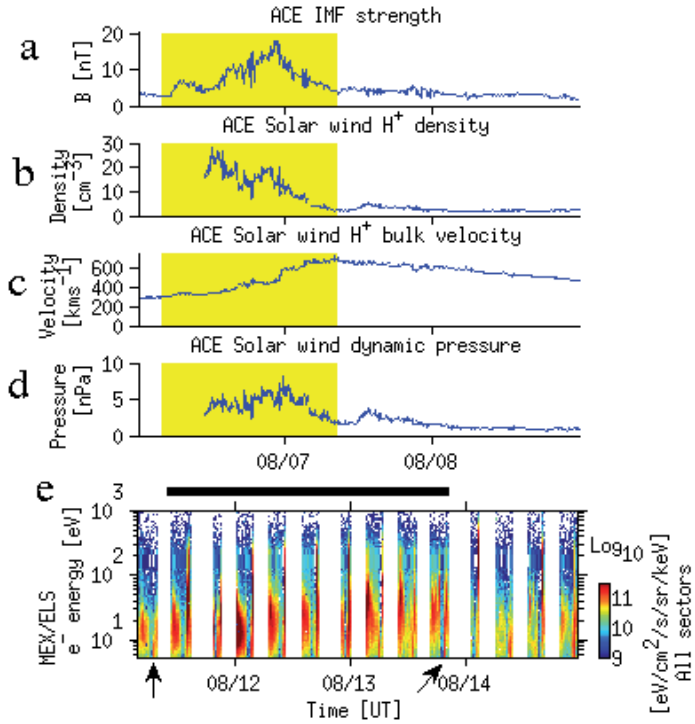


Figure 2. (a), (b), (c), and (d): time series of ACE data. (a): IMF strength. (b): solar wind proton density. The density until 6 August 2007 at 1100 UT is poorly determined and is not shown. (c): solar wind proton bulk velocity. (d): solar wind proton dynamic pressure. The period of the CIR encounter with ACE is indicated by the yellow shading, from 6 August 2007 (0400 UT) to 7 August 2007 (0830 UT). (e): electron energy-time spectrogram (averaged over all sectors) observed by MEX. The white vertical bands are data gaps corresponding to no data taking when the spacecraft is sufficiently far away from the Martian bow shock. The estimated period of the CIR encounter with Mars is indicated by a horizontal black bar, from 11 August 2007 (~0930 UT) to 13 August 2007 (~2300 UT). The times of the two precipitation events previously discussed are indicated by arrows.

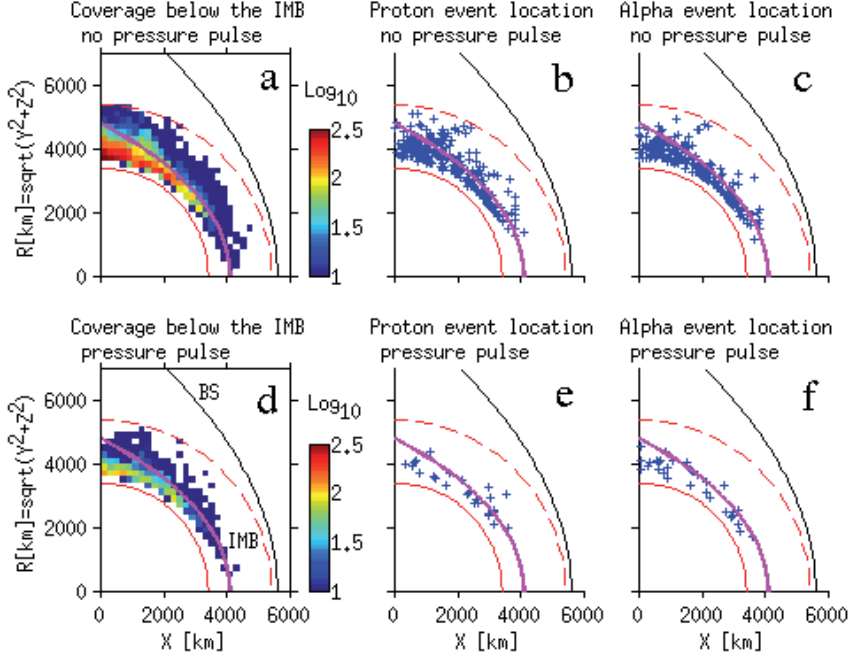


Figure 3. Each panel shows the $X_{\text{MSO}}\text{-}R_{\text{MSO}}$ plane. The horizontal axis is the distance along the Mars Sun line. The vertical axis is the distance $R_{\text{MSO}} = \sqrt{Y_{\text{MSO}}^2 + Z_{\text{MSO}}^2}$ from the Mars Sun line. The spatial bin size is $200 \text{ km} \times 200 \text{ km}$. The red solid curve, the black solid curve and the magenta solid curve, indicate Mars, the bow shock model of *Vignes et al.* [2000], and the IMB model of *Dubinin et al.* [2006], respectively. The red dashed curve shows the altitude limit of 2000 km below which data were considered. Top row (panels a, b, and c): periods of quiet solar wind. Bottom row (panels d, e, and f): periods during solar wind pressure pulses. (a) and (d): data coverage below the IMB, excluding invalid scans. The colorbar indicates the number of IMA scans obtained in each spatial bin. (b), (e), (c), and (f): location of the precipitation events indicated by '+' symbols.

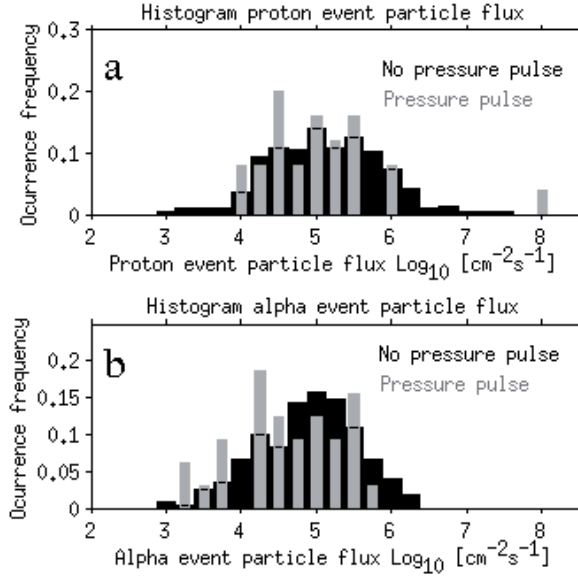


Figure 4. Histograms of the particle flux (a) of the proton precipitation events and (b) of the alpha particle precipitation events. The black shaded histogram and the grey shaded histogram correspond to periods during quiet conditions and periods during solar wind pressure pulses, respectively. Each distribution is normalized by the total number of samples of the population. The grey shaded bin on the far right in panel a contains one outlier event with a flux of $8.1 \cdot 10^7 \text{ cm}^{-2}\text{s}^{-1}$.

PAPER VI

He²⁺ transport in the Martian upper atmosphere with an induced magnetic field

V. I. Shematovich¹, D. V. Bisikalo¹,
G. Stenberg², S. Barabash², C. Dieval^{2,3}
J.-C. Gerard⁴

V. I. Shematovich, Institute of Astronomy, Russian Academy of Sciences, 48 Pyatnitskaya str., Moscow, Russian Federation, (shematov@inasan.ru)

D. V. Bisikalo, Institute of Astronomy, Russian Academy of Sciences, 48 Pyatnitskaya str., Moscow, Russian Federation, (bisikalo@inasan.ru)

G. Stenberg, Swedish Institute of Space Physics, Kiruna SE-98128, Sweden, (gabriella@irf.se)

S. Barabash, Swedish Institute of Space Physics, Kiruna SE-98128, Sweden, (stas@irf.se)

C. Diéval, Swedish Institute of Space Physics, Kiruna SE-98128, Sweden and Division of Space Technology, Department of Computer Science, Electrical and Space Engineering, Luleå University of Technology, Kiruna, Sweden, (catherine@irf.se)

J.-C. Gérard, LPAP, Université de Liège, Liège, Belgium, (jc.gerard@ulg.ac.be)

Abstract

Solar wind helium may be a significant source of neutral helium in the Martian atmosphere. The precipitating particles also transfer mass, energy and momentum. To investigate the transport of He²⁺ in the upper atmosphere of Mars we have applied the Direct Simulation Monte Carlo method to solve the kinetic equation. We calculate the upward He, He⁺ and He²⁺ fluxes, resulting from energy spectra of the downgoing He²⁺ observed below 500 km altitude by the ASPERA-3 instrument onboard Mars Express. The particle and energy fluxes of the downward moving He²⁺ ions were $1-2 \times 10^6 \text{ cm}^{-2} \text{ s}^{-1}$, and the energy flux is equal to $9-10 \times 10^{-3} \text{ erg cm}^{-2} \text{ s}^{-1}$. The calculations of the upward flux have been made for the Martian atmosphere during solar minimum.

It was found, that if the induced magnetic field is not introduced in the simulations the precipitating He²⁺ ions are not backscattered at all by the Martian upper atmosphere. If we include a 20 nT horizontal magnetic field, a typical field measured by Mars Global Surveyor (MGS) in the altitude range of 85 km – 500 km, we find that up to the 30% - 40% of the energy flux of the precipitating He²⁺ ions is backscattered depending on the velocity distribution of the precipitating particles. We thus conclude that the induced magnetic field plays the crucial role in the transport of charged particles in the upper atmosphere of Mars and, therefore, that it determines the energy deposition of the solar wind.

¹Institute of astronomy, Russian Academy of Science, Moscow, Russian Federation

²Swedish Institute of Space Physics, Kiruna, Sweden

³Division of Space Technology, Department of Computer Science, Electrical and Space Engineering, Luleå University of Technology, Kiruna, Sweden

⁴LPAP, Université de Liège, Liège, Belgium

1. Introduction

Mars is immersed in the magnetized, supersonic solar wind flow and as a response induced currents are set up in the Martian ionosphere. The currents result in magnetic fields deviating the solar wind. A void in the solar wind is created, the induced magnetosphere. The interplanetary magnetic field lines pile up and drape around this obstacle. A bow shock is also formed, which enable the solar wind flow to slow down from supersonic to subsonic velocities [e.g. *Nagy et al.*, 2004]. The boundary between the (shocked) solar wind and the induced magnetosphere, often referred to as the induced magnetosphere boundary (IMB), is, however, not completely closed. The gyro-radii of the solar wind particles are large enough, compared to the size of the IMB, to enable the particles to gyrate through the piled up magnetic field and directly interact with the Martian upper atmosphere. This unique property of the small Martian induced magnetosphere allowing solar wind protons and alpha-particles assimilation in the Martian atmosphere represents an important source of some atmospheric species.

There are two principal reasons to investigate the transport of helium through the induced magnetosphere. Firstly, precipitating solar wind particles may transfer mass, energy and momentum to the Martian upper atmosphere. Secondly, solar wind He^{2+} is likely a significant source of neutral helium in the atmosphere and a detailed knowledge of the helium transport to and from the Martian atmosphere is the key for understanding the evolution of Mars. Radioactive decay of uranium and thorium in the interior of the planet leads to the formation of ${}^4\text{He}$, which slowly outgasses to the atmosphere. On Earth the outgassing of helium is balanced by a continuous loss of atmospheric helium due to photoionization and electron impact ionization followed by escape from the cusp region ("polar wind") [*Krasnopolsky*, 1993]. The situation could be expected to be similar on Mars. However, comparing the spectroscopic observations of neutral helium

made by the EUVE satellite [*Krasnopolsky et al.*, 1994] with the observations of escaping He^+ made by the PHOBOS-2 spacecraft [*Barabash and Norberg*, 1994; *Barabash et al.*, 1995] lead to the conclusion that the production of helium does not balance the loss. An additional source of helium is needed and currently solar wind He^{2+} is believed to be the main source of the Martian neutral helium [*Krasnopolsky and Gladstone*, 2005], constituting 90% of the total production. Recent studies using data from Mars Express strengthen this picture. Solar wind He^{2+} is regularly observed deep inside the Martian ionosphere [*Stenberg et al.*, 2011] and it is likely that a substantial part of it is neutralized and captured in the atmosphere. Ultimately, a quantitative understanding of the helium balance will improve the estimates of the uranium and thorium abundances and put constraints on the differentiation process in the primordial nebula.

Observations are sparse. The mixing ratio of neutral helium in the Martian atmosphere is obtained from spectroscopic observations of the helium line at 584 Å [*Krasnopolsky and Gladstone*, 2005]. Evidence of solar wind penetration of the IMB is reported in a few papers [*Lundin et al.*, 2004; *Stenberg et al.*, 2011; *Diéval et al.*, *in press* 2012] but no quantitative analysis of the average net precipitation is yet presented. The estimate of escaping He^+ from the atmosphere is still based on the observations by PHOBOS-2 made during solar maximum only [*Barabash et al.*, 1995].

Precipitation of solar wind particles has also been studied with computer models [e.g., *Brecht*, 1997; *Kallio and Janhunen*, 2001; *Modolo et al.*, 2005]. *Chanteur et al.* (2009) focus especially on the entry of solar wind He^{2+} . They show that approximately 30% of the He^{2+} flux through an area corresponding to the cross section of the planet is removed from the solar wind due to charge exchange into either He^+ or neutral He atoms. A substantial part of the created neutrals eventually impacts the exobase and are considered captured in the atmosphere. The deposition rate of neutral helium is estimated

to about $1.5 \times 10^{23} \text{ s}^{-1}$. The ultimate fate of the He^+ ions is not discussed further and it is just assumed that all precipitating helium assimilates in the atmosphere. In this paper we address the issue how the precipitating He^{2+} interacts with the Martian atmosphere.

To investigate the He^{2+} transport through the upper Martian atmosphere we used the Direct Simulation Monte Carlo (DSMC) model [Shematovich *et al.*, 2011] and measurements of He^{2+} inside the induced magnetosphere by the ASPERA-3 experiment (Analyzer of Space Plasmas and Energetic Atoms) onboard Mars Express [Barabash *et al.*, 2006]. The main features of the model are discussed in Sections 2 and 3 including a comprehensive review of the available cross sections for the relevant processes. In Section 4 results of simulations are presented. Section 5 summarizes the results and the conclusions.

2. The model description

He^{2+} precipitation

Interactions of precipitating energetic He^{2+} ions with the main atmospheric constituents include the momentum and energy transfer in elastic and inelastic collisions, ionization of target atmospheric molecules/atoms, charge transfer and electron capture collisions. Energetic He atoms and He^+ ions produced by He^{2+} ion impacts further collide with the main atmosphere constituents, transferring their momentum and kinetic energy to atmospheric particles by elastic and inelastic collisions, ionization and stripping processes. The collisional processes describing the penetration of the energetic $\text{He}^{2+}/\text{He}^+/\text{He}$ through the ambient atmospheric gas can be written as:

$$\text{He}^{2+}(\text{He}^+, \text{He}) + M \rightarrow \begin{cases} \text{He}_f^{2+}(\text{He}_f^+, \text{He}_f) + M^* \\ \text{He}_f^{2+}(\text{He}_f^+, \text{He}_f) + M^+ + e \\ \text{He}_f(\text{He}_f^+, \text{He}_f^{2+}) + M^+(M) + (e). \end{cases}$$

Here, M denotes the major atmospheric constituents included in the model. Secondary fast He_f atoms and He_f^+ and He_f^{2+} ions produced by momentum transfer and stripping reactions loop the reaction set shown above. Consequently, the interaction

of the precipitating He_f^{2+} ions with the main neutral constituents of the thermosphere must be considered as a cascade process producing a growing set of translationally and internally excited particles M^* of the ambient atmospheric gas.

Mathematical description

To analyze the penetration of energetic $\text{He}/\text{He}^+/\text{He}^{2+}$ particles into the atmospheric gas, we use the kinetic Boltzmann equations [Gérard *et al.*, 2000; Shematovich *et al.*, 2011] with the collision term:

$$\begin{aligned} \mathbf{v} \frac{\partial}{\partial \mathbf{r}} f_\alpha + \left(\mathbf{g} + \frac{e}{m_\alpha} \mathbf{v} \times \mathbf{B} \right) \frac{\partial}{\partial \mathbf{v}} f_\alpha &= \\ = Q_\alpha(\mathbf{v}) + \sum_{M=H, H_2, He, O, N_2, CO_2} J_{mt}(f_\alpha, f_M), & \quad (1) \\ \alpha = \text{He}^{2+}, \text{He}^+, \text{He} & \end{aligned}$$

where $f_\alpha(\mathbf{r}, \mathbf{v})$, and $f_M(\mathbf{r}, \mathbf{v})$ are the velocity distribution functions for helium atoms or ions, and components of ambient gas, respectively, e the electron charge, and m_α the helium mass. The left side of the kinetic equation describes the transport of particles in the planetary gravitational and induced magnetic fields. The right-hand side term Q_α is the production rate of respective particles in charge-exchange and stripping collisions. The elastic and inelastic scattering terms J_{mt} for $\text{He}/\text{He}^+/\text{He}^{2+}$ collisions with the ambient atmospheric species are written in the standard form [Shematovich *et al.*, 1994]. It is assumed that the ambient atmospheric gas is characterized by local Maxwellian velocity distribution functions.

Stochastic approach

The DSMC method used to solve the kinetic equation (1) implies generation of a sample of paths for the state of the physical system under study – $\text{He}/\text{He}^+/\text{He}^{2+}$ thermalization and transport in the transition region of the upper atmosphere. It is an efficient tool for studying such complex kinetic systems in the stochastic kinetic systems in the stochastic approximation [Shematovich *et al.*, 1994; Bisikalo *et al.*, 1995; Gérard *et al.*, 2000;

Shematovich et al., 2011]. The details of the algorithmic realization of this numeric model were given earlier [*Shematovich et al.*, 1994; *Bisikalo et al.*, 1995]. The statistics in the DSMC model is controlled using the standard procedures [*Shematovich*, 2008]. When the steady state is reached then it is possible to accumulate the statistics with the needed accuracy. In the calculations presented below the fluxes and other characteristics were calculated with the variation below 10%. The low-energy parts of $\text{He}/\text{He}^+/\text{He}^{2+}$ fluxes were calculated with the sufficient accuracy because these particles were slowed down due to the wealth of collisions with the ambient atmospheric gas. The energy deposition rate of $\text{He}/\text{He}^+/\text{He}^{2+}$ flux is determined by the cross sections of the collisions with the ambient gas. The key point of this model is the stochastic treatment of the scattering angle distribution. This distribution influences both the energy degradation rate through the loss of energy in the momentum transfer collisions that is proportional to the sine of the scattering angle, and the angle redistribution of the precipitating He^{2+} ions.

Numerical model

We consider the $\text{He}/\text{He}^+/\text{He}^{2+}$ transport between altitudes where He^{2+} ions are efficiently thermalized and atmospheric gas becomes practically collisionless. For the Martian atmosphere, the boundaries are placed at 80 and 500 km. The 80 km altitude is well below the exobase placed near 180 km at low solar activity conditions. To link our model with the actual measurements we chose the upper boundary in the altitude range below 500 km, where measurements of precipitating He^{2+} were made by the ASPERA-3 instrument. The region of the atmosphere under the study was divided into 49 vertical cells, and the altitude dependent cell size is chosen according to the condition that it must be equal to or smaller than the free path length. In the model the radial position and three velocity components for each modeled particle are kept. The modeled particle trajectory is calculated in 3D space for each time step and after that the new radial position is kept. Therefore, He^{2+}

launched at a given angle versus nadir direction can move to different angles and planet curvature is also taken into account.

The altitude distributions of the main neutral species – CO_2 , N_2 , O , H , H_2 , and He were adopted from [*Fox and Hac*, 2009] for a low level of solar activity corresponding to the ASPERA-3 observations. The altitude profiles of the main neutral species adopted in the model are shown in Figure 1.

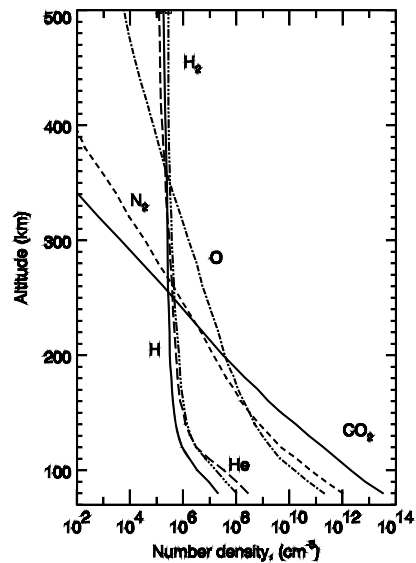


Figure 1. The altitude distributions of the main neutral species – CO_2 , N_2 , O , H , H_2 and He adopted from [*Fox and Hac*, 2009].

The temperature in the considered domain changes from 150 K at lower boundary up to 170 K at the upper boundary.

The Monte Carlo code to model the penetration of high-energy protons and hydrogen atoms into the Earth's atmosphere [*Gérard et al.*, 2000] was modified to take into account the effect of the horizontal magnetic field on the ion trajectories, Martian atmosphere profiles, and respective He^{2+} interaction cross sections. The induced magnetic field has been measured at Mars by the Mars Global Surveyor (MGS) orbiter [*Brain et al.*, 2003] and the Mars Express orbiter [*Akalin et al.*, 2010]. These authors show that the induced magnetic field is

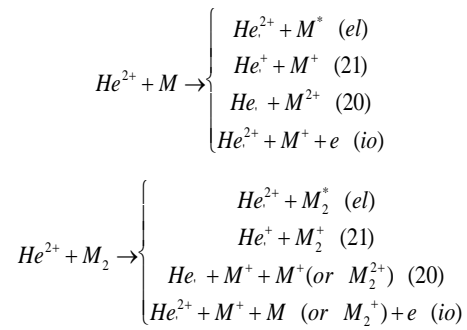
mainly horizontal; its strength decreases with increasing altitude and with increasing solar zenith angle (SZA). The induced magnetic field strength is typically the strongest near the subsolar point (about 40 nT) and reaches a value of 20 nT at the terminator in the altitude range 360-440 km [Alkalin *et al.*, 2010]. Following these measurements we assume the constant in time and uniform in space horizontal magnetic field $B=10, 20, 30, 40,$ and 50 nT for the different runs.

3. Compilation of cross sections for He/He⁺/He²⁺ collisions with atmospheric gas

In the model, the most recent measurements or calculations of the required cross sections were adopted. We consider the energy range 100 eV – 10 keV, relevant to energies of precipitating alpha-particles and include 49 reactions in the model. In general, data on the cross sections for the interaction in this energy range are very limited and we used a number of assumptions and approximations explained in the sections below.

Cross sections for He²⁺ collisions with CO₂, N₂, and O

We have considered 4 processes for the interaction of He²⁺ with atomic (M) and molecular (M₂) atmospheric gas; elastic (σ_{el}), one-electron charge exchange (σ_{21}), two electron charge exchange (σ_{20}), and ionization (σ_{i0}):



Unfortunately the cross sections for the elastic interactions He²⁺ + CO₂, N₂, and O are unknown. To approach these cross

sections we used the same analytic approximations of σ_{ei} as for H⁺ + O₂, N₂, and O taken from the model of the proton aurora at Earth [Gérard *et al.*, 2000] in the energy range [100 eV, 10keV]. The only calculation we found in the literature was cross sections for elastic He + O collisions up to 5 eV [Bovino *et al.*, 2011]. Therefore, we normalized the analytic approximation for the elastic collisions He²⁺ + CO₂ to be equal to the calculated one at 1 eV, i.e., by the factor $\sigma_{ei}(\text{He}+\text{O}; E=1 \text{ eV})/\sigma_{ei}(\text{H}^++\text{O}_2; E=1 \text{ eV})=3.8\times 10^{-15}/3.02\times 10^{-14} = 0.119$. After that we assume that a 3-atom molecule (like CO₂) can be described by the same curve shape with cross section values 3/2 times larger than the ones for a 2-atom molecule. Further we assume that the elastic cross section for He²⁺ + O collisions can be described by the same curve shape as one for H⁺ + O₂ but the scaling factor calculated above should be reduced by factor of 2. For the elastic collisions He²⁺ + N₂ the same procedure as for He²⁺+CO₂ was used, but the scaling factor was evaluated from the paper by Newman *et al.* (1985). We normalized the analytic approximation to be equal to the calculated one at 0.5 keV, i.e., by factor of $\sigma_{ei}(\text{He}+\text{N}_2; E=500 \text{ eV})/\sigma_{ei}(\text{H}^++\text{N}_2; E=500 \text{ eV})=1.92\times 10^{-15}/7.\times 10^{-15} = 0.274$.

For the one-electron and two-electron charge exchange processes σ_{21} and σ_{20} in the collisions of He²⁺ ions with CO₂ and N₂ molecules the cross sections were taken from the Table II in [Kusakabe *et al.*, 2006]. In case of collisions of He²⁺ ions with atomic oxygen O the cross section σ_{21} was taken following [Chanteur *et al.*, 2009], the same as the one for the process He²⁺ + O₂ → He⁺ + O⁺ + O from [Rudd *et al.*, 1985]. The cross section σ_{20} for He²⁺ collisions with O was taken from [Rudd *et al.*, 1985]. Values of σ_{20} and σ_{21} for the interaction of He²⁺ with atomic oxygen were given at energies above 5 keV, therefore following [Chanteur *et al.*, 2009] we adopt the constant values for low energies as $2.\times 10^{-16} \text{ cm}^2$ and $4.\times 10^{-16} \text{ cm}^2$, respectively.

The ionization cross section for the He²⁺ + CO₂ process was not found in the literature. To get σ_{i0} for He²⁺ collisions with

CO₂ molecules we assume that it has the same shape as H⁺+CO₂ in Haider's compilation of cross sections [Haider *et al.*, 2002]. We did not find even a single point to normalize this cross section, therefore we assume that the scaling factor is the same as for interaction with atomic oxygen. For atomic oxygen there are cross sections for ionization by H⁺ from compilation [Haider *et al.*, 2002] and calculations of ionization by He²⁺ ions from [Sahoo, 2000]. Using these data we evaluated the scaling factor as 0.5 at 10 keV, and apply it to $\sigma_{\text{io}}(\text{H}^+ + \text{CO}_2)$ to get an the approximation of the $\sigma_{\text{io}}(\text{He}^{2+} + \text{CO}_2)$ cross section. In case of He²⁺ + N₂ collisions the cross section σ_{io} shape was adopted from [Haider *et al.*, 2002] and the scaling factor was assumed to be equal to 1. For He²⁺ + O collisions the σ_{io} shape was adopted from [Haider *et al.*, 2002] and the scaling factor was taken equal to 0.5 [Sahoo, 2000].

Cross sections for He²⁺ collisions with H, H₂, and He

We assumed that for elastic collisions of He²⁺ ions with H the shape of σ_{el} cross section is similar to the one for the elastic collisions of protons H⁺ with helium atoms given in [Krstic and Schultz, 2006], but to evaluate the scaling factor of $1.08 \times 10^{15} / 2.46 \times 10^{15} = 0.439$ value we used the measurements of elastic cross sections for the process He + He at a collision energy of 500 eV from [Newman *et al.*, 1985]. For elastic collisions of He²⁺ ions with H₂ molecules it was again assumed that the shape of σ_{el} cross section is similar to the one for the elastic collisions of protons H⁺ with helium atoms given in [Krstic and Schultz, 2006], but to evaluate the scaling factor of $9.3 \times 10^{-16} / 5. \times 10^{-16} = 1.86$ value we used the measurements of the elastic cross sections for the process He + H₂ at collision energy of 1500 eV from [Newman *et al.*, 1985]. Similar approximation procedure was used for elastic collisions of He²⁺ ions with He, but the scaling factor of $1.08 \times 10^{-15} / 2.46 \times 10^{-15} = 0.439$ was used in accordance with data for He + He collisions at 0.5 keV from [Newman *et al.*, 1985].

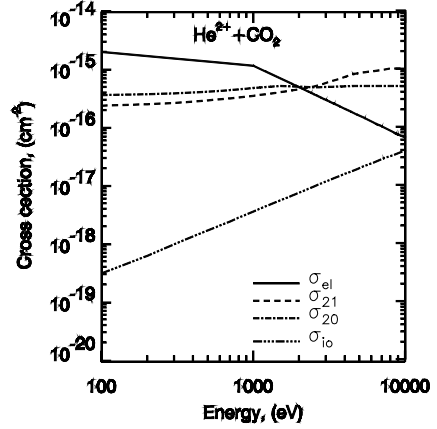


Figure 2a. Compilation of cross sections for He²⁺ elastic (el), 1-electron (21), 2-electron (20) charge transfer, and ionization (io) collisions with CO₂.

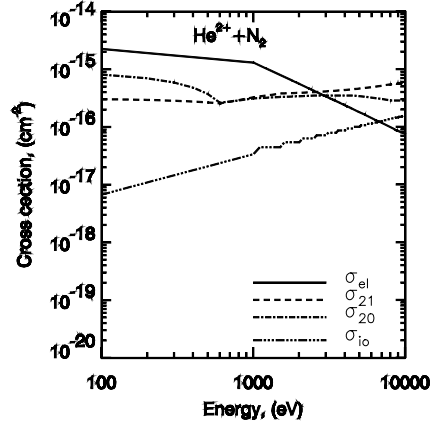


Figure 2b. Compilation of cross sections for He²⁺ elastic (el), 1-electron (21), 2-electron (20) charge transfer, and ionization (io) collisions with N₂.

For the one-electron and two-electron charge exchange processes σ_{21} and σ_{20} in the collisions of He²⁺ ions with H₂ molecules the cross sections were taken from the Table II in [Kusakabe *et al.*, 2006]. In case of collisions of He²⁺ ions with hydrogen and helium atoms the cross sections σ_{21} were taken from [Ito *et al.*, 1993]. For two-electron charge exchange process of He²⁺ collisions with He the value σ_{20} was taken equal to $2.5 \times 10^{-16} \text{ cm}^2$ [Janev *et*

al., 1987; Barnett, 1990]. The cross section $\sigma_{20}\text{He}^{2+} + \text{H}$ is assumed to be negligible.

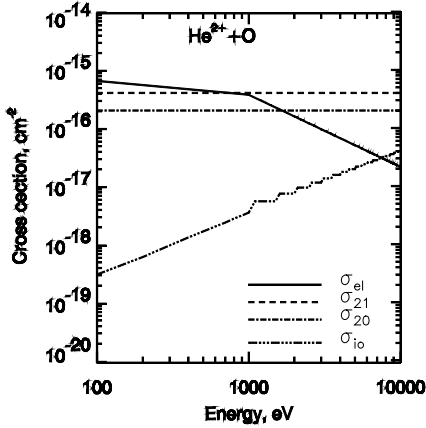


Figure 2c. Compilation of cross sections for He^{2+} elastic (el), 1-electron (21), 2-electron (20) charge transfer, and ionization (io) collisions with O.

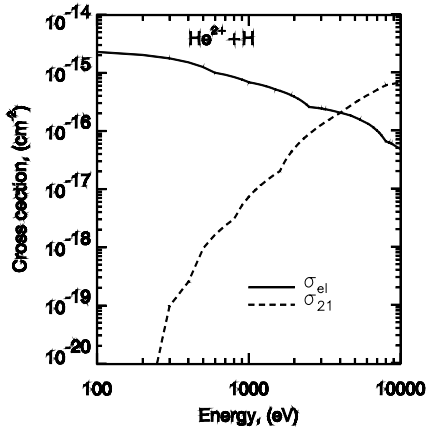


Figure 2d. Compilation of cross sections for He^{2+} elastic (el) and 1-electron (21) collisions with H. The 2-electron (20) charge transfer, and ionization (io) collisions are neglected.

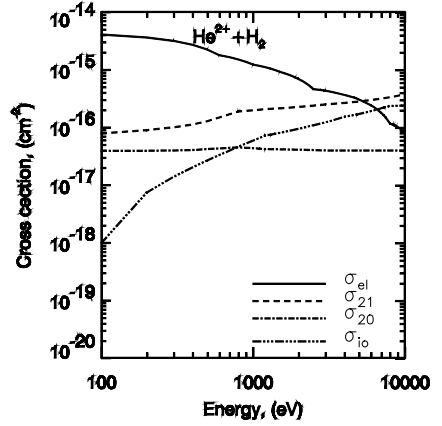


Figure 2e. Compilation of cross sections for He^{2+} elastic (el), 1-electron (21), 2-electron (20) charge transfer, and ionization (io) collisions with H_2 .

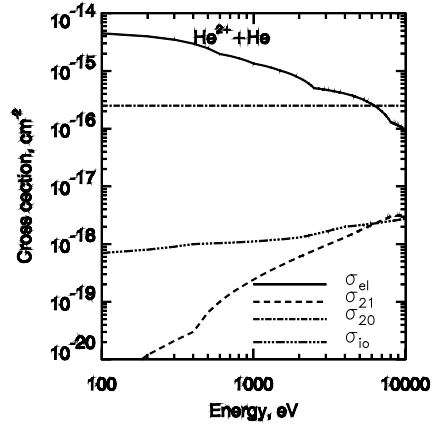


Figure 2f. Compilation of cross sections for He^{2+} elastic (el), 1-electron (21), 2-electron (20) charge transfer, and ionization (io) collisions with He.

The ionization cross sections for the He^{2+} ions collisions with H, H_2 , and He were adopted from the compilation by *Ito et al.* (1995). It is necessary to point out that the values of $\sigma_{\text{io}}(\text{He}^{2+} + \text{H})$ at collision energies below 10 keV are less than 10^{-21} cm^2 , therefore in the model this cross section was assumed to be equal to zero.

The compiled cross sections for He^{2+} collisions with CO_2 , N_2 , O, H, H_2 and He are

shown in Figures 2a-f, correspondingly and summed up in Table 1.

Cross sections for He⁺ collisions with CO₂, N₂, O, H, H₂, and He

We have considered 4 processes for the interaction of He⁺ ions with atomic (M) and molecular (M₂) atmospheric gas - elastic (σ_{el}), charge exchange (σ_{10}), ionization (σ_{i0}), and stripping (σ_{12} , i.e., He⁺ + M → He²⁺ + M + e). Unfortunately we did not find any laboratory or computational data on the cross sections for elastic collisions of He⁺ ions with the atmospheric species under study in the literature. Therefore we assumed in the model that σ_{el} for elastic collisions between He⁺ ions and atmospheric species are the same as ones for the He²⁺ ions (see the previous subsection). For the elastic process He⁺ + He σ_{el} was assumed to be equal to the cross section for the elastic process H⁺ + He taken from [Krstic and Schultz, 2006], but to evaluate the scaling factor of $1.08 \times 10^{-15} / 2.46 \times 10^{15} = 0.439$ we used the measurements of elastic cross sections for the process He + He at the collision energy 0.5 keV from [Newman et al., 1985].

For the charge exchange collisions between He⁺ ions and CO₂, N₂, and O species the shape of the cross sections σ_{10} were taken the same as σ_{21} for the one-electron charge exchange processes He²⁺ + CO₂, N₂, and O, but with scaling factors adopted from [Gao et al., 1990], where measurements at 1.5 keV were made for He⁺ + N₂ and O₂ charge exchange collisions. The scaling factors are equal to $8.3 \times 10^{-16} / 3.98 \times 10^{-16} = 2.09$ for CO₂, $3.7 \times 10^{-16} / 3.76 \times 10^{-16} = 0.98$ for N₂, and $8.3 \times 10^{-16} / 8.45 \times 10^{-16} = 0.98$ for O. Cross sections for charge exchange collisions He⁺ + H, H₂, He → He + H⁺, H₂⁺, He⁺ were adopted from the compilation [Ito et al., 1993].

The ionization cross sections σ_{i0} for the He⁺ + CO₂, N₂, and O processes were not found in the literature, therefore it was assumed in the model that these cross sections are the same as for He²⁺ + CO₂, N₂, and O ionization processes. The ionization cross sections σ_{i0} of the He⁺ collisions with atomic hydrogen H, molecular hydrogen H₂, and helium He were taken from the compilation

[Ito et al., 1995]. It is necessary to mention that values of cross section for the ionization process He⁺ + H are extremely small below 10 keV.

Laboratory and/or computed data on the cross sections for stripping processes (He⁺ + CO₂, N₂, O → He²⁺ + CO₂, N₂, O + e) were not found in the literature. Cross sections for stripping collisions (He⁺ + H, H₂, He → He²⁺ + H, H₂, He + e) are given in the compilation [Ito et al., 1995], but their values are extremely small $< 10^{-20} - 10^{-21}$ at energies below 10 keV. Therefore, the stripping processes were not considered in the model.

Cross sections for He collisions with CO₂, N₂, O, H, H₂, and He

We have considered 3 processes for the interaction of He atoms with atomic (M) and molecular (M₂) atmospheric gas - elastic (σ_{el}), ionization (σ_{i0}), and stripping (σ_{01} , i.e., He + M → He⁺ + M + e). We did not find any laboratory or computational data on the elastic and ionization cross sections of He atoms with the atmospheric species CO₂, N₂, and O in the literature. Therefore we assumed in the model that σ_{el} and σ_{i0} for elastic and ionization collisions between He atoms and atmospheric species CO₂, N₂, and O are the same as ones for the He⁺ ions (see the previous subsection). The cross sections for elastic collisions He + H, and H₂ were assumed to be the same as for He⁺ + H, and H₂ collisions. In case of elastic process He + He σ_{el} was assumed to be equal to the cross section for the elastic process H⁺ + He taken from [Krstic and Schultz, 2006], but to evaluate the scaling factor of $1.08 \times 10^{-15} / 2.46 \times 10^{15} = 0.439$ we used the measurements of elastic cross sections for the process He + He at a collision energy of 0.5 keV from [Newman et al., 1985].

The ionization cross sections σ_{i0} in the He collisions with molecular hydrogen, and helium were taken from the compilation [Ito et al., 1995]. It is necessary to mention that values of cross section for the ionization process He + H were not found in the literature, therefore this cross section was equal to zero in the model.

We did not find any laboratory or computed data on the cross sections for stripping processes ($\text{He} + \text{CO}_2, \text{N}_2, \text{O} \rightarrow \text{He}^+ + \text{CO}_2, \text{N}_2, \text{O} + e$) in the literature, therefore these processes were not taken into account in the model. Cross sections for stripping collisions ($\text{He} + \text{H}, \text{H}_2, \text{He} \rightarrow \text{He}^+ + \text{H}, \text{H}_2, \text{He} + e$) were taken from the compilation [Ito *et al.*, 1995]. It is necessary to mention that the measurements for stripping collisions with atomic hydrogen were made for energies above 80 keV, therefore this cross section was taken equal to zero in the model. For collisions with molecular hydrogen and helium there are additional channels ($\text{He} + \text{H}_2, \text{He} \rightarrow \text{He}^{2+} + \text{H}_2, \text{He} + 2e$) but the magnitudes of the cross sections for such channels are extremely small $< 10^{-20} - 10^{-21}$ at energies below 10 keV.

Scattering angle distributions for collisional processes

Collisions of high-energy $\text{He}/\text{He}^+/\text{He}^{2+}$ particles with the ambient atmospheric gas are characterized by the scattering angle distributions (SADs), which were measured in laboratory at given energies of the projectile particles [Lindsay and Stebbins, 2005].

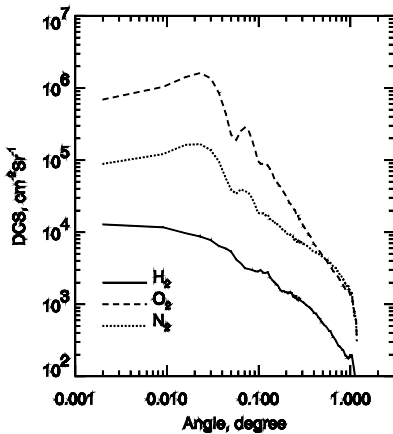


Figure 3. Scattering angle distributions in the elastic collisions of He^{2+} with $\text{H}_2, \text{N}_2,$ and O_2 at a collision energy of 500 eV.

Such distributions are usually peaked at small scattering angles (see Figure 3) reducing the efficiency of energy transfer from high-

energy impact particles to the target atmospheric particles.

To take into account this effect the following scattering angle distributions were used in the model:

- for $\text{He} + \text{CO}_2, \text{N}_2,$ and O processes we adopted the SADs measured for elastic scattering and ionization in the high-energy $\text{He} + \text{O}_2, \text{N}_2,$ and O_2 collisions [Newman *et al.*, 1985]. For stripping $\text{He} + \text{CO}_2, \text{N}_2,$ and $\text{O} \rightarrow \text{He}^+ + \dots$ collisions we did not find any data on the scattering angle distributions therefore we used the measured SADs for $\text{He}^+ + \text{O}_2, \text{N}_2,$ and O_2 charge transfer collisions at 1.5 keV energy [Gao *et al.*, 1990];

- for $\text{He} + \text{H}, \text{H}_2,$ and He processes we adopted the SADs measured for elastic scattering and ionization in the high-energy $\text{He} + \text{H}, \text{H}_2,$ and He collisions [Newman *et al.*, 1985]. For stripping $\text{He} + \text{H},$ and $\text{H}_2 \rightarrow \text{He}^+ + \dots$ collisions we did not find any data on the scattering angle distributions therefore we used the measured SADs for $\text{He}^+ + \text{H}_2$ charge transfer collisions at 1.5 keV energy [Gao *et al.*, 1990]. For stripping $\text{He} + \text{He} \rightarrow \text{He}^+ + \text{He} + e$ collisions we did not find any data on SAD: there we used the SAD measured for elastic and charge transfer $\text{He}^+ + \text{He}$ collisions at 1.5 keV energy [Gao *et al.*, 1988];

- for $\text{He}^+, \text{He}^{2+} + \text{CO}_2, \text{N}_2, \text{O}, \text{H}, \text{H}_2,$ and He collisions we did not find the measurements. Therefore we use the same the SADs as for the He collisions with these neutral species.

4. Results of the calculations

The most interesting effects of solar wind $\text{He}/\text{He}^+/\text{He}^{2+}$ precipitation onto the Mars' upper atmosphere are heating of the neutral gas due to momentum transfer collisions, excitation of the ambient gas emissions, and formation of the backscattered flux of the energetic helium atoms and ions. The later is of particular importance because it defines the helium deposition rate into the neutral atmosphere from the solar wind.

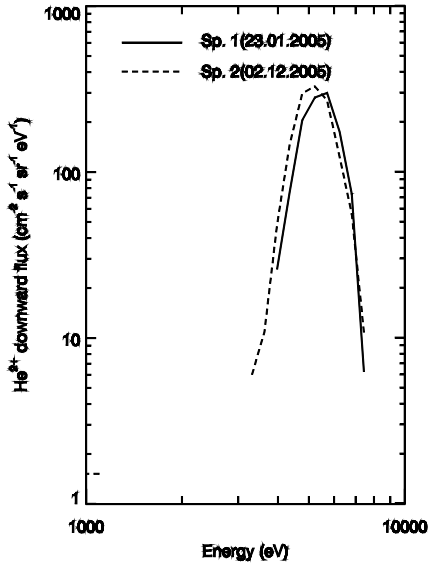


Figure 4. Energy spectra of the downward moving He^{2+} ions measured by ASPERA-3 at an altitude of 500 km for the dates 23.01.2005 and 03.12.2005.

In this work, we use two spectra of the downward moving He^{2+} ions, measured by the Mars Express ASPERA-3, Analyzer of Space Plasmas and Energetic Atoms [Barabash *et al.*, 2006] for two dates: January, 23 and December, 3 2005 (hereafter we call these spectra 1-st, and 2-nd, respectively). The spectra were observed below but close to the IMB at an altitude of about 300-500 km at a solar zenith angles of 35-40 degrees. The energy range of the ASPERA-3 instrument is 10 eV/q–36 keV/q and, hence, covers the full energy range of interest. For the 1-st spectrum the particle flux is equal to $1.07 \times 10^6 \text{ cm}^{-2} \text{ s}^{-1}$, and the energy flux is equal to $9.4 \times 10^{-3} \text{ erg cm}^{-2} \text{ s}^{-1}$. For the 2-nd spectrum the particle flux is equal to $1.77 \times 10^6 \text{ cm}^{-2} \text{ s}^{-1}$, and the energy flux is equal to $9.9 \times 10^{-3} \text{ erg cm}^{-2} \text{ s}^{-1}$. The energy spectra of the downward moving He^{2+} ions measured by ASPERA-3 are shown in Figure 4. He^{2+} energy spectra measured below the IMB are usually narrower in energy than spectra observed in the magnetosheath but with an average energy comparable to solar wind energies. Downgoing He^{2+} is often observed

with most of the flux concentrated in a certain direction and in the simulations we use a monidirectional beam to model the typical distribution.

We have conducted 6 runs that are listed in Table 2 to estimate the magnitudes of the He^{2+} , He^+ , and He backscattered fluxes from the Martian atmosphere. Runs 1, 2, and 3 were conducted for the 1-st spectrum incident flux with different angles of He^{2+} flux relative to nadir: 45° , 60° , and 75° , when an induced magnetic field of strength 20 nT is present. Runs 1, 4, and 5 allow us to evaluate the influence of the induced magnetic field ($B=0, 20$, and 40 nT) on the solution, taking the 1-st spectrum at 45° relative to nadir. Run 6 was made with the same parameters as Run 1, but for the 2-nd spectrum.

Runs with different angles of He^{2+} flux relative to nadir

Run 1 (Table 2) was conducted for the monidirectional incident flux with an angle of nadir of 45° .

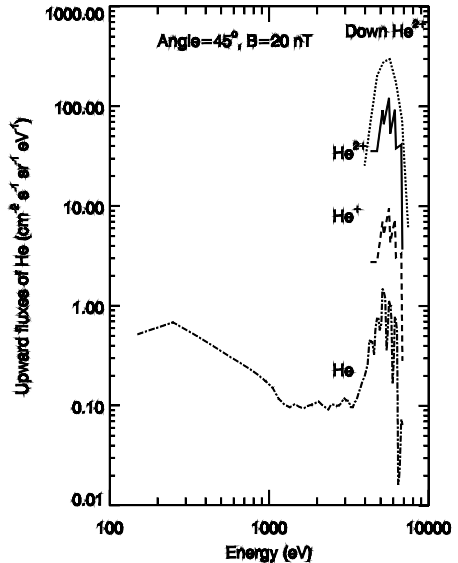


Figure 5a. Energy spectra of the downward (spectrum 1 marked by dotted line) and upward moving He^{2+} (solid line), He^+ (dashed line), and He (dashed-dotted line) for the run with induced magnetic field $B=20 \text{ nT}$ and with direction angle of 45° versus nadir.

The calculated energy spectra of the He^{2+} , He^+ , and He moving upward at the model upper boundary 500 km are given in Figure 5a.

In the calculations with the DSMC model it was found that the interaction of the precipitating He^{2+} with the upper atmosphere results in the formation of the following upward moving fluxes: for He^{2+} the particle flux is equal to $3.1 \times 10^5 \text{ cm}^{-2} \text{ s}^{-1}$ and the energy flux is equal to $2.7 \times 10^{-3} \text{ erg cm}^{-2} \text{ s}^{-1}$; for He^+ - $1.7 \times 10^4 \text{ cm}^{-2} \text{ s}^{-1}$, and $1.5 \times 10^{-4} \text{ erg cm}^{-2} \text{ s}^{-1}$; for He - $9.5 \times 10^3 \text{ cm}^{-2} \text{ s}^{-1}$, and $5.9 \times 10^{-5} \text{ erg cm}^{-2} \text{ s}^{-1}$. In this case 29.1% of the particle flux and 29.2% of the energy flux of the precipitating He^{2+} are backscattered as upward moving α -particles by the Martian upper atmosphere (see Table 3). For He^+ , and He the upward particle fluxes are 1.6% and 0.6%, and the energy fluxes - 1.6%, and 0.9%, respectively. The energy spectrum of the up going He^{2+} follows well the spectrum of the precipitating α -particles. In total, $29.2+1.6+0.6=31.3\%$ of the precipitating particles are reflected backwards.

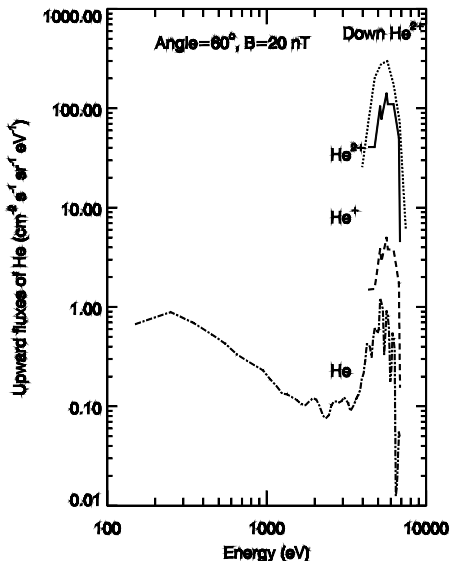


Figure 5b. The same as in Fig. 5a for the direction angle of 60° versus nadir.

Run 2 (Table 2) was conducted for the monodirectional incident flux with an angle to

nadir of 60° . The calculated energy spectra of the He^{2+} , He^+ , and He moving upward at the model upper boundary 500 km are given in Figure 5b. The following values of upward moving fluxes were calculated: for He^{2+} the particle flux is equal to $2.5 \times 10^5 \text{ cm}^{-2} \text{ s}^{-1}$ and the energy flux is equal to $2.2 \times 10^{-3} \text{ erg cm}^{-2} \text{ s}^{-1}$; for He^+ - $8.8 \times 10^3 \text{ cm}^{-2} \text{ s}^{-1}$, and $7.7 \times 10^{-5} \text{ erg cm}^{-2} \text{ s}^{-1}$; for He - $9.0 \times 10^3 \text{ cm}^{-2} \text{ s}^{-1}$, and $4.8 \times 10^{-5} \text{ erg cm}^{-2} \text{ s}^{-1}$. To calculate the relative values of the upward flux it is necessary to take into account that for the monodirectional case the incident flux becomes smaller with increasing of the angle to nadir θ (as $\cos(\theta)$). So, in this case for He^{2+} , He^+ , and He the upward particle fluxes are 33.2%, 1.2% and 0.7%, and the energy fluxes - 33.3%, 1.2%, and 1.2%, respectively (see Table 3). In total, $33.2+1.2+0.7=35.1\%$ of the precipitating particles are reflected backwards.

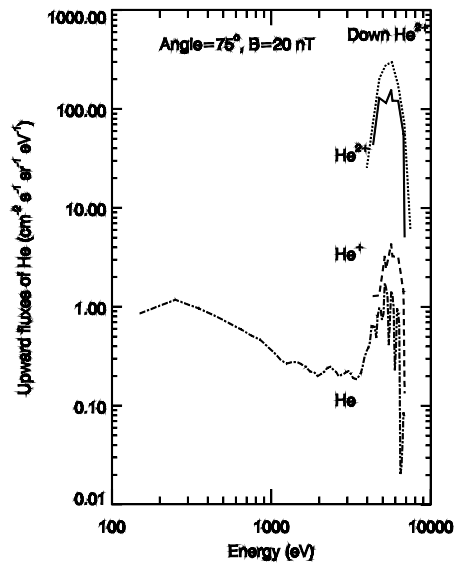


Figure 5c. The same as in Fig. 5a for the direction angle of 75° versus nadir.

Run 3 (Table 2) was conducted for the monodirectional incident flux with an angle to nadir of 75° . The calculated energy spectra of the He^{2+} , He^+ , and He moving upward at the model upper boundary at 500 km altitude are given in Figure 5c. The following values of

upward moving fluxes were calculated: for He^{2+} the particle flux is equal to $1.4 \times 10^5 \text{ cm}^{-2} \text{ s}^{-1}$ and the energy flux is equal to $1.2 \times 10^{-3} \text{ erg cm}^{-2} \text{ s}^{-1}$; for He^+ - $7.1 \times 10^3 \text{ cm}^{-2} \text{ s}^{-1}$, and $6.2 \times 10^{-5} \text{ erg cm}^{-2} \text{ s}^{-1}$, for He - $1.4 \times 10^4 \text{ cm}^{-2} \text{ s}^{-1}$, and $7.5 \times 10^{-5} \text{ erg cm}^{-2} \text{ s}^{-1}$. In this case of He^{2+} , He^+ , and He the upward particle fluxes are 35.6%, 1.8% and 2.2%, and the energy fluxes - 35.6%, 1.8%, and 3.5%, respectively (see Table 3). In total, $35.6+1.8+3.5=40.9\%$ of the precipitating particles are reflected backwards.

Runs with the induced magnetic field

For the incident α -particles spectrum 1, and for the monodirectional flux with angle value of 45° we have conducted three runs for $B=0, 20,$ and 40 nT (Runs 4, 1, and 5 from Table 2). Calculations for the non magnetic case show that there are no upward fluxes. For the case of $B=20 \text{ nT}$ the values of the backscattered (upward) particle and energy fluxes are listed above in the description of the Run 1.

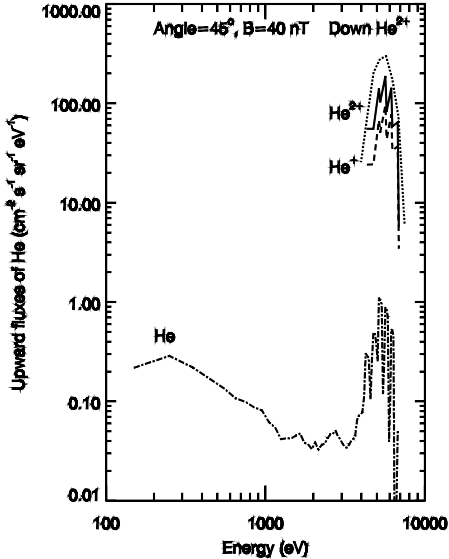


Figure 6. Energy spectra of the downward (spectrum 1 marked by dotted line) and upward moving He^{2+} (solid line), He^+ (dashed line), and He (dashed-dotted line) for the run for spectrum 1 with the 40 nT horizontal component of the induced magnetic field and with direction angle of 45° versus nadir.

For the case of $B=40 \text{ nT}$ we have obtained the following estimates of the backscattered (upward) particle and energy fluxes (see Figure 6): for He^{2+} the particle flux is equal to $5.4 \times 10^5 \text{ cm}^{-2} \text{ s}^{-1}$ and the energy flux is equal to $4.8 \times 10^{-3} \text{ erg cm}^{-2} \text{ s}^{-1}$; for He^+ - $1.5 \times 10^5 \text{ cm}^{-2} \text{ s}^{-1}$, and $1.3 \times 10^{-3} \text{ erg cm}^{-2} \text{ s}^{-1}$, and for He - $5.2 \times 10^3 \text{ cm}^{-2} \text{ s}^{-1}$, and $3.5 \times 10^{-5} \text{ erg cm}^{-2} \text{ s}^{-1}$. For He^{2+} , He^+ , and He the upward particle fluxes are 50.9%, 14.3%, and 0.5%, and energy fluxes - 50.7%, 14.3%, and 0.4%, respectively (see Table 3). In total, $50.9+14.3+0.5=65.7\%$ of the precipitating particles are reflected backwards.

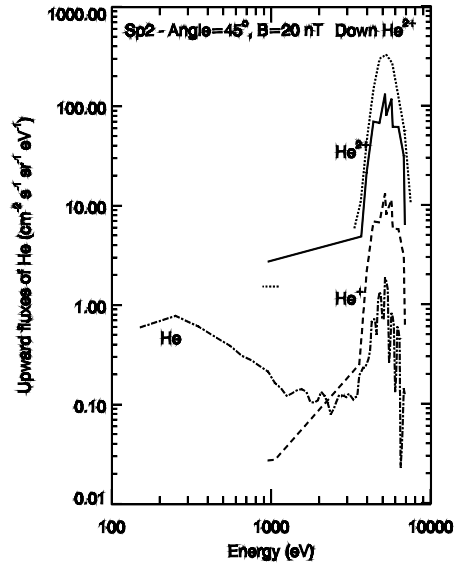


Figure 7. Results of calculations for incident spectrum 2 (03.12.2005). Energy spectra of the downward (dotted line) and upward moving He^{2+} (solid line), He^+ (dashed line), and He (dashed-dotted line) for the run with the 20 nT horizontal component of the induced magnetic field and with direction angle of 45° versus nadir.

For the incident He^{2+} spectrum 2 we have conducted the run (Run 6 from the Table 2) with typical value of the horizontal component of the induced magnetic field $B=20\text{nT}$, and with angle to nadir value of 45° . We have obtained the following estimates of the relative backscattered (upward) particle and energy fluxes (see

Figure 7): for He^{2+} the particle flux is equal to $3.5 \times 10^5 \text{ cm}^{-2} \text{ s}^{-1}$ and the energy flux is equal to $2.9 \times 10^{-3} \text{ erg cm}^{-2} \text{ s}^{-1}$; for He^+ - $2.3 \times 10^4 \text{ cm}^{-2} \text{ s}^{-1}$, and $1.9 \times 10^{-4} \text{ erg cm}^{-2} \text{ s}^{-1}$, and for He - $1.1 \times 10^4 \text{ cm}^{-2} \text{ s}^{-1}$, and $6.4 \times 10^{-5} \text{ erg cm}^{-2} \text{ s}^{-1}$. For He^{2+} , He^+ , and He the upward particle fluxes are 29.4%, 1.9%, and 0.7%, and energy fluxes - 29.6%, 2.0%, and 0.9%, respectively (see Table 3). In total, $29.4 + 1.9 + 0.7 = 32.0\%$ of the precipitating particles are reflected backwards. The particle and energy fluxes of backscattered $\text{He}/\text{He}^+/\text{He}^{2+}$ of solar wind origin are summarized in Table 3a and 3b, correspondingly.

5. Summary and Conclusions

We developed a DSMC model to investigate the transport of the solar wind helium ions and atoms in the Martian upper atmosphere. The model takes into account all physical interaction processes of the $\text{He}/\text{He}^+/\text{He}^{2+}$ propagation through the atmosphere. The important features of the elaborated model are: the detailed consideration of the scattering angle in each collision and the use of the most recent set of cross sections.

We calculated the backscattered flux of energetic $\text{He}/\text{He}^+/\text{He}^{2+}$ particles and the total energy deposition rates. The calculations have been performed for the Martian atmosphere during the solar minimum conditions. We use two spectra of the incident He^{2+} ions at the altitude of 500 km measured by the Mars Express ASPERA-3 in the energy range 700 eV - 20 keV for the dates: January, 23 and December, 3 2005. The particle and energy fluxes of the incident He^{2+} ions is equal to $1.07 \times 10^6 \text{ cm}^{-2} \text{ s}^{-1}$, and $9.4 \times 10^{-3} \text{ erg cm}^{-2} \text{ s}^{-1}$ for the first measurement, and to $1.77 \times 10^6 \text{ cm}^{-2} \text{ s}^{-1}$, and to $9.9 \times 10^{-3} \text{ erg cm}^{-2} \text{ s}^{-1}$ for the 2-nd measurement.

It was found, that with increase of the angle of He^{2+} incident flux relative to nadir, the fluxes of $\text{He}/\text{He}^+/\text{He}^{2+}$ particles backscattered by the Martian upper atmosphere increase. For the angles 45° , 60° , and 75° we found that the total upward flux can be as much as 31.3%, 35.1%, and 39.6%, respectively.

The horizontal magnetic field induced by solar wind leads to an increase of the $\text{He}^+/\text{He}^{2+}$ upward flux because of the ion gyro-motion. Including a 20 nT (40 nT) horizontal magnetic field in the altitude range of 85 km–500 km in the model gives the total backscattered flux of 31.3% (65.7%). The magnetic field plays thus a crucial role in the transport of charged particles and determines the energy deposition of the solar wind protons in the upper atmosphere of Mars. Not more than 70% of all helium ions penetrating the induced magnetosphere are assimilated in the atmosphere. It means the capture efficiency is at least 30% lower than one normally assumes.

The gyro-radius of 1 keV He^{2+} ion in a 20 nT magnetic field is about 230 km that is close the distance between the induced magnetosphere boundary and the exobase. Therefore, the majority of the ions cannot reach the high neutral densities and turn back by the Lorentz force rather than get scattered by the atmospheric particles.

The runs with magnetic field also show that the main component of the backscattered flux is He^{2+} . This is a somewhat unexpected result due to the larger cross section of the elastic scattering than the sum of all processes with the change of the charge state of the precipitating He^{2+} ions.

It is instructive to compare the obtained results with the similar studies of the proton/hydrogen precipitation [Shematovich *et al.*, 2011]. In the case of no magnetic field the total protons and hydrogen backscattered flux is about 22% of the impinging flux while for He^{2+} it is less than 1%. Due to the larger mass ratio between hydrogen and the main atmospheric constituents at the exobase (O and CO_2) than for alpha-particles, the backward scattering is more effective for hydrogen. Yet, the fraction of the neutral component relative to the original ions is larger for hydrogen due to small charge-exchange cross sections for the He^{2+} interactions. For the runs with the magnetic fields, the backscattering of helium ions and atoms significantly increases (up to 31.3, and 65.7% for $B=20$, and 40 nT, respectively). Therefore, similarly to the proton

precipitation it is the magnetic field inside the induced magnetosphere that prevents the precipitating particles from reaching the atmosphere and thus reduces the inflow of matter and energy.

Acknowledgements

The contribution by V.S. and D.B. was supported by the Swedish Research Council via grant "Physics of induced magnetospheres" to the Swedish Institute of Space Physics and the Basic Research Program of the Presidium of the Russian Academy of Sciences, Russian Foundation for Basic Research (Project 11-02-00479a), Federal Targeted Program "Science and Science Education for Innovation in Russia 2009-2013". C.D and G.S are supported by the National Graduate School of Space Technology at Luleå University of Technology.

References:

- Akalin, F., D.D. Morgan, D.A. Gurnett, D.L. Kirchner, D.A. Brain, R. Modolo, M.H. Acuna, and J.R. Espley, Dayside induced magnetic field in the ionosphere of Mars, *Icarus*, 206, 104–111, 2010.
- Brain, D.A., F. Bagenal, M.H. Acuna, and J.E.P. Connerney, Martian magnetic morphology: Contributions from the solar wind and crust, *J. Geophys. Res.*, 108, 1424, 2003, doi:10.1029/2002JA009482.
- Barabash, S., and O. Norberg, Indirect detection of the Martian helium corona, *Geophys. Res. Lett.*, 21, 1547–1550, 1994.
- Barabash, S., E. Kallio, R. Lundin, and H. Koskinen, Measurements of the nonthermal helium escape from Mars, *J. Geophys. Res.*, 100, 21,307–21,316, 1995.
- Barabash, S. et al., The analyzer of space plasmas and energetic atoms (ASPERA-3) for the Mars Express mission, *Space Sci. Rev.*, 126, 1-4, 113-164, 2006.
- Barnett, C.F., Hunter, H.T., Fitzpatrick, M.I., Alvarez, I., Cisneros, C., and R. A. Phaneuf, Atomic data for fusion. Volume 1: Collisions of H, H₂, He and Li atoms and ions with atoms and molecules, NASA STI/Recon Technical Report, 91, 13238, 1990.
- Bisikalo, D. V., V. I. Shematovich, and J.-C. Gérard, Kinetic model of the formation of the hot oxygen geocorona. II. Influence of O⁺ ion precipitation, *J. Geophys. Res.*, 100, 3715-3720, 1995.
- Bovino, S., P. Zhang, F. A. Gianturco, A. Dalgarno, and V. Kharchenko, Energy transfer in O collisions with He isotopes and Helium escape from Mars, *Geophys. Res. Lett.*, 38, L02203, doi:10.1029/2010GL045763, 2011.
- Chanteur, G. M., Dubinin, E., Modolo, R., and M. Fraenz, Capture of solar wind alpha-particles by the Martian atmosphere, *Geophys. Res. Lett.*, 36, DOI: 10.1029/2009GL040235, 2009.
- Decker, D.T., B.V. Kozelov, B. Basu, J.R. Jasperse, and V.E. Ivanov, Collisional degradation of the proton-H atom fluxes in the atmosphere: A comparison of theoretical techniques, *J. Geophys. Res.*, 101, 26947, 1996.
- Diéval C., E. Kallio, S. Barabash, G. Stenberg, H. Nilsson, Y. Futaana, M. Holmström, A. Fedorov, R. A. Frahm, R. Jarvinen and D. A. Brain, A case study of proton precipitation at Mars: Mars Express observations and hybrid simulations, *J. Geophys. Res.*, 117, A06222, doi: 10.1029/2012JA017537, 2012.
- Figueira da Silva, S., H. P. Winter, and F. Aumayr, Single- and double-electron capture cross sections for slow He²⁺ impact on O₂, H₂, and D₂, *Phys. Rev. A* 75, 042706, 2007.
- Fox, J.L., and A.B. Hac, Photochemical escape of oxygen from Mars: A comparison of the exobase approximation to a Monte Carlo method, *Icarus*, 204, 527-544, 2009.
- Futaana, Y., et al. First ENA observations at Mars: ENA emissions from the Martian upper atmosphere, *Icarus*, 182, 424-430, 2006.
- Gao, R. S.; L. K. Johnson, C. L. Hakes, K. A. Smith, and R. F. Stebbings, Collisions of kilo-electron-volt H⁺ and He⁺ with molecules at small angles: Absolute differential cross sections for charge transfer, *Phys. Rev. A* 41 5929, 1990.
- Gao R. S., L. K. Johnson, D. A. Schafer, J. H. Newman, K. A. Smith, and R. F. Stebbings, Absolute differential cross sections for small-

- angle He⁺- He elastic and charge-transfer scattering at keV energies, *Phys. Rev. A* 38, 2789, 1988.
- G rard J.-C., B. Hubert, D.V. Bisikalo, and V.I. Shematovich, A model of the Lyman-  line profile in the proton aurora, *J. Geophys. Res.*, 105, 15795-15806, 2000.
- G rard J.-C., V.I. Shematovich, D.V. Bisikalo, and D. Lummerzheim, A Monte Carlo model of auroral hydrogen emission line profiles, *Annales Geophysicae*, 23, 1432-1439, 2005.
- Haider, S.A., S. P. Seth, E. Kallio, and K.I. Oyama, Solar EUV and electron-proton-hydrogen atom-produced ionosphere on Mars: Comparative studies of particle fluxes and ion production rates due to different processes, *Icarus*, 159, 18-30, 2002.
- Ito R., T. Tabata, T. Shirai, and R. A. Phaneuf, Analytic Cross Sections for Collisions of H, H2, He and Li Atoms and Ions Colliding with Atoms and Molecules. I, *JAERI-M* 93-117, 1993.
- Ito R., T. Tabata, T. Shirai, and R. A. Phaneuf, Analytic Cross Sections for Collisions of H, H2, He and Li Atoms and Ions Colliding with Atoms and Molecules. III, *JAERI-Data/Code* 95-008, 1995.
- Janev, R. K., Langer, W. D., and K. Evans, Elementary processes in Hydrogen-Helium plasmas - Cross sections and reaction rate coefficients, Springer Series on Atoms and Plasmas, Berlin: Springer, 1987.
- Johnson, L. K., R. S. Gao, R. G. Dixson, K. A. Smith, N. F. Lane, R. F. Stebbings, and M. Kimura, Absolute differential cross sections for small-angle H⁺-He direct and charge-transfer scattering at keV energies, *Phys. Rev. A* 40, 3626, 1989.
- Kallio, E., and S. Barabash, Atmospheric effects of precipitating energetic hydrogen atoms on the Martian atmosphere, *J. Geophys. Res.*, 106, 165-178, 2001.
- Kallio, E., J. G. Luhmann, and S. Barabash, Charge exchange near Mars: The solar wind absorption and neutral atom production, *J. Geophys. Res.*, 102, 22183-22198, 1997.
- Krasnopolsky, V. A., and G. R. Gladstone, Helium on Mars and Venus: EUVE observations and modeling, *Icarus*, 176, 395-407, 2005.
- Krasnopolsky, V. A., S. Chakrabarti, and G. R. Gladstone, Helium in the Martian atmosphere, *J. Geophys. Res.*, 98, 15,061-15,068.,1993.
- Krasnopolsky, V. A., S. Bowyer, S. Chakrabarti, G. R. Gladstone, and J. S. McDonald, First measurements of helium on Mars: Implications for the problem of radiogenic gases on the terrestrial planets, *Icarus*, 109, 337-351, 1994.
- Kusakabe T., Y. Miyamoto, M. Kimura, and H. Tawara, Charge-transfer processes in collisions of He2⁺ ions with H2, N2, O2, CO, and CO2 molecules below 4 keV/u, *Phys. Rev. A* 73, 022706, 2006.
- Lindsay, B. G., and R. F. Stebbings, Charge transfer cross sections for energetic neutral atom data analysis, *J. Geophys. Res.*, 110, A12213, 2005, doi: 10.1029/2005JA011298.
- Lindsay, B. G., W. S. Yu, K. F. McDonald, and R. F. Stebbings, Electron capture and loss by kilo-electron-volt oxygen atoms in collisions with He, H2, N2, and O2 ,*Phys. Rev. A* 70, 042701, 2004.
- Lundin, R., et. al., Solar wind-induced atmospheric erosion at Mars: first results from ASPERA-3 on Mars Express, *Science*, 305, 5692, 1933-1936, 2004, doi:10.1126/science.1101860.
- Nagy, A. F., et al. , The plasma environment of Mars, *Space Sci. Rev.*, 111, 33-114, 2004, doi: 10.1023/B:SPAC.0000032718.47512.92.
- Newman, J. H., K. A. Smith, and R.F. Stebbings, Differential scattering cross sections for collisions of 0.5-, 1.5-, and 5.0-keV helium atoms with He, H2, N2, and O2, *J. Geophys. Res.*, 90, 11,045-11,054, 1985.
- Nakai, Y., T. Shirai, T. Tabata, and R. Ito, Cross sections for charge transfer of hydrogen atoms and ions colliding with gaseous atoms and molecules, *Atomic Data and Nuclear Data Tables*, 37, 69-101, 1987.
- Sahoo S., Ionization of atomic oxygen in collision with proton and alpha particle, *Physica Scripta*, 62, 145-147, 2000.
- Shematovich, V. I., Kinetics of suprathermal atoms and molecules in the rarefied planetary atmospheres, In: RARIFIED GAS DYNAMICS: Proceedings of the 26th International Symposium on Rarefied Gas

Dynamics. *AIP Conference Proceedings*, 1084, 1047-1054, 2008.

Shematovich, V. I., D.V. Bisikalo, and J.-C. Gérard, A kinetic model of the formation of the hot oxygen geocorona. I. Quiet geomagnetic conditions, *J. Geophys. Res.*, 99, 23217-23228, 1994.

Shematovich V. I., D. V. Bisikalo, C. Diéval, S. Barabash, G. Stenberg, H. Nilsson, Y. Futaana, M. Holmstrom, and J.-C. Gérard, Proton and hydrogen atom transport in the Martian upper atmosphere with an induced magnetic field, *J. Geophys. Res.*, 116, 2011, doi:10.1029/2011JA017007

Rudd, M. E., Goffe, T. V., and A. Itoh, Ionization cross sections for 10-300-keV/u and electron-capture cross sections for 5-150-

keV/u $^3\text{He}^{2+}$ ions in gases, *Phys. Rev. A*, 32, 2128-2133, 1985.

Smith, G. J., L. K. Johnson, R.S. Gao, K. A. Smith, and R. F. Stebbings, Absolute differential cross sections for electron capture and loss by kilo-electron-volt hydrogen atoms, *Phys. Rev. A* 44, 5647, 1991.

Stenberg, G., H. Nilsson, Y. Futaana, S. Barabash, A. Fedorov and D. Brain, Observational evidence of alpha-particle capture at Mars, *Geophys. Rev. Lett.*, 38, L09101, doi:10.1029/2011GL047155, 2011.

Tabata T., and T. Shirai, Analytic Cross Sections for Collisions of H⁺, H₂⁺, H₃⁺, H, H₂, and H⁻ with Hydrogen Molecules, *Atomic Data and Nuclear Data Tables* 76,1-25, 2000.

Table 1. Summary of cross sections for the He/He⁺/He²⁺ impact on the atmospheric species

No.	Reactions	Reference	Comment / Assumptions
1. Elastic interactions. He²⁺ + M → He²⁺ + M*			
1.1	He ²⁺ + CO ₂	Not available	Based on H ⁺ + O ₂ from <i>Gérard et al.</i> , [2000] for 0.1 – 10 keV normalized by the factor 0.119 to match the theoretically calculated cross section for He + O at 1 eV [<i>Bovino et al.</i> , 2011].
1.2	He ²⁺ + N ₂	Not available	Based on H ⁺ + N ₂ from <i>Gérard et al.</i> , [2000] for 0.1 – 10 keV normalized by the factor 0.274 to match the measured cross section for He + N ₂ at 500 eV [<i>Newman et al.</i> , 1985].
1.3	He ²⁺ + O	Not available	Based on H ⁺ + O ₂ from <i>Gérard et al.</i> , [2000] for 0.1 – 10 keV normalized by the factor 0.119/2 to match the theoretically calculated cross section for He + O at 1 eV [<i>Bovino et al.</i> , 2011].
1.4	He ²⁺ + H	Not available	Based on He + H ⁺ from <i>Krstic and Schultz</i> , [2006] for 0.1 – 10 keV normalized by the factor 0.439 to match the measured cross section for He + H ⁺ at 0.5 keV [<i>Newman et al.</i> , 1985].
1.5	He ²⁺ + H ₂	Not available	Based on He + H ⁺ from <i>Krstic and Schultz</i> , [2006] for 0.1 – 10 keV normalized by the factor 1.86 to match the measured cross section for He + H ₂ at 1.5 keV [<i>Newman et al.</i> , 1985].
1.6	He ²⁺ + He	Not available	Based on He + H ⁺ from <i>Krstic and Schultz</i> , [2006] for 0.1 – 10 keV normalized by the factor 0.439 to match the measured cross section for He + He at 0.5 keV [<i>Newman et al.</i> , 1985].
1.7-11	He ⁺ + CO ₂ , N ₂ , O, H, H ₂	Not available	Assumed to be equal to respective collisions for He ²⁺
1.12	He ⁺ + He	Not available	Based on He + H ⁺ from <i>Krstic and Schultz</i> , [2006] for 0.1 – 10 keV normalized by the factor 0.439 to match the measured cross section for He + He at 0.5 keV [<i>Newman et al.</i> , 1985].
1.13-17	He + CO ₂ , N ₂ , O, H, H ₂	Not available	Assumed to be equal to respective collisions for He ⁺
1.18	He + He	Not available	Based on He + H ⁺ from <i>Krstic and Schultz</i> , [2006] for 0.1 – 10 keV normalized by the factor 0.439 to match the measured cross section for He + He at 0.5 keV [<i>Newman et al.</i> , 1985].
2. One-electron charge exchange: He²⁺ + M → He⁺ + M⁺			
2.1	He ²⁺ + CO ₂	<i>Kusakabe et al.</i> ,	

		2006	
2.2	$\text{He}^{2+} + \text{N}_2$	<i>Kusakabe et al.</i> , 2006	
2.3	$\text{He}^{2+} + \text{O}$	<i>Rudd et al.</i> , 1985	In accordance to [<i>Chanteur et al.</i> , 2009] σ_{21} was taken equal to $4 \times 10^{-16} \text{ cm}^2$ for $E < 5 \text{ keV}$.
2.4	$\text{He}^{2+} + \text{H}$	<i>Ito et al.</i> , 1993	
2.5	$\text{He}^{2+} + \text{H}_2$	<i>Kusakabe et al.</i> , 2006	
2.6	$\text{He}^{2+} + \text{He}$	<i>Ito et al.</i> , 1993	
2.7-10	$\text{He}^+ + \text{CO}_2, \text{N}_2, \text{O}$	Not available	Based on $\text{He}^{2+} + \text{CO}_2, \text{N}_2, \text{O}$ normalized by the respective factors to match the measured cross section for $\text{He}^+ + \text{N}_2, \text{O}_2$ at 0.5 keV [<i>Gao et al.</i> , 1990].
2.11-13	$\text{He}^+ + \text{H}, \text{H}_2, \text{He}$	<i>Ito et al.</i> , 1993	
3. Two-electron charge exchange. $\text{He}^{2+} + \text{M} \rightarrow \text{He} + \text{M}^{++}$			
3.1	$\text{He}^{2+} + \text{CO}_2$	<i>Kusakabe et al.</i> , 2006	
3.2	$\text{He}^{2+} + \text{N}_2$	<i>Kusakabe et al.</i> , 2006	
3.3	$\text{He}^{2+} + \text{O}$	<i>Rudd et al.</i> , 1985	In accordance to [<i>Chanteur et al.</i> , 2009] σ_{20} was taken equal to $2 \times 10^{-16} \text{ cm}^2$ for $E < 5 \text{ keV}$.
3.4	$\text{He}^{2+} + \text{H}_2$	<i>Kusakabe et al.</i> , 2006	
3.5	$\text{He}^{2+} + \text{He}$	<i>Janev et al.</i> , 1987 ; <i>Barnett</i> , 1990	In accordance to [<i>Chanteur et al.</i> , 2009] σ_{20} was taken equal to $2.5 \times 10^{-16} \text{ cm}^2$ for $E < 5 \text{ keV}$.
4. Ionization. $\text{He}^{2+} + \text{M} \rightarrow \text{He}^{2+} + \text{M} + \text{e}$			
4.1	$\text{He}^{2+} + \text{CO}_2$	Not available	Based on $\text{H}^+ + \text{CO}_2$ from <i>Haider et al.</i> , [2002] with the scaling factor same as for $\text{He}^{2+} + \text{O}$.
4.2	$\text{He}^{2+} + \text{N}_2$	Not available	Based on $\text{H}^+ + \text{N}_2$ from <i>Haider et al.</i> , [2002].
4.3	$\text{He}^{2+} + \text{O}$	Not available	Based on $\text{H}^+ + \text{O}$ from <i>Haider et al.</i> , [2002] normalized by the factor 0.5 to match the calculated cross section for $\text{He}^{2+} + \text{O}$ at 10 keV [<i>Sahoo</i> , 2000].
4.4-6	$\text{He}^{2+} + \text{H}, \text{H}_2, \text{He}$	<i>Ito et al.</i> , 1995	$\sigma_{i0}(\text{He}^{2+} + \text{H})$ is $< 10^{-21} \text{ cm}^2$ for $E < 10 \text{ keV}$
4.7-9	$\text{He}^+ + \text{CO}_2, \text{N}_2, \text{O}$	Not available	Same as for $\text{He}^{2+} + \text{CO}_2, \text{N}_2, \text{O}$
4.10-12	$\text{He}^+ + \text{H}, \text{H}_2, \text{He}$	<i>Ito et al.</i> , 1995	$\sigma_{i0}(\text{He}^+ + \text{H})$ is $< 10^{-20} \text{ cm}^2$ for $E < 10 \text{ keV}$
4.13-14	$\text{He} + \text{H}_2, \text{He}$	<i>Ito et al.</i> , 1995	
4.15	$\text{He} + \text{H}$	Not available	Neglected
5. Stripping. $\text{He}^+ + \text{M} \rightarrow \text{He}^{2+} + \text{M} + \text{e}$ or $\text{He} + \text{M} \rightarrow \text{He}^+ + \text{M} + \text{e}$			
5.1-3	$\text{He}^+ + \text{CO}_2, \text{N}_2, \text{O}$	Not available	Neglected in the model
5.4-6	$\text{He}^+ + \text{H}, \text{H}_2, \text{He}$	<i>Ito et al.</i> , 1995	Values of $\sigma_{12} < 10^{-21} \text{ cm}^2$ for $E < 10 \text{ keV}$
5.7-9	$\text{He} + \text{CO}_2, \text{N}_2, \text{O}$	Not available	Neglected in the model
5.10-12	$\text{He} + \text{H}, \text{H}_2, \text{He}$	<i>Ito et al.</i> , 1995	Values of $\sigma_{01} < 10^{-21} \text{ cm}^2$ for $E < 10 \text{ keV}$

Table 2. Input data for the DSMC model.

Run #	B, horiz., nT	Precipitating He ²⁺ distribution versus nadir	Precipitating spectrum
1	20	Monodirectional 45°	ASPERA-3 (spectrum 1)
2	20	Monodirectional 60°	ASPERA-3 (spectrum 1)
3	20	Monodirectional 75°	ASPERA-3 (spectrum 1)
4	0	Monodirectional 45°	ASPERA-3 (spectrum 1)
5	40	Monodirectional 45°	ASPERA-3 (spectrum 1)
6	20	Monodirectional 45°	ASPERA-3 (spectrum 2)

Table 3a. Calculated values of the backscattered energy fluxes of He/He⁺/He²⁺

R un #	B, horiz., nT	Precipitating He ²⁺ distribution versus nadir	Energy up, He, %	Energy up, He ⁺ , %	Energy up, He ²⁺ , %	Energy up, Total, %
1	20	Monodirectional 45° (spectrum 1)	0.6	1.6	29.1	31.3
2	20	Monodirectional 60° (spectrum 1)	0.7	1.2	33.2	35.1
3	20	Monodirectional 75° (spectrum 1)	2.2	1.8	35.6	39.6
4	0	Monodirectional 45° (spectrum 1)	0.0	0.0	0.0	0.0
5	40	Monodirectional 45° (spectrum 1)	0.5	14.3	50.9	65.7
6	20	Monodirectional 45° (spectrum 2)	0.7	1.9	29.4	32.0

Table 3b. Calculated values of the backscattered particle fluxes of He/He⁺/He²⁺

R un #	B, horiz., nT	Precipitating He ²⁺ distribution versus nadir	Particles up, He, %	Particles up, He ⁺ , %	Particles up, He ²⁺ , %	Particles up, Total, %
1	20	Monodirectional 45° (spectrum 1)	0.9	1.6	29.2	31.7
2	20	Monodirectional 60° (spectrum 1)	1.2	1.2	33.3	35.7
3	20	Monodirectional 75° (spectrum 1)	3.5	1.8	35.6	40.9
4	0	Monodirectional 45° (spectrum 1)	0.0	0.0	0.0	0.0
5	40	Monodirectional 45° (spectrum 1)	0.4	14.3	50.7	65.4
6	20	Monodirectional 45° (spectrum 2)	0.9	2.0	29.6	32.5

